Technische Universität München
Fakultät für Physik
Physics of Energy Conversion and Storage

Top-Down Synthesis and Characterization of Nanostructured Oxygen Reduction Reaction Catalysts for PEM Fuel Cells

Johannes Fichtner

Vollständiger Abdruck der von der Fakultät für Physik der Technischen Universität München zur Erlangung des akademischen Grades eines

Doktors der Naturwissenschaften (Dr. rer. nat.)

genehmigten Dissertation.

Vorsitzende(r):	Prof. Dr. David Egger
Prüfer der Dissertation:	1. Prof. Dr. Aliaksandr Bandarenka
	2. Prof. Dr. Julien Bachmann

Die Dissertation wurde am 20.05.2020 bei der Technischen Universität München eingereicht und durch die Fakultät für Physik am 20.08.2020 angenommen.

<<Art is meant to disturb. Science reassures>>

- Georges Braque

Abstract

In an attempt to make the polymer electrolyte membrane fuel cell (PEMFC) technology commercially competitive and thus enable its widespread use, a significant reduction in costs is necessary. This especially applies for the cathode catalyst layer composition, which accounts for one of the largest shares of the production costs of such a hydrogen fuel cell. In this thesis, a simple top-down synthesis technique for the production of PEMFC cathode catalysts was elaborated, which allows the fabrication of supported Pt-based nanoparticles. To achieve nanoparticle formation, macroscopic Pt host electrodes were immersed into an alkali metal cation containing electrolyte (in the presence of a high surface area carbon support material) and subjected to a high external alternating potential. Notably, the synthesis was performed in one step, in one pot and without the utilization of any additives such as capping or stabilizing agents. Using this simple approach, it is illustrated that tailoring of the Pt nanoparticle shape and especially size is possible over a wide range (from ~1 nm to more than 10 nm). Moreover, Pt nanoparticles possessing (concave) surface defects were prepared, which are predicted to be particularly active toward the oxygen reduction reaction (ORR) in acidic media. The nature of these surface defects was investigated using various microscopic, crystallographic and spectroscopic techniques, unambiguously supporting the assumption of a strained and concave surface structure. In addition, the activity with respect to the ORR was investigated in a half-cell setup as well as in a membrane electrode assembly. In the half-cell configuration, a mass activity of up to 712 mA/mg_{Pt} and a specific activity of up to 1.6 mA/cm^2_{Pt} were measured (in 0.1 M $HClO_4$ at 0.9 V relative to the reversible hydrogen electrode). These values are ~1.7- and 2.7-times higher than those measured for the commercial Pt/C_{TKK} reference electrocatalyst, respectively. Finally, the applicability toward the synthesis of alloyed Pt-based nanomaterials, especially Pt-lanthanide nanoparticles, was examined. Using Pt_xPr as a model system, formation of different alloy phases was verified and correlated to the observed ORR activity enhancement *vs* Pt/C_{TKK}. Attempts to prepare nanostructured alloys of Pt with 3d transition metal elements (Pt_xM) in the same manner led to segregation of the non-noble element. Hence, a simple alternative to achieve Pt_xM alloying was elaborated.

Zusammenfassung

Bei dem Versuch, die Polymerelektrolytbrennstoffzellen (PEMFC)-Technologie kommerziell wettbewerbsfähig zu machen und damit ihren breiten Einsatz zu ermöglichen, ist eine deutliche Kostenreduzierung notwendig. Dies gilt insbesondere für die Zusammensetzung der Kathoden-Katalysatorschicht, die einen der größten Anteile an den Produktionskosten einer solchen Wasserstoff-Brennstoffzelle ausmacht. In dieser Arbeit wird ein einfaches Top-Down-Syntheseverfahren für Kathoden-Katalysatoren von PEMFCs vorgestellt, welches die Herstellung von geträgerten Pt-basierten Nanopartikeln ermöglicht. Um die Bildung von Nanopartikeln zu erreichen, wurden makroskopische Pt Wirtselektroden in einen alkalimetallhaltigen Elektrolyten (in Gegenwart eines Kohlenstoff-Trägermaterials mit großer Oberfläche) getaucht und einer hohen externen Wechselspannung ausgesetzt. Es ist hervorzuhaben, dass die Synthese in einem Schritt, in einem Topf und ohne Zugabe von Additiven, wie z.B. Abdeck- oder Stabilisierungsmitteln, durchgeführt wurde. Anhand dieses einfachen Ansatzes wird aufgezeigt, dass eine Anpassung der Pt-Nanopartikelform und insbesondere -größe über einen weiten Bereich (von ~1 nm bis über 10 nm) möglich ist. Zudem wurden Pt Nanopartikel mit (konkaven) Oberflächendefekten hergestellt, die besonders aktiv gegenüber der Sauerstoffreduktionsreaktion (ORR) im sauren Medium sein sollen. Die Art dieser Oberflächendefekte wurde mit verschiedenen mikroskopischen, kristallographischen und spektroskopischen Techniken untersucht, die die Annahme einer spannungsreichen und konkaven Oberflächenstruktur eindeutig unterstützen. Darüber hinaus wurde die Aktivität in Bezug auf die ORR sowohl in einem Halbzellenaufbau, als auch in einer Membran-Elektroden-Anordnung untersucht. In der Halbzellenkonfiguration wurde eine Massenaktivität bis zu 712 mA/mg_{Pt} und eine spezifische Aktivität bis zu 1,6 mA/cm^2_{Pt} gemessen (in 0.1 M $HClO_4$ bei 0.9 V relativ zur reversiblen Wasserstoffelektrode). Diese Werte sind ~1,7- beziehungsweise 2,7-mal höher als die für den kommerziellen Pt/C_{TKK} Referenz-Elektrokatalysator gemessenen Werte. Schließlich wurde die Anwendbarkeit auf die Synthese von legierten Pt-basierten Nanomaterialien, insbesondere Pt-Lanthanid-Nanopartikeln, untersucht. Unter Verwendung von Pt_xPr als Modellsystem wurde die Bildung verschiedener Legierungsphasen verifiziert und mit der beobachteten Steigerung der ORR-Aktivität im Vergleich zu Pt/C_{TKK} korreliert. Die Versuche, nanostrukturierte Legierungen aus Pt mit 3d Übergangsmetallelementen (Pt_xM) mit derselben Methode zu synthetisieren, führten zu einer Separation des unedlen Elements. Deshalb wurde eine einfache Alternative zur Bildung von Pt_xM Legierungen erarbeitet.

Acknowledgements

In the last three years, several people supported this work, for which I would like to express my greatest thanks and respect.

First of all, I would like to thank my supervisor **Aliaksandr Bandarenka** for providing this interesting topic and for his great scientific support. For the financial funding during my doctorate, I would like to thank the TUM *International Graduate School of Science and Engineering (IGSSE)*. I would also like to thank my office colleagues **Sebastian Watzele**, **Song Xue, Batyr Garlyyev** and **Yunchang Liang** for the friendly atmosphere and the scientific discussions. I would like to particularly emphasize the contributions of **Sebastian Watzele** and **Batyr Garlyyev**, who have strongly supported this work with their expertise in the field of electrochemistry and contributions to the synthesis and analysis of the electrocatalysts investigated within this work. I would also like to thank all other (former) members of the TUM *Physics of Energy Conversion and Storage* group for the friendly relationship, including **Philipp Marzak, Daniel Scieszka, Regina Kluge, Jeongsik Yun, Richard Haid, Tim Lochner, Jarek Sabawa, Leon Katzenmeier and Shujin Hou**. Shujin deserves special thanks for the XRD measurement of Pt_xCu/C (Chapter 6). I am thankful to our technical staff **Siegfried Schreier** for his great work and the great conversations we had in the last years. Our master students **Xiaohan Sun** and **Theophilus Sarpey**, our bachelor students **Felix Haimerl, Leonardo Stamerra, Simon Lechner, Johannes Figueiredo** and **Casper Galen** and our research assistants **Viktoriia Olevskaia** and **Mateo Flohr Reija** deserve my greatest thanks for their work. In particular, the support of **Felix** and **Mateo** in the synthesis of Pt/C_{TD} samples (Chapters 3 and 4), **Leonardo**'s assistance in the synthesis of Pt_xNi/C samples (Chapter 6) and **Theophilus**' work on Pt_xCu/C (Chapter 6) under my guidance have to be highlighted.

In addition, the work presented here would not have been possible without the help of several external collaborators. First of all, I would like to especially thank **Frédéric Maillard** and **Laetitia Dubau** from the *Laboratoire d'Electrochimie et de Physico-chimie des Matériaux et des Interfaces* (CNRS, France; Grenoble INP, France), as well as **Raphaël Chattot** from the *European Synchrotron Radiation Facility* (Grenoble, France), for their help with the *post-mortem* STEM imaging, WAXS analysis and Rietveld refinement of Pt/C_{TD} and Pt/C_{TKK} samples, the STEM-EDX and SEM imaging of Pt_xPr/C and Pt_5Pr samples, as well as the STEM-EDX imaging of Pt_xNi/C samples (Chapters 4, 5 and 6) and the great scientific discussions.

Moreover, I am particularly thankful to **Frédéric Maillard** and **Ifan Stephens** for hosting me during my research stays abroad at the *Grenoble Institute of Technology* and the *Imperial College London,* respectively.

I would like to thank **Hubert Gasteiger, Hany El-Sayed** and **Jan Schwämmlein** from the TUM *Chair of Technical Electrochemistry* for their help with the TEM imaging and single-cell PEMFC measurements of Pt/C_{TD} samples, TEM imaging and TGA measurement of Pt_xPr/C samples and the constructive discussions (Chapters 3, 4, 5).

Besides, I would like to thank **Jan Macák** and **Jan Michalička** from the *Central European Institute of Technology* (Brno, Czech Republic) for their help with the STEM(-HAADF) imaging, HR-TEM imaging, STEM-HAADF tomography and Fourier analysis of Pt_{TD} or Pt/C_{TD}, (HR-)TEM imaging of Pt_xPr/C, as well as STEM(-EDX) imaging of Pt_xCu/C samples (Chapters 3, 4, 5, 6). I would like to thank **Wei-Jin Li** from the TUM *Chair of Inorganic and Metal-Organic Chemistry* and *Catalysis Research Center* for the help with the TGA measurement of Pt/C_{TD} samples and the XRD analysis of Pt_xPr/C (Chapters 4, 5). I would like to thank **Christoph Hugenschmidt** and **Thomas Gigl** from TUM *FRM II* for their help with Positron Annihilation Spectroscopy analysis of Pt/C_{TD} (Chapter 4). I would also like to thank **Viktor Hlukhyy** from the TUM *Chair of Inorganic Chemistry with Focus on Novel Materials* for his help with the preparation of macroscopic PtNi alloys (Chapter 6).

Finally, I would like to thank my parents for their endless support during my studies and my doctorate, as this work would not have been possible without them, as well as my fiancée **Alexandra**, who has accompanied me in the last years with all her grace, love and endless support.

List of Publications

- Garlyyev, B.; Watzele, S.; Fichtner, J.; Michalička, J.; Schökel A.; Senyshyn, A.; Perego, A.; Pan, D.; El-Sayed, H. A.; Macak, J. M.; Atanassov, P.; Zenyuk, I. V.; Bandarenka, A. S. Electrochemical Top-Down Synthesis of C-Supported Pt Nanoparticles with Controllable Shape and Size: Mechanistic Insights and Application. *Nano Research* **2020**, accepted, https://doi.org/10.1007/s12274-020-3281-z.

- Xue, S.; Haid, R. W.; Kluge, R. M.; Ding, X.; Garlyyev, B.; Fichtner, J.; Watzele, S.; Hou, S.; Bandarenka, A. S. Enhancing the Hydrogen Evolution Reaction Activity of Platinum Electrodes in Alkaline Media Using Ni-Fe Clusters. *Angewandte Chemie International Edition* **2020,** accepted, https://doi.org/10.1002/anie.202000383.

- Garlyyev, B.; Xue, S.; Fichtner, J.; Bandarenka, A. S.; Andronescu. C. Prospects of Value-Added Chemicals and Hydrogen via Electrolysis. *ChemSusChem* **2020**, accepted, https://doi.org/10.1002/cssc.202000339.

- Fichtner, J.; Watzele, S.; Garlyyev, B.; Kluge, R. M.; Haimerl, F.; El-Sayed, H. A.; Li, W.-J.; Maillard, F. M.; Dubau, L.; Chattot, R.; Michalička, J.; Macak, J. M.; Wang, W.; Wang, D.; Gigl, T.; Hugenschmidt, C.; Bandarenka, A. S. Tailoring the Oxygen Reduction Activity of Pt Nanoparticles through Surface Defects: A Simple Top-Down Approach. *ACS Catalysis* **2020**, *10* (5), 3131−3142.

- Li, W.-J.; Xue, S.; Watzele, S.; Hou, S.; Fichtner, J.; Semrau, A. L.; Zhou, L.; Welle, A.; Bandarenka, A. S.; Fischer, R. A. Advanced Bifunctional Oxygen Reduction and Evolution Electrocatalyst Derived from Surface-Mounted Metal-Organic Frameworks. *Angewandte Chemie International Edition* **2020**, *59* (14), 5837-5843.

- Watzele, S.; Hauenstein, P.; Liang, Y.; Xue, S.; Fichtner, J.; Garlyyev, B.; Scieszka, D.; Claudel, F.; Maillard, F.; Bandarenka, A. S. Determination of Electroactive Surface Area of Ni-, Co-, Fe-, and Ir-Based Oxide Electrocatalysts. *ACS Catalysis* **2019**, *9* (10), 9222-9230.

- Garlyyev, B.; Fichtner, J.; Piqué, O.; Schneider, O.; Bandarenka, A. S.; Calle-Vallejo, F. Revealing the Nature of Active Sites in Electrocatalysis. *Chemical Science* **2019**, *10* (35), 8060-8075.

- Garlyyev, B.; Kratzl, K.; Rück, M.; Michalička, J.; Fichtner, J.; Macak, J. M.; Kratky, T.; Günther, S.; Cokoja, M.; Bandarenka, A. S.; Gagliardi, A.; Fischer, R. A. Optimizing the Size of Platinum Nanoparticles for Enhanced Mass Activity in the Electrochemical Oxygen Reduction Reaction. *Angewandte Chemie International Edition* **2019**, *58* (28), 9596-9600.

- Fichtner, J.; Garlyyev, B.; Watzele, S.; El-Sayed, H. A.; Schwämmlein, J. N.; Li, W.-J.; Maillard, F. M.; Dubau, L.; Michalička, J.; Macak, J. M.; Holleitner, A.; Bandarenka, A. S. Top-Down Synthesis of Nanostructured Platinum-Lanthanide Alloy Oxygen Reduction Reaction Catalysts: Pt_xPr/C as an Example. *ACS Applied Materials and Interfaces* **2019**, *11* (5), 5129-5135.

- Garlyyev, B.; Liang, Y.; Xue, S.; Watzele, S.; Fichtner, J.; Li, W.-J. Ding, X.; Bandarenka, A. S. Theoretical and Experimental Identification of Active Electrocatalytic Surface Sites. *Current Opinion in Electrochemistry* **2019**, *14*, 206-213.

- Watzele, S.; Fichtner, J.; Garlyyev, B.; Schwämmlein, J. N.; Bandarenka, A. S. On the Dominating Mechanism of the Hydrogen Evolution Reaction at Polycrystalline Pt Electrodes in Acidic Media. *ACS Catalysis* **2018**, *8* (10), 9456-9462.

- Xue, S.; Garlyyev, B.; Watzele, S.; Liang, Y.; Fichtner, J.; Pohl, M. D.; Bandarenka, A. S. Influence of Alkali Metal Cations on the Hydrogen Evolution Reaction Activity of Pt, Ir, Au and Ag Electrodes in Alkaline Electrolytes. *ChemElectroChem* **2018**, *5* (17), 2326-2329.

- Scieszka, D.; Sohr, C.; Scheibenbogen, P.; Marzak, P.; Yun, J.; Liang, Y.; Fichtner, J.; Bandarenka, A. S. Multiple Potentials of Maximum Entropy of a $Na_2Co[Fe(CN)_6]$ Battery Electrode Material: Does the Electrolyte Composition Control the Interface? *ACS Applied Materials and Interfaces* **2018***, 10* (25), 21688-21695.

- Bors, R.; Yun, J.; Marzak, P.; Fichtner, J.; Scieszka, D.; Bandarenka, A. S. Chromium(II) Hexacyanoferrate-Based Thin Films as a Material for Aqueous Alkali Metal Cation Batteries. *ACS Omega* **2018**, *3* (5), 5111-5115.

Conference Contributions

Oral Presentations:

- “Top-Down Synthesis of Nanostructured Electrocatalysts for the Oxygen Reduction Reaction”. **23rd European Fuel Cell Forum**, Lucerne, Switzerland, 02.-05.07.2019.

- “Active Nanostructured PEM Fuel Cell Oxygen Reduction Reaction Catalysts Produced by Cathodic Corrosion”. **GDCh Electrochemistry Conference**, Ulm, Germany, 24.-26.09.2018.

- “Active Nanostructured PEM Fuel Cell Oxygen Reduction Reaction Catalysts Produced by Cathodic Corrosion”. **69th Annual Meeting of the International Society of Electrochemistry**, Bologna, Italy, 02.-07.09.2018.

Poster Presentations:

- “Top-Down Synthesis of Nanostructured Platinum-Lanthanide Alloy Electrocatalysts: Pt_xPr as an Example”. **8th Energy Colloquium of the Munich School of Engineering**, Munich, Germany, 19.07.2018.

Abbreviations

β	Full peak width at half maximum intensity
η_{HOR}	Hydrogen oxidation reaction overpotential
η_{ORR}	Oxygen reduction reaction overpotential
η_{tx}	Gas transport resistance-induced overpotential
θ	Bragg Angle
κ	Scherrer constant
λ	Wavelength
ϱ	Density
ϕ	Work function
ω	Rotation speed
2D	Two-dimensional
3D	Three-dimensional
A	Area
AC	Alternating current
ACL	Anode catalyst layer
ad	Adsorbed
AST	Accelerated stress test
BoP	Balance of Plant
BPP	Bipolar plate
BSE	Backscattered electron
c	Concentration
CE	Counter electrode
CCL	Cathode catalyst layer
cn	Conventional coordination number
$\overline{CN}$	Generalized coordination number
CV	Cyclic voltammogram/Cyclic voltammetry
$\overline{\mathrm{D}}$	Dispersion parameter
D	Diffusion coefficient
$\mathrm{d_F}$	Feret diameter
$\mathrm{d_P}$	Interplanar distance

d_N	Number-averaged diameter (TEM)
d_S	Surface-averaged diameter (TEM)
d_C	XRD-derived crystallite size
des	Desorbed
DOE	Department of Energy
e^-	Electron
E	Potential
E_{bin}	Binding energy
E_{Cell}	Cell voltage
$E_{IR\text{-}free}$	IR drop-corrected potential
E_{kin}	Kinetic energy
E_m	Measured potential
E_{Rev}	Reversible cell voltage
ECSA	Electrochemically active surface area
EDX	Energy-dispersive X-ray spectroscopy
EIS	Electrochemical impedance spectroscopy
EtOH	Ethanol
EV	Electric vehicle
f	Chemical disorder
F	Faraday constant
FC	Fuel cell
FCEV	Fuel cell electric vehicle
GDL	Gas diffusion layer
Geo	Geometrical
H^+	Proton
H_{UPD}	Hydrogen underpotential deposition
HAADF	High-angle annular dark-field
HER	Hydrogen evolution reaction
HGS	Hollow graphitic spheres
HOR	Hydrogen oxidation reaction
HR-(S)TEM	High-resolution (S)TEM
HSAC	High surface area carbon

hν	Photon energy
TEM	Transmission electron microscopy
I	Electric current
I_{kin}	Kinetic current
I_{lim}	Limiting current
I_m	Measured current
I/C	Ionomer to carbon ratio
ICE	Internal combustion engine
J	Current density
MA	Mass activity
MEA	Membrane electrode assembly
MOF	Metal-organic framework
MPL	Microporous layer
OCV	Open circuit voltage
OER	Oxygen evolution reaction
ORR	Oxygen reduction reaction
PAS	Positron annihilation spectroscopy
PDF	Powder diffraction file
PEM	Polymer electrolyte membrane
PEMFC	Polymer electrolyte membrane fuel cell
ppm	Parts per million
PSD	Particle size distribution
Pt/C	Carbon-supported Pt nanoparticles
$Pt/C_{E\text{-}TEK}$	Commercial Pt/C from E-TEK company
Pt/C_{TD}	Top-down synthesized Pt/C
Pt/C_{TKK}	Commercial Pt/C from TKK company
Pt_xCu/C	Carbon-supported Pt-Cu alloy nanoparticles
Pt_xM/C	Carbon-supported Pt–3d transition metal alloy nanoparticles
Pt_xNi/C	Carbon-supported Pt-Ni alloy nanoparticles
Pt@Ni/C	Carbon-supported Pt-Ni core-shell nanoparticles
Pt_xPr/C	Carbon-supported Pt-Pr alloy nanoparticles
PTFE	Polytetrafluoroethylene

Q	Charge
R	Resistance
$\bar{R}$	Ideal gas constant
R_{HF}	High frequency resistance
$R_{H^+}^{an}$	Anode proton transport resistance
$R_{H^+}^{cat}$	Cathode proton transport resistance
RDE	Rotating disk electrode
RE	Reference electrode
r.f.	Roughness factor
RH	Relative humidity
RHE	Reversible hydrogen electrode
rpm	Rotations per minute
SA	Specific activity
SD	Surface distortion
SEM	Scanning electron microscopy
SHE	Standard hydrogen electrode
SSA	Specific surface area
STEM	Scanning transmission electron microscopy
T	Temperature
TEM	Transmission electron microscopy
TD	Top-down
TGA	Thermogravimetric analysis
TKK	Tanaka Kikinzoku Kogyo K.K. company
UHV	Ultra-high vacuum
v	Kinematic viscosity
WAXS	Wide-angle X-ray scattering
WE	Working electrode
XPS	X-ray photoelectron spectroscopy
XRD	X-ray diffraction

Table of Contents

Chapter 1. Introduction and Overview

The commercialization of the hydrogen fuel cell (FC) technology is one of the most promising opportunities to decouple our energy production, both stationary and mobile, from the carbon cycle. The reduction of air pollution, partly caused by internal combustion engine (ICE)-driven cars, is one of the demanding challenges of the 21th century, particularly in the light of the climate change. The emphasis of this chapter, therefore, lies on the key fundamentals behind the FC technology. Thereby, it is not only of paramount importance to comprehend the functional principle of a (hydrogen) fuel cell, but also to grasp the processes occurring at the electrified electrode-electrolyte interface.

1.1 Electric Vehicles, Hydrogen Economy and Renewable Energy Provision Schemes

In the recent years, the automotive industry was undergoing a revolution: Electric vehicles (EVs) gained growing attention, based on the ambitions to cope with the climate change and reduce the impact of humanity on the carbon cycle, since fossil fuels are environmentally harmful and limited in quantity on earth. At the end of the 19th and beginning of the 20th century, battery-powered EVs occasionally had the largest share of the total car market, but were repressed by the rapid development of ICE-powered cars with greater driving ranges and the falling (fuel) prices.[1] Since the beginning of the 21st century, however, the EV industry experiences a renaissance. Especially since the market launch of the Tesla Model S in 2012, the public perception of EVs has improved,[2] which is for instance based on an improved technology but also on an increasing public environmental awareness. In addition, based on the Paris climate agreement, national and international climate and energy policies have enacted strict emission regulations for greenhouse gases, some of which require a rapid reduction in the CO_2 balance, *e.g.* in the automotive sector.[3,4] Hence, almost every relevant commercial car company has expressed strong ambitions to at least partially "electrify" its product range.[4] Statistically speaking, however, even in large industrialized countries still only a comparatively small proportion of EVs is licensed per year,[5] since consumers apparently are still more likely to opt for an ICE-driven car. The reasons for this can be manifold. For example, the selection of available products is still small compared to the amount of ICE-driven vehicles released annually.[6] Moreover, utilization of the battery technology, which is currently the most common way to power EVs, leads to many disadvantages compared to classical combustion engines such as a lower driving range, long charging times and high acquisition costs, which does not always meet the customer requirements.[7] In the search of suitable alternatives for the operation of EVs, the hydrogen FC technology stands out in particular. Primarily, this is owed to the higher driving range and rapid refueling, which are more comparable to ICE-driven vehicles.[8,9,10] Simply put, the principle of such a cell is to generate electricity through the controlled electrochemical reaction of H_2 with atmospheric oxygen (O_2), which can be used to power an electric motor.[11]

The first attempts to replace combustion engines by hydrogen fuel cells can be traced back to the 1960s, when General Motors developed a prototype of a roadworthy fuel cell electric vehicle (FCEV), but the specifications could not compete with that of ICE-driven cars at that time.[12] In the following years, steady research by different car manufacturers led to the demonstration of the

Honda FXC Clarity as a retail-ready hydrogen FCEV in the first decade of the 21th century, followed by the release of other series production-ready cars such as the Hyundai ix35 and the Toyota Mirai in the recent years.[9,10] Ever since then, FC technology has steadily developed, and current generations of FCEVs show promising specifications outperforming battery-driven vehicles. Comparing state-of-the-art FC cars, *e.g.* the Hyundai Nexo, with similar-sized state-of-the-art battery-powered vehicles, *e.g.* the Tesla Model X, one notes clear differences. Not only does the driving range of the Nexo beat the one of the Model X (~666 km compared to ~507 km according to the worldwide harmonized light vehicles test procedure, WLTP),[13,14] the charging times also differ drastically. While the Nexo's 6 kg H_2 tank can be refueled in about 5 minutes at 700 bar pressure, [13,15] a full top-up of the 100 kWh battery of the Model X takes a multiple of that time (depending on the charging power), even at the dedicated Tesla fast charging stations (150 kW).[16,17] Despite the advantages, the widespread use of the FC technology is not yet conceivable. One reason for this is that the H_2 gas station network has not been developed far enough to ensure extensive usability, especially on long-distance travels. As of 2020, almost 20,000 battery charging stations were available to customers in Germany, compared to less than 100 H_2 gas stations.[18,19]

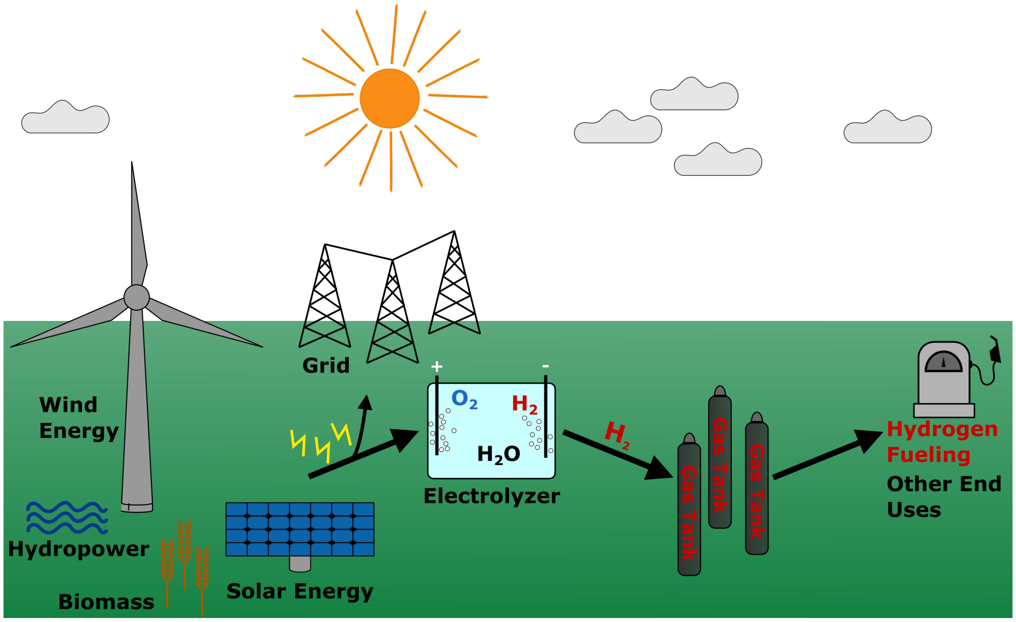

Figure 1. Schematic generation, storage and distribution of H_2 from renewable energy sources such as wind energy, hydropower, biomass or solar energy using water electrolysis.

Moreover, in order to meet sustainability targets, a sufficient amount of hydrogen has to be generated from renewable energy sources. At present, large amounts of H_2 are still obtained from natural gas steam reforming processes, which demand the exploitation of fossil fuel sources.[20] The most promising alternative to produce ecological H_2 is the use of electricity to split water into its elements, *i.e.* hydrogen and oxygen, during water electrolysis.[21] In the case of an acidic electrolyte, the reactions proceed according to

$$\sum: \quad 2H_2O \rightarrow 2H_2 + O_2 \qquad \textbf{(1)}$$

$$\text{OER (Anode):} \quad 2H_2O \rightarrow 4H^+ + 4e^- + O_2 \qquad \textbf{(2)}$$

$$\text{HER (Cathode):} \quad 4H^+ + 4e^- \rightarrow 2H_2 \qquad \textbf{(3)}$$

where OER is the so-called oxygen evolution reaction and HER is the so-called hydrogen evolution reaction.[22] Consequently, generated hydrogen can be stored in a gaseous form using pressure tanks or in a chemical form using, for example, liquid organic hydrogen carriers, which enables facile transportation and on-demand utilization. [23,24,25,26] Again, for closing the sustainable energy cycle, electricity used in this type of power-to-gas conversion has to be produced from renewable energy sources such as wind farms, hydroelectric power stations, biomass plants or solar energy plants (Figure 1).[27] At present, however, water electrolysis only contributes to a low share (about 4%) of the global H_2 production, due to the high acquisition and operating costs of the technology compared to industrial steam reforming plants,[28,29] which is currently tackled by extensive research in the field.[30,31]

Another point limiting the spread of the FC technology is the comparably high cost of the fuel cell stack,[32] which particularly limits the development of vehicles in the low- and mid-range price segments. Figure 2 shows the projected costs of the major FC stack constituents at an annual production volume of 500,000 units.[33] One of the most significant shares is the catalyst material, which contributes to more than 40% of the overall production costs. In the case of the polymer electrolyte membrane fuel cell (PEMFC) technology, the catalytically active material at both electrodes is typically based on Pt and/or Pt alloy nanoparticles, which are highly expensive due to the scarcity of Pt and complex synthesis procedures.[11] At the anode, comparably low amounts of the Pt catalyst are required due to fast kinetics. In contrast, the Pt content at the cathode has to be reduced in order to cut costs. As summarized by Kongkanand and Mathias, typical state-of-the-art cathode Pt loadings have to be approximately halved (from ~0.2 to ~0.1 mg_{Pt}/cm^2),[34] in order to meet the US Department of Energy (DOE) targets and make the technology commercially competitive. Considering this, reasonable ways to reduce the Pt amount in a PEMFC's cathode catalyst layer (CCL) have to be developed, which is the main objective of this work (see also Chapter 1.7) and will be discussed in more detail in the following chapters.

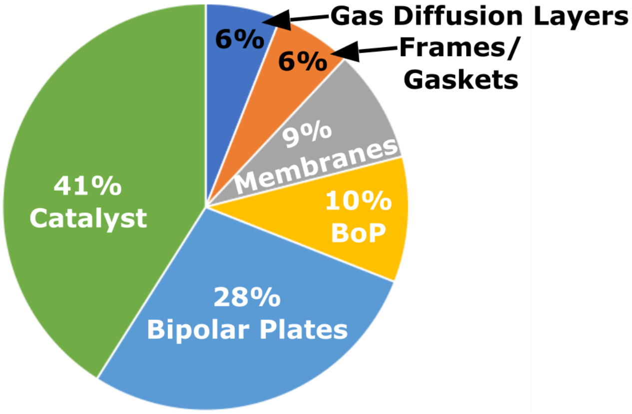

Figure 2. PEMFC stack cost shares projected for 500,000 annually produced units. Even at high quantities, one of the largest cost shares can be assigned to the catalyst material used. Data taken from ref. 33. BoP abbreviates balance of plant, *i.e.* peripherals, supporting components.

1.2 (Hydrogen) Fuel Cells and their Applications

To date, fuel cells are one of the best choices to convert chemical energy, stored in the form of a fuel (such as electrolytically generated H_2), into electrical energy. Briefly, the working principle of such a cell is based on the reaction of the fuel with an oxidant, which is typically a net exothermic process, but needs to be catalyzed to reach effective conversion rates.[11] Due to their adjustable power and size in different performance ranges, as well as their high reliability, fuel cells can be used in both stationary and mobile applications.[35] Today, fuel cell systems are therefore used in stationary devices such power generators,[36] or to power electric motors in cars or trucks.[37] In addition to the production of passenger cars and trucks with PEMFC drive systems, ambitious projects for the electrification of long-distance and local public transport have been launched in recent years, for example by the FlixMobility GmbH (intercity bus company) in Germany.[38] The main characteristic of common fuels used (such as the aforementioned H_2, but also *e.g.* methanol) is their relatively high specific energy. In the recent decades several different types of fuel cells have been investigated and developed, such as alkaline fuel cells, direct methanol fuel cells, phosphoric acid fuel cells, solid oxide fuel cells or PEMFCs.[11] While all types of FCs exhibit different pros and cons, the PEMFC can be highlighted due to its low operating temperature (typically < 100 °C) and weight, as well as comparatively high electrical efficiency in transport applications (~60%), power density and robustness (*e.g.* against corrosion).[11,39,40] Hence, PEMFCs are considered as the most promising type of fuel cell in the automotive industry and will, therein, be discussed in more detail in the following chapters.[41] For more detailed fundamentals of the technology, please also always see ref. 11.

1.2.1 The Polymer Electrolyte Membrane Fuel Cell

Briefly, the PEMFC can be described as a kind of acidic fuel cell, consuming hydrogen as a fuel. As a type of a galvanic cell, it consists of two electrodes in contact with a solid electrolyte. At the anode, catalytic oxidation of hydrogen leads to the formation of protons (in the form of H_3O^+, as the system is humidified continuously) and electrons. While the electrons move along an external circuit to power an electrical load, the protons move toward the cathode through the electrolyte in the form of a so-called polymer electrolyte membrane (PEM). The reaction of protons with reduced (atmospheric) oxygen and electrons at the cathode side, typically catalyzed by carbon-supported Pt nanoparticles (Pt/C), leads to the generation of only water as an exhaust.[11] Thus, the PEMFC technology can be considered as one of the most environment-friendly energy conversion processes. The schematic working principle of a PEMFC is depicted in Figure 3.

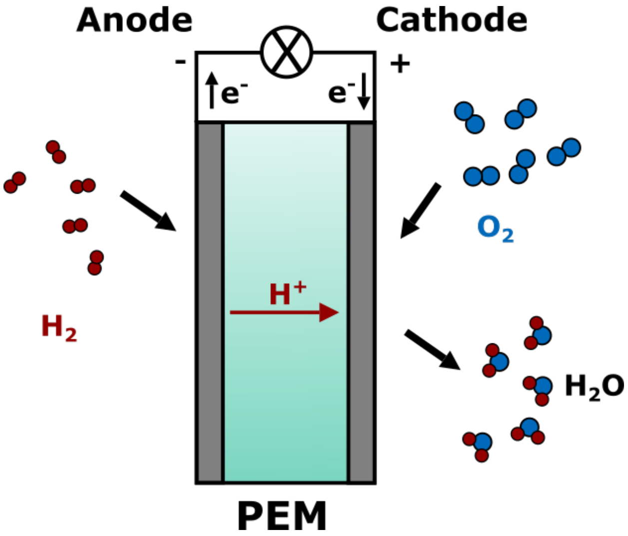

Figure 3. Schematic working principle of a PEMFC. H_2 and O_2 reactant gases are delivered to the anode and cathode side of the cell, respectively. At the anode, H_2 is oxidized, generating protons that travel through the solid electrolyte (PEM), while the electrons move through an external circuit (used to power a load). At the cathode, O_2 is reduced and reacts with the protons and electrons, forming H_2O as an exhaust.

The corresponding overall reaction is summarized in equation 4. The hydrogen oxidation reaction (HOR, equation 5) at the anode is a rapid catalytic process. However, the oxygen reduction reaction (ORR, equation 6) taking place at the cathode of the cell suffers from sluggish kinetics, which is one of the main drawbacks of the system. Hence, further detailed insight into the PEMFC reaction kinetics and how to mitigate the associated problems is given in sections 1.3 and 1.4.

$$\sum: \quad 2H_2 + O_2 \rightarrow 2H_2O \qquad \textbf{(4)}$$

$$\text{HOR (Anode):} \quad 2H_2 \rightarrow 4H^+ + 4e^- \qquad \textbf{(5)}$$

$$\text{ORR (Cathode):} \quad O_2 + 4H^+ + 4e^- \rightarrow 2H_2O \qquad \textbf{(6)}$$

For automotive applications, up to hundreds of single PEMFCs are typically connected in series in a so-called fuel cell stack to generate an optimal voltage output and power density.[11] For mobile applications, the power of typical state-of-the-art PEMFC stacks is in the order of ~100 kW. For instance, the PEMFC stack of the Hyundai Nexo FCEV consists of 440 cells, exhibiting an electric power of 95 kW.[13] Moreover, several automotive suppliers such as the ElringKlinger AG or the Bosch GmbH launched commercialized hydrogen fuel cell systems in the recent years, which are customizable in a broad power range and can, therefore, be utilized for multiple stationary and mobile applications.[42,43] Besides anodes, cathodes and electrolytes, a PEMFC stack and single cell consist of several subcomponents, as schematically shown in Figure 4. The core part of a PEMFC is the so-called membrane electrode assembly (MEA), where the energy conversion reactions take place. The MEA of a single cell consists of only one anode catalyst layer (ACL) and one CCL, the PEM and usually combined microporous and gas diffusion layers (MPLs and GDLs) on both sides. Due to the importance of these integral parts, their composition and working principles are described in more detail in the following subchapter. Other noteworthy hardware components of the PEMFC stack are the current collectors and the bipolar plates (BPPs) with incorporated flow fields. The schematized channel structure of the BPPs has several essential targets. Primarily, one of them is the even distribution of the gases along the reaction area, next to proper reaction water management. Since BPPs still account for a large share of the total costs of a PEMFC (see Figure 2), the choice of material is particularly important. In addition to the gas distribution and water drain, high chemical, thermal and mechanical stability, as well as electrical conductivity have to be ensured.[44,45]

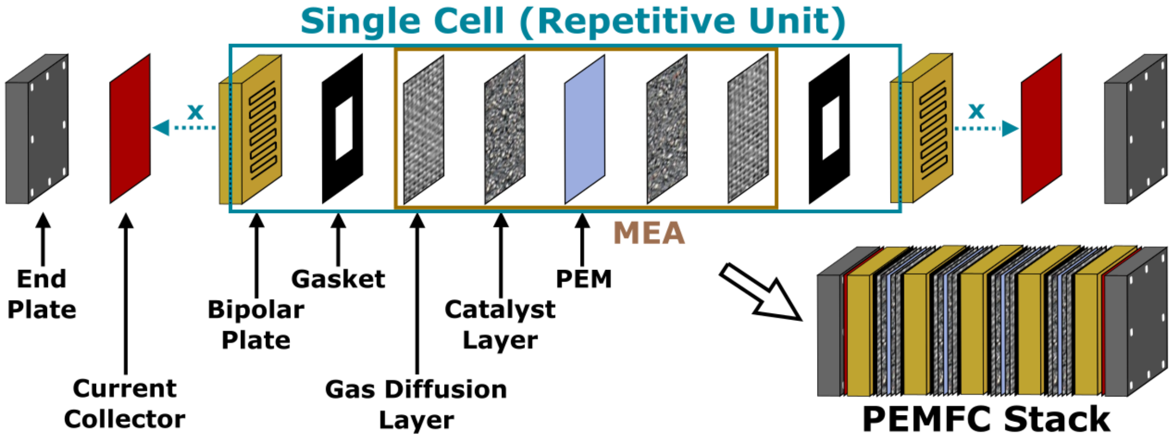

Figure 4. Schematic setup of a PEM fuel cell stack, composed of a variable number of assembled single cells, terminated by current collectors and end plates. The single cells consist of gas diffusion layers, a membrane sandwiched between the electrodes, as well as bipolar plates used for the gas distribution, water management and conductivity.[44]

Carbon-based materials, various (coated) metals, or composite materials can be considered suitable for this purpose. Currently, stainless steel and graphite are among the most promising candidates, but in the latter case, cost-efficiency often suffers from complex manufacturing.[46,47] Moreover, the operation of PEMFC stacks requires a large number of peripheral devices such as control units, H_2 tanks, valves, gas dosing, gas compressors, gas purifiers (especially to avoid CO poisoning at the anode side, since Pt reacts very sensitive to it), water drains and gas humidifiers, as well as a sufficient thermal management.[48] Since this work mainly deals with the optimization of the cathode layer catalysts, one can find further information on this topic in the literature.[11]

1.2.2 The Heart of the PEMFC: The Membrane Electrode Assembly

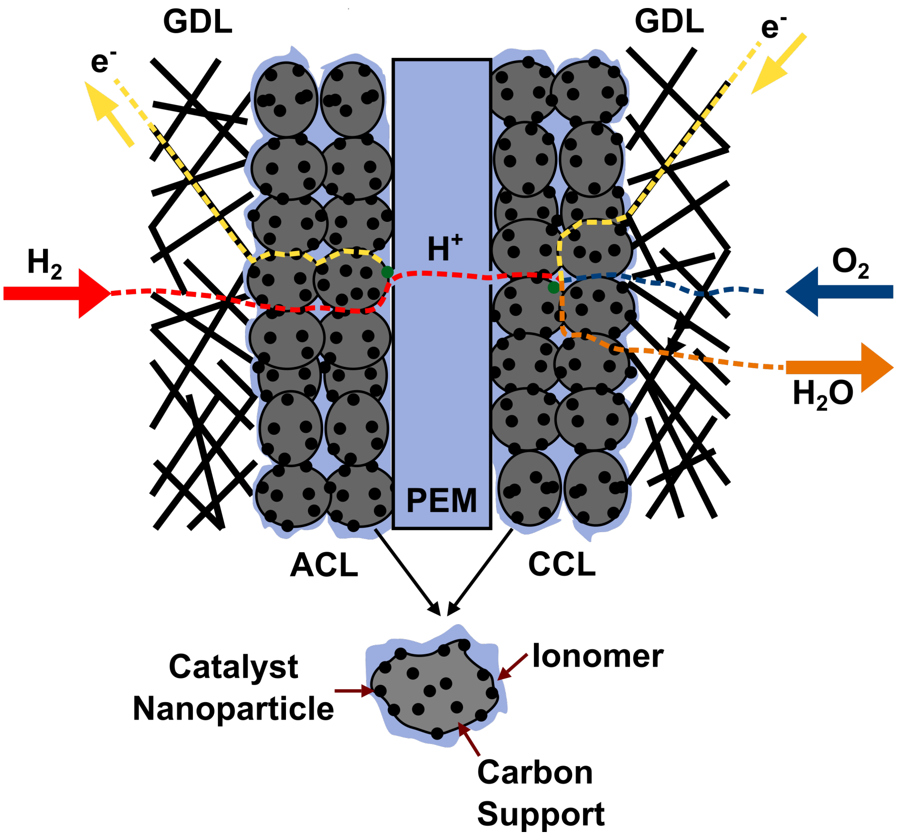

Figure 5. Schematic working principle of a MEA. H_2 is homogeneously distributed across the ACL by the GDL, and the HOR takes place at a catalyst nanoparticle (as highlighted in green). Electrons move through an external circuit and protons move through the PEM, exploiting the proton conductivity of the ionomer and membrane. At the cathode side, O_2 is distributed across the CCL by the GDL. The ORR takes place at a catalyst nanoparticle and reaction water is removed.[44]

As briefly discussed in the previous subchapters, the MEA is the key part of each PEMFC. Figure 5 shows the schematic working principle and layer structure of the MEA, which is composed of a PEM sandwiched between the two catalyst layers and GDLs. The latter ones typically consist of a macroporous assembly of carbon fibers. They are primarily utilized to properly distribute the flux of reactant gas (from the BPP flow fields) across the catalyst layers, provide electrical contact to the BPPs and CLs and remove excess water.[44] At the ACL, the HOR takes place, while the ORR proceeds in the CCL of the MEA. As protons have to move from the anode to the cathode side, good proton conductivity between the CLs (through the PEM) is essential. Typically, a hydrated solid proton-conductive polymer is used as the membrane of a PEMFC. The commercially most common PEM material is Nafion®, which was developed by DuPont de Nemours (Figure 6).[44]

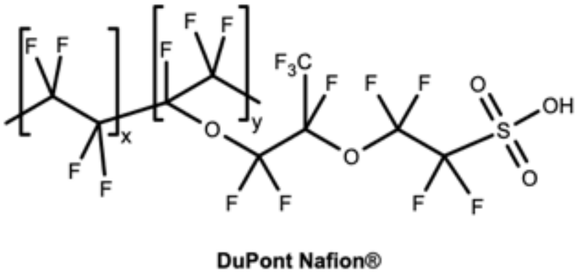

Figure 6. Structural formula of DuPont Nafion®. In PEMFCs, the Nafion® polymer (and its derivatives) are widely used as membrane material due to good proton conductivity, chemical and mechanical stability.

Membranes based on the Nafion® polymer are not only characterized by good proton conductivity but also relatively good chemical and mechanical stability, which must be ensured under the given harsh corrosive operation conditions. Structurally, the polytetrafluoroethylene (PTFE) backbone of Nafion® warrants the high stability, whereas hydrolyzed sulfonate groups provide proton conduction (*e.g. via* the Grotthuss mechanism).[49] However, proper humidification of the system at all times is crucial, which becomes problematic at too high temperatures and can cause dry-out of the membrane (*i.e.* decreased protonic conductivity) with subsequent degradation.[50] Another issue arising with Nafion®-based membranes is the frequently observed hydrogen gas crossover to the cathode, which promotes degradation and lowers the efficiency of the cell.[51] To guarantee proton conductivity between the catalyst layers and the membrane, which is pivotal for the cell performance, both layers are wetted with an ionomer structurally similar to the membrane material.[52] Besides the dry-out of the membrane, flooding of the cell (*i.e.* accumulation of water) can occur with excessive humidification in combination with electroosmotic drag and reaction water formed at the cathode, which impedes gas feed through the flow channels/GDL and requires a complicated water management.[50] In order to mitigate these problems, hydrophobic impregnation of the GDL in form of carbon fibers and incorporation of a partly hydrophilic MPL, consisting of high surface area carbon material, can improve interlayer contact and support removal of surplus water from the cell.[53,54] On both sides, the catalyst layers typically contain Pt or Pt alloy nanoparticles of few nanometers in size, which are electrocatalytically active toward both the HOR and ORR. For instance, the current generation of the Toyota Mirai cars uses PtCo alloy nanoparticles to catalyze the ORR.[55] Since Pt is scarce, improvement of the sluggish ORR kinetics to reduce costs is currently one of the main research topics in the field. To improve the dispersion of the nanoparticles (*i.e.* to enhance accessible surface area) and to improve electrical conductivity, high surface area active carbon materials are utilized as a support. Typical active carbon supports used in PEMFC applications consist of aggregated carbon nanoparticles (~30-60 nm spheres in the case of *e.g.* Cabot Vulcan XC72R active carbon),[56] with surface areas ranging from ~250 m^2/g to more than 1000 m^2/g, depending on the degree of porosity.[57]

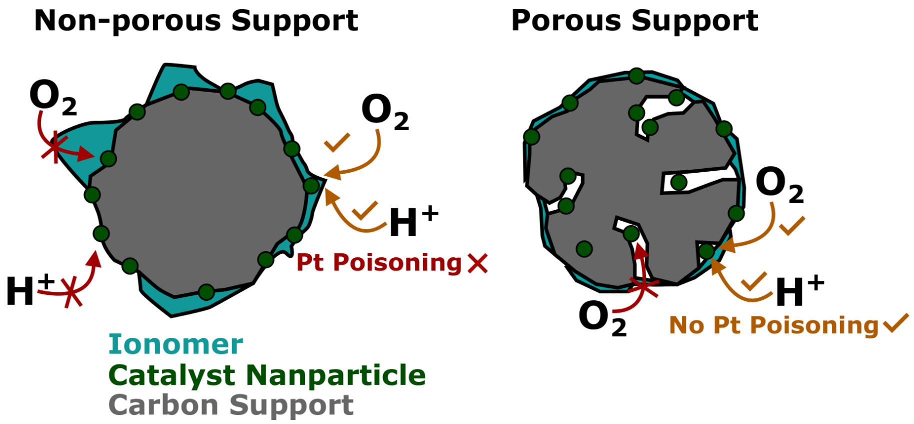

Figure 7. Schematic illustration of the impact of carbon porosity and ionomer wetting on the ORR performance. Depending on the carbon morphology (*i.e.* the porosity of the support), the Pt nanoparticles can be located inside the pores, on the outer surface of the support or both. Besides, the thin-film ionomer wetting of the support has to be considered in ORR catalyst design and partially depends on the pretreatment of the support. The location of the Pt nanoparticles, as well as the ionomer distribution/thickness affect the degree of catalyst poisoning, O_2 and proton transport to the catalyst and, in turn, the corresponding ORR activity. [58,59,60,61]

A point striking from the recent Toyota Mirai progress report is the improved PtCo utilization due to optimized carbon support structure.[55] Indeed, recent studies highlight ORR catalyst performance differences depending on the nanoparticle location (inside or outside of pores),[58] the pore size,[59] ionomer wetting and adherent Pt poisoning,[60,61] which are schematized in Figure 7. For instance, inhomogeneous ionomer wetting/thickness can lead to diminished O_2 transport, poor proton conduction and Pt poisoning (if Pt sits on the outer surface of the support). Similarly, too large pore sizes can hinder the O_2 transport to Pt nanoparticles sitting inside the pores. Accordingly, besides optimization of the ORR kinetics, recent considerations also focus on optimum Pt accessibility and utilization. Promising strategies include utilization of mesoporous catalyst supports that are easily accessible by reactant gases and prevent Pt poisoning,[59] as well as carbon surface functionalization to optimize homogeneous ionomer wetting.[61]

For further illustration of the MEA components, representative scanning electron microscopy (SEM) images of the MEA interfaces and of a commercial GDL, as well as an electron tomogram of Pt/C electrocatalyst are depicted in Figure 8A, B and C (taken from the literature, as indicated in the caption of the Figure), respectively. Please also see ref. 11 for more detailed insight into the fundamental principles associated.

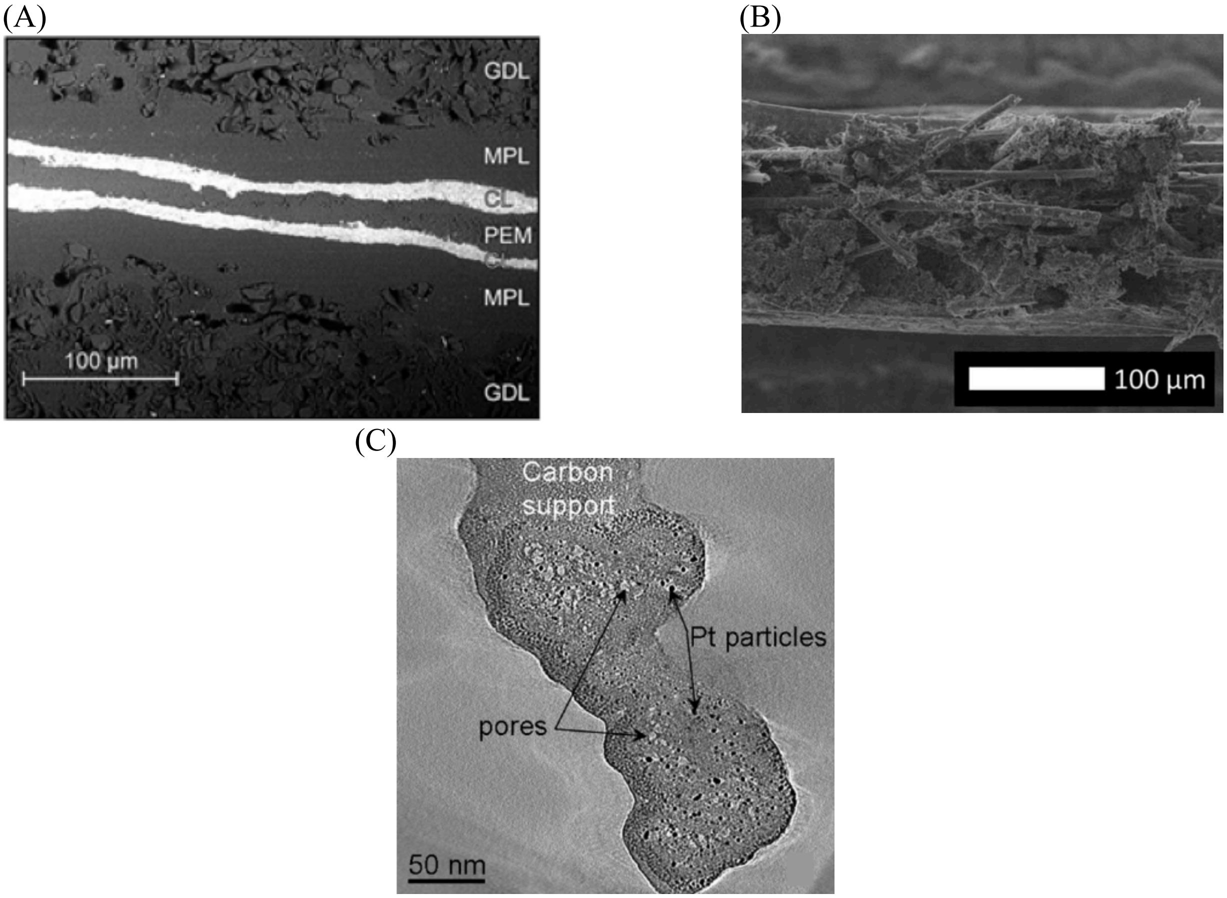

Figure 8. (A) An example cross-section SEM image of a MEA, reprinted with permission from ref. 62. Licensed under the terms of CC BY 3.0. Published by The Royal Society of Chemistry. (B) Cross-section SEM image of a commercial GDL without MPL, showing the carbon fiber structure of the layer. Reprinted with permission from ref. 63. Licensed under the terms of CC BY 4.0. Copyright 2017 The Electrochemical Society. (C) Visualization of a part of a CCL *via* electron tomography. The image shows the porous carbon support structure, as well as the Pt nanoparticles attached to it. Adapted with permission from ref. 64. Copyright 2011 The American Chemical Society.

1.3 Fuel Cell Electrocatalysis – The Backbone of Renewable Energy Conversion

1.3.1 Fuel Cell Voltage Losses

As summarized in the literature,[65,66] the cell voltage E_{Cell} of a PEMFC is classically based on the following relation:

$$E_{Cell} = E_{Rev} - I \cdot R_{HF} - I \cdot \left(R_{H^+}^{cat} + R_{H^+}^{an}\right) - |\eta_{ORR}| - \eta_{HOR} - \eta_{tx} \qquad \textbf{(7)}$$

with E_{Rev} being the temperature- and gas partial pressure-dependent reversible cell voltage, R_{HF} being the high frequency (ohmic) resistance (*i.e.* contact and membrane resistance), R_{H^+} corresponding to the effective proton transport resistance of the ACL and CCL, η_{HOR} and η_{ORR} being the kinetic overpotential of the anode and cathode electrocatalytic reactions and η_{tx} being the overpotential caused by gas transport resistances. Since voltage losses observed in a PEMFC are manifold, it requires complex test protocols to deduce individual contributions. Moreover, the performance is largely dependent on various parameters such as the gas pressure and distribution, the relative humidification (RH), temperature (distribution), oxygen transport, as well as on proper preparation of the setup and test equipment.[67,68] A typical PEMFC polarization curve with assigned voltage loss contributions (as proposed in the literature)[69,70] is schematized in Figure 9A. It should be noted that the open circuit voltage (OCV) of a cell typically does not equal the reversible potential, due to *e.g.* internal gas crossover. To specifically access the ORR kinetics of an electrocatalytic system, which is the main focus of this work, and to quantify corresponding overpotential-induced voltage losses, it is often beneficial to utilize a half-cell setup due to simple handling. Here, the ORR performance of an electrocatalyst thin film electrode is investigated in a three-electrode setup configuration using an O_2-saturated aqueous acidic electrolyte. Besides simple handling, only small quantities of active material are required for testing and the significance level of the results is mostly dependent on the film quality and the cell/electrolyte cleanliness. However, one main drawback of the technique is that only a comparably small current density range can be investigated, which is only sufficient to extract kinetic parameters.[68] A representative schematic polarization curve (and an idealized one) are shown in Figure 9B for comparison. Here, the ORR activity can easily be investigated in the mixed kinetically- and mass transport-controlled domain after application of few corrections, which will be elucidated in more detail later.

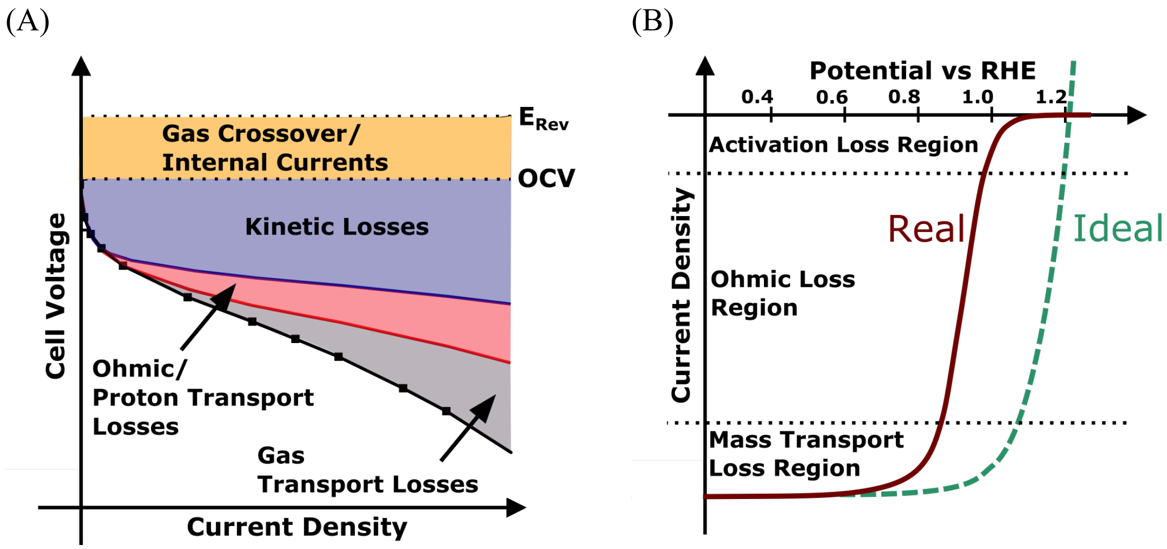

Figure 9. (A) Schematic PEMFC polarization curve showing typical primary voltage loss sources, compared to a (B) schematic idealized and realistic representation of an ORR polarization curve recorded in a half-cell setup under electrode rotation. Please note that the loss ratios cannot be considered accurate.[68,69,70]

1.3.2 Electrocatalysis of the Hydrogen Oxidation Reaction

The HOR (*i.e.* the electro-oxidation of molecular hydrogen forming protons and electrons) at the anode side of a PEMFC is extensively studied on Pt-based materials (*e.g.* Pt/C) in acidic media, which pose the most active class of catalysts to date.[71,72,73,74] Typically, two combinations of the mechanistic steps are proposed for the corresponding reaction. In detail, the reaction can either follow the Heyrovsky-Volmer (equations 8 and 10) or the Tafel-Volmer (equations 9 and 10) sequence, in turn determining the kinetic parameters of the HOR.[44]

Heyrovsky: $$Pt + H_2 \rightarrow Pt - H_{ad} + H^+ + e^- \qquad \textbf{(8)}$$

Tafel: $$2Pt + H_2 \rightarrow 2Pt - H_{ad} \qquad \textbf{(9)}$$

Volmer: $$Pt - H_{ad} \rightarrow Pt + H^+ + e^- \qquad \textbf{(10)}$$

As the HOR on Pt surfaces exhibits fast reaction kinetics,[74,75,76] current low anode catalyst layer Pt loadings of ~0.02 mg_{Pt}/cm^2 can be employed without significant voltage losses (*i.e.* $\eta_{HOR} \sim 0$), compared to loadings of ~0.1 mg_{Pt}/cm^2 still being targeted at the cathode side.[77] However, one main drawback of the Pt/C-type catalysts is their low tolerance toward CO, which is naturally contained in the H_2 gas produced from steam reforming processes. Typical amounts center between

1-2%, however, Pt surfaces are already sensitive to amounts in the low ppm range.[78] To prevent so-called CO poisoning of Pt, complex and expensive purification of H_2 is required prior to utilization, for instance by filtering the gas through a Pd (alloy) membrane at elevated temperature.[79,80] In detail, adsorbed CO can block the dissociation step of hydrogen, leading to suppressed HOR kinetics.[81] Strategies to circumvent such effects are, for instance, the use of Pt-alloy catalysts such as PtRu/C,[82] which alter the CO oxidation potential, *in-situ* generation of active O_2 to oxidize the CO,[83] as well as catalytic on-board purification using *e.g.* finely dispersed Fe-based layers on Pt nanoparticles for preferential CO oxidation in hydrogen.[84] However, in the long term perspective it is highly desirable to replace H_2 generation *via* steam reforming by water electrolysis, which not only enhances sustainability, but also strongly reduces many issues related to the CO poisoning.

1.3.3 Electrocatalysis of the Oxygen Reduction Reaction

Unlike the HOR, the ORR (*i.e.* the electrochemical reduction of dioxygen to form water) at the cathode side of a PEMFC substantially contributes to the operational voltage losses observed, due to high reaction overpotentials. While the multi-step ORR reaction mechanism is still not fully understood, efforts were made to investigate the kinetics and deduce or clarify the involved pathways since decades.[85,86,87,88,89] Fundamentally, the ORR can proceed *via* a sequential 2-electron pathway to form H_2O_2 (which can further be reduced into H_2O) or a direct 4-electron pathway to form H_2O in acidic media, as shown below.[90]

Indirect: $$O_2 + 2H^+ + 2e^- \longrightarrow H_2O_2 \qquad \textbf{(11)}$$

$$H_2O_2 + 2H^+ + 2e^- \longrightarrow 2\,H_2O \qquad \textbf{(12)}$$

Direct: $$O_2 + 4H^+ + 4e^- \longrightarrow 2\,H_2O \qquad \textbf{(13)}$$

Theoretical investigations led to a more detailed differentiation of the ORR into a dissociative, an associative and a “peroxo” mechanism, as depicted in Figure 10, which depends on the catalyst material and the electrode potential.[91,92] While the former one consists of a primary dissociation step and subsequent protonation, the latter ones are initiated by protonation steps and followed by dissociation. In the “peroxo” mechanism, H_2O_2 can readily be desorbed after the 2 e^- transfer process, which results in an incomplete reduction path and thus low energy efficiency. Moreover, due to its highly oxidizing properties, the presence of H_2O_2 molecules in a PEMFC can cause or severely accelerate degradation of both PEM (*via* peroxide radical attack) and catalyst layers (*via* carbon support oxidation).[93,94] Accordingly, it is of general interest to design catalysts with low affinity toward the H_2O_2-forming pathway. While the rate of H_2O_2 formation is comparably low on extended Pt surfaces in a relevant potential range,[95] up to 20% were reported for the case of carbon-supported Pt nanoparticles.[96] Importantly, the ORR catalytic activity of a material is based on the binding strength between the main intermediate species, namely O_{ad}, OH_{ad} and OOH_{ad}, and the catalyst, which should be balanced between too weak and too strong surface interactions according to the Sabatier principle. Consequently, the results of Viswanathan *et al.* indicate that the selectivity of either 4 or 2 e^- pathway depends on the OH_{ad} free adsorption energy, used as the main descriptor.[97] The corresponding comparison of different well-defined metal surfaces led to the conclusion that the weak binding of *e.g.* Au(111) surfaces preferably leads to the 2 e^- reduction, while reverse was observed for *e.g.* Pd and Pt(111). Further, Chorkendorff, Nørskov and co-workers showed that in the case of certain Pt-based electrocatalysts a stronger OOH_{ad} binding and, in contrast, weaker O_{ad} and OH_{ad} would be required to achieve maximum efficiency.[98,99] Compared to the Pt(111) surface, which shows the best ORR performance of pure metal low-index surfaces in acid, a ~0.1 eV weaker OH_{ad} binding energy has to be targeted according to the literature.[100,101] However, the correlation of the adsorption free energies of all three reaction intermediates (so-called scaling relations) hinders the adjustment of the binding strength of individual intermediates and, in turn, limits the maximum ORR performance of a catalyst.[98] Hence, it is desirable to find catalysts with a binding energy that is closest to the optimum for all intermediate species.

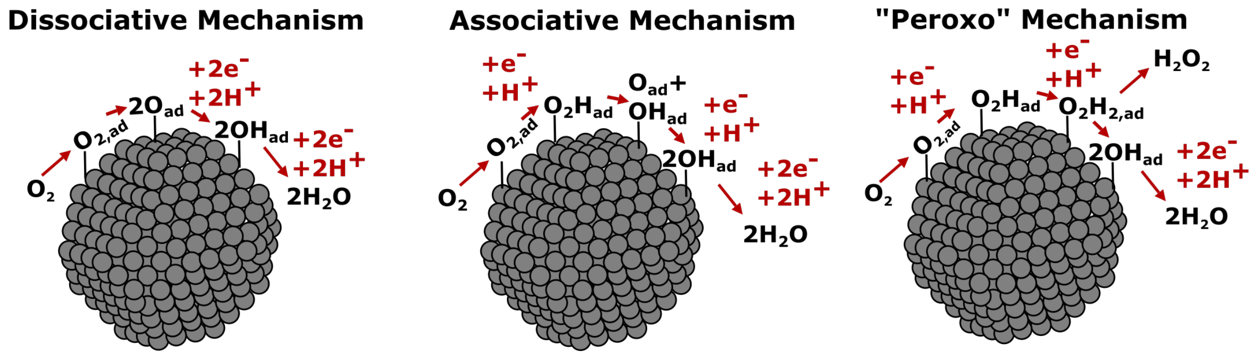

Figure 10. Schematic description of different possible ORR pathways, *i.e.* the dissociative, associative and "peroxo" mechanisms, involving adsorbed O_{ad}, OH_{ad} and OOH_{ad} reaction intermediates species.[92]

1.4 Driving Fuel Cell Catalysis – Nanostructured Platinum and its Alloys

1.4.1 Oxygen Reduction on Platinum Surfaces

As elucidated earlier, Pt-based materials are well suited to meet the requirements for commercial ORR catalysis in acidic media, however, further optimization is necessary.[102] In their seminal study,[91] Nørskov *et al.* deciphered the ORR on different metal surfaces using density functional theory. They found that regarding pure metals, Pt is located on top of a volcano-type relation of the ORR activity and calculated oxygen binding energies (and OH binding accordingly), as shown in Figure 11.

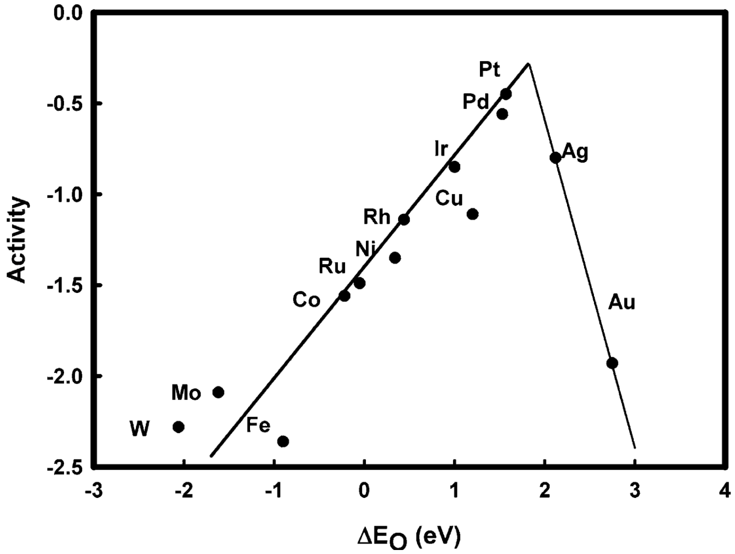

Figure 11. ORR activity (as defined by the authors) *vs* calculated oxygen binding energy of different pure metal surfaces. Reproduced with permission from ref. 91. Copyright 2004 American Chemical Society.

To gain basic understanding of the high ORR activity of Pt-based materials, studies on extended surfaces as well as theoretical investigations are particularly suitable and in turn strongly influence "real life" catalyst design. For instance, the structure sensitivity of extended Pt surfaces toward the ORR was largely shown, *e.g.* by the means of single crystal studies.[103] In such studies, terrace sites on certain stepped single crystals were found to weaken OH_{ad} binding and to impact the ORR performance in a positive way accordingly.[99,101] In applied systems, nanoparticles in a size range of few nanometers, homogeneously distributed on high surface area carbon support (Pt/C) are used to achieve a maximum surface-to-volume ratio. In particular, their size and shape can be named as the determining factors for good ORR performance. Perez-Alonso *et al*. investigated the effect of the Pt nanoparticle size in a range of 2-11 nm on ORR performance using mass-selected model particles and correlated it to the experimentally determined fraction of terrace sites.[104] Regarding the ORR activities normalized to the electrochemically active surface area (ECSA) of Pt (specific activity, SA) or to the mass of the Pt nanoparticles (mass activity, MA), they observed clear trends. While the specific activity increases almost linearly with increasing particle size (until it equals the activity of an extended Pt surface), the mass activity shows a maximum at ~3 nm, followed by a flattening of the curve. Moreover, the increase of the SA is approximately proportional to the number of the terraces, which increases with particle size. Roughly similar trends were reported by Shao *et al*. (where the detected MA maximum is located between 2 and 2.5 nm),[105] and Shinozaki *et al*.[106]

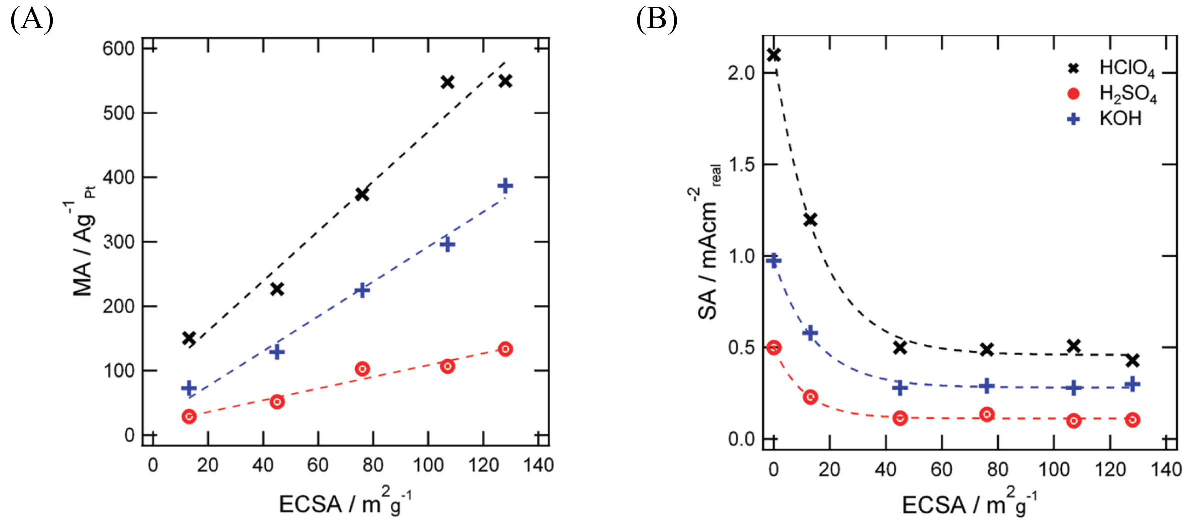

Figure 12. (A) Mass and (B) specific ORR activity trends as a function of the ECSA per Pt mass, showing increasing MA with increasing ECSA, in contrast to the decreasing SA. The different electrolytes used are indicated in the top right corner of (B).The average Pt nanoparticle sizes corresponding to the ECSA data points are (from low to high ECSA): Extended Pt surface (only in B), Pt black, 4-5 nm, 2-3 nm, 2 nm, 1-1.5 nm. Adapted with permission from ref. 107. Copyright 2011 American Chemical Society.

In Figure 12A and B, the MA and SA trends reported by Nesselberger *et al*. are shown as a function of the ECSA per mass of Pt,[107] which is an important descriptor for nanoscale catalysts since it relates the nanoparticle mass to the actual Pt surface available for the ORR. Notably, the ECSA scales with the particle size, *i.e.* decreases linearly with increasing particle diameter.[108] For illustration, the Pt nanoparticle sizes corresponding to the ECSA values are listed in the caption of Figure 12. The MA trend observed by Nesselberger *et al*. shows increasing MA with increasing ECSA, until the maximum is reached above ~100 m^2/g (~2 nm Pt nanoparticle size) in $HClO_4$.[107] Contrary, the SA drops and reaches a plateau as expected. Accordingly, it is particularly important to tailor both, the particle size and the adjacent ECSA toward a maximum.

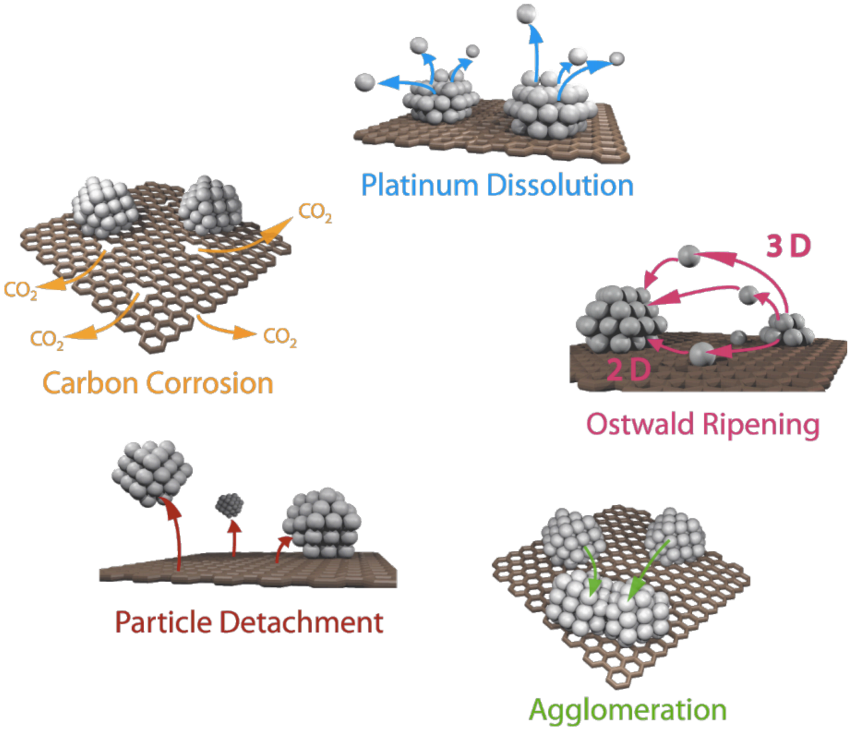

Figure 13. Schematic description of typical Pt/C degradation mechanisms, namely Pt dissolution, Pt detachment, Ostwald ripening, particle agglomeration and carbon corrosion. Reprinted with permission from ref. 109 (licensed under the terms of CC BY 2.0). Copyright 2014 Meier *et al.*

For PEMFC applications, not only the initial activity of a catalyst but also its long-term performance has to be considered. Hence, it is important to rate stability accordingly. Typical degradation phenomena of Pt/C-type catalyst are summarized in Figure 13, as proposed by Meier *et al*.[109] For instance, this involves the agglomeration (*i.e.* a loss of surface area) or detachment of Pt nanoparticles. Dissolution of Pt in acidic media at relevant potentials can further lead to particle growth (*via* re-deposition) or to the formation of a Pt band in the membrane, due to reduction of the Pt-ions by crossover hydrogen.[110,111] Moreover, oxidation of the carbon support has to be prevented, since it strongly accelerates the performance losses. In the case of bimetallic Pt-alloy nanoparticles, which will be discussed in the following section, dissolution (or “de-alloying”) of the non-noble element can occur, which cannot only lead to a reduced performance, but also to a poisoning of the PEM.[112] As summarized by Asset *et al.*, it is also known that particles with a complex, non-spherical shape show restructuring (structural collapse) during voltage cycling (especially at elevated temperatures), in order to minimize their surface energy.[113]

1.4.2 Oxygen Reduction on Bimetallic 3d Transition Metal Alloys of Platinum

In the current PEMFC applications, bimetallic Pt-based alloy catalysts (Pt_xM/C, where M is a 3d transition metal element) play a predominant role due to the ORR performance enhancements compared to pure Pt electrocatalysts. Similarly important, utilization of such alloys enables to reduce the amount of scarce and precious Pt metal used in the catalyst layers of the cell.[11] Disassembly and analysis of MEAs used in Toyota's Mirai FCEV has shown that Pt_xCo alloy nanoparticles with an average nanoparticle size of 4.7 nm were used to catalyze the ORR.[114] Interestingly, a rather broad particle size distribution (PSD) was found, with small particles located inside the pores of the acetylene black support used, and bigger particles present on the surface of the support. As shown by Papadias *et al.*, commercial state-of-the-art Pt_xCo/C catalysts tend to be active and durable during the PEMFC operation, depending on the initial Co content and retention, size and morphology.[115] In particular, they found that while high initial Co content and porosity benefit the beginning-of-life performance, they are detrimental to the long-term stability. On the other hand, higher initial nanoparticle size prevents extensive particle growth (*i.e.* loss of ECSA). On the lab scale, a broad variety of different bimetallic electrocatalysts was synthesized in the past years, and tested in-depth for ORR applications using both, liquid half-cell as well as single-cell PEMFC configurations. Besides Pt_xCo alloy catalysts, Ni, Cu or Fe are among the most frequently investigated base metals.[116] For instance, seminal extended surface studies showed that the $Pt_3Ni(111)$ surface surpasses the ORR specific activity of Pt(111) by a factor of ~10, which corresponds to ~90-times the SA of commercial Pt/C (according to the authors of the study).[117] Importantly, the activity gain is strongly correlated with the surface orientation, since $Pt_3Ni(110)$ and (100) showed only comparably low improvements. However, it is challenging to replicate such high improvements on the nanoscale. Attempts to synthesize Pt_3Ni nanoparticles with preferential (111) orientation resulted in ~4-times higher MA compared to commercial Pt/C.[118] In order to mitigate PEM poisoning and uncontrolled degradation associated with the dissolution of the non-noble metal element during PEMFC operation,[112] certain pretreatment of alloy catalysts has been established as a promising approach. Early studies by Strasser and co-workers indicate more than 3-fold enhanced MA of de-alloyed (*i.e.* surface non-noble metals were (electro)chemically leached in a controlled manner) $PtCu_3/C$ or $PtCo_3/C$ compared to Pt/C in an acidic electrolyte.[119,120] Recently, Han *et al*. reported "record activity and stability" of chemically de-alloyed $PtNi_3/C$ electrocatalyst in single-cell PEMFC tests, which exhibit a so-called core-shell architecture.[121] In detail, such catalysts consist of an alloy core, surrounded by a thin strained Pt shell, which prevents (or reduces) leaching of the alloying element, while being highly active and stable in relevant PEMFC potential and temperature ranges.[122] Importantly, the presented catalyst even surpasses the US DOE targets for 2017 at both the beginning and the end of life. The results are in agreement with early studies of Stamenković and co-workers, which validate the improved performance of Pt_xM alloys with exposed pure Pt skin surfaces toward the ORR.[123,124] In the literature, the origin of superior activity of Pt_xM/C electrocatalysts compared to pure Pt/C is typically rationalized by (an interplay of) different effects, as listed below.

i) The so-called strain effect, corresponding to the change of the lattice parameter of Pt surface atoms by alloying (often also caused by dissolution of the soluble metal),[122] which leads to a variation (slight weakening) of the oxygen intermediate bonding to the catalysts' surface.[125,126,127]
ii) The so-called ligand effect, corresponding to an alternation of the electronic structure/properties of surface Pt atoms due to charge transfer with adjacent subsurface elements other than Pt.[125,127,128,129]
iii) The so-called ensemble effect, corresponding to the surface atomic arrangement/geometry at active sites or crystallographic orientation.[130,131]

Hence, next to an adjustment of particle size and alloying, tailoring the shape/surface structure of Pt-based nanoparticles is another popular attempt to boost the ORR performance, since it enables to alter the particle morphology in order to maximize the amount of particularly active surface centers or to increase the available surface area with respect to the particle size.[132] However, considerably different approaches are presented in the literature, ranging from *e.g.* highly ordered surfaces with a high number of active (111) facets (such as octahedral nanoparticles), to porous frameworks or defective surfaces, which will be discussed in more detail later. To illustrate the impact of the strain, ligand and ensemble effect on ORR performance, a selection of active and/or durable nanostructured ORR electrocatalysts is compared by means of mass activity in Figure 14. Here, the impact of structural as well as compositional differences on the ORR performance is clearly elucidated. In particular, up to 22-fold increase in the mass activity of an open Pt_3Ni alloy framework has to be highlighted, which represents one of the most active classes of ORR catalysts reported to date. Corresponding publications are noted in the caption of the figure.

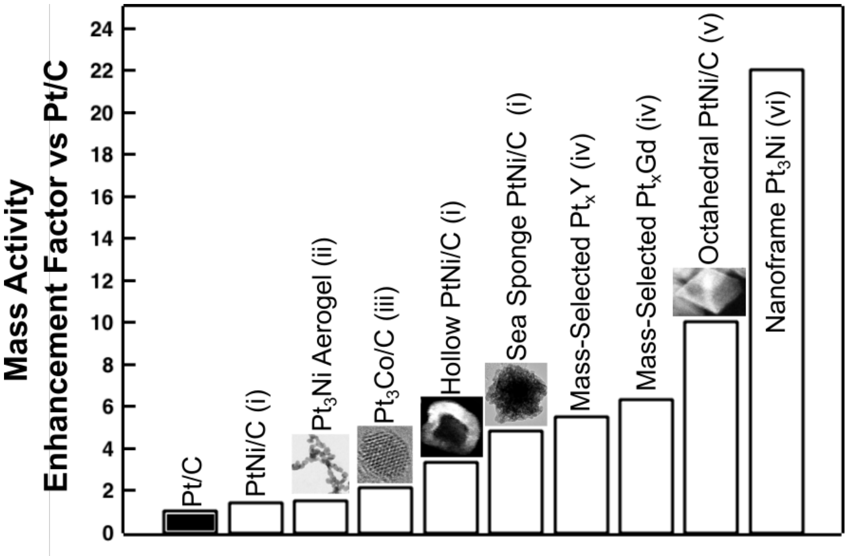

Figure 14. Mass activity enhancement of selected state-of-the-art bimetallic electrocatalysts *vs* (commercial) Pt/C reference catalysts, as reported in the corresponding literature. All activity measurements were performed in O_2-saturated 0.1 M $HClO_4$ electrolytes and compared at either 0.9 or 0.95 V *vs* the reversible hydrogen electrode (RHE). (i) Maillard *et al.*, data taken and images adapted with permission from ref. 133 (licensed under the terms of CC BY 4.0). Copyright 2017 American Chemical Society. (ii) Schmidt *et al.*, data taken and image adapted with permission from ref. 134 (licensed under the terms of CC BY 4.0). Copyright 2016 The Electrochemical Society. (iii) Shao-Horn *et al.*, data taken and image adapted with permission from ref. 135. Copyright 2009 American Chemical Society. (iv) Chorkendorff *et al.*, data taken and from refs 136 and 137. (v) Strasser *et al.*, data taken and image adapted with permission from ref. 138. Copyright 2012 American Chemical Society. (vi) Stamenković *et al.*, data taken from ref. 139. The graph is inspired by ref. 113, where a more detailed comparison of state-of-the-art ORR electrocatalysts in a similar representation can be found.

1.4.3 Oxygen Reduction on Bimetallic Lanthanide and Rare-Earth Metal Alloys of Platinum

In recent years, another class of Pt-based alloys has received an increasing attention. As summarized in Figure 15, in addition to implementation of 3d transition metals, lanthanides and rare-earth elements can attenuate the binding energy of ORR intermediates and, in turn, favor the ORR kinetics. For example, Čolic *et al.* compared the ORR activity maxima of different Pt alloy catalysts (as reported in the literature with respect to the pure Pt references used) as a function of the atomic radius of the alloying element.[140] As indicated on the right side of the "double volcano", Pt_3Y, Pt_5Tb and Pt_5Gd are among the most active extended polycrystalline alloy surfaces, each showing up to almost 6-times enhanced SA over polycrystalline Pt in acidic electrolyte at 0.9 V *vs* RHE.[98,141,142] In the underlying studies, the authors rationalize the activity enhancements by the dissolution of the lanthanide or rare-earth elements from the catalysts' surface and subsequent formation of a highly stable, compressively strained Pt overlayer. In accordance, Garlyyev *et al.* reported up to 4-times enhanced SA of Pt_5Pr electrodes compared to polycrystalline Pt, which fulfills the atomic radius-related activity trend shown in Figure 15.[143]

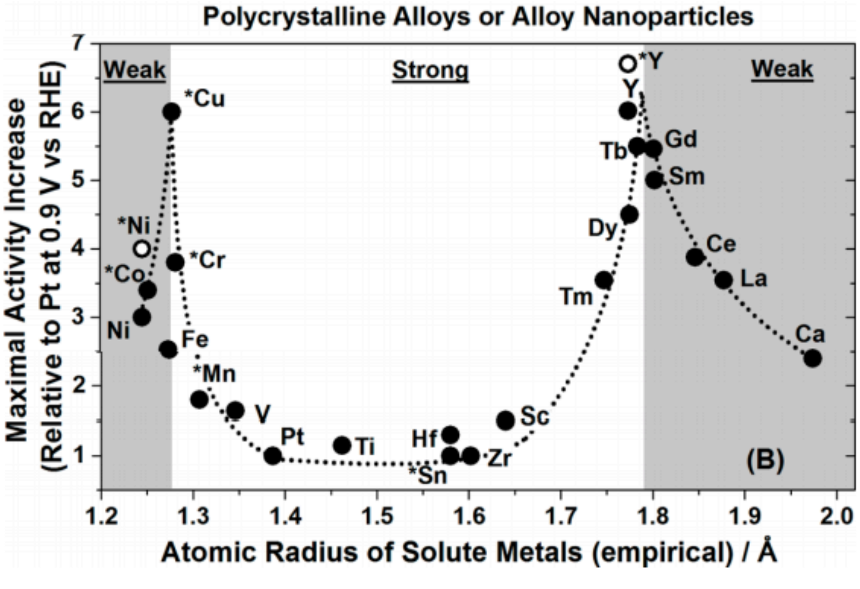

Figure 15. Comparison of different literature-based ORR activity enhancements of Pt alloy surfaces and the corresponding atomic radii of the alloying elements, reported by Čolic *et al.* The enhancements are shown with respect to the reference pure Pt surfaces reported in the investigated studies. Reprinted with permission from ref. 140. Copyright 2016 American Chemical Society.

While extended surface studies suggest good ORR performance of Pt-lanthanide catalysts, a key problem arises when switching to the nanoscale. As highlighted by Roy *et al.*, synthesis of properly alloyed Pt-lanthanide nanocatalysts is highly sophisticated, owed to the high reduction potential difference of Pt and lanthanide metals. Moreover, their highly oxophilic behavior (*i.e.* high propensity to form corresponding oxide species) complicates alloy phase formation, especially under ambient conditions and in aqueous environment.[144,145] First successful attempts in the group of Chorkendorff to synthesize Pt_xY and Pt_xGd model nanoparticles showed more than 5- and 6-times enhanced mass activity compared to a commercial Pt/C catalyst. However, they used a complicated synthesis approach based on gas-aggregation and mass-selection under ultra-high vacuum (UHV) conditions.[136,137] For the activity comparison also see Figure 14. Interestingly, the activity increase is in accordance with the values gathered from the disk electrode studies.[98,141,142] In order to overcome the existing problems, Roy *et al.* developed a scalable synthesis method based on the annealing (800 °C) of anhydrous YCl_3 and Pt/C electrocatalyst precursor under H_2 atmosphere in a metal reactor. Importantly, according to the authors, the method is also suitable for the synthesis of Pt-lanthanide alloys. However, a core problem of this synthesis method is governed by the strong particle growth at high temperatures, which in turn negatively affects the mass activity of the catalysts.[144] Accordingly, the development of a scalable synthesis route toward Pt-lanthanide nanocatalysts with controllable size is still pending, which gives rise to the investigations presented in Chapter 5 of this work.

1.5 (Concave) Surface Defects and Their Impact on the Oxygen Reduction Reaction Performance

As noted above, the ORR performance is highly sensitive to the structure, size and composition of Pt-based nanomaterials. Since experimental elucidation of particularly active surface sites is often a non-trivial endeavor, Calle-Vallejo *et al.* proposed a simple correlation between structural surface geometry around such sites and reaction overpotential (or intermediate binding strength) to rate the ORR performance.[146] Since the description of the coordination environments *via* a "conventional" coordination number, *cn*, fails in the case of nanoparticles, the authors introduced a so-called "generalized" coordination number $\overline{CN}$. It accounts for the coordination number of the first-nearest neighbors and the highest individual coordination number of these first-nearest neighbors, cn_{max}, according to

$$\overline{CN}(i) = \sum_{j=1}^{n_i} \frac{cn(j)}{cn_{max}} \qquad \textbf{(14)}$$

Correlation of herein determined $\overline{CN}$ values of different Pt catalysts with theoretical ORR overpotentials shows a volcano-type relationship with a maximum located at $\overline{CN}$ of ~8.3. Compared to the extended Pt(111) surface ($\overline{CN}$ = 7.5), an optimal geometric environment of an active site was found to be based on a higher number of second-nearest neighboring atoms, while keeping the number of the first-nearest atoms constant, which can *e.g.* be fulfilled by the introduction of surface cavities in a controlled manner. Experimental validation confirmed up to ~3.5-times enhanced SA of Pt(111) with cavity-type surface defects compared to polycrystalline Pt. Following model studies on nanostructured Pt surfaces revealed that highly coordinated sites in concave surface regions are able to benefit ORR performance, while classical convex nanoparticles are rather inactive toward the ORR (maximum $\overline{CN}$ = 7.5).[147] However, the total ORR overpotential reduction clearly also depends on the number of particularly active sites, which has to be considered in experimental approaches. In Figure 16A, the impact of active site geometry on the $\overline{CN}$ values is schematized. Accordingly, Pt nanoparticles with various shapes exhibit differently active surface sites. As shown in Figure 16B, multiple architectures (*e.g.* hollow, cross-shaped or aggregated particles) possess active sites with $\overline{CN}$ > 7.5. Importantly, they commonly exhibit concave surface geometry. In the recent years, Gagliardi and co-workers systematically adapted and developed the arithmetical $\overline{CN}$ approach in order to screen for the optimum nanoparticle shape and size (distribution). Besides, a way to predict the absolute mass activity of investigated structures was elaborated. Their studies confirmed that the implementation of concave surface features on pure Pt nanostructures can lead to almost 8-times enhanced ORR mass activity (in the case of concave nanorods) compared to state-of-the-art pure Pt/C.[148,149,150]

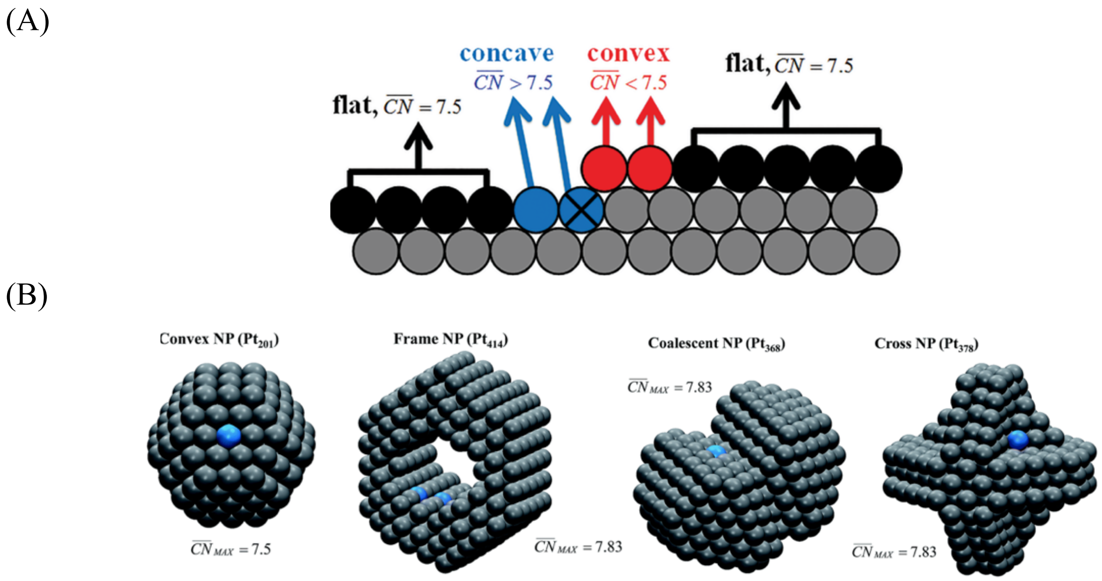

Figure 16. (A) Schematized impact of Pt surface site geometry on $\overline{CN}$ (and ORR performance accordingly) and (B) Pt nanostructures with the most active surface sites highlighted in blue. Adapted with permission from ref. 147. Published by the Royal Society of Chemistry, licensed under CC BY 3.0.

Experimentally, *e.g.* ultrafine jagged nanowires with a high number of surface defects are among the ORR catalysts with the highest activity reported to date.[151] Moreover, Dubau *et al.* showed ~6-times enhanced mass activity of hollow porous Pt_xNi/C nanoparticles compared to “convex” solid Pt/C in acidic media (~4-times relative to conventional Pt_xNi/C), confirming the theoretical predictions.[152] In accordance with aforementioned considerations, the activity gain can be traced back to a high surface-to-volume ratio (relative to a conventional nanoparticles of similar outer diameter), beneficial active site geometry at the interior of the nanoparticle, as well as alloying (strain and/or ligand) effects.

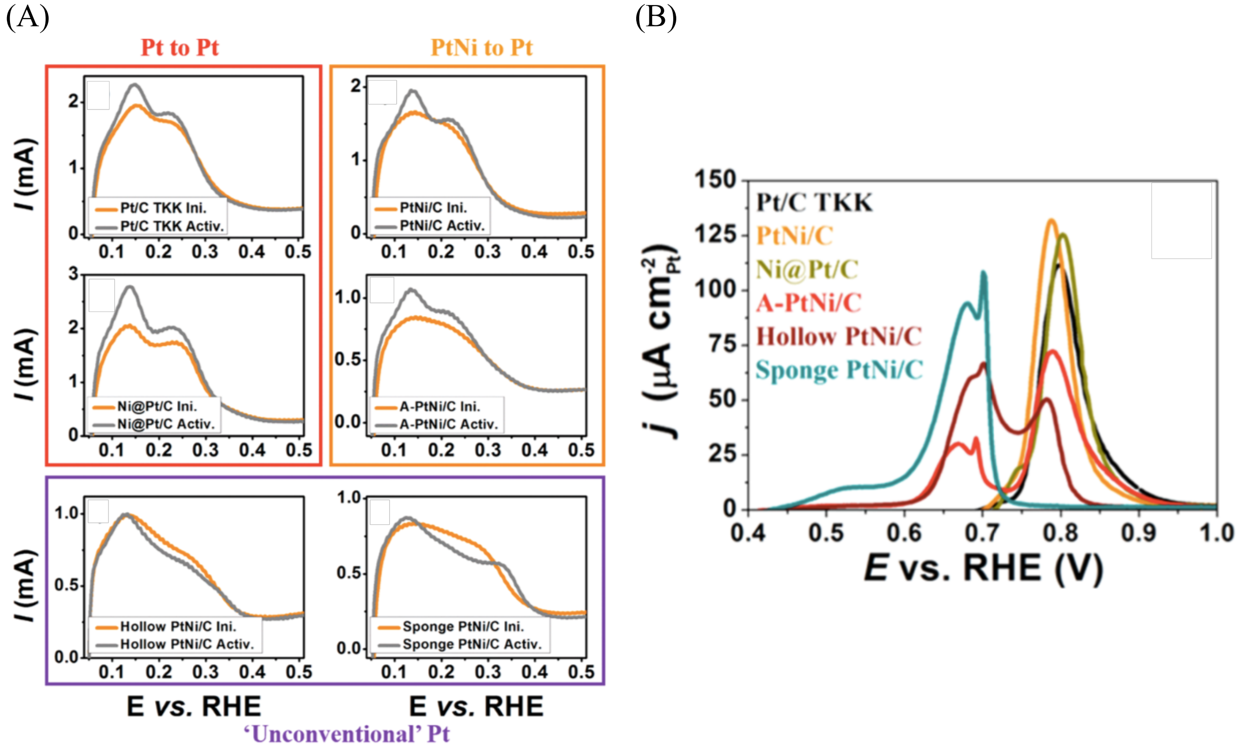

Figure 17. (A) Hydrogen desorption peaks of cyclic voltammograms (CVs) related to different electrocatalysts investigated by Dubau *et al*. in Ar-saturated 0.1 M $HClO_4$ before (orange) and after conditioning (50 cycles, grey). (B) Corresponding CO oxidation voltammograms, recorded in Ar-saturated 0.1 M $HClO_4$ after adsorption of a CO monolayer on the catalyst surfaces. All CVs show a dependence on the surface structural features. Adapted with permission from ref. 133 (licensed under the terms of CC BY 4.0). Copyright 2017 American Chemical Society.

In recent works, Maillard and co-workers rated the ORR performance of various state-of-the-art Pt_xNi/C catalysts with structurally ordered (sphere, cube, octahedron) and disordered (aggregated, hollow, aerogel, open-porous sponge) surfaces.[133, 153, 154] Representative transmission electron microscopy (TEM) images of aerogel, hollow, sponge and octahedral nanoparticles are depicted in Figure 14. On the base of crystallographic, electroanalytical and microscopic observations, the group showed that structural defects (*e.g.* grain boundaries, dislocations, stacking faults, vacancies and vacancy clusters, voids, pores) improve the activity and durability of ORR catalysts, while structurally ordered catalysts only show high initial activity, but are prone to fast degradation.[154] For instance, it was illustrated that controlled aggregation of Pt_xNi/C leads to a slightly improved ORR activity compared to well-dispersed spherical Pt_xNi/C, even though it is accompanied by a strong loss of surface area.[133] An easily accessible electroanalytical technique to monitor surface structural properties relies on the sensitivity of the Pt surface to H- and CO-adsorbates (explained in more detail in Chapter 2.2.3). The electrochemical CO oxidation on Pt (after adsorption of CO and hydroxyl species from dissociated water) can be described as

$$Pt - CO_{ad} + Pt - OH_{ad} \longrightarrow 2Pt \ + \ CO_2 + \ H^+ + e^- \qquad \textbf{(15)}$$

where Pt denotes an empty Pt side.[155] As shown in Figure 17, corresponding peaks in relevant potential regions differ depending on the morphology of the catalysts investigated. In the case of hydrogen desorption (H_{des}) peaks (Figure 17A), broadening or formation of an additional peak shoulder at higher electrode potentials can be observed with the increasing amount of structural surface defects. Similarly, considerable difference between ordered and defective nanoparticle surfaces is reported in the case of CO oxidation (Figure 17B). While the former ones only show a single, pronounced peak close to ~0.8 V *vs* RHE, defective nanostructures show additional double peaks at lower oxidation potentials, which is highly characteristic.[133]

1.6 Top-Down Synthesis of Metal Nanoparticles

Today, several ways to synthesize (supported) Pt-based nanostructures are known. The repertoire reported in the literature ranges from classical wet-chemical methods like the polyol process or reduction of Pt precursor salts with $NaBH_4$ to multiple physical (*e.g.* sputtering or atomic layer deposition), as well as electrochemical deposition methods.[156] Accordingly, a broad variety of Pt and Pt alloy nanostructures was prepared in the past and tested for electrochemical applications, which spans from well-defined surfaces to complex structures. However, such a synthesis is usually complex, involves surfactants or capping agents, often consists of several synthesis steps or might be limited to a laboratory scale, resulting in an uneconomical process.

In recent years, the top-down synthesis of metal nanostructures has attracted an increasing attention. In a seminal work, first observations regarding this method were reported by Bredig and Haber at the end of the 19th century, even decades before detailed research in the field of nanotechnology was conducted.[157] In particular, they experimentally observed an erosion of lead cathodes during electrolysis with direct current in acid and alkaline electrolytes at sufficiently high voltages. This decomposition was described as the formation of a "black cloud" in the electrolyte, starting from the metal cathode. However, despite the interesting observations, a plausible explanation of the phenomenon was not possible at that time. With the increasing interest in the field of nanotechnology, corresponding investigations were specifically resumed. In the recent years, the groups of Li and Koper reported the formation of metal nanoparticles using a similar methodology.[158,159,160,161,162] Both groups noticed that after application of an alternating current (AC) voltage perturbation (in the order of few V) to various metal electrodes (*e.g.* Rh, Bi, Sn, Pb, Pt, Au) immersed in a cation-containing electrolyte (primarily alkali metal-based) one can produce and subsequently disperse nanoparticles of the corresponding metal in the electrolyte (more details on the experimental realization of the nanoparticle synthesis can be found in Chapter 2). It should be noted that the synthesis was shown to work using a cathodic treatment only, however, is strongly accelerated under AC voltage conditions.[162] Hence, this method provides a facile way to produce clean metal nanoparticles and was extended to different materials in the following, including other pure metals (*e.g.* Ir, Cu, Ni), metal oxide materials (*e.g.* $BiVO_4$, TiO_2 photocatalysts) and metal alloys (*e.g.* Pt_xRu, Pt_xNi) by Rodriguez' and Koper's groups.[163,164,165,166,167] Especially Ir-based nanoparticles, Pt_xRu and Pt_xNi nanoalloys can be highlighted, due to their frequent utilization as electroactive materials in PEM electrolyzers and PEM fuel cells.[82,83,154,168,169,170,] Furthermore, the group of Smirnova used the technique to synthesize Pt/C electrocatalyst, which showed promising preliminary electrocatalytic activity toward the oxygen reduction and methanol oxidation reactions, which gives reason for further, more comprehensive investigations.[171,172] A typical CV (black scan) recorded in acidic media and a SEM image of a Pt wire after exposure to a high cathodic potential in alkaline electrolyte are shown in Figure 18A and B, respectively (both by Yanson *et al.*).[162] Notably, a surface enlargement compared to the fresh wire (grey scan) was confirmed *via* the CV after "cathodic corrosion" (as termed by the authors of the work). The Pt wire exhibits a rough and porous surface, fully consisting of densely aggregated Pt nanoparticles. A corresponding SEM image of the generated Pt nanoparticles at higher magnification is shown in Figure 18C. It has to be noted that the highly aggregated form of the nanoparticles is detrimental for ORR applications, due to the associated loss of active surface area.

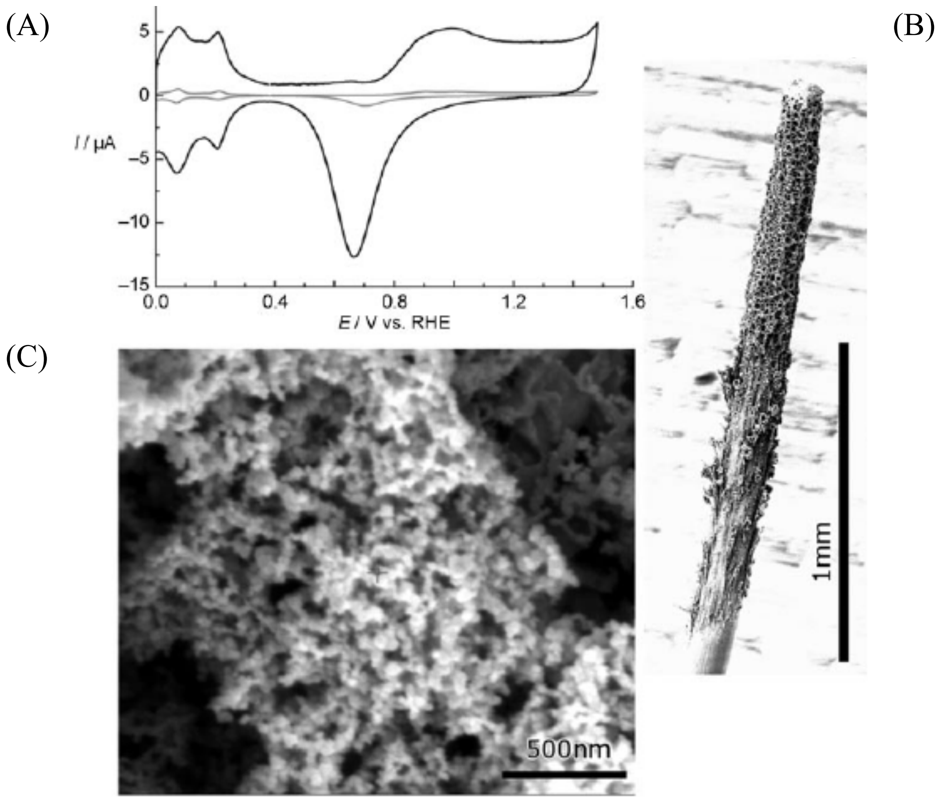

Figure 18. (A) CV of a fresh Pt wire (grey curve) and the same wire after exposure to a high cathodic potential in alkaline electrolyte (black curve). Comparison of the CVs shows a change of the wires' surface area. Both CVs were recorded in sulfuric acid electrolyte. (B) A corresponding SEM image of the Pt wire and the generated nanoparticles after cathodic treatment. (C) A corresponding SEM image of the generated Pt nanoparticles at higher magnification. Reprinted with permission from ref. 162. Copyright 2011 WILEY-VCH Verlag GmbH & Co. KGaA, Weinheim.

While the mechanism of the "cathodic corrosion" is still unknown, the groups of Li, Koper and Smirnova independently proposed different hypotheses on the nanoparticle formation. Commonly, the synthesis was shown to work in different electrolytes, however, alkali metal cations were shown to facilitate the procedure. In their original work, Koper and co-workers proposed that the host metal becomes reduced and the hypothetical metal anionic species formed herein are stabilized by the cations from the electrolyte, prior to re-oxidation. In the final step, the metallic species aggregate, generating metal nanoparticles.[162] Further investigations led to the conclusion of metal hydride species being formed as a main intermediate species.[173] In contrast, Li and co-workers proposed that in the case of Rh, surface oxide formation and subsequent reduction is necessary to form corresponding particles.[158] However, hydride formation was also hypothesized. Thirdly, Smirnova's group suggested that the intercalation of alkali metal cations into the host metal's surface (*e.g.* at grain boundaries) and an adherent generation of surface vacancies is the driving force for the decomposition of the metal.[171] It has to be noted that all proposed mechanisms are solely based on fundamental experimental observations, but lack of clear (*e.g.* spectroscopic) evidences.

Besides mechanistic studies, ensuing investigations gave more detailed insight into the customizability of the top-down synthesis procedure. In particular, a dependence of the determined crystallite size from synthesis parameters such as electrolyte concentration and applied current density were shown. Moreover, detailed SEM investigation of the metal electrode surface after particle synthesis revealed the appearance of varying surface etch pits, such as triangular, rectangular or distorted ones, depending on conditions such as the electrolyte concentration or composition.[174,175,176] While the studies provide important fundamental insight on the impact of the synthesis conditions, detailed investigation of supported and well-dispersed nanoparticles (*e.g. via* TEM) is still missing, in order to access their specific morphological properties. In conclusion, the key advantages of this technique can be highlighted as follows: The methodology can be applied to different host materials including promising catalytic systems. First results indicate that the size and the shape of the nanoparticles can be predictably tailored. Besides, the method is simple and fast, requires only one pot and one step, as well as low amount of post-treatment. In the light of rising demand for PEMFC catalyst materials, this method could provide a promising alternative to the state-of-the-art wet-chemical methods used to synthesize HOR and ORR electrocatalysts. In particular, it could be used to save production costs on an industrial scale, which is desirable since catalyst layers still represent one of the biggest cost shares of an automotive PEMFC stack.[33]

1.7 The Aim of this Work

Since Pt is scarce and expensive, further cost reductions in the field of cathode catalysts are necessary to power cars and utility vehicles by PEMFCs rather than ICEs in a commercially competitive manner. Accordingly, strategies to facilitate the catalyst synthesis and to improve ORR performance are of paramount importance. In this thesis a simple top-down synthesis procedure for highly active nanostructured Pt-based ORR catalysts is investigated. Based on the top-down methodology presented in Chapter 1.6, the principle is exploited, adapted and optimized toward ORR catalyst preparation. In particular, the target of this work is not only to optimize the top-down synthesis of Pt nanoparticles, but also to extend it to the preparation of well-dispersed active carbon-supported electrocatalysts. We focus on the development of a facile one-step, one-pot top-down synthesis route that gets along without the addition of any surfactants or capping agents. The corresponding experimental and methodological fundaments are summarized in **Chapter 2** of this work. To achieve an optimal stability and activity, it is crucial to be able to tailor size and shape of the Pt nanoparticles. Corresponding investigations are summarized in **Chapter 3** of this work and include detailed analysis of various synthesis parameters. Due to the high predicted activity of concave nanoparticles, preparation of nanostructures with highly defective surface regions, including negative curvature, is aimed. Owed to the dissolution of the non-noble metal components of Pt_xM/C alloy catalysts during PEMFC operation and associated degradation and PEM poisoning, it is targeted to boost the ORR kinetics of pure Pt nanostructures *via* surface defects, circumventing aforementioned limitations. Detailed analysis of such a system is presented in **Chapter 4**, including spectroscopic, crystallographic, microscopic, as well as electroanalytical characterization. Moreover, ORR activity and long-term stability evaluation of such nanostructures is conducted in both, a half-cell and MEA configuration. Considering the high ORR activity of certain alloyed Pt nanostructures with 3d transition metal elements such as Ni, Co, Cu or lanthanide and rare-earth metals reported in the literature, we further expand the top-down approach toward the synthesis of such alloys. Detailed investigations of the synthesis and performance of Pt_xPr/C alloy electrocatalyst, as well as attempts to synthesize Pt_xNi/C and Pt_xCu/C alloy catalysts are presented in **Chapter 5 and 6**, respectively.

Chapter 2. Experimental Techniques and Methodology

In this chapter, experimental techniques and corresponding methodologies to synthesize ORR electrocatalysts and characterize their structure, activity and stability are summarized. This includes the electrochemical top-down synthesis of Pt/C and how to evaluate its activity and stability using the rotating disk electrode (RDE) technique, as well as single-cell PEMFC measurements. For structural and compositional electrocatalyst evaluation, microscopic, crystallographic and spectroscopic data are introduced, namely (high-resolution) TEM (HR-TEM), (high-resolution) scanning transmission electron microscopy (HR-STEM) and STEM tomography, SEM, X-ray diffraction (XRD), energy-dispersive X-ray spectroscopy (EDX), wide-angle X-ray scattering (WAXS), thermogravimetric analysis (TGA) and X-ray photoelectron spectroscopy (XPS).

2.1 Electrocatalyst Synthesis

2.1.1 Top-Down Synthesis of Pt/C_{TD}

For the synthesis of Pt/C using the top-down approach (hereinafter referred to as Pt/C_{TD}) illustrated in Chapter 1.6, two Pt wires were corroded in an aqueous alkali metal-based electrolyte by application of an AC voltage. The application of the AC voltage induces the formation of Pt nanoparticles at the surface of the wires, which subsequently disperse into the electrolyte. In order to support the particles after detachment from the Pt wires, active carbon was dispersed in the electrolyte prior to the synthesis.

For the synthesis of the Pt/C_{TD} electrocatalysts discussed in Chapter 3, commercial Vulcan XC72R (Cabot, USA) carbon powder was pretreated in hydrogen peroxide, leading to an oxidation of the carbon surface and hence increased hydrophilicity and improved wettability of the support.[177] To achieve this, 1 g of Vulcan XC72R was dispersed in 100 ml of 30% H_2O_2 solution (Rotipuran® p.a., Roth, Germany) and heated to 60°C for 24 hours under constant stirring at 500 rotations per minute (rpm). The oxidized carbon was diluted with ultrapure water (Evoqua, Germany), filtered in a Büchner funnel, washed with ultrapure water until neutral pH was reached and subsequently dried at 60°C to receive the clean product. Prior to the nanoparticle synthesis, 20 mg of pretreated Vulcan XC72R were dispersed in 25 ml of an alkali metal-containing aqueous (ultrapure water) electrolyte *via* ultrasonication. As the starting material, two Pt wires (99.999%, Goodfellow, Germany; diameter: 0.2 mm) were placed in the electrolyte dispersion. The wires were decomposed into Pt nanoparticles by subjecting them to an AC voltage (under constant ultrasonication) using a BioLogic VSP-300 potentiostat (BioLogic, France). Particle formation could be traced by the formation of dark black spots near both wires. In order to estimate the proportion of the Pt wires to be decomposed, a weight per length unit of wire was determined using a balance and a caliper. The wire was immerged in the suspension to a corresponding extent. Following the nanoparticle synthesis, the suspension was stirred for 12 hours at 500 rpm. The resulting electrocatalyst was filtered in a Büchner funnel, washed with ultrapure water (Evoqua, Germany) and stored at 60°C in a drying oven for 24 hours to obtain the Pt/C_{TD} catalyst powder.

In order to tailor the synthesis of Pt/C_{TD}, the particles were produced at different potential amplitudes (±4V, ±10V, ±15V, ±25V *vs* a Pt-pseudo reference), frequencies (20 Hz, 100 Hz, 200 Hz), electrolyte concentrations (0.2 M, 1 M, 5 M aqueous KOH [85%, analytical grade, Grüssing, Germany]), wave forms (sinusoidal, square wave) and in different electrolytes (1 M aqueous NaOH [99%, analytical grade, Grüssing, Germany], 1 M aqueous KOH, 1 M aqueous LiOH [99.995% trace metals basis, Sigma Aldrich, USA] and 1 M aqueous CsOH [50 wt% in H_2O, 99% trace metals basis, Sigma Aldrich, USA]). All electrolytes were prepared using ultrapure water (Evoqua, Germany).

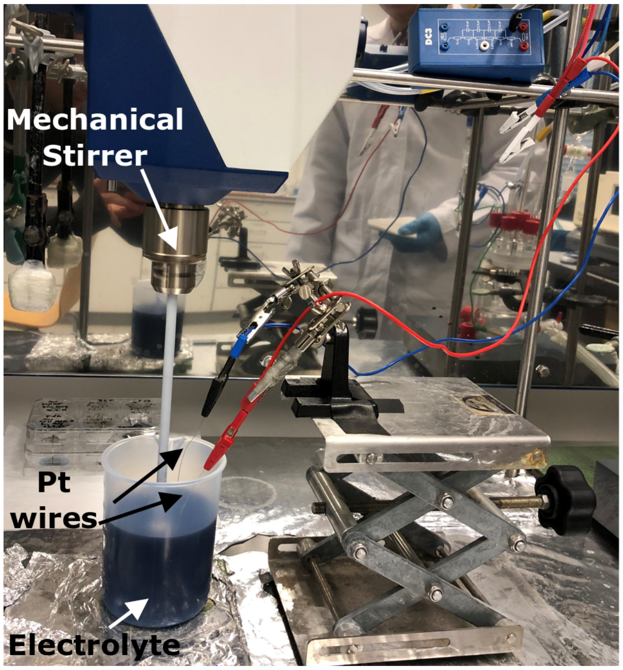

Figure 19. Photo of the setup used for the synthesis of Pt/C_{TD}. Two Pt wires connected to a potentiostat are immersed in a suspension of carbon support and electrolyte while being constantly stirred at ~500 rpm. Alternatively, either ultrasonication or a combination of both can be used to ensure homogeneous distribution of the Pt nanoparticles on the support material.

For the Pt/C_{TD} electrocatalysts discussed in Chapter 4, a slightly modified procedure was applied. 20 mg of untreated Vulcan XC72R were dispersed in 1 M aqueous KOH electrolyte *via* ultrasonication. Approximately 100 µl of ethanol (puriss, >99.8%, Sigma Aldrich, Germany) were added to the electrolyte in order to disperse the highly hydrophobic carbon support. The wires were added and a sinusoidal potential signal of ±10 V *vs* Pt-pseudo reference (frequency: 200 Hz) was applied under constant mechanical stirring. The following steps were as described above. For the fuel cell measurements, this synthesis procedure was up-scaled to ~100 mg of the catalyst powder per batch and additional ultrasonication was applied to suppress particle agglomeration. A typical setup used in this work is shown in Figure 19, while the synthesis of the Pt/C_{TD} catalyst is schematized in Figure 20.

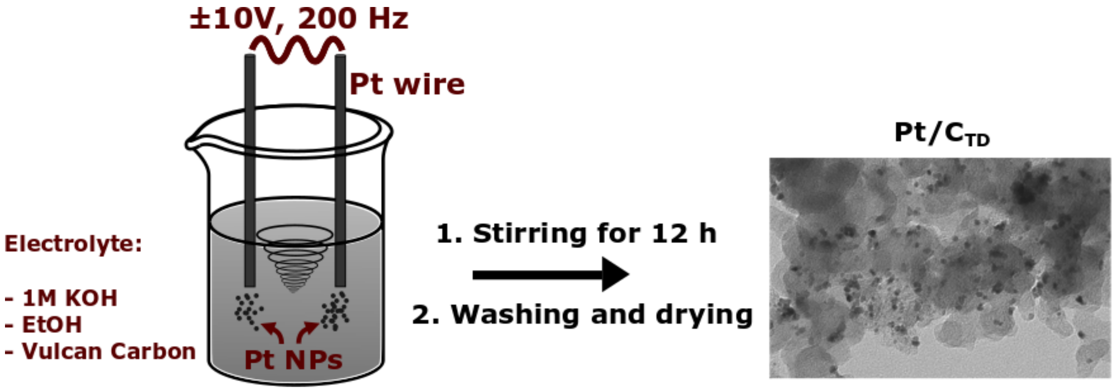

Figure 20. Schematic of the top-down synthesis of Pt/C_{TD}. Two Pt wires are immersed in a dispersion of Vulcan XC72R in 1 M aqueous KOH. Ethanol (EtOH) is added for an improved carbon dispersion. By subjecting the wires to an AC voltage, followed by stirring, washing and drying, electrocatalyst powder is obtained. Adapted with permission from ref. 178. Copyright 2020 American Chemical Society.

2.1.2 Top-Down Synthesis of Pt_xPr/C

The synthesis of Pt_xPr/C was conducted using a three-electrode configuration. In detail, a polycrystalline Pt_5Pr disk electrode of 5 mm diameter (MaTeck, Jülich, Germany) was used as the working electrode (WE). Freudenberg H2315 carbon fiber paper (Freudenberg, Germany) and a commercial Hg/Hg_2SO_4 (0.6 M K_2SO_4, Schott, Germany) electrode served as counter (CE) and reference (RE) electrodes, respectively. As the electrolyte, 8 M aqueous KOH was utilized. By subjecting the WE to a sinusoidal potential signal of ±8 V *vs* RHE at a frequency of 200 Hz, Pt_xPr nanoparticles were produced. The particles were collected and washed *via* centrifugation (6000 rpm) with ultrapure water until neutral pH was adjusted. Afterwards, the particles were supported by addition of Vulcan XC72R carbon, which is described in more detail in Chapter 2.2.2.

2.1.3 Top-Down Synthesis of Pt_xNi/C

To obtain a macroscopic PtNi bulk alloy (1:1 atomic ratio) as the host material for the synthesis of Pt_xNi alloy nanoparticles, corresponding amounts of Pt and Ni wire (>99.99%, Goodfellow, Germany) were alloyed in an arc furnace at the TUM Chair of Inorganic Chemistry with Focus on Novel Materials (for further information see acknowledgement).[179]

For the synthesis of the nanostructured Pt_xNi/C electrocatalyst, the macroscopic PtNi alloy served as the WE. Freudenberg H2315 carbon fiber paper and a Hg/Hg_2SO_4 electrode were used as CE and RE, respectively. As the electrolyte, 4 M aqueous KOH was utilized. Application of ±9 V *vs* RHE sinusoidal potential (200 Hz) led to the formation of the corresponding nanoparticles. *Via* pipetting, the prepared nanoparticles were continuously transferred into a suspension of H_2O/EtOH (ratio 7:1) and Vulcan XC72R carbon under vigorous stirring. The resulting electrocatalyst was stirred for 24 h at 500 rpm, filtered in a Büchner funnel, washed with ultrapure water and stored at 60°C in a drying oven for 24 hours in order to obtain the catalyst powder.

2.1.4 Top-Down Synthesis of Pt_xCu/C

The synthesis of Pt_xCu/C was conducted according to the standard procedures described in Chapter 2.1.1. However, a 0.5 mM amount of $CuSO_4$ x 5 H_2O (>99.5%, Roth, Germany) was dissolved in the carbon/electrolyte suspension (1 M KOH and H_2O_2 pretreated Vulcan XC72R) prior to the Pt nanoparticle synthesis. Subsequently, an AC voltage of ±15 V *vs* Pt-pseudo reference (200 Hz) was applied to the pure Pt wires immersed into the suspension under constant ultrasonication. After synthesis, the resulting electrocatalyst was stirred for 24 h, filtered in a Büchner funnel, washed with ultrapure water and stored at 60°C in a drying oven for 24 hours to obtain the final catalyst powder.

2.2 Electrochemical Measurement Techniques and Preparation

2.2.1 Catalyst Screening using Rotating Disk Electrode Measurements

While the performance of a PEMFC is dependent on many different factors and components, catalysis of the ORR significantly influences voltage losses observed in such a system. Although it is desirable to test novel promising catalysts in a single-cell PEMFC setup or even stack, the preparation of MEA components and following test procedures are time-consuming. In order to enable fast catalyst screening, measurements in a liquid half-cell setup have been established as the method of choice to quickly estimate the ORR performance of various catalytic systems. To investigate half-cell reactions such as the ORR, a three-electrode cell setup is typically utilized, consisting of a glass cell filled with an electrolyte, as well as the corresponding WE, CE and RE. To gain more fundamental information about electrochemical measurements, please see ref. 180. While the usage of H_2SO_4 as an electrolyte is probably more suitable to mimic actual PEMFC conditions, in this work $HClO_4$ was employed in order to prevent poisoning of Pt and rate the activity of the electrocatalysts accordingly.[181,182] Moreover, it can be highlighted that such experiments only require considerably small quantities of active material compared to real FC tests. To gather information about an electrochemical system, voltammetry experiments are typically performed. One of the most frequently used electroanalytical techniques is CV. Here, the potential applied at the working electrode is ramped linearly between a lower and an upper potential limit at a certain scan rate (mV/s), while the current can be recorded simultaneously. After reaching one of the limits, the potential is swept in the reverse direction. Such a cycle can be further repeated in order to observe electrochemical processes and changes at the electrode/electrolyte interface over time.[183,184] Depending on the requirements, certain valuable information cannot be directly accessed using such CV measurements in static electrolyte or with a stationary electrode, as mass transport often strongly influences many electrochemical processes.

Hence, in order to be able to differentiate between the reaction kinetics and mass transport phenomena, RDE measurements have been established as a versatile method for fast electrocatalyst screening over the past decades, especially in the case of the ORR.[185,186,187] In this hydrodynamic technique, the WE of a three-electrode setup is rotated during the measurements. This induces a constant forced convective flow of the electrolyte toward the electrode disk, which influences the corresponding diffusion layer thickness and enables steady-state mass transport investigation of an electrochemical system over time.[188] Typically, the RDE consists of an insulating holder (*e.g.* PTFE-based) and a disk embedded in this holder, which offers control over the geometrical area exposed to the electrolyte. The disk can either consist of an electrocatalytically active material (*e.g.* a polycrystalline Pt disk) or of a conductive substrate (*e.g.* glassy carbon disk), being uniformly coated with a thin film of the investigated active material. In this work, the latter configuration is employed to investigate the carbon-supported Pt electrocatalyst powders. The RDE is immersed in the electrolyte and connected to a rotator, which enables a precise adjustment of the angular velocity. Schematically, such an RDE is depicted in Figure 21. Here, the convectional flow of the electrolyte is indicated by blue arrows, where the analyte first moves toward the electrode center and is then directed away from the electrode.

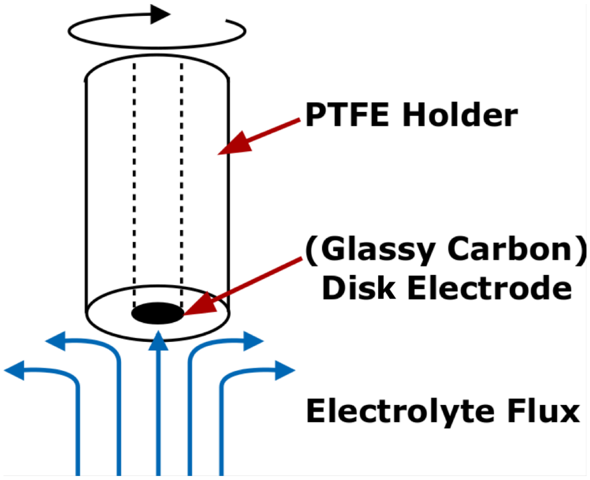

Figure 21. Schematic depiction of an RDE electrode tip. The tip, consisting of a disk electrode embedded in a non-conducting holder, is immersed into an electrolyte and can be rotated at varying velocity. Rotation of the electrode induces a convective electrolyte flux toward the electrode surface, which enables a precise mass transport control.

As depicted in Figure 22A, the variation of the RDE's rotation speed allows a control over the O_2 diffusion-limited current (I_{lim}) during the ORR activity measurements, which is pivotal for an accurate ORR analysis due to the slow kinetics. In detail, with the increasing rotation speed, a uniform increase of the limiting current density can be observed. The correlation between the limiting current and the rotation speed can be described using so-called Levich equation

$$I_{lim} = 0.2 \cdot nFAcD^{2/3}\, \upsilon^{-1/6} \omega^{1/2} \qquad \textbf{(16)}$$

with *n* being the number of electrons involved, *F* being the Faraday constant, A being the area of the disk electrode, *c* being the concentration of oxygen in the electrolyte, *D* being the O_2 diffusion coefficient, *v* being the electrolyte's kinematic viscosity and *ω* being the rotation speed (in rpm).[180,189,190] After gathering the polarization curves at different rotation speeds, one can access the number of involved electrons using an adjusted Levich equation (see inset of Figure 22B) by plotting the reciprocal geometrical current density in the limiting current region as a function of the reciprocal square root of the angular velocity (Figure 22B). Here, B is the slope of the linear regression. In the case of Pt-based catalysts in $HClO_4$ electrolyte this value typically corresponds to a primary four-electron transfer reaction.[189,191,192]

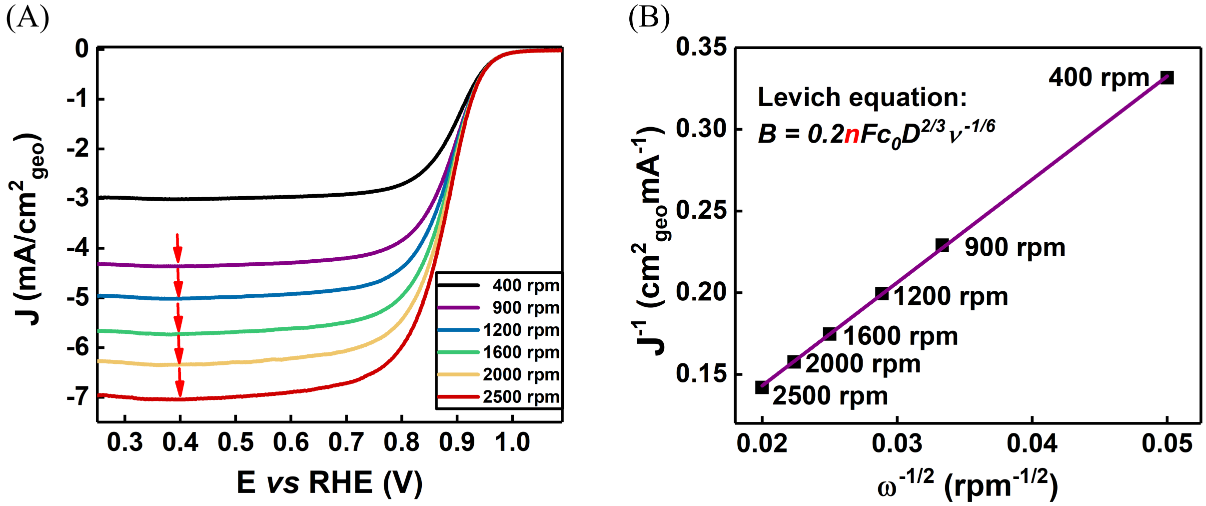

Figure 22. (A) Anodic ORR polarization curves of commercial Pt/C material recorded at different rotation speeds. The current is normalized to the glassy carbon electrode surface area. The curves were recorded in O_2-saturated 0.1 M $HClO_4$ at a scan rate of 10 mV/s and room temperature. The increasing limiting current with increasing rotation speed is indicated by red arrows. (B) Corresponding Levich plot used to determine the number of electrons transferred during the reaction.

2.2.2 RDE Setup, Ink Preparation and Electrode Coating

Prior to electroanalytical investigation of the synthesized catalysts, suspensions of each electrocatalyst (so-called inks) were prepared. Typically, 10 mg of the catalyst powder were finely grinded and mixed with 3.6 ml of ultrapure water (Evoqua, Germany), 1.466 ml of 2-propanol (puriss, Sigma Alrich, Germany) and 30 µl of a 5 wt% Nafion® dispersion in lower aliphatic alcohols and water (Sigma Alrich, Germany) using an ultrasonic cleaner until a homogenous black catalyst ink was obtained (~20 minutes). The corresponding mass ratio of ionomer to Vulcan support material (I/C) was ~0.2. To prepare Pt_xPr/C catalyst inks, a cleaned dispersion of pure nanoparticles in ultrapure water was mixed with a fraction of Vulcan XC72R carbon and Nafion® ionomer, and the resulting metal weight fraction was determined using TGA (see Chapter 2.5). The typical three-electrode RDE setup utilized in this work consisted of a MSR electrode rotator (Pine Instruments, USA), a corresponding glassy carbon disk electrode with an area of 0.196 cm^2 (Pine Instruments, USA), a VSP-300 potentiostat (BioLogic, France), a three-electrode electrochemical cell, a mercury/mercurous sulfate RE (0.6 M K_2SO_4, Schott, Germany) connected *via* a custom-made Luggin capillary and a Pt wire (99.9%, Goodfellow, Germany) as the CE. The (preparation of the) setup is shown in Figure 23.

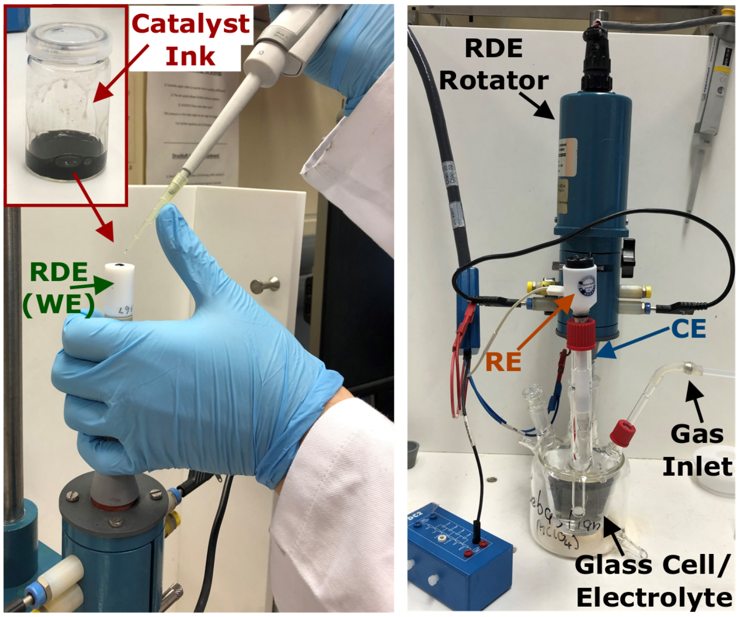

Figure 23. Typical RDE setup and electrode preparation used for the ORR activity evaluation of the electrocatalyst samples. Left: Coating of a glassy carbon disk electrode with an electrocatalyst ink (top left) *via* drop-casting. Right: RDE rotator, electrochemical cell and electrodes connected to a potentiostat.

In all RDE tests, the cell was filled with 0.1 M $HClO_4$ (Suprapur®, Merck, Germany) electrolyte. The electrolyte was purged with Ar (5.0, Air Liquide, Germany), O_2 (4.5, Air Liquide, Germany) or 1000 ppm CO in Ar (4.7/5.0, Westfalen, Germany) for 20-30 minutes prior to each electrochemical experiment. Electrochemical measurements were performed using the EC-Lab software. For reproducibility of the results, the electrochemical cell used for the experiments was frequently freed from unwanted residues with a Piranha solution (sulfuric acid and 30% hydrogen peroxide in a 3:1 ratio), thoroughly rinsed with and boiled in ultrapure water. In order to prepare electrocatalyst-coated RDE electrode tips, the glassy carbon disk electrode was first polished using alumina paste with 0.05, 0.3 and 1.0 µm grain size (MicroPolish^{TM}, Buehler, USA), rinsed using ultrapure water and dried. Subsequently, 10 µl of an as-prepared catalyst ink were drop-casted on the glassy carbon disk and dried under rotation (400 rpm) using a heat gun at the lowest setting level (~100°C). For the evaluation of the Pt_xNi/C electrocatalyst samples, as well as for CO stripping voltammetry and accelerated stress tests (ASTs) of Pt/C_{TD}, a modified setup was utilized. A custom-made cell, a HydroFlex® RHE reference electrode (Gaskatel, Germany) in combination with a Pt wire to filter electrical noise, a glassy-carbon CE and an OrigaTrod RDE system (OrigaLys, France) were utilized. In all cases, high purity gases from Messer, Germany were used. OriginPro (OriginLab, USA) was utilized for data evaluation. If not noted differently, the potential values in this work are referred to the RHE scale according to

$$E(RHE) = E(SHE) + \frac{2.303 \cdot \bar{R} \cdot T}{F} \cdot pH \qquad \textbf{(17)}$$

with *E(SHE)* being the reference electrode potential *vs* the standard hydrogen electrode (SHE), $\bar{R}$ being the ideal gas constant, T being the temperature in Kelvin and F being the Faraday constant.[187] All steps are based on (slightly modified) best practices proposed in the literature, since proper preparation of homogeneous and uniform thin film electrodes and following measurement steps are crucial for reproducibility. Further information on proper cell preparation, ink formulation, thin film preparation and corresponding ORR test protocols (discussed in the following) can be found in refs 186, 187, 193, 194, 195, 196, 197.

2.2.3 Determination of the Electrochemically Active Surface Area of Pt/C-type Electrocatalysts

To rate the ORR activity of electrocatalysts, it is pivotal to accurately determine their ECSA, which is closely associated with the actual Pt area available during electrochemical processes. While more elaborated methods to determine the ECSA can be highlighted,[198] for Pt-based materials two methods are well known to provide accurate results, namely hydrogen underpotential deposition (H_{UPD}) and CO oxidation (or CO stripping).[199,200,201,202,203,204] Both methods are based on the strong affinity of Pt toward H- and CO-adsorbate species, respectively, which leads to an assumed full monolayer coverage of the available Pt surface area. To assess the electrochemical behavior of Pt/C and investigate its structural properties, CVs can be used. A typical voltammogram of Pt/C electrocatalyst recorded in Ar-saturated 0.1 M $HClO_4$ electrolyte is shown in Figure 24A. Here, one has to differentiate between the capacitive contributions (mostly due to the carbon support material, often referred to as double layer region) and Faradaic contributions (*i.e.* charge transfer related).[187] As Pt surfaces are very sensitive to the hydrogen adsorption taking place according to

$$H^{+} + e^{-} + Pt \rightarrow Pt - H_{ad} \qquad \textbf{(18)}$$

where Pt is an empty Pt site and H_{ad} is the adsorbed hydrogen, characteristic adsorption and desorption (H_{des}) peaks can be observed in a potential range of ~0.05 and 0.40 V *vs* RHE. Moreover, formation and corresponding reduction of surface Pt oxide species is observed in higher potential regions (each highlighted in the figure).[44] In Figure 24B, the corresponding $H_{ad/des}$ features are depicted in more detail. In order to determine the ECSA of each individual Pt/C sample, the mean of the charge $Q(H_{ad})$ and $Q(H_{des})$ in µC was determined by integration of the corresponding peaks considering an appropriate baseline. The value was divided by a charge density of 210 $\mu C/cm^2_{Pt}$ required to ad- and desorb a monolayer of hydrogen on Pt, as typically observed in the literature for mono- and bimetallic Pt-based nanomaterials.[187,205]

$$ECSA\ (cm^2) = \frac{0.5 \cdot (Q(H_{ad}) + Q(H_{des}))}{210\ \mu C/cm^2_{Pt}} \qquad \textbf{(19)}$$

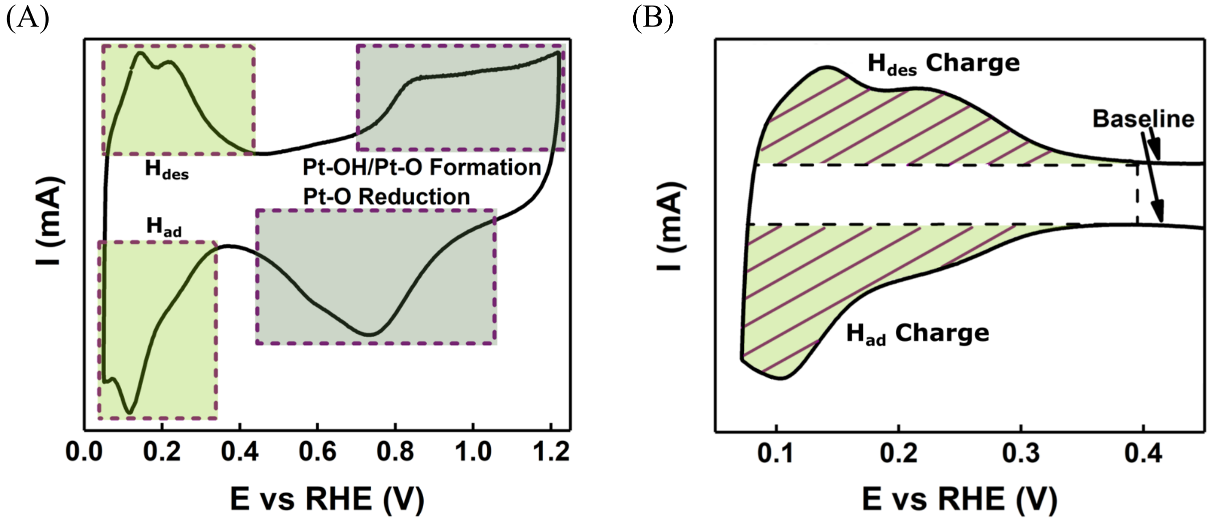

Figure 24. (A) Typical cyclic voltammogram of a commercial Pt/C catalyst, recorded in Ar-saturated 0.1 M $HClO_4$ at the potential scan rate of 50 mV/s. The regions of hydrogen ad- and desorption on the Pt surface, as well as the formation and reduction of Pt surface oxides is indicated by dotted squares. (B) Typical evaluation of the H_{UPD}-charge for the Pt/C by integration of the hydrogen ad- and desorption peaks (stripped area).

In CO stripping voltammetry, a monolayer of CO is adsorbed on the Pt surface, followed by subsequent oxidation and herein removal of the adsorbates, which results in a peak in the corresponding voltammogram.[44,187] For the adsorption of a CO monolayer on Pt nanoparticles, the electrolyte (0.1 M $HClO_4$) was purged with either pure CO for ~6 minutes (Chapter 4) or diluted CO (Chapter 5) for ~30 minutes. During CO adsorption, a potential of 0.1 V *vs* RHE was applied to the WE. To clear the electrolyte from CO afterwards, the electrolyte was purged with Ar for ~30 minutes. To oxidize the adsorbed CO, a full CV (in a potential range of 0.05 to 1.2 V *vs* RHE) was recorded at 20 mV/s scan rate. The first and second scans of such an experiment are depicted in Figure 25A. In the first scan, suppressed hydrogen peaks due to the adsorbed CO are visible, while a novel peak is seen close to 0.8 V *vs* RHE. To determine the ECSA of the catalyst, the CO stripping peak was integrated (see Figure 25B) and the corresponding Coulombic charge (in μC) was divided by the charge density of 420 $\mu C/cm^2_{Pt}$, as proposed in the literature.[187,205]

$$ECSA\ (cm^2) = \frac{Q(CO)}{420\ \mu C/cm^2_{Pt}} \qquad \textbf{(20)}$$

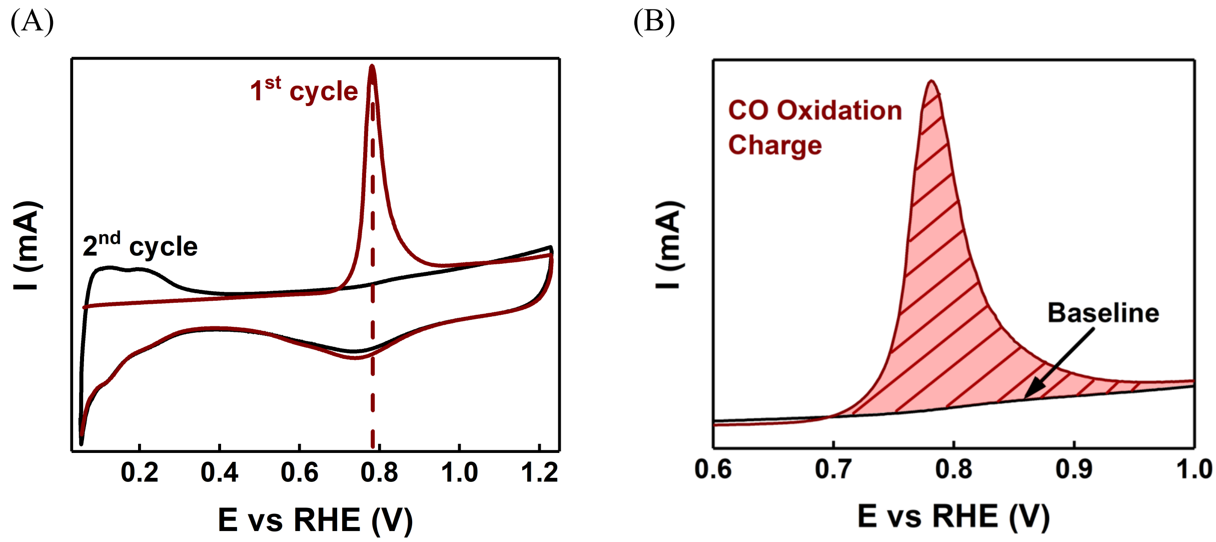

Figure 25. (A) Typical CO stripping voltammogram (red) and base CV (black) of a commercial Pt/C sample, recorded in Ar-saturated 0.1 M $HClO_4$ at a scan rate of 20 mV/s after adsorption of CO for ~6 minutes and purging of the electrolyte with Ar for ~30 minutes. A single CO oxidation peak is visible at ~0.8 V *vs* RHE. (B) Typical evaluation of the CO oxidation charge of Pt/C by integration of the peak.

Accordingly, the ECSA per mass of Pt on the glassy carbon disk (determined *via* thermogravimetric analysis and the ink ratio, see 2.5) can be calculated, which will be referred to as mass-specific surface area (SSA) in the following.

$$SSA = \frac{ECSA\ (m^2)}{Pt\ mass\ (g)} \qquad \mathbf{(21)}$$

2.2.4 Oxygen Reduction Reaction Activity Evaluation

To investigate the ORR kinetics of the electrocatalysts prepared in this work, it was important to accurately investigate the prepared electrocatalyst thin films using the RDE technique. The utilized ORR evaluation test protocol involved the steps summarized in the following. After drop-casting and subsequent drying of a catalyst thin film on the glassy carbon substrate, the coated disk electrode was immersed into an Ar-saturated (~20 minutes) 0.1 M $HClO_4$ electrolyte. First, the catalyst was conditioned by cycling the electrode potential between 0.05 and 1.2 V *vs* RHE at the scan rate of 50 mV/s until a stable CV was obtained (~25 cycles). In order to correct the ORR polarization curves for the *IR* drop, the uncompensated ohmic resistance (*i.e.* primarily the electrolyte resistance between RE and WE) was determined *via* electrochemical impedance spectroscopy (EIS). To suppress measurement artifacts, a shunt capacitor was connected between RE and CE.[206,207,208]

Following Ohm's law

$$R = E/I \tag{22}$$

it is possible to correct the recorded potential E_m using the measured current I_m and the high-frequency resistance R_{HF} according to

$$E_{IR-free} = E_m - (I_m \cdot R_{HF}) \tag{23}$$

The *IR* drop-correction is indicated in the caption of each graph. In order to correct the ORR polarization curves for (pseudo-)capacitive currents, a background CV between 0.2 and 1.1 *vs* RHE was recorded in Ar-saturated 0.1 M $HClO_4$ at a scan rate of 10 mV/s. Subsequently, the electrolyte was saturated with O_2 for ~30 minutes.

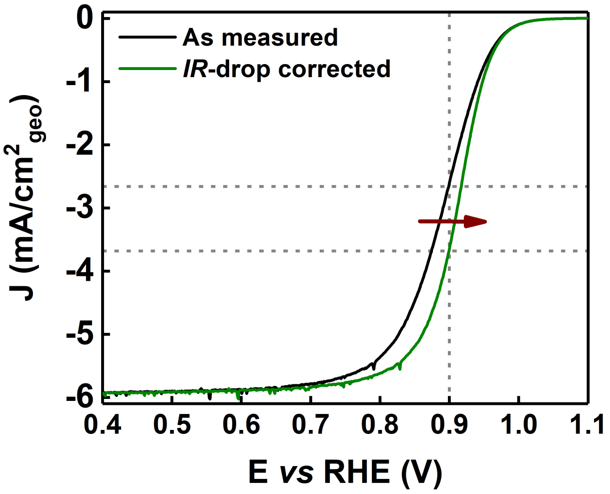

Figure 26. RDE anodic polarization curves for the commercial Pt/C before (black) and after (green) *IR* drop-correction. The curve was recorded in O_2-saturated 0.1 M $HClO_4$ at a scan rate of 10 mV/s and rotation speed of 1600 rpm. The current is corrected for (pseudo-)capacitive contributions and normalized to the glassy carbon electrode's surface area. The shift of the curve upon *IR* correction is indicated by a red arrow.

While the CVs in Ar were recorded without any rotation, the ORR polarization curves were recorded at a rotation speed of 1600 rpm in order to control the oxygen mass transport (scan rate of 10 mV/s in a potential region of 0.2 to 1.1 V *vs* RHE). All measurements were conducted at room temperature. Processing of the recorded data includes subtraction of the background CV and the correction of the *IR* drop, as depicted in Figure 26.

For determination of the ORR kinetics, the anodic scan of each polarization curve was analyzed at a potential of 0.9 V *vs* RHE. At this point, the current density is close to half of the limiting current density and close to the half-wave potential of the polarization curve, as described in the guidelines of Mayrhofer *et al.*[209] After the applied corrections, the kinetic current (I_{kin}), *i.e.* the current, which is free from mass transport limitations, can be determined using the so-called Koutecký–Levich equation shown below.[187] Here, I_{lim} corresponds to the O_2 diffusion-limited current of a polarization curve introduced earlier, while I_m corresponds to the measured current.

$$I_{kin} = |(I_m \cdot I_{lim})|/|(I_{lim} - I_m)| \qquad \textbf{(24)}$$

Using the kinetic current value obtained at 0.9 V *vs* RHE, it is possible to determine the surface-specific (referred to as specific activity, SA) and mass-specific (referred to as mass activity, MA) ORR activity of an electrocatalyst sample, that is, the activity per ECSA (determined *e.g. via* H_{UPD} analysis) or mass of Pt (determined *via* thermogravimetric analysis and ink ratio, see 2.5), respectively.

$$SA = \frac{I_{kin}\,(mA)}{ECSA\,(cm^2)} \qquad \textbf{(25)}$$

$$MA = \frac{I_{kin}\,(mA)}{Pt\ mass\,(mg)} \qquad \textbf{(26)}$$

To investigate the behavior of the Pt/C electrocatalysts during simulated long-term operation, as-synthesized samples were first subjected to the above-shown test protocol. In a second step, the electrocatalyst thin film electrodes were subjected to 10,000 square wave potential cycles (3s at each potential limit) between 0.6 and 1.0 V *vs* RHE at a temperature of 80 °C. For the following ORR activity evaluation, the electrolyte was replaced to avoid contaminations.

2.2.5 The Benchmark Commercial Pt/C Electrocatalysts

As the reference catalyst in this work, commercial 19.6 wt% Pt/C (TEC10V20E, denoted as Pt/C_{TKK}) from Tanaka Kikinzoku Kogyo K.K. was used. A typical CV and ORR polarization curve are shown in Figure 27A and B, respectively.

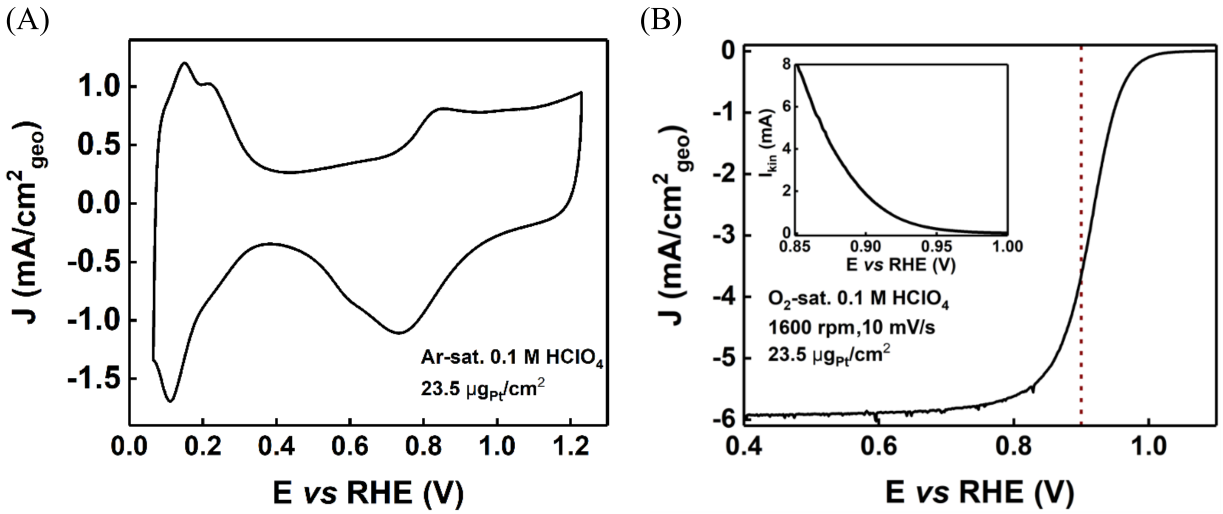

Figure 27. (A) Typical CV of Pt/C_{TKK} recorded in Ar-saturated 0.1 M $HClO_4$ at a scan rate of 50 mV/s. (B) Representative ORR polarization curve (anodic scan) recorded in O_2-saturated 0.1 M $HClO_4$ at a scan rate of 10 mV/s, room temperature and a rotation speed of 1600 rpm. The curve is corrected for the *IR* drop and (pseudo-)capacitive currents. In the insets of the figure, the corresponding kinetic current curve and detailed measurement parameters are shown. Reprinted with permission from ref. 178. Copyright 2020 American Chemical Society.

The ORR activity comparisons performed in Chapters 4 and 5 are based on the Pt/C_{TKK} electrocatalysts. Regarding the Pt nanoparticle size of Pt/C_{TKK}, a number-averaged diameter (d_N) of 2.8 ± 0.8 nm and a surface-averaged diameter (d_S) of 3.2 nm is reported in the literature.[210,211] In Chapter 6, 5 wt% Pt/C from E-TEK company was used as the reference catalyst mainly due to a more comparable Pt weight fraction and, according to the literature, a more comparable average particle size of ~1.8 nm.[212]

2.2.6 Single-Cell PEMFC Measurements

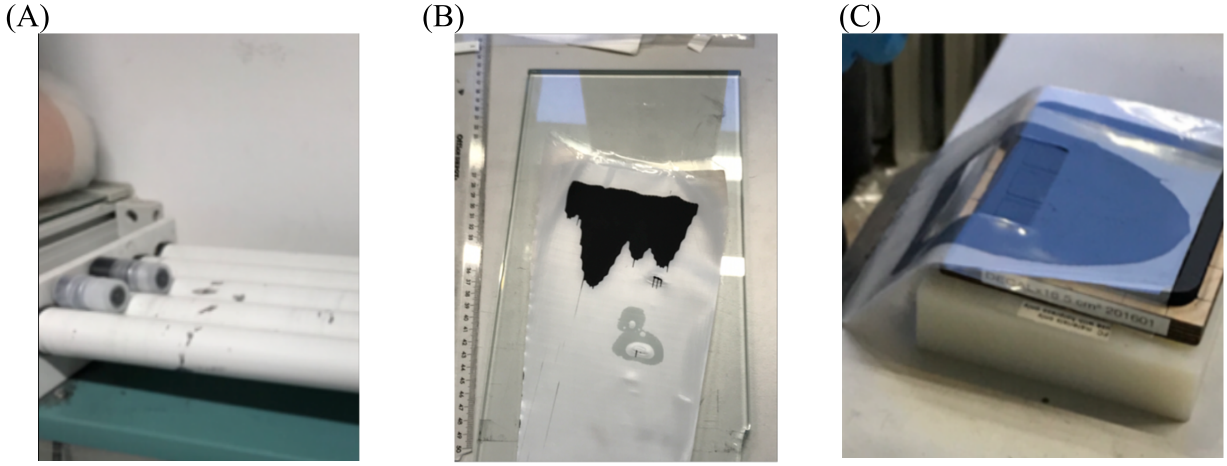

Figure 28. CCL preparation steps. (A) Catalyst ink mixing on a roller mill, (B) rod coating of the catalyst ink on a PTFE decal, (C) punching of the CCL.

Single-cell PEMFC measurements were performed at the TUM Chair of Technical Electrochemistry. Synthesis of the cathode Pt/C catalyst was conducted as described in Chapter 2.1.1 using untreated Vulcan XC72R carbon. The Pt/C_{TKK} material was used as the anode catalyst. The catalyst inks were prepared by mixing the catalyst powder, 1-propanol, ~10 wt% water and Nafion® ionomer (5 wt% in lower aliphatic alcohols and water, Sigma-Aldrich, Germany) on a roller mill for 18 hours at ambient conditions (Figure 28A). The I/C mass ratio was set to 0.65. Before mixing, ZrO_2 beads were added to the ink as a grinding medium. The Pt content of the ACL and CCL was set as 0.08 mg_{Pt}/cm^2 and 0.1 mg_{Pt}/cm^2, respectively. The catalyst layers were manufactured on a 50 µm PTFE decal utilizing a coating bar. The catalyst layers were dried at ambient conditions (Figure 28B). Subsequently, 5 cm^2 catalyst layers were punched using a template (Figure 28C) and hot-pressed with a 15 µm Nafion®-based membrane for 3 minutes at 155°C to receive the MEA. Fuel cell testing was carried out in a homemade single-cell PEMFC setup. Besides catalyst layers and the membrane, the cell consisted of homemade flow fields and ~20% compressed GDLs (H14C7, Freudenberg & Co. KG, Germany; thickness: ~160 µm). A G60 Greenlight Innovation test station (Greenlight Innovation Corp., Canada) and a Gamry reference 3000 potentiostat (Gamry Instruments, USA) were used to control the experiments. To investigate the SSA and activity of Pt/C_{TD}, CO stripping voltammetry was conducted. First, 10% CO (in N_2) was adsorbed for 10 minutes at a cell potential of 0.1 V. Afterwards, the CO was removed from the cell for more than 1 h by flushing the cell with pure N_2. Subsequently, CO stripping was performed between 0.1 and 1.1 V at 100 mV/s. Differential flow polarization curves were obtained at a constant reactant flow of 2000 and 5000 nccm for H_2 and O_2/Air, a temperature of 80°C, 170 kPa_{abs} and full humidification (100% RH) under current control. A hydrogen crossover current of ~4.8 mA/cm^2_{geo} was determined under similar conditions. However, H_2 and N_2 gases were supplied to the anode and cathode of the cell, respectively. The high-frequency resistance used to correct for the *IR* drop was determined *via* EIS.

2.3 Spectroscopic Techniques

2.3.1 X-ray Photoelectron Spectroscopy

In material science, XPS is widely used to investigate the surface elemental composition of a specimen. By irradiating a sample with an X-ray beam of sufficiently high energy, photoelectrons are ejected from its surface atoms. Consequently, the kinetic energy of the ejected electrons can be detected, which requires UHV conditions due to typically long physical distance between sample and detector setup in order to prevent undesired interactions. According to equation 27, the binding energy (E_{bin}) of the detected electrons can be calculated if the photon energy ($h\nu$) of the incident X-ray beam, the system-specific work function ϕ, as well as the kinetic energy (E_{kin}) of the ejected electrons are known:

$$E_{bin} = h\nu - (E_{kin} + \phi) \qquad \textbf{(27)}$$

These binding energies are characteristic for certain species and their "chemical states" and surroundings, which enables a precise chemical analysis of the near-surface atomic layers of an investigated specimen.[213]

In this work, XPS samples were prepared by drop-casting of an aliquot of a liquid sample onto a copper adhesive tape or a gold arandee™ substrate followed by drying at ambient conditions or in a furnace at 60 °C. XPS patterns shown in Chapters 4 and 5 were collected utilizing a custom-made UHV setup, which includes a commercial SPECS XR50 X-ray source with Al-Kα anode (monochromatic beam, $h\nu$ =1487 eV), a SPECS spectrometer and a SPECS PHOIBOS 150 hemispherical analyzer setup. Data were acquired using the SpecsLab Prodigy software (SPECS Surface Nano Analysis GmbH, Germany). For the peak analysis, Shirley background subtraction and Gaussian fitting were performed utilizing the OriginPro software.

2.3.2 Energy-Dispersive X-ray Spectroscopy

Another technique enabling elemental surface analysis of solids is EDX. In this technique, a sample is subjected to an external stimulation by an electron beam, which leads to the excitation of electrons from the inner shells of the surface and near-surface atoms. As this instable state is filled by other higher-energy electrons, characteristic X-rays are emitted. These X-rays can be detected and since their energy is element-specific, they can be utilized as a measure for the sample's chemical composition.[214] Importantly, EDX can be coupled with electron microscopic techniques such as STEM (Chapter 2.4), which allows to combine microscopic images with elemental maps of a specimen (*e.g.* STEM-EDX). STEM-EDX measurements of Pt_xPr/C and Pt_xNi/C shown in Chapters 5 and 6 were acquired at Grenoble Institute of Technology (Laboratoire d'Electrochimie et de Physicochimie des Matériaux et des Interfaces, for further information see acknowledgement). STEM-EDX analysis of the Pt_xCu/C electrocatalysts was performed at the Brno University of Technology (Central European Institute of Technology, for further information see acknowledgement). For detailed microscope and equipment specifications, see Chapter 2.4.

2.4 Electron Microscopic Techniques and Analysis

In the field of materials science, electron microscopic techniques are the most suitable choice to image various types of samples, due to the high possible angular resolution in the sub-nanometer range.[215,216] Commonly, imaging in electron microscopy is based on an electron beam (accelerated at voltages in the order of keV) probing that is focused onto a specimen *via* electron optics (*i.e.* electrostatic or magnetic lenses) in high vacuum. Depending on the sample, beam energy and, in turn, sample penetration depth, different interactions of highly energetical electrons and the investigated matter can be detected and are further used for imaging. The high resolution of such microscopes is a result of the small wavelength of electrons. Accordingly, such techniques are frequently used to characterize electrocatalyst samples, which are typically based on nanostructures due to their high surface-to-volume ratio.[217,218] Moreover, the high resolution enables investigation of particularly active surface structures on an atomic scale, which is pivotal for optimum catalyst design.

In this work, different types of electron microscopy were employed, in order to access structural and morphological properties, as well as "material contrast" of the electrocatalyst samples analyzed. In particular, this includes SEM and TEM investigation. In the case of SEM, a fine electron beam is scanned over an impermeable sample. As the primary source for imaging, secondary electrons or backscattered electrons (BSEs) are selectively detected. While secondary electrons provide topographical information, the BSEs can be used to gather information about chemical compositions.[219,220] In the latter case, a contrast can be obtained since heavier elements cause a stronger backscattering than lighter ones. Accordingly, brighter spots in the image can be assigned to heavier elements. Contrary, a transparent sample is irradiated by a broad (stationary) beam in TEM. This leads to direct transmission and scattering of the incident electrons, which can hereinafter be detected and further used for imaging.[221] More precisely, in the case of common bright-field imaging, directly transmitted electrons are detected and used to gather morphological information. The image contrast relies on the sample spot thickness and the atomic number of the elements.[222] For instance, carbon support structures appear as a light transparent shading, while Pt nanoparticles manifest themselves as "solid" and dark structures in TEM. Moreover, electron diffraction in TEM can be utilized to obtain structural and crystallographic information about the sample investigated.[223] As a combination of both techniques, a finely focused beam is scanned over a transparent sample in STEM. As elucidated in the previous subchapter, it is possible to combine

STEM with elemental mapping. Moreover, operation of STEM in high-angle annular dark-field (HAADF) mode provides an improved contrast compared to the conventional bright-field imaging, since electrons scattered at a high angle are primarily detected (rather than un-scattered ones) and used for imaging.[222,224] Using state-of-the-art STEM tomography, it is possible to investigate the three-dimensional (3D) structure of nanosized materials. Here, two-dimensional (2D) STEM-HAADF images are recorded in a tilt-series experiment (*i.e.* a set of images recorded at different angles around the sample) and are used to reconstruct a 3D tomogram.[225] For more fundamental information about the functional principles of electron microscopy, please also see ref. 226.

2.4.1 (Scanning) Transmission Electron Microscopy and Tomography

For the preparation of (S)TEM samples, an aliquot of sonicated catalyst ink or unsupported nanoparticles dispersed in ultrapure water/2-propanol was drop-casted on TEM grids (Formvar/carbon film-coated Cu 400 mesh, Science Services, Germany or graphene oxide film-supported Quantifoil® holey carbon grids, Quantifoil, Germany). The STEM analysis of Pt/C_{TD} samples (Chapter 3), the HR-STEM-HAADF and HR-TEM analysis of Pt/C_{TD} (Chapter 4), the (HR-)TEM analysis of unsupported Pt_xPr nanoparticles (Chapter 5), as well as the STEM(-EDX) analysis of Pt_xCu/C samples (Chapter 6) were performed at the Central European Institute of Technology (Brno, Czech Republic, see acknowledgement) and recorded on a FEI Titan Themis 60-300 (Thermo Fisher Scientific, USA) microscope equipped with a HAADF (Fischione, USA) detector and EDX spectrometer at 300 kV accelerating voltage. STEM-HAADF tomography of Pt nanoparticles (Chapter 4) was performed on a FEI Titan 80-300 (FEI Company, USA) at the Karlsruhe Institute of Technology (see acknowledgment and ref. 178). The tilt-series was acquired in 2° steps in a range of ±72° using a dedicated field-of-view tomography holder. Regular TEM images of Pt/C_{TD} samples (Chapters 3 and 4), as well as of Pt_xPr/C electrocatalyst (Chapter 5) were recorded on a Philips CM100 EM device at 100 kV accelerating voltage (see acknowledgement). STEM-EDX images and maps of Pt_xPr/C (Chapter 5) and Pt_xNi/C (Chapter 6) were recorded at the Grenoble Institute of Technology (Grenoble, France, see acknowledgement) on a JEM-2100F microscope (JEOL, Japan), equipped with an EDX detector, at 200 kV accelerating voltage.

2.4.2 Scanning Electron Microscopy

The surface of the Pt_5Pr disk electrode (Chapter 5) was investigated using an Ultra 55 (Zeiss, Germany) SEM device, operated at an accelerating voltage of 15 kV. The images were acquired at the Grenoble Institute of Technology (Grenoble, France, see acknowledgement).

2.4.3 Evaluation of Particle Size (Distributions)

To analyze the particle size and PSD of supported and unsupported Pt-based nanoparticles, corresponding (S)TEM images with suitable resolution were acquired using the imageJ software.[227] For each particle, the Feret diameter

$$d_F = \frac{d_{min} + d_{max}}{2} \tag{28}$$

was determined (if no spherical shape was observed), where d_{min} and d_{max} are the shortest and longest diameter of each particle, respectively. The d_N was calculated according to

$$d_N = \frac{\sum_{i=1}^{n} l_i d_i}{\sum_{i=1}^{n} l_i} \tag{29}$$

with l_i being the particle number and d_i being the corresponding particle diameter.[211] The corresponding d_S was calculated according to

$$d_S = \frac{\sum_{i=1}^{n} l_i d_i^3}{\sum_{i=1}^{n} l_i d_i^2}\,.^{211} \tag{30}$$

Per sample, at least 100 individual nanoparticles were evaluated, in order to ensure reproducible results. Assuming a statistically significant d_S value (in meters), it is possible to estimate the SSA (in m^2/g_{Pt}) of Pt nanoparticles using the following relation, considering homogeneous ionomer wetting of the catalyst investigated, approximately spherical Pt nanoparticle shape and uniform particle distribution on the support (*i.e.* low degree of aggregation):[211,228]

$$SSA = \frac{6}{\varrho \cdot d_S} \tag{31}$$

In the equation presented above, ϱ corresponds to the density of Pt (21.5 g/cm^3) in g/m^3. It should be noted that TEM analysis is prone to statistical uncertainties. Hence, the calculated value is only used to roughly compare values, while a certain error has to be considered.

2.5 Determination of Pt/C Weight Fractions *via* Thermogravimetric Analysis

In order to determine the weight fraction of Pt (alloy) nanoparticles of a synthesized catalyst powder (*i.e.* carbon support and nanoparticles), TGA was utilized. Accurate determination of this weight fraction is crucial for the evaluation of the MA of the electrocatalysts, since the metallic nanoparticles can be regarded as the only part that is active toward the ORR. To achieve this, a certain proportion of the electrocatalyst powder was investigated using a Mettler-Toledo TG-MS device. First, the sample was heated up to 135°C to remove water residues followed by determination of the initial weight of the sample. Afterwards, the temperature was ramped to 1100 °C at the rate of 50 K per minute under a constant air flow (50 ml per minute), which causes oxidation of the carbon support. The temperature was hold at the peak temperature until no further weight loss was observed. Finally, the weight of the remaining pure Pt was evaluated after cooling to the temperature of 135°C. A typical TGA curve of a Pt/C sample is depicted in Figure 29. The green arrows indicate the weight difference between the initial sample and after carbon support oxidation. TGA was acquired at TUM Catalysis Research Center. For further information, see acknowledgement.

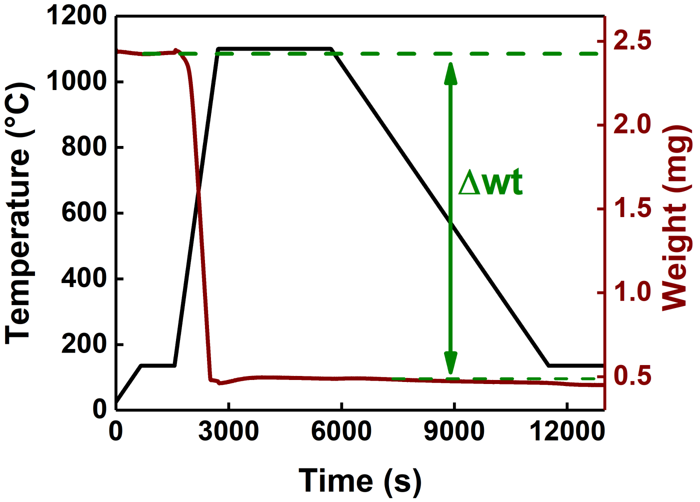

Figure 29. Representative results of the thermogravimetric analysis of a Pt/C sample showing the temperature ramp as a function of time (black curve) and the change of weight as a function of time (red curve). The green arrows indicate the weight transition induced by the oxidation of the carbon support, leaving pure Pt nanoparticles.

2.6 X-ray Diffraction Analysis of Nanomaterials

In material science, XRD is a prominent technique to investigate crystallographic and structural properties of *e.g.* nanosized materials. In the employed method, a powder sample (*e.g.* electrocatalyst powder) is subjected to a monochromatic X-ray beam. In the crystal lattice of the investigated specimen, X-rays are elastically scattered, which leads to both, constructive and destructive interference. Constructive interference (*i.e.* waves are in phase) can be described according to Bragg's law

$$2d_P \sin\theta = n \cdot \lambda \tag{32}$$

with d_P being the distance between two lattice planes, θ being the Bragg angle and n being an integer of the X-ray beam wavelength λ. Typically, XRD is measured in a broad range of 2θ angles. Resulting interactions are detected, leading to signals in a so-called diffraction pattern, if constructive interference is satisfied.[229] Using the so-called Scherrer equation,

$$d_C = \frac{\kappa \cdot \lambda}{\beta \cdot \cos\theta}, \tag{33}$$

it is possible to estimate the average crystallite size of the sample, given the Scherrer constant κ (~0.9) and the XRD peak width at half maximum intensity β.[230] However, precise estimation and differentiation of crystallite size and microstrains (*i.e.* lattice parameter differences/deviations from the regular case, resulting from *e.g.* structural defects) is needed, as both influence the XRD peak width.[133,154] Since both parameters are of importance in this work, so-called Rietveld refinement can be utilized, where simulated (based on the known parameters) and measured patterns are compared and refined to minimize differences.[231,232] To rate the (successful) alloying of bimetallic Pt-based nanoparticles, XRD was employed in this work, since (partial) alloying of Pt nanoparticles is typically accompanied by a peak shift with respect to pure Pt phases. Moreover, peak positions are compared using corresponding powder diffraction files (PDF) obtained from the International Centre For Diffraction Data database. For more fundamental information about the XRD analysis of nanomaterials, please see refs 230 and 233. WAXS (which refers to the wide scattering angles) of synthesized and commercial Pt/C samples (Chapter 4) was acquired and evaluated at the European Synchrotron Radiation Facility, beamline ID31 (Grenoble, France, see acknowledgement) at a X-ray energy of 70 keV. For Rietveld refinement (*via* the Fullprof software), an additional Ni phase had to be added, due to a slight contamination.[178] Powder XRD of as-synthesized and acid treated Pt_xPr/C (Chapter 5) was measured at the TUM Catalysis Research Center (see acknowledgment) on a X'Pert Pro powder diffractometer (PANalytical, Netherlands) using a Cu-Kα X-ray source and a Ni-based filter. Samples were prepared by drop-casting an aliquot of catalyst ink on a Si substrate, followed by drying. XRD patterns were recorded in 0.01313°/300 ms steps in a 2θ range of 5 to 90°.

Chapter 3. Toward a Versatile Top-Down Synthesis of Pt/C: How to Control the Particle Size and Shape

In this chapter, synthesis strategies to tailor Pt nanoparticle size and shape during the top-down synthesis of Pt/C are described and discussed. In particular, deduction of an optimal Pt nanoparticle size and shape for the ORR applications was targeted. This includes investigation of the impact of the most important synthesis parameters, namely the potential amplitude, the applied frequency, the wave shape, as well as the electrolyte concentration and composition, using TEM studies.

Parts of this chapter have been published in: Garlyyev, B.; Watzele, S.; Fichtner, J.; Michalička, J.; Schökel A.; Senyshyn, A.; Perego, A.; Pan, D.; El-Sayed, H. A.; Macak, J. M.; Atanassov, P.; Zenyuk, I. V.; Bandarenka, A. S. Electrochemical Top-Down Synthesis of C-Supported Pt Nanoparticles with Controllable Shape and Size: Mechanistic Insights and Application. *Nano Research* **2020**.[234]

https://doi.org/10.1007/s12274-020-3281-z

3.1 Tailoring the Pt Nanoparticle Size

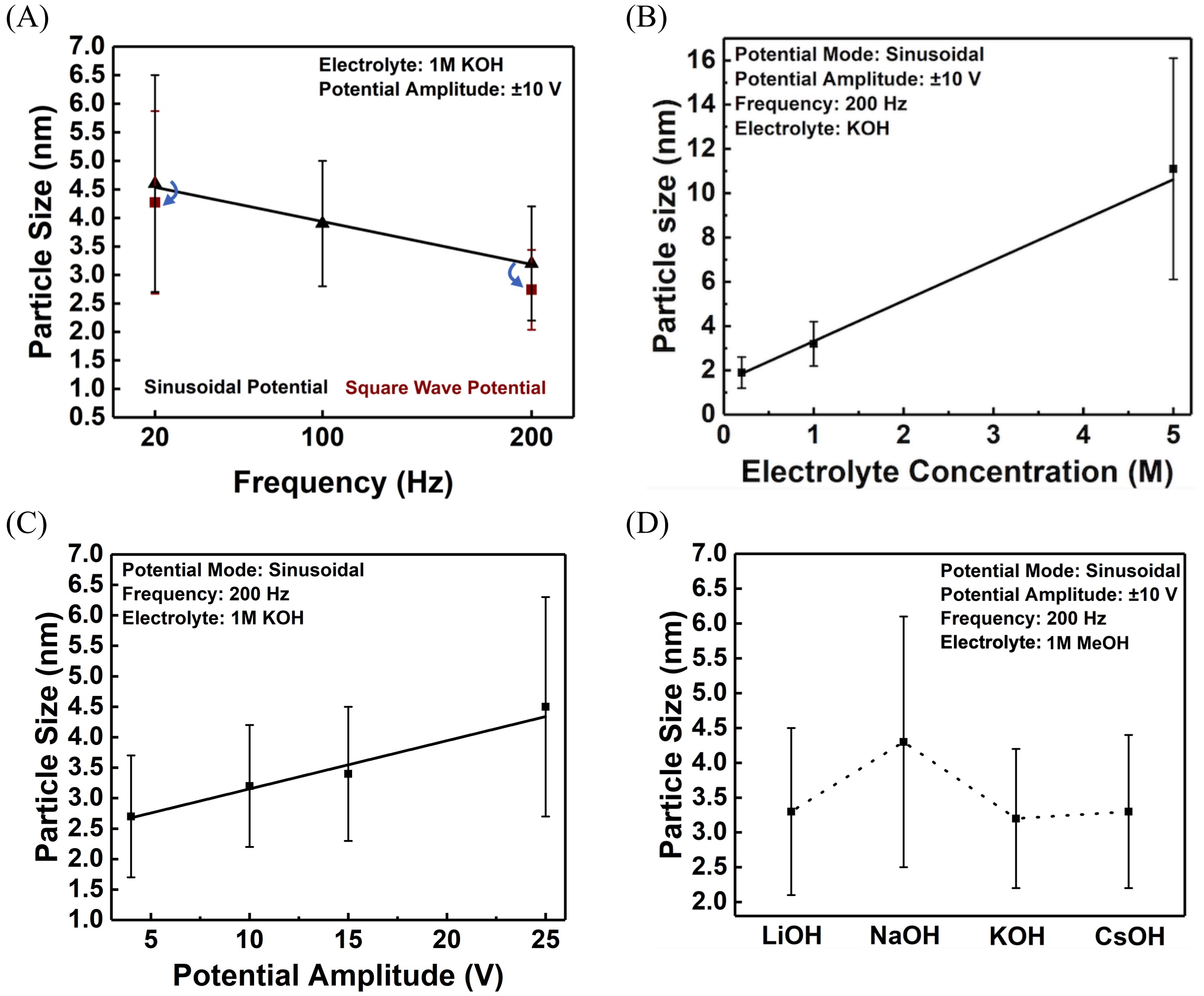

Figure 30. Particle size of the synthesized Pt/C_{TD} samples as a function of the (A) frequency (for both square wave and sinusoidal potential shapes), (B) electrolyte concentration, (C) electrode potential amplitude and (D) alkali metal cations present in the electrolyte. Me = Li, Na, K, Cs. Constant parameters are shown in the inset of each figure. Linear fits are displayed as solid lines.[234]

As described in Chapter 1.6, the top-down synthesis of Pt nanoparticles is in general a simple way to prepare electrocatalyst samples. For most applications, however, it is particularly important to be able to control the size and shape of such particles. As explained earlier (Chapters 1.4 and 1.5), both characteristics significantly contribute to an optimal ORR activity. For example, we have recently demonstrated through experimental and theoretical studies that pure, spherical (or spheroidal) Pt nanoparticles can achieve an absolute ORR mass activity of up to 2.3 A/mg_{Pt} when the nanoparticle diameter is precisely adjusted with a very small particle size distribution (*e.g.* 2.87 nm).[235] In practice, it is a challenging task to tailor such exact particle diameters, particularly with low PSD. However, commercial ORR catalysts such as Pt/C_{TKK} (used as a reference in this work) exhibit a similar average nanoparticle size but their performance is (amongst others) limited by their wide PSD (2.8 ± 0.8 nm).[210] In order to ensure a precise adjustment of the desired properties of our catalysts, this chapter discusses the influence of the most important synthesis parameters on Pt nanoparticle size and shape. This includes potential amplitude, frequency, waveform, electrolyte concentration and composition. While the impact of some of these parameters was already investigated in the literature (see section 1.6), SEM and XRD analysis of the host metal surfaces and unsupported nanoparticle aggregates performed in the respective works cannot be considered sufficient for a precise tailoring of the electrocatalytic properties of the nanoparticles.[174,175,176] Hence, TEM analysis of carbon-supported Pt nanoparticles is utilized in this section to get an adequate insight in the top-down synthesis procedure. In detail, a particle size close to 3 nm with the smallest possible PSD was sought to achieve optimal specific and mass activity toward the ORR. The standard experimental synthesis procedure was as presented in the experimental section 2.1.1, and all further variations are indicated here. For the investigation of the nanoparticles, the number-averaged diameter was calculated according to equation 29. For each data point, ~100 nanoparticles were examined using the imageJ software.

Figure 30 shows the variation of the TEM-derived Pt nanoparticle diameters as a function of frequency (A), electrolyte concentration (B), potential amplitude (C) and electrolyte composition (D). Indeed, the nanoparticle size seems to be linearly dependent on the frequency, electrolyte concentration and the electrode potential amplitude. In the case of frequency and potential amplitude, however, the measured steps show only small changes. For example, at a constant concentration and sinusoidal potential amplitude, the nanoparticle size changes by ~1 nm (4.6 ± 1.9 nm to 3.2 ± 1.0 nm) at the step from 20 to 200 Hz. It also shows that the waveform (sinusoidal compared to square wave) has a minor effect on the resulting particle size. Similarly, the potential amplitude (at a constant frequency) varies the nanoparticle diameter by ~0.08 nm per voltage step, which allows the size alignment in a narrow range. In contrast, a coarse size adjustment can be obtained through the variation of the electrolyte concentration. In 0.2 M KOH, Pt nanoparticles with a mean diameter smaller than 2 nm and a very narrow PSD are formed. In contrast, the particles produced in 5 M KOH show an average diameter of 11.1 ± 5.0 nm, which corresponds to a significant enlargement, also with respect to the PSD. Moreover, extrapolation of the concentration dependence to saturated KOH solution would result in a theoretical Pt nanoparticle diameter of ~40 nm. This is remarkable, since typical polyol-based and microwave-assisted synthesis methods often only allow the preparation of nanoparticles in a rather narrow or less defined size range.[236,237] Conversely, a combination of different synthesis parameters in the top-down approach could provide the possibility for accurate size modulation in a broad range, which is also beneficial for applications other than the ORR.

In order to investigate the influence of the electrolyte composition, Pt nanoparticles were prepared in 1 M aqueous MeOH (Me = Li, Na, K, Cs) electrolytes. The particle size as a function of the alkali metal seems to remain constant (if the outlier in the case of Na is neglected). Therefore, no direct influence of the cation type on the particle size can be observed. However, detailed investigation of the reaction mechanism has to be conducted in order to explain the observed phenomena. Although there is no direct relation to particle size, Koper and co-worker reported that the cations have an influence on the degree of surface structural order.[173] In particular, the presence of K^+ ions led to a high degree of surface disorder of the nanoparticles prepared in their study. Since this influence is of special interest for ORR applications, it is discussed in more detail in the following subchapter, as well as in Chapter 4.

3.2 Tailoring the Pt Nanoparticle Shape

As elucidated in Chapter 1.4 and 1.5, the shape of the Pt nanoparticles is one of the most crucial factors determining their ORR activity. Next to the size effect observed, previous investigations in the literature indicate that the nanoparticle shape is similarly influenced by the different synthesis parameters,[175,176] independent of the underlying mechanism.

Accordingly, we monitored the impact of the frequency, waveform, electrolyte concentration and the different alkali metals on the appearance of the top-down prepared Pt nanoparticles using (S)TEM. Figure 31A-D shows images of Pt/C_{TD}, synthesized in 1 M KOH at a potential amplitude of ±10 V. However, the frequency was varied between 20 Hz (A and B) and 200 Hz (C and D) with a sinusoidal (A and C) or square wave shape (B and D). Interestingly, different Pt nanoparticle shapes were found in each case. While at low frequency sinusoidal potentials mostly cubic particles appear to be generated (A), in all other cases rather unordered, crescent- or flower-like structures were observed. Especially the particles depicted in the inset of Figure 31B, C are of interest for ORR applications, as they possess a high number of surface regions with a certain degree of concave curvature. Such "concave" particles have been described in the literature as particularly active candidates for the oxygen electroreduction (see Chapter 1.5).[146,147] Interestingly, this indicates that it is possible to synthesize both, nanoparticles with highly ordered surfaces and nanoparticles with a high degree of surface disorder using the same approach, which makes the technique appealing for a broad range of applications. A precise explanation of the observed phenomena, however, requires further investigations of the formation mechanism, for instance using *in-situ* spectroscopic techniques.

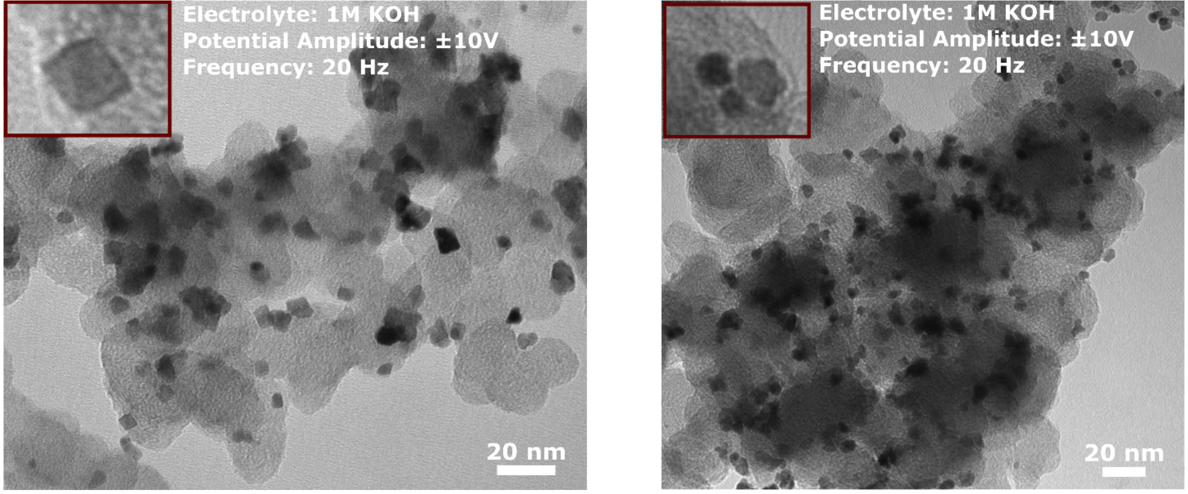
(A) Sinusoidal potential

(B) Square wave potential

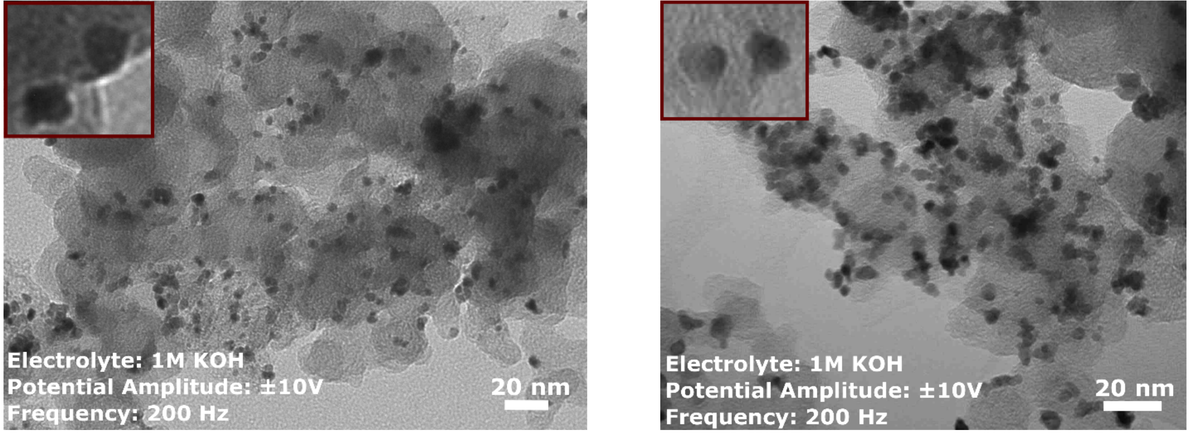
(C) Sinusoidal potential

(D) Square wave potential

Figure 31. TEM images of different Pt/C_{TD} samples prepared at a constant potential amplitude of ±10 V in 1 M KOH electrolyte. The wave shape was varied between sinusoidal (A, C) and square wave (B, D) and the frequency was varied between 20 Hz (A, B) and 200 Hz (C, D), respectively. Corresponding magnified excerpts of representative nanoparticles are shown in the inset of the images to enable detailed analysis of the particle shape.[234]

An even more pronounced effect was observed for nanoparticles synthesized in electrolytes with different concentrations of cations. In Figure 32A, Pt nanoparticles produced in 0.2 M KOH at a sinusoidal potential of ±10 V (200 Hz) are depicted. Under such conditions, mainly small, spheroidal particles are formed. Contrary, at a high concentration of 5 M KOH, various large and less definable structures can be observed (as shown in Figure 32B). In addition to the previously observed cubic nanoparticles, "crystal grain"-shaped nanoparticles and even complex, "twisted" structures can be observed. In the lower part of Figure 32 corresponding characteristic single nanoparticles are displayed at higher magnification.

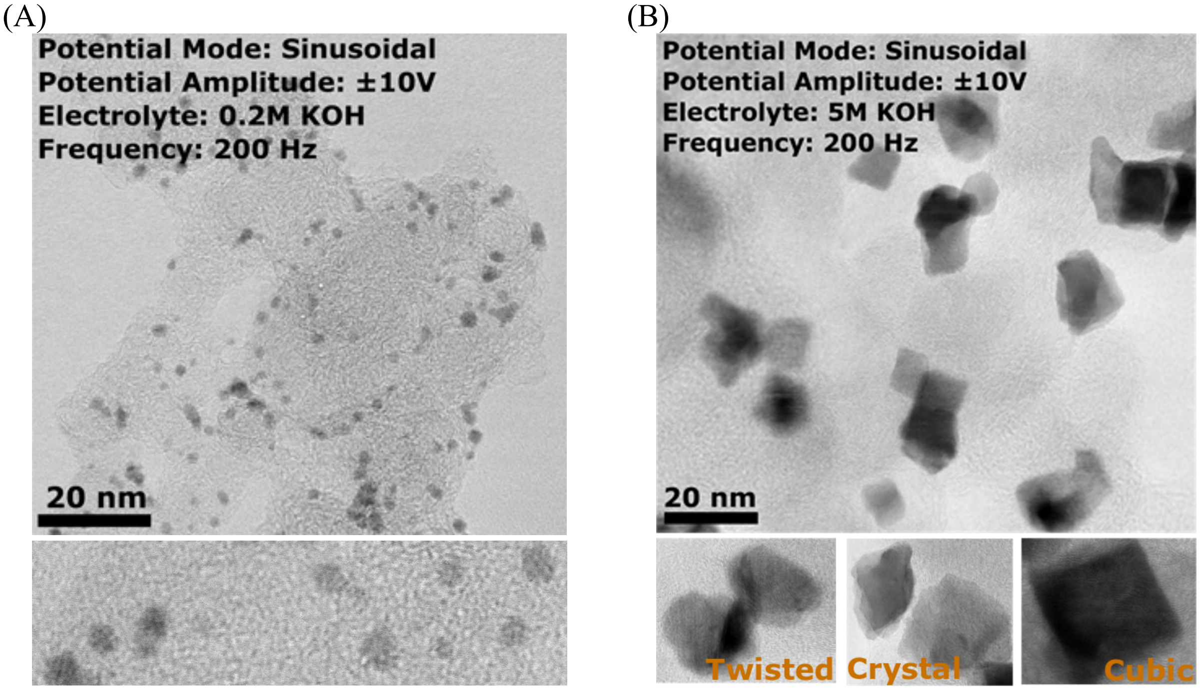

Figure 32. STEM images of Pt/C_{TD} samples prepared at a constant sinusoidal potential amplitude of ±10 V (200 Hz frequency) in (A) 0.2 M and (B) 5 M KOH electrolyte. Corresponding magnified images of selected nanoparticles are shown underneath to enable detailed structural analysis of the particle shape.[234]

The impact of different alkali metal cations on the Pt nanoparticle shape is presented in Figure 33. Selected nanoparticles of similar size, prepared by the top-down synthesis in 1 M CsOH, NaOH and LiOH are shown in Figure 33A-C, respectively. In all electrolytes, complex non-spherical particle shapes can be observed. Certainly, particles produced in CsOH appear to be more ordered than the ones synthesized in NaOH and LiOH. The latter ones, however, do not show significant differences in morphology. As shown above, in 1 M KOH, a similar conspicuous concave particle geometry was observed. In turn, no clear trend can be derived, in accordance with similar average particle diameters determined for all samples. Overall, it is evident that other parameters investigated have a more dominating effect on the particle shape and size than the electrolyte species. In case of both, the particle shape and size, it was found that the electrolyte concentration has the most pronounced influence.

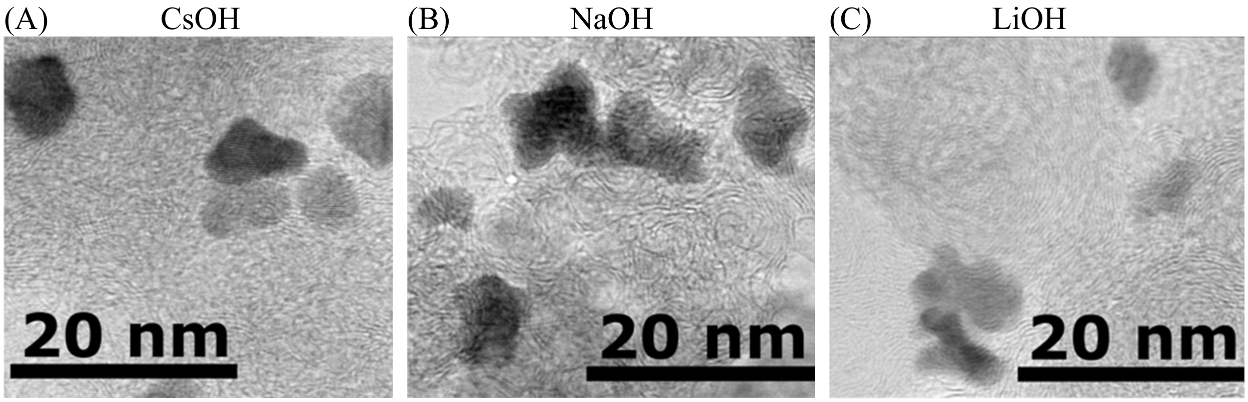

Figure 33. STEM images of the top-down synthesized Pt/C prepared in 1 M (A) CsOH, (B) NaOH and (C) LiOH using a sinusoidal potential signal of ±10 V (200 Hz).[234]

Regarding the synthesis procedure, it is still of interest if a combination of different selected parameters (according to the observations presented before) leads to the formation of desired particle size and shape. Accordingly, we intended to produce solely cubic particles with larger mean diameter than the ones displayed in Figure 31A. To achieve this, the Pt/C material was synthesized in a concentrated electrolyte (5 M KOH) by applying a sinusoidal potential of ±10 V at a low frequency of 20 Hz. As shown in Figure 34, this combination indeed leads to the formation of mainly cubic nanoparticles (a higher fraction than in Figure 31A, 32B), possessing an expected average diameter of ~10 nm. Hence, we assume that utilizing the proposed top-down synthetic route, it is possible to specifically tailor the particle shape and size of supported Pt nanoparticles, given the known dependences illustrated before. Although large monometallic Pt nanocubes are not considered effective for ORR applications due to adherent low mass activity,[154] they might be useful for other catalytic applications such as the methanol oxidation.[238]

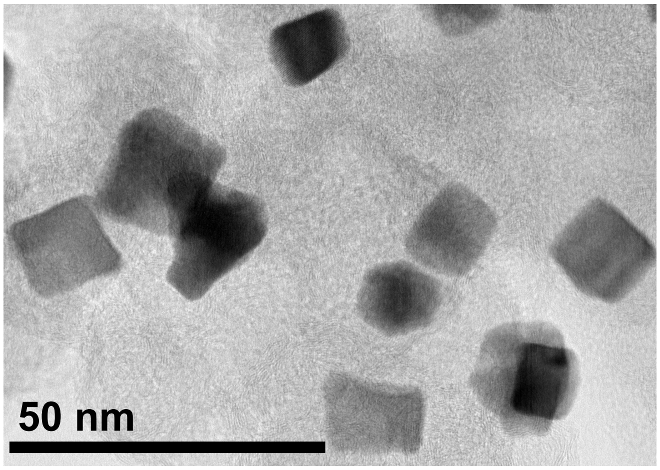

Figure 34. STEM image of Pt/C_{TD} nanoparticles, synthesized using a potential amplitude of ±10 V. Notably, the vast majority of generated particles exhibits cubic shape and uniform size, as a result of the low frequency (20 Hz) sinusoidal potential and high electrolyte concentration (5 M KOH).[234]

Chapter 4. Tailoring the Top-Down Synthesis of Pt/C for PEMFC Applications by the Means of Surface Defects

The following chapter addresses the top-down synthesis of carbon-supported pure Pt nanoparticles for the ORR applications in PEMFCs. In particular, during the electrochemical erosion of Pt nanoparticles from macroscopic Pt wires, the introduction of concave surface defects is monitored. These defective surface regions were characterized using different microscopic, spectroscopic, crystallographic and electroanalytical techniques. In turn, concave surface curvature is used to tailor one of highest ORR activities for pure Pt nanoparticles reported in the literature. In large parts, this chapter is based on the following publication:

Fichtner, J.; Watzele, S.; Garlyyev, B; Kluge, R. M.; Haimerl, F.; El-Sayed, H. A.; Li, W.-J.; Maillard, F. M.; Dubau, L.; Chattot, R.; Michalička, J.; Macak, J. M.; Wang, W.; Wang, D.; Gigl, T.; Hugenschmidt, C.; Bandarenka, A. S. Tailoring the Oxygen Reduction Activity of Pt Nanoparticles through Surface Defects: A Simple Top-Down Approach. *ACS Catalysis* **2020**, *10* (5), 3131−3142.[178]

https://doi.org/10.1021/acscatal.9b04974

4.1 Fundamental Characterization of Pt/C$_{TD}$

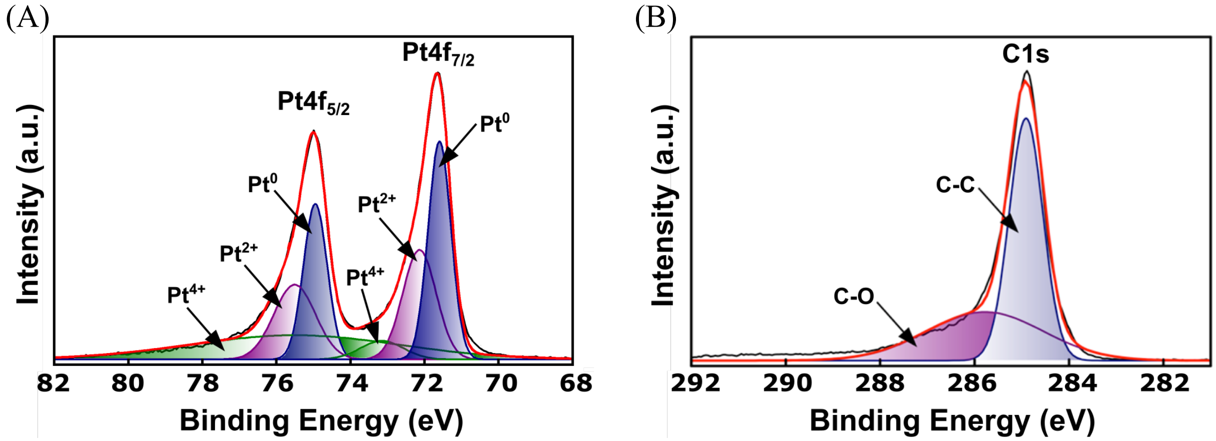

Figure 35. Recorded (black curves) Pt 4f and C1s XPS spectra of Pt/C$_{TD}$ and corresponding fits (red curves). (A) Fitted Pt 4f core level region with corresponding oxidation states, as well as (B) fitted C1s core level region with determined carbon binding states assigned.

According to the previous literature reports on the electrochemical top-down synthesis exploited in this work (see Chapter 1.6),[174,175] it is possible to tailor the size and shape of metal nanoparticles toward different (catalytic) applications. One of these possible utilizations is the ORR catalysis in PEM fuel cells, which is typically based on well-defined Pt nanoparticle structures supported on active carbon. Accordingly, the top-down route provides a simple way to prepare such PEMFC catalysts and could be used to reduce processing costs, even on an industrial scale. Besides simple synthesis, competing with bimetallic state-of-the-art catalysts (see Chapter 1.4) demands similarly good ORR performance of the catalysts prepared. As elucidated earlier, studies on the Pt nanoparticle size effect toward the ORR activity have shown that the maximum performance of Pt/C-type catalysts is located at ~2-3 nm particle diameter.[104,105] Moreover, for the comparison, it is desirable to achieve a diameter close to the commercial Pt/C$_{TKK}$ reference catalyst used in this study, being 2.8 ± 0.8 nm.[210] Due to their diameter close to 3 nm, Pt nanoparticles produced in 1 M KOH electrolyte at a sinusoidal potential amplitude of ±10 V *vs* a Pt-pseudo reference electrode (200 Hz frequency) are one of the suitable choices for ORR applications. In particular, this also accounts for the flower-like shape of the particles observed in the previous chapter. Indeed, their concave curvature could be highly beneficial for the ORR activity of the electrocatalyst prepared, as predicted in the literature (see Chapter 1.5).[147] Hence, a detailed microscopic, spectroscopic, crystallographic and electroanalytical analysis of the synthesized Pt/C$_{TD}$ electrocatalyst is necessary, in order to link its morphological and structural features to the evaluated ORR performance. In Figure 35, *ex-situ* XPS spectra (*i.e.* after air exposure) of Pt/C_{TD} are shown. Deconvolution of the Pt 4f core level region (Figure 35A) shows metallic Pt (~40%) next to a high fraction of (sub)surface Pt oxides (PtO and PtO_2), as determined by integration of the peak areas. Please note that neither a fitting without a Pt^{4+} signals, nor a more accurate fitting of the Pt^{4+} signals was possible. This may cause a slight deviation of the relative fractions reported, however, doesn't alter the overall trend (*i.e.* a high fraction of oxide species). In the literature, similar fittings and oxide fractions >50% were previously shown (*e.g.* for commercial Pt/C_{TKK} reference catalyst used in this study).[238,239,240,241] Besides air exposure on the sample, the conditions of the electrochemical synthesis could be the determining factor for the relatively high oxide values reported, however, no detailed explanation can be derived from *ex-situ* spectroscopic studies. Deconvolution of the C1s region of Pt/C_{TD} (Figure 35B) appears unobtrusive, as expected for untreated carbon black supports. The peak at lower binding energy can be assigned to C-C single or double bonds of mixed sp2 and sp3 hybridized carbon, while the shoulder at higher binding energy indicates partial oxidation of the carbon support.[238,242,243]

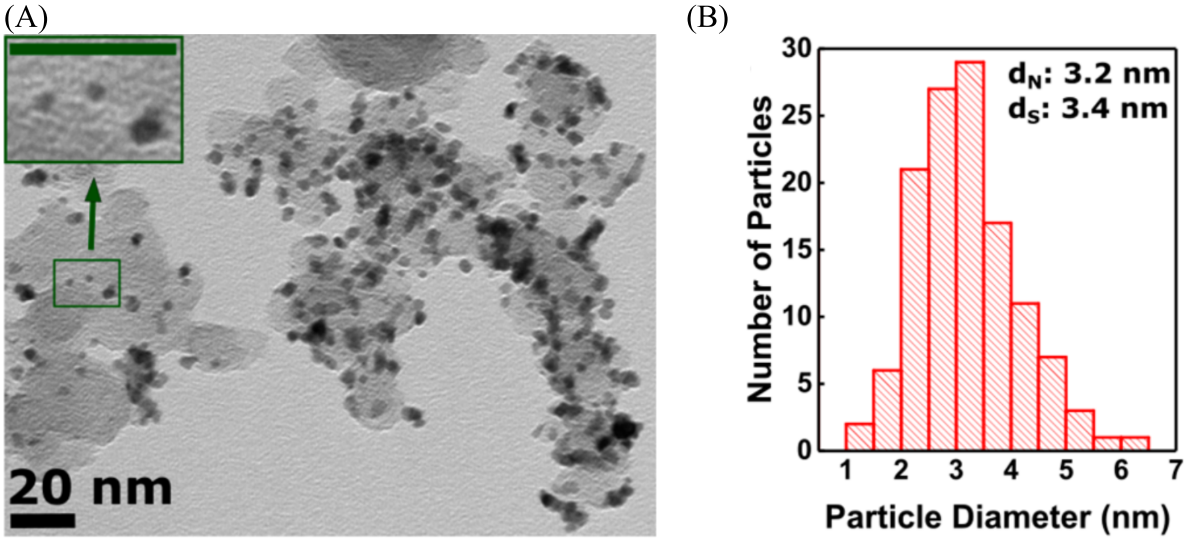

Figure 36. (A) Typical TEM image of Pt/C_{TD} synthesized in 1 M KOH at a sinusoidal potential of ±10 V (200 Hz). A magnified cutout is shown in the inset of the image (green frame, scale bar: 20 nm), illustrating the typical particle size of non-aggregated Pt nanoparticles. (B) PSD of the electrocatalyst, determined from the investigation of 125 isolated Pt nanoparticles. Reprinted with permission from ref. 178. Copyright 2020 American Chemical Society.

An overview TEM image of the synthesized Pt/C_{TD} is shown in Figure 36A. Analysis of the image shows that the Pt nanoparticles are distributed over the entire support material (Vulcan XC72R). While the distribution on the right carbon branch is even and dense, the left side shows multiple vacant areas such that the particle density is rather low. In addition to many homogeneously dispersed, isolated particles, a number of particle aggregates can be observed. The size of these aggregates spans the range of a few nanometers up to ~20 nm. These aforementioned points should be especially emphasized, since the correlated ECSA value drop could directly impact the materials' ORR activity. Evaluation of the corresponding PSD is shown in Figure 36B. The average values and distribution are based on the analysis of 125 isolated nanoparticles, using the imageJ software. Only isolated, well-definable particles were investigated, while particle aggregates were neglected. For each individual particle, d_F was considered and the d_N and d_S were calculated according to equations 29 and 30. As a result, a d_N of 3.2 ± 1.0 nm and d_S of 3.4 nm were determined. As shown in the graph, the vast majority of particles exhibits a diameter of 2-4 nm, which are accompanied by several particles with diameters <2 nm (see magnified inset of Figure 36A) and larger particles with a diameter up to >6 nm (see also Figure 37). Conversely, WAXS measurements performed at the European Synchrotron Radiation Facility indicate a global crystallite size of ~8.3 nm for Pt/C_{TD}. This is surprising since the WAXS-determined crystallite size is significantly larger than the Pt nanoparticle size obtained from TEM analysis. In the case of Pt/C_{TKK}, the opposite can be observed, *i.e.* a smaller crystallite size than TEM-derived nanoparticle size (~1.5 nm *vs* ~2.8 nm), which is expected since bottom-up synthesized nanoparticles often consist of several crystallite grains.[244] The observation suggests that the Pt/C_{TD} nanoparticle erosion is largely affected by the crystal structure of the macroscopic Pt host wire, as expected for top-down methods.[244] However, this does not explain the increased global crystallite size compared to the TEM-derived nanoparticle size. As TEM analysis only covers a relatively small fraction of the electrocatalyst sample, the presence of several significantly larger crystalline structures, which have not been monitored by TEM, could cause a shift of the mean size toward increased values. Moreover, volume sensitivity is more pronounced in the case of WAXS compared to the analysis of 2D-projected TEM images. Besides, findings of Maillard and co-workers suggest that the nanoparticle aggregation influences the WAXS-derived crystallite size. WAXS and TEM analysis of intentionally aggregated Pt/C electrocatalyst ("A-Pt/C") investigated in their work revealed a large difference between crystallite size (7.4 ± 0.6 nm *via* WAXS) compared to a Pt nanoparticle diameter (3.4 ± 1.1 nm *via* TEM),[154] which is not fully explainable. Similarly, investigation of aggregated PtNi/C ("A-PtNi/C") revealed a larger WAXS-derived crystallite size relative to TEM particle size analysis in their study. It should be noted that in the referenced work, the majority of analyzed "non-aggregated" materials showed a smaller or similar crystallite size compared to their respective TEM nanoparticle diameters, further validating the conclusions presented.

4.2 Investigating the Degree of Pt Surface Defects Introduced by the Top-Down Synthesis Conditions

HR-STEM-HAADF and HR-TEM analysis allows to study the morphology of the individual Pt nanoparticles in a more detailed manner, as depicted in Figure 37A-F. Overall, the nanoparticles shown have an average diameter in the order of 5 nm, which is slightly larger than the average value of 3.2 nm shown in the PSD before. However, it should be kept in mind that the analysis of single nanoparticles cannot be considered statistically significant.

Figure 37A and D show selected unsupported Pt nanoparticles investigated *via* HR-STEM-HAADF. Clearly, several concave regions are conspicuous. For illustration, the most prominent ones are marked by red arrows in the Fourier-filtered image presented in Figure 37B. Additionally, multiple small surface voids can be identified. In contrast, a more elongated and less distorted nanoparticle morphology is detected in Figure 37D. Importantly, again several concave and non-uniform surface regions can be observed. The most pronounced one is marked by a red arrow in the Fourier-filtered projection depicted in Figure 37E. Moreover, while Fourier analysis of the particle shown in Figure 37A and B indicates a monocrystalline lattice structure, the elongated particle was found to consist of multiple twin grains, as indicated by yellow dotted lines in the Fourier-filtered projection (Figure 37E). Based on this and the image contrast difference within the pure Pt nanoparticle, the formation of complex 3D structures can be assumed, which is hardly accessible using conventional electron microscopic techniques. For a more detailed Fourier analysis of Pt/C$_{TD}$, please also see ref. 178. Finally, the shape of the particles depicted in Figure 37C and F rather resemble that of a strawberry, which is accompanied by a high degree of concave curvature accordingly.

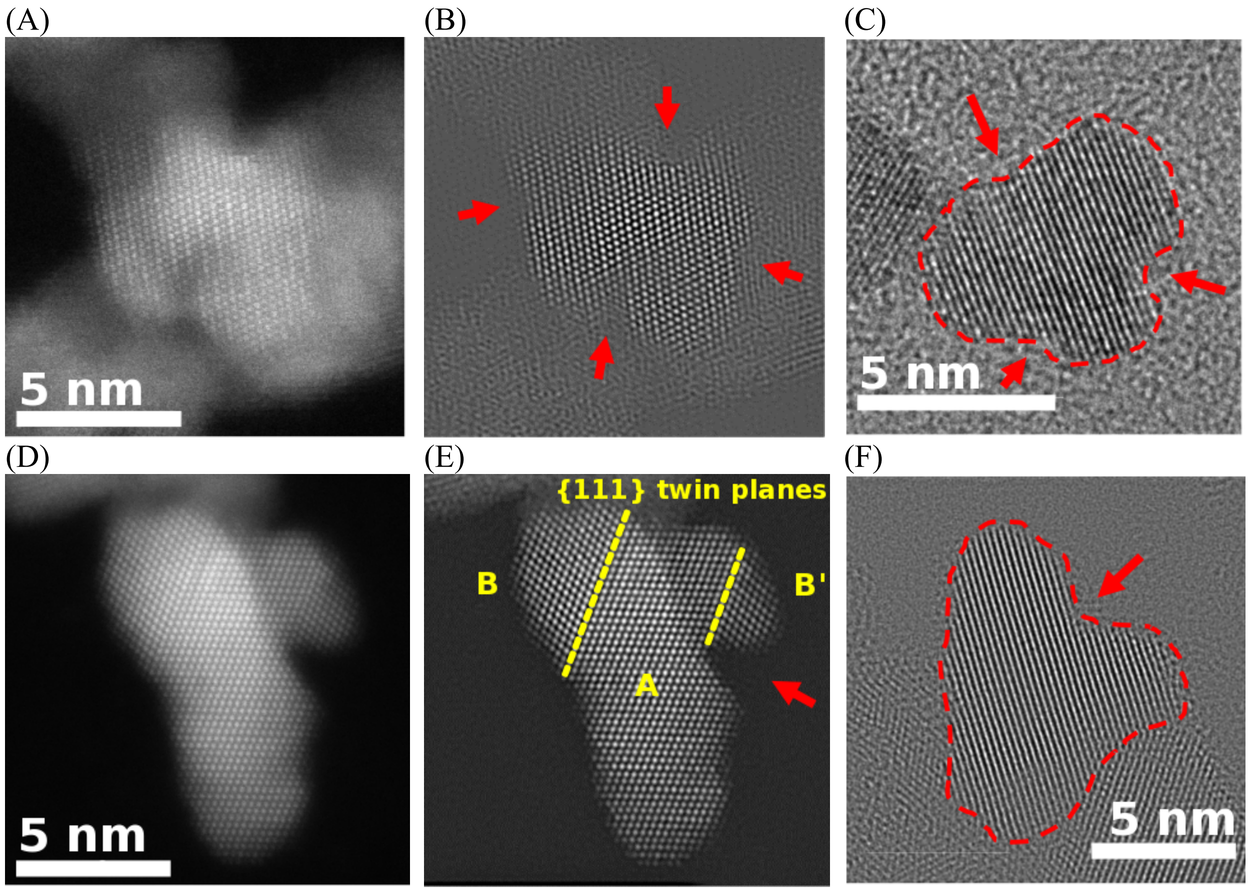

Figure 37. (A, D) Selected STEM-HAADF images of differently-shaped unsupported Pt_{TD} nanoparticles and (B, E) corresponding Fourier-filtered projections. Identified crystal grains are separated by yellow dotted lines and marked as A, B and B'. (C, F) HR-TEM analysis of the unsupported nanoparticles. Red arrows mark the most pronounced concave surface regions. Adapted with permission from ref. 178. Copyright 2020 American Chemical Society.

Overall, it can be concluded that the Pt nanoparticles synthesized in this work do not show a spherical or spheroidal shape, which distinguishes them from typical commercially available mono- and bimetallic Pt/C and Pt_xM/C catalysts from suppliers such as E-TEK, Johnson Matthey or TKK.[245,246,247,248,249] For illustration, STEM images of two commercial Pt/C catalysts from TKK (40 wt% Pt nanoparticles supported on high surface area carbon [HSAC] and Vulcan XC72), recorded by Sneed *et al.*,[247] are shown in Figure 38A and B. Cleary, spherical morphology of the vast majority of nanoparticles is characteristic.

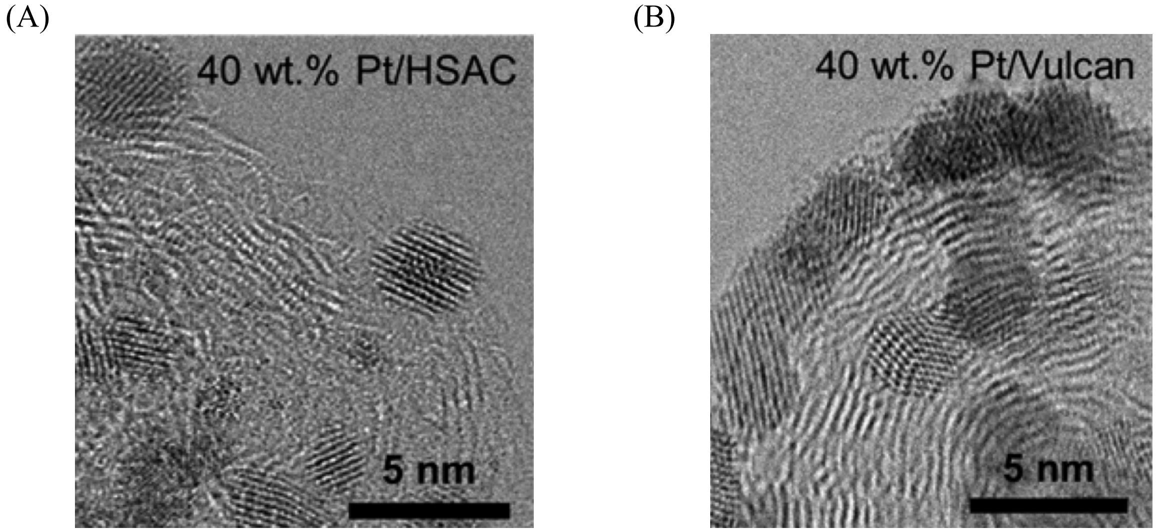

Figure 38. STEM images of untreated Pt/HSAC (A) and Pt/Vulcan (B), indicating a spherical particle shape of the Pt nanoparticles of commercial Pt/C electrocatalyst samples. The reference in this study is similar to the one shown in (B), except for lower Pt loading. Adapted with permission from ref. 247. Copyright 2017 American Chemical Society.

In contrast, the shape of Pt_{TD} nanoparticles differs significantly in each individual case. This can be explained by the harsh conditions of the top-down synthesis route, where the Pt wires are exposed to strongly polarizing conditions. Since the formation mechanism is largely unknown, only hypotheses can be made now. However, it can be assumed that the particles are "torn" from the host metal surface rather than a controlled growth takes place. Accordingly, asymmetric and uneven shapes are the outcome observed. However, all particles consistently possess concave surface regions, which is of primary importance for further discussions.

In order to additionally access 3D information of the catalyst nanoparticles prepared, STEM-HAADF tomography was performed on unsupported Pt_{TD} nanoparticles. On the left side of Figure 39, two isolated, differently-sized Pt_{TD} nanoparticles are depicted. In both cases, the tomogram confirms the presence of concave surface regions. While the particles appear spherical at the first glance, deep cavities are noticeable, which are particularly pronounced on the smaller nanoparticle. On the right side of Figure 39, a corresponding large Pt nanoparticle aggregate is shown as an example. Interestingly, the tomogram reveals how boundaries of aggregated nanoparticles form concave surface regions. However, aggregation is fairly reduced in case of the supported electrocatalyst materials used here in order to prevent active surface area losses and enhance the overall Pt utilization.

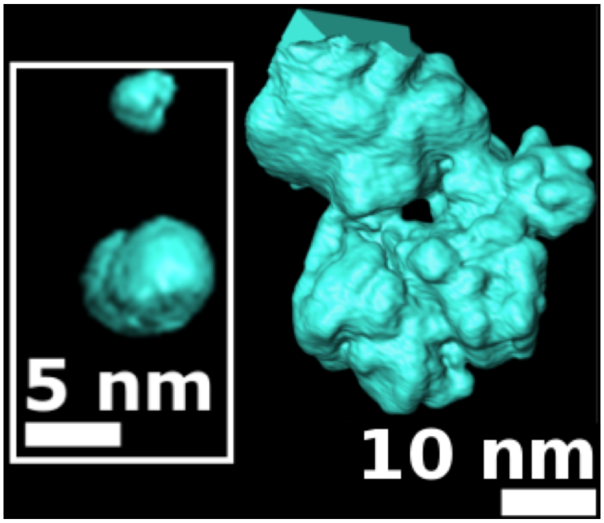

Figure 39. STEM-HAADF tomogram of unsupported Pt_{TD} nanoparticles. Individual particles are shown on the left side of the image, while the large structure corresponds to a 3D-visualized nanoparticle aggregate. Adapted with permission from ref. 178. Copyright 2020 American Chemical Society.

As described earlier, it is known from theoretical and experimental model studies that in the case of Pt, the presence of surface concave regions has a positive impact on the ORR activity.[146,147] Such highly active concave regions, as well as lattice dislocations, are present on the surface of various types of nanostructures, such as hollow nanoparticles, aerogels or at the grain boundary of aggregated particles.[154,250,251] However, it should be noted that in the case of aggregation (depending on its degree), a detrimental effect on PEMFC performance can be observed, which is mainly due to the associated loss of active surface area and low Pt utilization.[252] Considering the highly sensitive correlation of the available active surface area and the amount of surface defective regions with respect to ORR activity, it is necessary to tailor both parameters toward an optimum. For example, the previously introduced aggregated "A-Pt/C" electrocatalyst investigated by Maillard and co-workers exhibits lower mass activity than commercial Pt/C_{TKK} in RDE studies.[154] In the recent years, several different methods to prepare nanosized concave mono- and bimetallic electrocatalysts with high-index facets in a controlled manner were presented in the literature.[253,254,255,256,257] However, their widespread availability often suffers from complex multi-step preparation procedures, which includes additives such as capping agents, or from large particle sizes, which often results in low mass activities. In detail, typical diameters of such concave particles can be in the order 10 nm to several tens of nanometers. Moreover, bimetallic catalysts are often prone to dissolution of the non-noble metal component,[112] as illustrated earlier. However, in most cases, an activity enhancement toward the ORR was reported for such structures. For instance, Xia and co-workers prepared pure Pt concave nanocubes with diameters in the order of ~15 to 40 nm.[258] Compared to conventional Pt/C, ~3.5-times higher specific activity was reported, which might partially be owed to the particle size effect.[104,105,106,107] Further works by Ma *et al.*, Wan *et al.* or Kühl *et al.* report the formation of alloys of Pt with Cu, Co or Ni, all possessing a pronounced concave geometry and high ORR mass activities relative to pure Pt/C.[259,260,261]

As microscopic characterization only covers a small fraction of Pt nanoparticles, structural (surface) defects of the Pt/C_{TD} electrocatalyst need to be investigated in a more global range. It should be noted that it is difficult to extract the sole contribution of the concave defects. However, as shown in Chapter 1.5, multiple types of surface defects are known to boost ORR performance. Few techniques have been employed to judge the global degree of (surface) structural defects in nanosized catalyst materials. One of the possible choices to investigate such characteristics is the usage of the WAXS technique. In the past, WAXS was used to determine the degree of (surface) defectiveness of several structurally ordered and unordered Pt/C and Pt_xNi/C electrocatalysts, including *e.g.* spherical, octahedral, cubic, hollow, aggregated, aerogel or "sea sponge" Pt/C and Pt_xNi/C electrocatalyst samples.[133,154] In the cited studies, Rietveld refinement of the WAXS patterns was utilized to analyze the peak broadening, which is a measure of the microstrain or "local lattice strain" caused by structural (surface) defects and adherent displacements of atoms relative to their ideal lattice location.[154] For instance, this includes *e.g.* grain boundaries or local atomic vacancies, as well twins or stacking faults.[262] To analyze and compare the microstrain and adherent degree of defects in Pt/C_{TD} and Pt/C_{TKK} electrocatalysts, similar measurements were performed. Based on the here determined microstrain of 0.6%, Pt/C_{TD} shows a high degree of defects, while Pt/C_{TKK} shows an ordered structure featuring no microstrain (for more detailed evaluation of WAXS patterns, including lattice parameters, see the supporting information of ref. 178). Next to the direct correlation of the raw microstrain value and surface defectiveness, Maillard and co-workers introduced so-called "surface distortion" (SD) as a novel metric and descriptor for structural (dis)order in nanosized materials.[154]

The SD descriptor was defined as

$$SD = \frac{Microstrain - f(\%Ni)}{\bar{D}} \qquad \textbf{(34)}$$

where *f* corresponds to a correction factor for the impact of inhomogeneous Ni alloying. As no Ni is present in both, the Pt/C$_{TD}$ and Pt/C$_{TKK}$ samples, 0% can be assumed here. $\overline{D}$ corresponds to a dispersion parameter introduced by Montejano-Carrizales *et al.*[263,264] and is associated with the crystallite size determined from WAXS (Pt/C$_{TD}$: 8.3 ± 0.5 nm; Pt/C$_{TKK}$: 1.47 ± 0.1), as well as the covalent radius of Pt (for further information on the detailed evaluation see ref.154). This leads to a SD of 3.9 ± 0.2% for Pt/C$_{TD}$, which is comparable or higher than aggregated Pt/C and PtNi/C and slightly lower than hollow PtNi/C electrocatalyst.[154] Consequently, due to zero microstrain value found in the commercial Pt/C$_{TKK}$ sample, a corresponding SD of zero is calculated.

WAXS provides clear evidence of a strained and defective nanoparticle structure, however, it is of general interest to further verify the results obtained. While utilization in the electrocatalysis research community is scarce, positron annihilation spectroscopy (PAS) can be considered as another technique to monitor voids, dislocations or vacancy (cluster) defects in crystal lattices of solids,[265] as previously shown for various types of nanomaterials.[266,267] Briefly, positrons implanted in a material can be trapped at defect sites, followed by annihilation with core or valence electrons. The adherent emission of γ-quanta can be detected and analyzed. Thus, the degree of defectiveness of Pt/C$_{TD}$ and commercial Pt/C$_{TKK}$ electrocatalyst samples was compared at the Research Neutron Source (FRM II) of the Technical University of Munich. The results obtained from PAS unambiguously support previous findings, *i.e.* a higher defect density (in particular assigned to vacancies and vacancy clusters) of Pt/C$_{TD}$ compared to Pt/C$_{TKK}$. For a detailed analysis, which is out of the scope of this work, please see ref. 178.

Apart from the spectroscopic and crystallographic methods, electroanalytical techniques can be used to obtain insight into the morphological properties of electrocatalytic materials such as Pt/C. Characteristic CVs of Pt/C$_{TD}$ and Pt/C$_{TKK}$ are compared in Figure 40A and B. The measurement parameters are shown in the inset of the graphs. In general, both CVs show typical features of Pt nanoparticle samples recorded in 0.1 M HClO$_4$ electrolyte, *i.e.* H$_{ad/des}$ features between ~0.05-0.40 V *vs* RHE, followed by Pt oxide formation and reduction at higher potentials. Notably, the peak positions of commercial Pt/C$_{TKK}$ are in accordance with previous literature studies.[241] In both cases, a dominating peak is located close to ~0.15 V, followed by a less distinct peak shoulder at ~0.22 V *vs* RHE. Both peak shoulders are marked by red dotted lines. In the literature, this former peak is frequently designated to the (110) facets of Pt. Contrary, Pt (100) and (111) facets are often not well resolvable in perchloric acid electrolyte or overlaid by other features.[268,269] Surprisingly, Pt/C$_{TD}$ shows a third peak shoulder at ~0.27 V *vs* RHE, indicated by an orange dotted line.

Interestingly, such an additional peak shoulder (or peak broadening) was previously observed in CVs of concave cubic nanocrystals.[256] Moreover, several defect-rich Pt_xNi alloyed nanoparticles show similar behavior (see Figure 17), which further confirms the high degree of surface defects of the Pt/C_{TD} sample prepared.[133]

In accordance, the CO stripping voltammograms of Pt/C_{TKK} and Pt/C_{TD} differ significantly. As shown in Figure 40C and in agreement with reports in the literature,[133] a single peak close to 0.78 V can be observed for the commercial catalyst. According to previous studies, such a single peak indicates a homogeneous distribution of isolated Pt nanoparticles on a support material. With an increase of the degree of Pt aggregation, the peak shifts toward lower potentials,[250,270] probably due to the formation of grain boundaries. In the case of Pt/C_{TD}, two peaks can be noticed. In detail, a small single peak is located at the similar position as the one for the Pt/C_{TKK}. However, it is slightly shifted to lower electrode potentials (as indicated by a red arrow). This peak can be attributed to isolated particles, and the shift can be explained by the slight increase in TEM-derived particle size compared to Pt/C_{TKK} (~3.2 *vs* ~2.8 nm).[271] Moreover, a broad, split peak is located close to 0.68 V *vs* RHE. Besides aggregation, structural surface defects on individual particles can cause similar behavior. For instance, Chattot *et al*. showed similar double peak structure in the case of aggregated PtNi/C, hollow PtNi/C and sponge PtNi/C (see Figure 17).[133] Overall, it should be noted, that the conclusions from CO stripping voltammetry further support both a high degree of surface defects, as well as a certain degree of aggregated particles and a smaller fraction of isolated ones.

Another indicator for the degree of structural disorder was recently introduced by Chattot *et al*. and is defined as the ratio between the integrated CO stripping charge and the H_{UPD} charge $Q(CO)/2Q(H_{UPD})$ obtained from the consecutive first and second cycles of a CO stripping voltammetry experiment.[272] Importantly, the group found that in the case of structurally distorted Pt surfaces (*i.e.* SD > 0%, $Q(CO)/2Q(H_{UPD}) < 0.94$), this ratio scales linearly with the SD value introduced earlier, while a plateau is reached for structurally ordered catalysts (*i.e.* SD ~ 0, $Q(CO)/2Q(H_{UPD}) > 0.94$. For Pt/C_{TD}, a ratio of 0.85 was calculated according to the evaluation steps suggested by Chattot *et al*. In comparison, Chattot *et al.* report a ratio close to 0.97 for the commercial Pt/C_{TKK},[272] which indicates a structurally ordered surface. While the SD value of Pt/C_{TD} is close to the one of aggregated Pt/C,[154] its charge ratio is higher and comparable to hollow PtNi/C samples.[272] In particular, this observation indicates that aggregation of the particles is not the only source of the surface disorder and confirms defect implementation during the synthesis procedure.

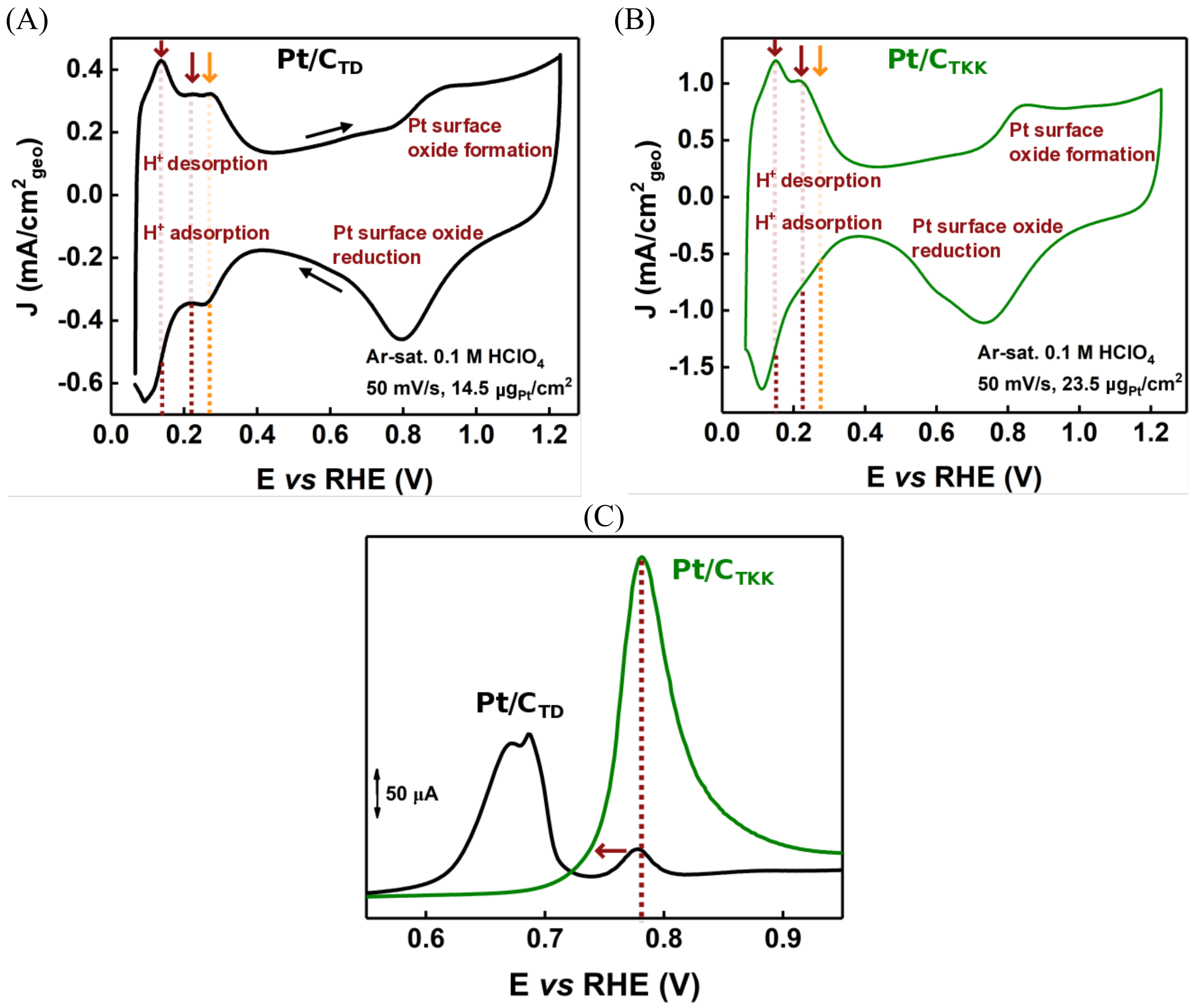

Figure 40. Characteristic CVs of (A) Pt/C_{TD} and (B) Pt/C_{TKK} recorded in Ar-saturated 0.1 M $HClO_4$ at room temperature and a scan rate of 50 mV/s. Pt mass loadings are shown in the inset of the graphs. Red dotted lines correspond to typical CV peak shoulders of "conventional" Pt nanoparticles observed in perchloric acid electrolytes. The orange line marks an additional shoulder, which is associated with the surface defects. In both curves the current is normalized to the glassy carbon electrode's surface area. (C) CO oxidation voltammograms of the Pt/C_{TKK} and Pt/C_{TD} electrocatalysts in the potential range of 0.55-0.95 V *vs* RHE, recorded in 0.1 M $HClO_4$ after adsorption of a CO monolayer and subsequent electrolyte saturation with Ar. Scan rate: 20 mV/s. Adapted with permission from ref. 178. Copyright 2020 American Chemical Society.

4.3 Tailoring the Oxygen Reduction Activity of Pt-Based Electrocatalysts Through Surface Concavities

Combining the findings from the microscopic, spectroscopic, crystallographic and electroanalytical analysis of the Pt/C_{TD} and Pt/C_{TKK} materials, the former catalyst consistently shows a defect-rich (surface) structure, while the latter one consistently shows an ordered structure. Hence, an improved ORR activity is expected in the case of Pt/C_{TD} catalyst, particularly due to the concave regions formed, which was previously demonstrated by means of theoretical calculations, as well as on model Pt surfaces.[146,147] To gain an initial insight into the performance of the systems investigated here, RDE studies were carried out in 0.1 M $HClO_4$ electrolyte. A representative anodic polarization curve of Pt/C_{TD} is shown in Figure 41A. The measurement parameters are shown in the inset of the graph. Besides, the corresponding kinetic current (calculated according to equation 24) as a function of the potential is shown in the relevant region.

SSAs of 46 ± 8 m^2/g_{Pt} and 68 ± 2 m^2/g_{Pt} were determined for the Pt/C_{TD} and Pt/C_{TKK} electrocatalysts, respectively (Figure 41B). In both cases, the ECSA was obtained according to equation 19 *via* the integration of the H_{UPD} charge of the corresponding CVs and normalized to the Pt electrode loading subsequently (equation 21). The SSA of the reference catalyst is in agreement with previous studies.[60] Slight deviations can be traced back to different I/C ratios and adherent catalyst surface poisoning. Although similar in the surface-averaged diameter, the SSAs of Pt/C_{TKK} and Pt/C_{TD} differ by more than 30%. According to equation 31, a theoretical SSA of ~87 m^2/g_{Pt} *vs* ~82 m^2/g_{Pt} can be calculated for these two catalysts, respectively. It has to be noted that this is only a rough estimation, as the equation assumes idealized parameters such as spherical particle geometry (for further information see section 2.4.3). As reported by Garsany *et al.*, typical Pt utilization (*i.e.* estimated *vs* experimental SSA) of various commercial Pt/C catalysts should be in the order of 80%, presupposing proper electrode preparation.[228] As our preparation and examination protocols are similar to the ones proposed by Garsany *et al.*, we assume similar results. Indeed, in the case of Pt/C_{TKK}, the Pt utilization is close to 80%, while in the case of Pt/C_{TD} it is substantially lower (~55%). This finding confirms previous findings from TEM, *i.e.* that particle agglomeration takes place, leading to a reduced Pt surface utilization.

Normalization of the kinetic current values obtained at 0.9 V *vs* RHE to the corresponding ECSA or Pt mass loading of the electrode leads to the specific or mass activities shown in Figure 41C and D, as described in equation 25 and 26. As a reference, the SA and MA values of highly active commercial Pt/C_{TKK} are shown. The activity was determined under similar conditions, following the same evaluation protocol. For further comparison, the activity values of another commercial reference catalyst (20 wt% Pt/$C_{E\text{-}TEK}$) were included. The depicted data of Pt/$C_{E\text{-}TEK}$ were obtained from the literature.[273] In the cited study, similar preparation and test protocols were conducted (0.1 M $HClO_4$, 1600 rpm, 10 mV/s, 10 $\mu g_{Pt}/cm^2$) and the values are in accordance with further independent literature reports.[274]

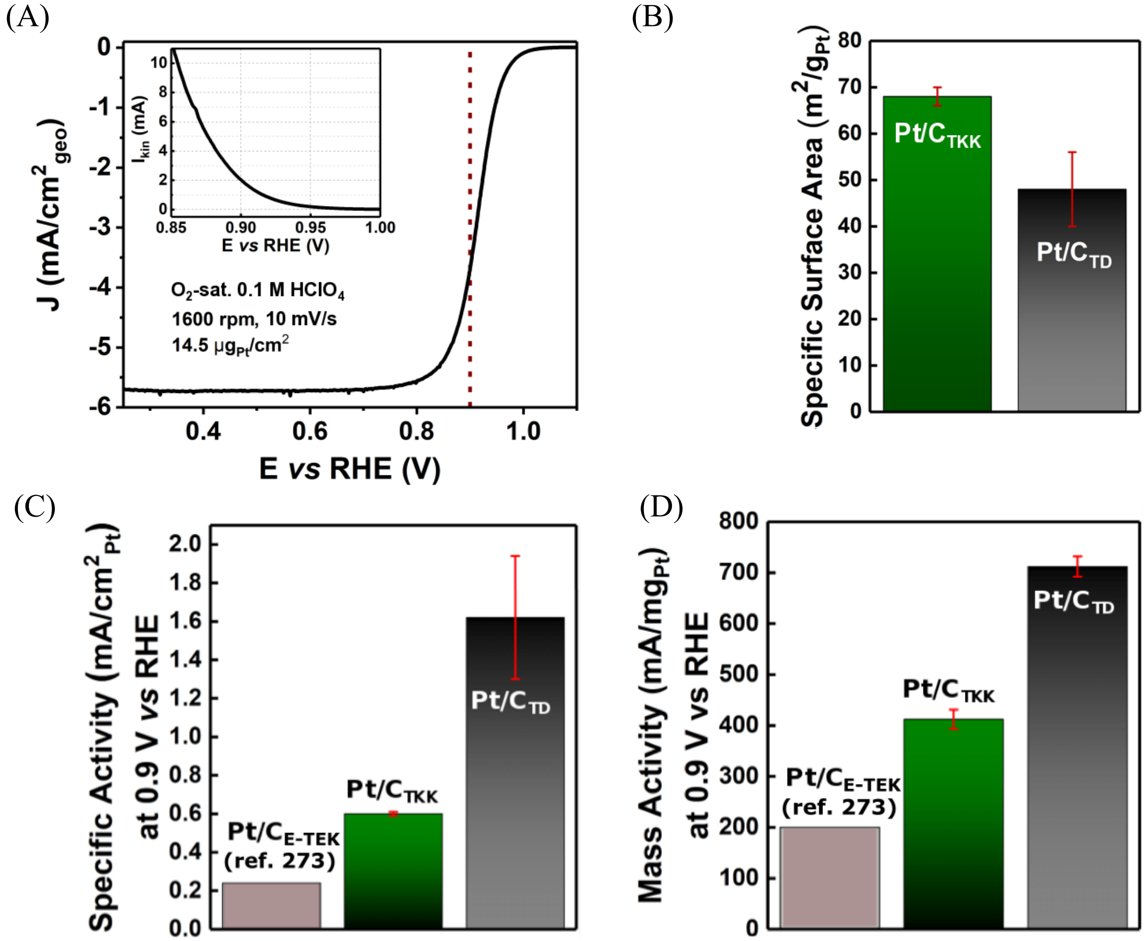

Figure 41. (A) Characteristic *IR*-free and (pseudo-)capacitive current-corrected anodic polarization curve and corresponding kinetic current curve (inset) of Pt/C_{TD}. Measurements parameters are shown in the inset of the graph. Recorded at room temperature. (B) Comparison between the Pt/C_{TD} and Pt/C_{TKK} materials in terms of SSA. (C) SA and (D) MA for the Pt/C_{TD}, Pt/C_{TKK} and Pt/$C_{E\text{-}TEK}$ electrocatalysts evaluated at 0.9 V *vs* RHE. The activity values of Pt/$C_{E\text{-}TEK}$ were obtained from the literature (ref. 273), however, were recorded under conditions similar to those applied in this work. Adapted with permission from ref. 178. Copyright 2020 American Chemical Society.

Comparison of the different catalysts unambiguously supports the assumed positive correlation between the surface disorder and high ORR activity of Pt-based materials. At this point, it is again noteworthy that the aggregated "A-Pt/C" electrocatalyst investigated by Chattot *et al.* does not show any activity improvement over commercial Pt/C_{TKK}, which elucidates that grain boundaries formed upon aggregation cannot be the sole determining factor for the high ORR activity.[154] In relative values, "concave" Pt/C_{TD} electrocatalysts outperform "spherical" Pt/C_{TKK} electrocatalyst by a factor ~1.7 in terms of MA and ~2.7 in terms of SA (at 0.9 V *vs* RHE). Compared to Pt/$C_{E\text{-}TEK}$, MA and SA enhancements by a factor of ~3.6 and ~6.8 can be observed, respectively. Although a correlation between low specific surface area and high specific activity (*i.e.* shift toward bulk surface properties, see Figure 12) was demonstrated by Nesselberger *et al.*,[107] in this case the comparably lower SSA of ~46 m^2/g_{Pt} *vs* ~68 m^2/g_{Pt} for the Pt/C_{TKK} material should only have a marginal impact, since a SA plateau is observed above ~50 m^2/g_{Pt}. Hence, the almost 3-times increased SA can be majorly attributed to the intrinsically high activity of the catalyst. In contrast, MA is negatively influenced by the low SSA, which has to be optimized in further experimental studies (*i.e.* aggregation has to be prevented).

Moreover, the absolute activity values of ~712 ± 20 mA/mg_{Pt} and 1.62 ± 0.32 mA/cm^2_{Pt} are even comparable or superior to Pt_xM/C-type catalysts reported in the literature. For illustration, Pizzutilo *et al.* reported a MA of 690 mA/mg_{Pt} and SA of 0.72 mA/cm^2_{Pt} at 0.9 V *vs* RHE for highly active Pt_3Co@HGS (HGS = hollow graphitic spheres) alloyed catalysts with a nanoparticle diameter close to 3 nm (evaluated under similar conditions to the ones used in this work).[275] However, the SSA of Pt_3Co@HGS is strikingly higher than the one of Pt/C_{TD} (101 *vs* 46 m^2/g_{Pt}), which positively contributes to its mass activity. It should be noted that in the cited study, 46 wt% Pt/C_{TKK} (on Vulcan carbon) was utilized as the reference, which showed slightly lower but comparable MA to the one of Pt/C_{TKK} reported in this study. This is expected due to the higher Pt weight fraction (*i.e.* higher Pt density and lower associated SSA). Considering that the CCLs of the recent Toyota Mirai FCEV are based on Pt_xCo/C electrocatalysts,[55] the performance of Pt/C_{TD} might be in-line with the state-of-the-art industrial catalysts, presuming the similarly important stability targets are met. However, one main advantage of the pure Pt/C catalytic system is that dissolution of the alloying element and associated poisoning of PEMFC components (*e.g.* the PEM) are prevented effectively. In conclusion, Pt/C_{TD} shows promising activity toward the ORR. In addition, it is likely that the MA of the catalyst can be further boosted by increasing its SSA to a value comparable to that of the reference. In order to investigate if Pt/C_{TD} meets the stability requirements for PEMFC applications, preliminary ASTs were conducted and compared to the degradation of Pt/C_{TKK}. Both catalysts were independently subjected to 10,000 voltage cycles between 0.6 and 1.0 V *vs* RHE. Moreover, the electrolyte was heated to a realistic fuel cell operation temperature of ~80°C during the AST. After voltage cycling, the mass activities were determined at room temperature. Relative to the degraded Pt/C_{TKK}, the voltage-cycled Pt/C_{TD} still shows a slight MA improvement. However, the relative enhancement factor is reduced to less than 1.1-times (Figure 42A). From STEM *post-mortem* analysis of the voltage-cycled Pt/C_{TD} shown in Figure 42B, multiple conclusions on the reason for degradation can be drawn. Primarily, strong Pt nanoparticle sintering takes place, as frequently reported in the literature.[110,111,276] Moreover, as shown in case of a magnified Pt nanoparticle in the inset of the figure, the shape of the Pt nanoparticles relaxes toward a spherical particle shape. Hence, it can be assumed that the MA of Pt/C_{TKK} and Pt/C_{TD} adjust during the voltage cycling, since the morphological and structural properties of both catalysts become similar. Accordingly, retention of the Pt nanoparticle shape (*i.e.* the defective character) is pivotal for a good long-term performance. However, more detailed analysis of the degradation mechanism has to be performed and is targeted in the future experimental studies.

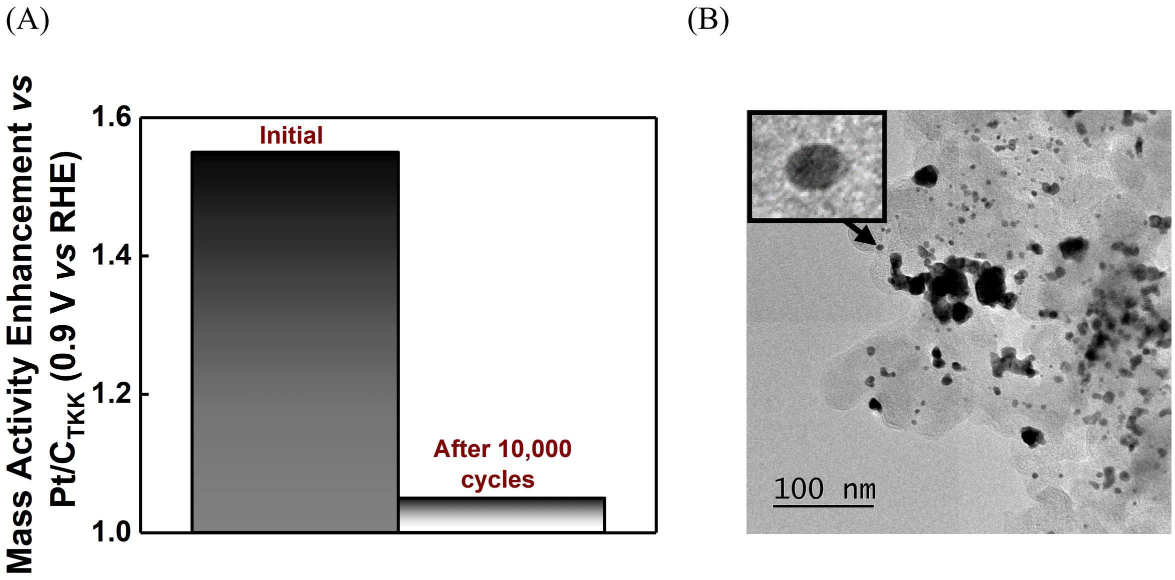

Figure 42. (A) MA of Pt/C_{TD} relative to Pt/C_{TKK} before and after these catalysts were subjected to 10,000 AST cycles between 0.6 and 1.0 V *vs* RHE. (B) STEM image of Pt/C_{TD} after 10,000 AST cycles. In the inset, a magnification of the particle marked by a black arrow is depicted. Adapted with permission from ref. 178. Copyright 2020 American Chemical Society.

4.4 H_2/O_2 and H_2/Air Performance of Pt/C_{TD} in a Membrane Electrode Assembly

On a laboratory scale, the synergy of simple synthesis and high activity (due to the implementation of the surface defects) indicates that Pt/C_{TD} is a promising CCL electrocatalyst for PEMFC applications. However, this finding cannot be fully applied to industrial scale utilization of the electrocatalyst, *e.g.* in automotive PEMFC stacks, which requires upscaling and separate performance evaluation in membrane electrode assembly configuration. Hence, we attempted to implement the top-down synthesized Pt/C into a 5 cm^2 single-cell PEMFC setup in order to quantify its activity. To fulfill the state-of-the-art US DOE targets,[77] we prepared cathode catalyst layers with a Pt loading of 0.1 mg_{Pt}/cm^2. Details on the MEA preparation and measurement procedure are summarized in the experimental section. The catalyst was prepared using the same synthesis route shown before. However, the batch sizes were up-scaled to about 100 mg (compared to about 10-20 mg per batch for the RDE tests). Moreover, the electrolyte was both sonicated and mechanically stirred during the synthesis in order to enable a homogeneous dispersion of both the Pt nanoparticles and the carbon support. Figure 43A shows a characteristic TEM image of the Pt/C_{TD} electrocatalyst prepared for the PEMFC testing. Figure 43B shows a corresponding CO stripping voltammogram of Pt/C_{TD} recorded in the PEMFC. After subtraction of the background, integration of the CO stripping peak reveals a SSA of 26.5 m^2/g_{Pt}, which is significantly lower than the value observed in the RDE experiments (46 m^2/g_{Pt}). Nevertheless, the voltammogram shows the typical double peak structure observed in the RDE experiments, indicating structural surface defects. Closer investigation of the corresponding TEM image gives an indication for the strongly reduced active surface area. While the Pt nanoparticles appear to be homogeneously distributed on the carbon support, several large agglomerates can be recognized, as exemplarily marked by red frames and arrows. The size of the particle aggregates was found to be up to 50 nm in diameter. We assume that in large scales, neither lab scale sonication nor stirring are sufficiently powerful to evenly distribute the individual components quickly enough to mitigate aggregation.

Figure 43C shows typical as-recorded or *IR*-free H_2/O_2 polarization curves of the MEA prepared with Pt/C_{TD} as the CCL catalyst. Measurement conditions are shown in the inset of the Figure. In Figure 43D, the corresponding as-measured H_2/Air polarization curve is shown. The kinetic activity values were extrapolated from the *IR*-free H_2/O_2 polarization curve at 0.9 V and are shown in Figure 44.

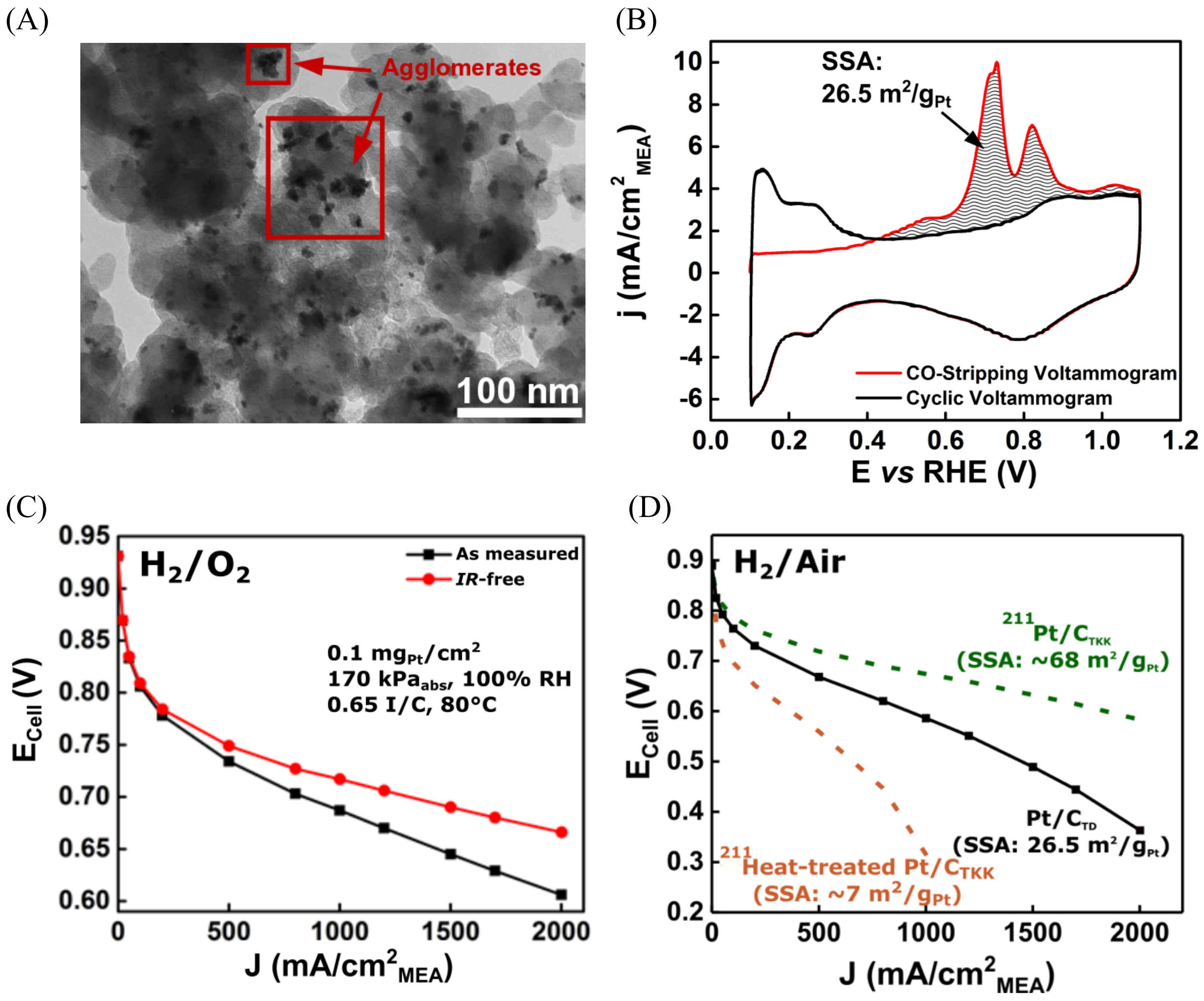

Figure 43. (A) TEM image of the Pt/C$_{TD}$ sample used for the MEA measurements. (B) First (red) and second (black) cycles of a typical CO stripping voltammogram of the Pt/C$_{TD}$-based CCL. A SSA of 26.5 m^2/g$_{Pt}$ was determined by integration of the peak charge after subtraction of the corresponding background CV. (C) Typical H_2/O_2 polarization curve of the Pt/C$_{TD}$-based CCL (black curve: as measured; red curve: *IR*-free), measured at 80°C, 170 kPa$_{abs}$ and 100% RH under differential flow conditions (H_2: 2000 nccm; O_2: 5000 nccm). Anode: ~0.08 mg$_{Pt}$/cm$^2_{MEA}$ (TEC10V20E), cathode: ~0.1 mg$_{Pt}$/cm$^2_{MEA}$ (16 wt% Pt/C$_{TD}$). (D) Corresponding H_2/Air polarization curves of Pt/C$_{TD}$, Pt/C$_{TKK}$ and heat-treated (HT)-Pt/C$_{TKK}$ (the latter ones were reproduced (digitized) from ref. 211). CCL Pt loading: 0.1 mg$_{Pt}$/cm^2. The reference measurements were recorded in the same setup, with similar electrode loadings and under similar conditions. (B,C) are reprinted with permission from ref. 178. Copyright 2020 American Chemical Society.

In order to ensure an accurate activity evaluation, correction for the H_2 crossover current (~4.8 mA/cm^2) was applied. Reference catalytic activities and SSA values are taken from ref. 211, since the samples were evaluated in the same test setup, using similar preparation techniques, electrode loadings (~0.1 mg_{Pt}/cm^2 in the CCL), as well as measurement conditions. It has to be highlighted that the Pt/C_{TKK} reference catalyst exhibits a SSA of ~68 m^2/g_{Pt} which is ~2.5-times larger than the one of the Pt/C_{TD} sample. As shown earlier, the SSA has a major impact on both the mass and specific activity of Pt/C electrocatalysts,[107] even at low current densities. Briefly, the MA typically increases with increasing SSA, while the opposite is observed in the case of the SA (Figure 12). The experimental ORR kinetics of the HT-Pt/C_{TKK} electrocatalyst were taken from ref. 211 (evaluated under similar conditions/same setup) and added to the figure in order to enable a reasonable assessment. In their study, Schwämmlein *et al*. subjected the as-received Pt/C_{TKK} to a heat treatment (10 h, 1200°C, 5% H_2/Ar atmosphere) in order to obtain a reduced SSA of the electrocatalyst (~7 m^2/g_{Pt}).[211] Surprisingly, even at ~2.5-times lower SSA, the analysis of the H_2/O_2 polarization curve of Pt/C_{TD} indicates higher MA of Pt/C_{TD} (~150 mA/mg_{Pt}) compared to Pt/C_{TKK} (~120 mA/mg_{Pt}). Compared to HT-Pt/C_{TKK}, ~4-times enhanced MA can be found. In terms of SA, Pt/C_{TD} shows ~3-fold enhancement over Pt/C_{TKK} (in accordance with the RDE measurements). More important, Pt/C_{TD} shows even higher specific activity than HT-Pt/C_{TKK} which contradicts the particle size effect. Hence, the high intrinsic activity of the catalyst is verified.

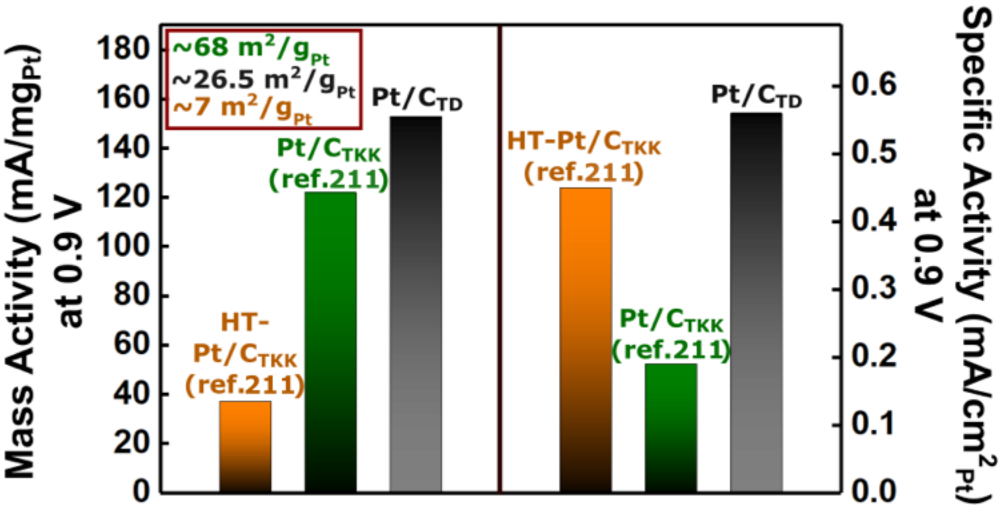

Figure 44. Mass (left) and specific (right) ORR activity of Pt/C_{TD}-, Pt/C_{TKK}- and HT-Pt/C_{TKK}-based CCLs. Activity data of Pt/C_{TD} were extrapolated from the corresponding H_2/O_2 polarization curve at 0.9 V after correction for the H_2 crossover current and the high frequency resistance. (HT-)Pt/C_{TKK} data were taken from ref. 211. The reference measurements were recorded in the same setup, with the same electrode loading and under similar conditions. Adapted with permission from ref. 178. Copyright 2020 American Chemical Society.

Under pure oxygen gas feed at the cathode, Pt/C_{TD} shows a higher "kinetic" performance than the commercial Pt/C_{TKK} at 0.9 V, which can probably be further boosted through an increase of the SSA. While the SSA-derived differences at high current densities are less pronounced in pure O_2 atmosphere, they become particularly apparent at low O_2 concentrations (*e.g.* 21% in air). Thus, the reverse is observed in H_2/Air atmosphere, where optimized O_2 mass transport is of paramount importance for a good performance. Comparison of the H_2/Air polarization curves of Pt/C_{TD} and Pt/C_{TKK} (taken from ref. 211) shows superior high current density performance of Pt/C_{TKK} (~200 mV difference at 2 A/cm^2). This observation is at least partially owed to the low SSA and hence roughness factor (r.f., that is, Pt loading multiplied with corresponding SSA in cm^2_{Pt}/cm^2_{MEA}) of the catalyst layer, which results in a bad mass transport behavior. In accordance with previous studies,[277] Kongkanand and Mathias recently showed that the r.f. of the catalyst layer correlates with the oxygen transport resistance.[34] At low r.f. values (Pt/C_{TD}: ~26.5 cm^2_{Pt}/cm^2_{MEA}), high non-Fickian O_2 transport resistance can be observed, which results in higher O_2 amounts required due to lower Pt availability. In comparison, the resistance reaches a plateau above ~70 cm^2_{Pt}/cm^2_{MEA} and is, in turn, significantly lower in the case of Pt/C_{TKK}. As this effect becomes dominant compared to the almost peripheral kinetics, optimization of the SSA has to be prioritized in further studies. In accordance, Pt/C_{TD} shows strongly enhanced high current density performance compared to HT-Pt/C_{TKK}, which drops to a geometric current density of ~1 A/cm^2 at the cell voltage of 0.3 V. The correlation of the MEA voltage of a Pt/C-based CCL at different roughness factors, evaluated at a fixed current density of 1.75 A/cm^2_{MEA}, is depicted in Figure 45 (taken from ref. 34). The results obtained in the cited work are in good agreement with the results presented in this work. It can be concluded that, to some extent, surface defects of Pt/C_{TD} compensate for the low SSA. Similar observations were also demonstrated by Maillard, Schmidt and co-workers using the example of agglomerated PtNi ("A-PtNi") and PtNi aerogel.[133,134,154] In both cases, an increase in activity compared to uniformly distributed PtNi nanoparticles was found, resulting from the formation of particularly active grain boundaries or concave defects. At the same time, however, the proportion of accessible surface area should be kept as high as possible (>40 m^2/g_{Pt} are proposed by Kongkanand and Mathias).[34] In accordance, Schwämmlein *et al.* showed that in the case of Pt_xY/C nanocatalyts synthesized in their work, a SSA increase is decisive for good O_2 mass transport and high (mass) activity. They recognized that in the MEA tests, Pt_xY/C with a SSA of ~15 m^2/g_{Pt} achieves approximately the same mass activity as Pt/C_{TKK}.[211] However, experimental model studies of mass-selected Pt_xY nanoparticles prefigured an up to 6-fold increase in the mass activity compared to pure Pt nanoparticles,[136] which highlights the importance to tailor the particle size and overall available active surface area. Thus, by optimizing the available catalyst surface area of Pt/C$_{TD}$, a further increase of performance in the low and high current density region can be expected, as indicated by the previous RDE results. One way to impede this problem is the use of surfactants or capping agents to prevent agglomeration. Since this would considerably complicate the synthesis and add additional purification steps, we propose the use of industrial agitators with vertical and horizontal stirring blades to mitigate the problem, which is a current subject to investigations in our group.

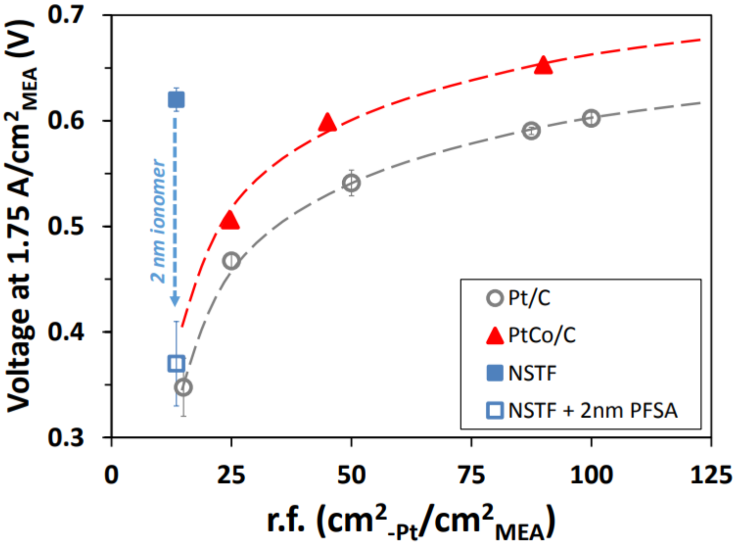

Figure 45. Voltage of the Pt/C and PtCo/C electrocatalyst-based MEAs with varying CCL roughness factors, evaluated at a fixed current density of 1.75 A/cm$^2_{MEA}$. Reprinted with permission from the supporting information of ref. 34. Copyright 2016 American Chemical Society.

Chapter 5. Top-Down Synthesis of Pt-Lanthanide Alloy Nanostructures

This chapter addresses the top-down synthesis of the nanostructured Pt-lanthanide alloys, a promising class of next-generation ORR catalysts, on the example of Pt_xPr/C. Characterization of Pt_xPr/C includes the microscopic investigation of structural properties and composition using SEM, (HR-)TEM and STEM-EDX, as well as the spectroscopic and crystallographic analysis of the catalyst's alloying state using XPS and XRD. In the final section, the ORR activity is evaluated using the RDE technique and perspectives are briefly summarized. Large parts of this chapter have been published in:

Fichtner, J.; Garlyyev, B.; Watzele, S.; El-Sayed, H. A.; Schwämmlein, J. N.; Li, W.-J.; Maillard, F. M.; Dubau, L.; Michalička, J.; Macak, J. M.; Holleitner, A.; Bandarenka, A. S. Top-Down Synthesis of Nanostructured Platinum-Lanthanide Alloy Oxygen Reduction Reaction Catalysts: Pt_xPr/C as an Example. *ACS Applied Materials & Interfaces* **2019**, *11* (5), 5129–5135.[278]

https://doi.org/10.1021/acsami.8b20174

5.1 Pt_xPr Alloy Nanostructures

As emphasized in Chapter 1.4.3, Pt-lanthanide alloys pose a promising class of next-generation PEMFC catalysts, which is mainly owed to their good ORR performance confirmed by means of the extended surface and model nanoparticle studies. The comparably high activity can partially be attributed to the lattice mismatch between the two elements, which leads to a strain effect. One particularly active combination of elements is Pt and Pr. As reported by Garlyyev *et al.*, polycrystalline Pt_5Pr electrodes show a noticeable ORR activity gain compared to polycrystalline pure Pt electrodes.[143] In detail, an approximately 4-times enhanced ORR specific activity was observed compared to pure Pt and was traced back to the formation of a compressively strained and active Pt surface layer. It is, however, a highly sophisticated endeavor to synthesize nanostructured Pt_xPr-type alloys due to the large reduction potential difference between the typical Pt and Pr redox couples. Moreover, owed to the strong oxophilicity of Pr, oxidation of the lanthanide element under ambient conditions is hardly avoidable.[144,145,180,279] Few attempts to produce such nanoparticles are reported in the literature, but they mostly lack of clear alloy phase evidence or were synthesized using complex techniques under UHV conditions.[136,137,280]

Here, we make use of the simple top-down procedure elaborated in this work in order to synthesize a nanostructured Pt_xPr/C electrocatalyst starting from a macroscopic Pt_5Pr alloy used as the precursor material. A precise description of the experimental steps can be found in the section 2.1.2. In brief, a polycrystalline Pt_5Pr disk electrode (used as the WE in a three-electrode configuration) was immersed into a 8 M KOH electrolyte and subjected to a sinusoidal potential of ±8 V at 200 Hz frequency. Subsequent generation and dispersion of nanoparticles in the electrolyte was observed, followed by washing and mixing with the support material (Vulcan XC72R).

5.2 Microscopic and Compositional Characterization of Pt_xPr/C

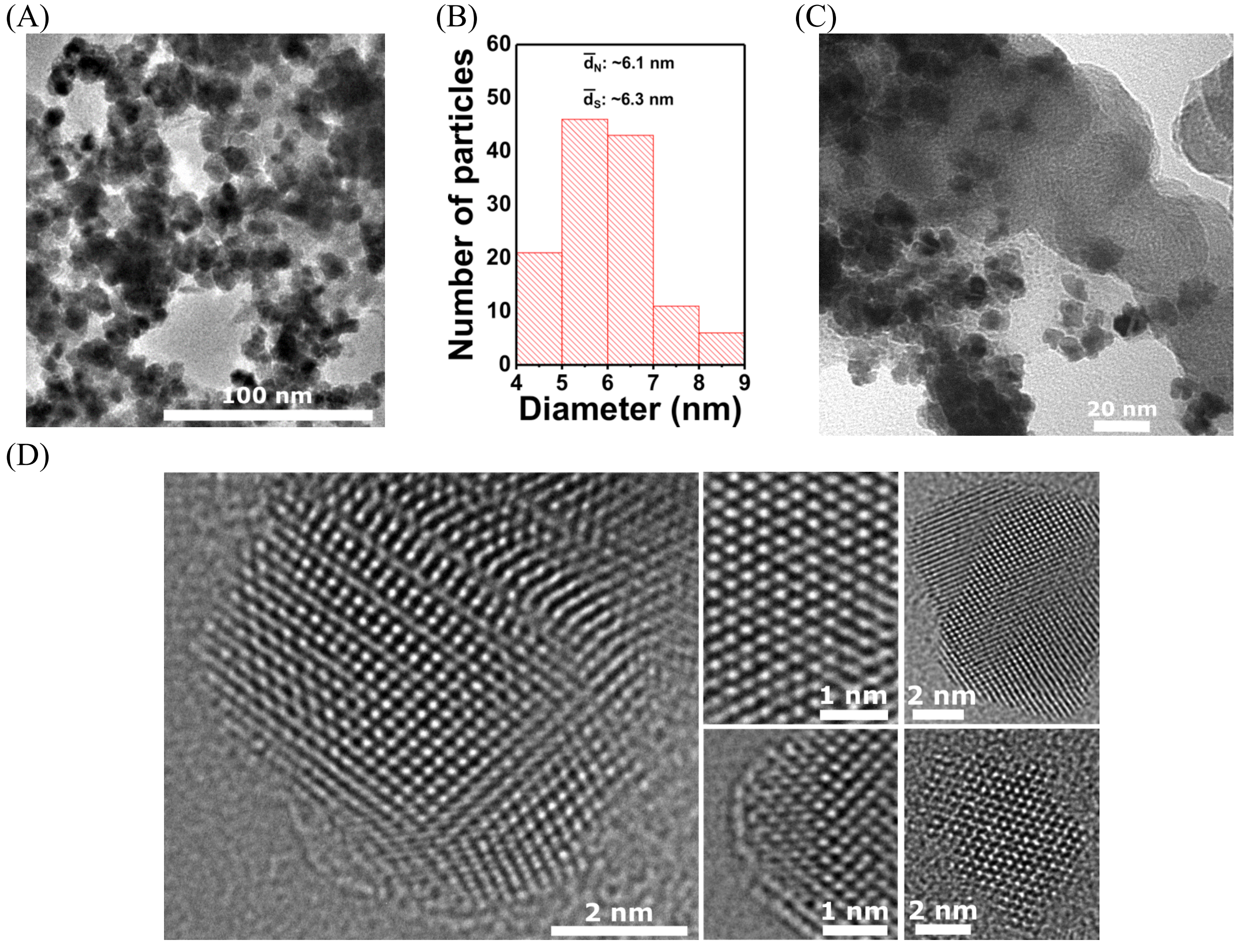

Figure 46. TEM analysis of (A) unsupported Pt_xPr nanoparticles with (B) corresponding PSD. Evaluation of the PSD discloses a d_N of 6.1 nm. (C) TEM image of the Vulcan-supported Pt_xPr/C electrocatalyst. (D) Corresponding HR-TEM images of representative Pt_xPr nanoparticles, indicating a high degree of surface disorder. Reprinted with permission from ref. 278. Copyright 2019 American Chemical Society.

(HR-)TEM analyses of as-synthesized Pt_xPr nanoparticles and carbon-supported Pt_xPr/C catalyst are depicted in Figure 46A-D. Unsupported, aggregated Pt_xPr nanoparticles are shown in Figure 46A, which were utilized to determine the corresponding PSD (Figure 46B). A d_N of 6.1 ± 1.1 nm and d_S of 6.3 nm were deduced from the evaluation of ~100 individual nanoparticles, not counting agglomerates. Overall, the distribution is centered around 5-7 nm mean size, with small fractions of smaller (down to 4 nm) and larger (up to 9 nm) particles. A typical TEM image of the supported electrocatalyst is shown in Figure 46C. The distribution of the particles on the support material reveals vacant areas, which is probably owed to the fact that the carbon was only added to the Pt_xPr

nanoparticles during the ink preparation. Moreover, a pronounced aggregation of the nanoparticles is observable, which has to be considered in further evaluations since it influences the fraction of the available active surface area. At low resolution, an inhomogeneous and asymmetric shape of the isolated Pt_xPr nanoparticles is already prefigured. The high-resolution TEM images shown in Figure 46D further confirm an unordered and distorted surface structure of the synthesized nanoparticles. As elucidated in the previous chapters, a certain degree of (surface) structural disorder can be prefigured, considering the harsh synthesis conditions. While such surface-defective regions may contribute to the performance boost regarding the ORR, they are no central subject of the investigation in this chapter. For more details on the formation and impact of the surface defects on the ORR performance, please also see Chapters 3 and 4 of this work.

While HR-TEM analysis shows indications of an inhomogeneous and defect-rich surface structure owed to the synthesis conditions, conclusions on the nanoparticle composition cannot be deduced. A helpful tool to gain insight into the elemental composition of such bimetallic samples is EDX. Hence, Figure 47 shows a combined STEM-EDX analysis of Pt_xPr/C, including a representative STEM image of supported Pt_xPr nanoparticles (A), as well as the corresponding elemental maps of Pt (B), Pr (C) and Pt + Pr combined (D). The elemental maps indicate a homogeneous distribution of Pt and Pr within the sample. However, distinct Pr traces seem to additionally concentrate on the surface of the nanoparticles. A possible explanation for this observation is the partial segregation of the elements due to the oxophilicity of Pr, followed by re-deposition or accumulation on the surface of the nanoparticles. Line scan analyses depicted in Figure 47E and F (along the pathways indicated in Figure 47A) further illustrate the partially inhomogeneous distribution of both elements.

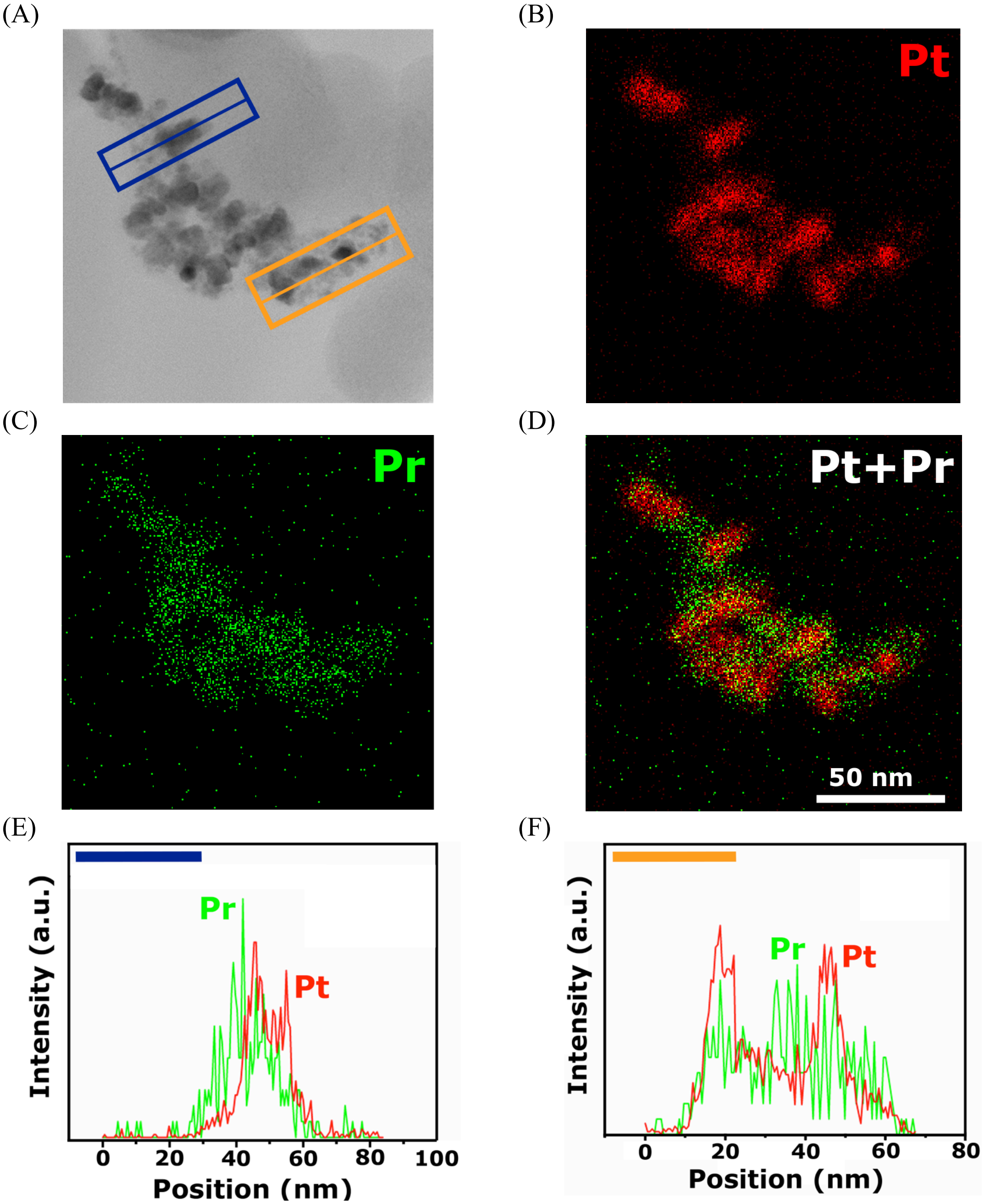

Figure 47. STEM-EDX analysis of Pt_xPr/C, depicting (A) an image of the supported nanoparticles, as well as elemental maps of (B) Pt, (C) Pr and (D) Pt + Pr. Line scan analyses of Pt_xPr/C shown in (E) and (F) follows the pathways highlighted in (A) and are marked in blue and orange, respectively. (A-D) are adapted with permission from ref. 278. Copyright 2019 American Chemical Society.

Detailed analysis of the local and global Pt to Pr ratios of a selected Pt_xPr aggregate is given in Figure 48. In the selected area, Pt_xPr/C shows an approximate global 4:1 Pt to Pr ratio, which is comparable to the composition of the Pt_5Pr host electrode. Locally, however, large deviations can be observed. Analysis of the STEM-EDX map shown on the right side of Figure 48 shows varying local composition, with Pr contents ranging between less than 10% up to ~50%. Assuming homogeneous alloying of the host material, previous observations on the segregation of Pr can thus be further confirmed.

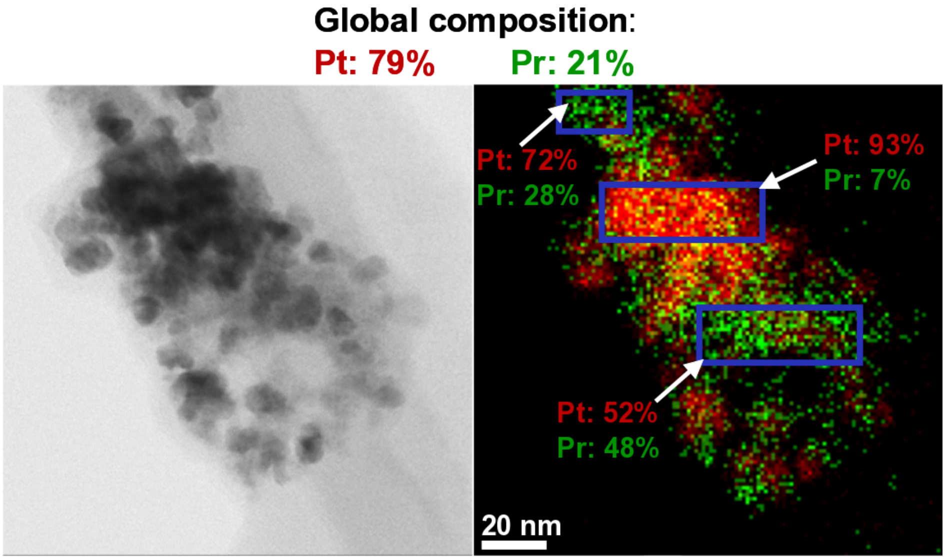

Figure 48. STEM image (left side) and STEM-EDX analysis (right side) of Pt_xPr/C. Local Pt:Pr ratios determined in selected areas of the sample (blue frames) indicate inhomogeneous distribution of Pr and Pt.

5.3 Probing the Alloying State of Pt_xPr/C Electrocatalyst

EDX analysis indicates the formation of an intermetallic Pt_xPr-type nanostructure with an inhomogeneous distribution of Pt and Pr and a surface accumulation of Pr. In order to distinguish between actual Pt_xPr alloy formation and a segregated compound, further spectroscopic and crystallographic characterization has to be performed.

Additional information about the chemical composition of the Pt_xPr sample can be obtained from XPS. *Ex-situ* XPS analysis of the Pt 4f (Figure 49A), as well as the Pr 3d (Figure 49B) region of unsupported Pt_xPr nanoparticles validates the occurrence of metallic Pt and Pr. Higher oxidation states of both elements can be detected as well, corresponding to their (surface) oxidized forms caused by air exposure and/or the synthesis conditions.

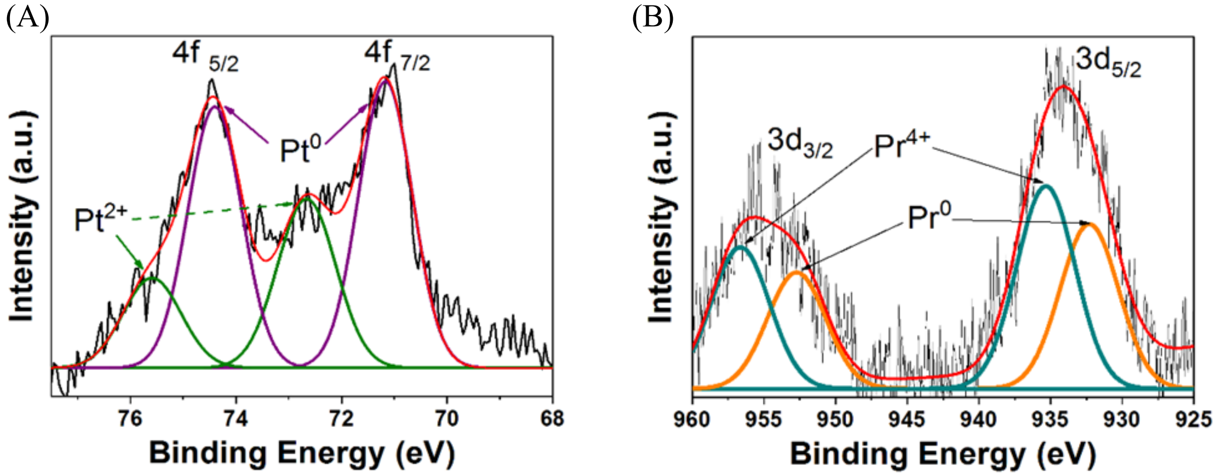

Figure 49. XPS analysis of the unsupported Pt_xPr nanoparticles. (A) Fitted Pt 4f region with corresponding oxidation states and (B) fitted Pr 3d region with corresponding oxidation states. Reprinted with permission from ref. 278. Copyright 2019 American Chemical Society.

Finally, clear evidence for an alloy phase formation can be gathered from X-ray diffraction experiments. Figure 50A shows the diffractogram of the as-synthesized Pt_xPr/C catalyst. As a reference, the characteristic 2θ values of pure Pt (taken from PDF 04-0802) are shown in the same angular range (green vertical bars). Compared to the signals expected for pure Pt, there is a significant positive angular shift, indicating the formation of Pt_xPr-type alloy phases. Assignment of the signals and comparison with the corresponding PDF values provides evidence for the formation of PtPr, Pt_2Pr and Pt_5Pr phases (Table 1). Besides, several additional phases are visible, which can be assigned to the formation of various Pr oxide species and Pt (for a detailed list see supporting information of ref. 278). However, the individual contributions of the different phases cannot be extracted. Hence, following experimental studies require a refinement of the XRD data, which was not possible due to the low resolution of the diffractogram and small amount of catalyst synthesized. However, (partial) formation of the alloy phases is evident. Additionally, alloy formation was verified through an acid leaching experiment. Since Pr surface oxides are prone to dissolution in acidic environment,[281,282] the catalyst was dispersed in 3.6 M H_2SO_4 for 2 h. After subsequent washing and drying steps, the powder was investigated *via* XRD. Most importantly, the alloy phases are still visible after acid treatment, including a constant angle shift compared to the pure Pt reference (Figure 50B). Indeed, this observation can only be attributed to the formation of stable bulk alloy phases, which are protected from dissolution in acidic media.

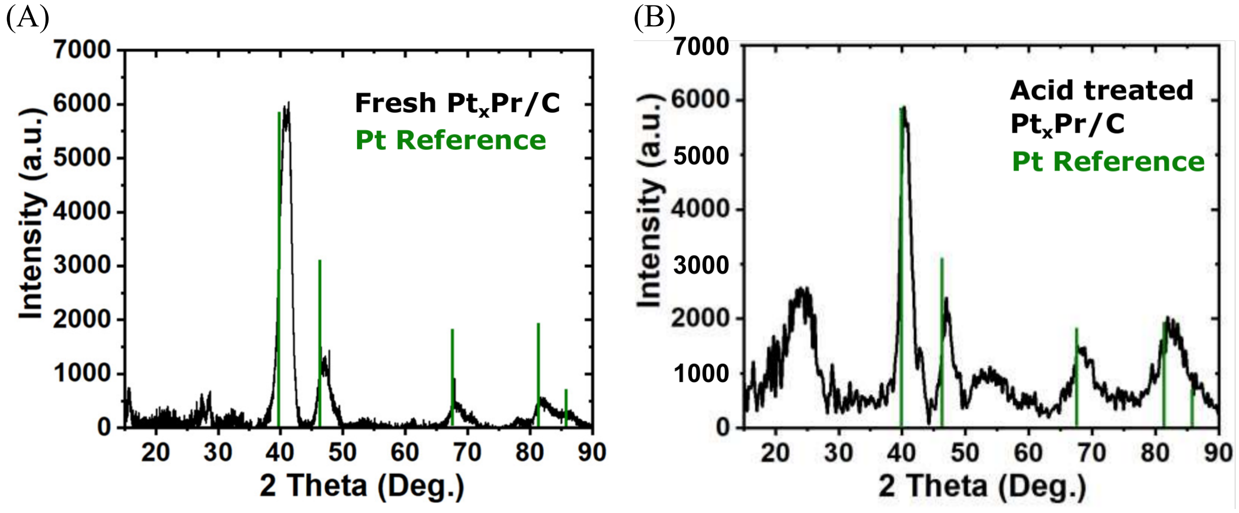

Figure 50. XRD patterns of (A) fresh and (B) acid-treated Pt_xPr/C. Acid treatment of the electrocatalyst was performed by dispersion in a constantly stirred 3.6 M H_2SO_4 aqueous solution for 2 h, followed by a washing step. Green bars correspond to the reference values of pure Pt taken from PDF 04-0802. Adapted with permission from ref. 278. Copyright 2019 American Chemical Society.

Table 1. Selected experimental XRD and corresponding PDF reference values (for detailed information see the supporting information of ref. 278) of the Pt_xPr/C sample, indicating the formation of PtPr, Pt_2Pr and Pt_5Pr alloy phases.

Phase	2θ (Experimental)	2θ (Taken from PDF)[278]
PtPr	67.89	67.81
	81.63	81.93
Pt_2Pr	40.60	40.60
	47.20	47.25
Pt_5Pr	41.30	41.20
	70.36	70.36

Explanation of the incomplete generation of Pt_xPr alloy phases derived from the XRD patterns demands a detailed knowledge of the nanoparticle formation mechanism. However, SEM studies of the Pt_5Pr host metal surface, shown in Figure 51, allow to draw first conclusions. In BSE mode, an elemental contrast between Pt (bright) and Pr (dark) is visible on the nanoscale. As marked by the red frame, local Pt enrichments are visible on the surface of the electrode. Hence, the formation of pure Pt phases might be due to the inhomogeneous composition of the utilized working electrode. In combination with the strong oxophilicity of Pr, which might partially dissolve and accumulate on the particle surface during the synthesis, the generation of mixed phases can be justified.

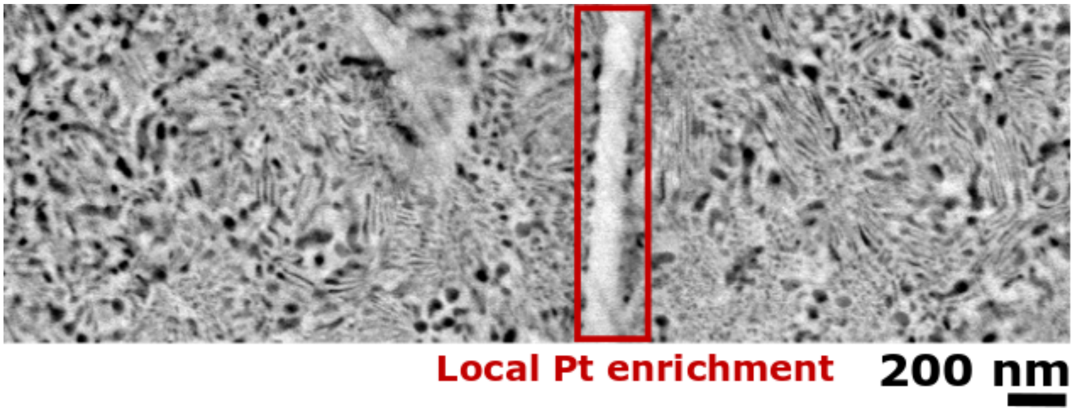

Figure 51. SEM image of the Pt_5Pr disk electrode surface used as the host material for the synthesis of Pt_xPr nanoparticles, recorded in the BSE mode. Bright spots correspond to Pt enrichments, while dark spots correspond to Pr enrichments. Adapted with permission from ref. 278. Copyright 2019 American Chemical Society.

5.4 Electrochemical Characterization and Stability

Considering the high ORR activity enhancement reported in case of polycrystalline Pt_5Pr compared to polycrystalline Pt, an activity gain of its nanostructured form *vs* pure Pt nanoparticles can be expected. In order to investigate the ORR activity of the synthesized bimetallic nanoparticles with respect to commercial pure Pt/C_{TKK}, RDE measurements were conducted. A typical CV of Pt_xPr/C recorded in Ar-saturated 0.1 M $HClO_4$ at a scan rate of 50 mV/s and temperature of 25°C is shown in Figure 52A. As expected, typical $H_{ad/des}$-peaks of Pt surfaces are visible in the range of approximately 0.1 to 0.4 V *vs* RHE. However, similar to the CV of the Pt_5Pr host material,[143] the H_{UPD} features seem to be less pronounced compared to the commercial Pt/C (Figure 27), which is most likely owed to initial surface presence of the alloying element. To determine the SSA of Pt_xPr/C, CO stripping voltammetry of both catalysts was performed and is shown in the inset of Figure 52A. Pt/C_{TKK} shows a peak at ~0.78 V *vs* RHE, which is typical for well-dispersed, monometallic Pt nanoparticles of comparable sizes (see Figure 17, 40). As an effect of the alloying and/or the nanoparticle size difference (~6 nm for Pt_xPr/C *vs* ~3 nm for Pt/C_{TKK}),[210,211] a shift toward lower potentials (~0.74 V *vs* RHE) and a slight peak broadening are observable.[133,250,271]

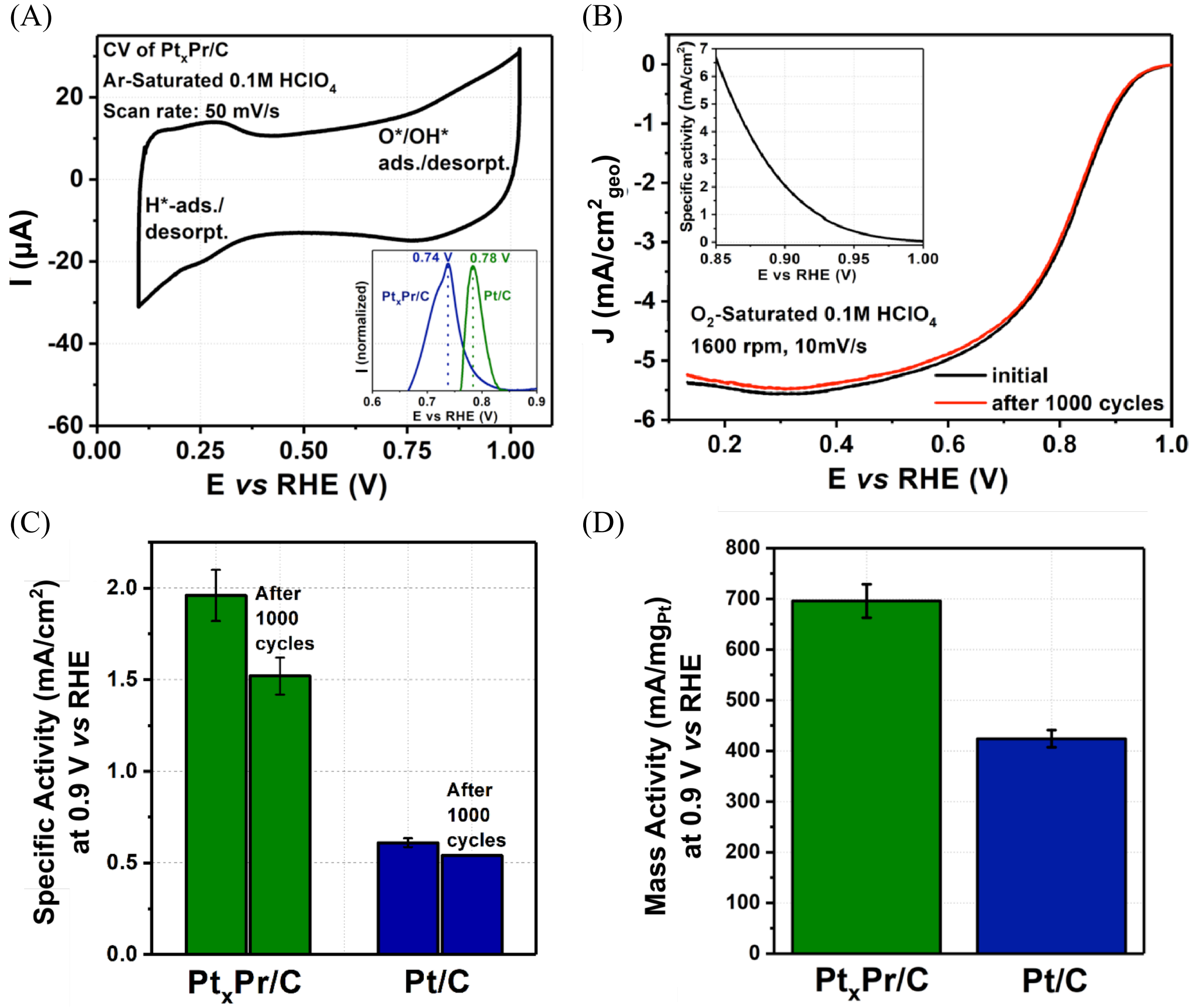

Figure 52. (A) Characteristic CV of the Pt_xPr/C electrocatalyst (metal loading: 1.5 µg/cm^2), recorded in Ar-saturated 0.1 M $HClO_4$ at room temperature and 50 mV/s scan rate. Inset: Comparison of the normalized CO stripping peaks of Pt_xPr/C (blue) and Pt/C_{TKK} (green).
(B) Characteristic anodic polarization curve (corrected for capacitive currents and the ohmic resistance) of Pt_xPr/C, before (black) and after (red) voltage cycling. The curves were recorded in O_2-saturated 0.1 M $HClO_4$ at room temperature, 1600 rpm and 10 mV/s. The current is normalized to the area of the glassy carbon substrate, being 0.196 cm^2 (metal loading: 1.5 µg/cm^2). Inset: typical SA curve between 0.85 and 1.0 V *vs* RHE. (C) Specific and (D) mass activity of Pt_xPr/C and Pt/C_{TKK} evaluated at 0.9 V *vs* RHE. Adapted with permission from ref. 278. Copyright 2019 American Chemical Society.

From the analysis of the respective CO stripping peaks (see experimental section), a SSA of 36 ± 2 m^2/g_{Pt} was determined for Pt_xPr/C, compared to 68 ± 2 m^2/g_{Pt} for Pt/C_{TKK}. Considering the different I/C ratio, the SSA of the reference catalyst is in a good agreement with previous reports in the literature.[60] In Figure 52B, a representative anodic polarization curve of fresh (*i.e.* after conditioning) Pt_xPr/C (black curve) recorded in O_2-saturated 0.1 M $HClO_4$ at a scan rate of 10 mV/s, rotation speed of 1600 rpm and temperature of 25°C is depicted. In order to rate the stability of Pt_xPr/C, additional polarization curves were recorded under similar conditions after the catalyst was subjected to 1000 cycles between 0.6 and 1.0 V *vs* RHE (100 mV/s) at 25°C (red curve). Here, no significant changes can be observed, indicating relatively good electrochemical stability. Using the recorded polarization curve, the corresponding kinetic current was determined according to the Koutecký–Levich equation (equation 24) and divided by the ECSA determined from the CO stripping voltammetry, as shown in the inset of Figure 52B (in the potential range of 0.85 – 1.0 V *vs* RHE). The averaged SA values at 0.9 V *vs* RHE, before and after voltage cycling, are shown in Figure 52C. For fresh Pt_xPr/C, a mean SA of 1.96 mA/cm^2_{Pt} was determined at 0.9 V *vs* RHE, which is ~3.5-times higher than the SA of the commercial Pt/C_{TKK}. Considering the particle size effect,[104,105,106,107] parts of this activity enhancement *vs* commercial Pt/C_{TKK} are assigned to the larger particle diameter and, accordingly, lower SSA compared to the reference catalyst. However, the 3.5-times increased SA cannot fully be explained by this effect, as only about 50% enhancement are expected according to the literature,[107] which leads to the conclusion of a significantly higher intrinsic activity of the prepared catalyst. Moreover, the 3.5-times increase of the SA is in accordance with the 4-times increased activity of the polycrystalline Pt_5Pr disk electrode *vs* pure polycrystalline Pt reported in the literature.[143] Comparing the losses observed after the voltage cycling, Pt_xPr/C seems to degrade slightly faster than the commercial Pt/C_{TKK}. In numbers, the former loses ~25% SA within 1000 cycles, compared to less than 10% in the case of Pt/C_{TKK}. Interpretation of the faster electrochemical degradation demands further (*post-mortem*) analytical investigations. However, it can be assumed that structural surface relaxation or compositional changes are responsible rather than particle growth, which would result in increased SA values. Moreover, analysis at elevated temperatures and in an MEA setup should be performed in further experimental studies, which are out of the scope of this work.

To evaluate the mass activity of both catalysts, the kinetic current at 0.9 V *vs* RHE was normalized to the mass of Pt deposited on the glassy carbon electrode. While in the case of Pt/C_{TKK} the Pt to carbon weight ratio was provided by the supplier, the weight fraction of Pt_xPr nanoparticles of the electrocatalyst powder (~4 wt%) was determined by TGA, and the corresponding Pt fraction was estimated using the average global Pt:Pr ratios from EDX and XPS. Accordingly, a MA enhancement of Pt_xPr/C over Pt/C_{TKK} by a factor of ~1.7 was determined, as shown in Figure 52D. The lower relative MA increase in comparison to the SA enhancement could be explained by the large particle size (as Pt nanoparticles show improved MA at lower particle size)[104,105,106,107] and the reduced available ECSA due to agglomeration of the particles. Hence, in order to achieve the expected improvements in terms of the mass activity, an increased SSA has to be ensured and surface blocking due to agglomeration has to be prevented effectively.

5.5 Perspective and Application to Different Alloys of Pt and Lanthanides/Rare-Earth Metals

Considering the generally high reported ORR activity gains of polycrystalline Pt-lanthanide alloys compared to pure polycrystalline Pt surfaces (up to 6-times increased specific activity) and the sophisticated state-of-the-art synthesis strategies for corresponding nanostructures (see Chapter 1.4.3),[136,137,141,144] our approach can be considered as a very promising alternative and has to be elaborated in future experimental studies. Besides facile one-step and one-pot synthesis, Pt_xPr/C shows a significant gain in activity compared to commercial Pt/C_{TKK}, which is consistent with studies on extended surface materials.[143] However, the mass activity of the synthesized nanocatalysts still needs to be improved. The comparatively low value is likely due to the large particle diameter and the non-uniform composition observed in EDX and XRD, which has to be adjusted in further optimization processes. Moreover, aggregation of the nanoparticles has to be suppressed in order to prevent the loss of active surface area. Importantly, one can assume that the synthesis can be applied universally for different Pt-lanthanide alloys. For instance, preliminary experiments conducted in our group (in cooperation with the research group of Dr. Oliver Schneider from TUM) indicate that the synthesis procedure is also applicable for the preparation of *e.g.* Pt_xGd nanoparticles. As mentioned earlier, Velázquez-Palenzuela *et al.* prepared mass-selected model Pt_xGd nanoparticles using a gas aggregation technique in UHV, which showed a high mass activity of up to ~3.6 A/mg_{Pt}.[137] However, a verification of these results is still pending at this point.

Chapter 6. Top-Down Synthesis of Pt_xNi/C and Pt_xCu/C

In this chapter, attempts to synthesize Pt_xNi/C and Pt_xCu/C alloy electrocatalysts are discussed. Based on the top-down synthesis route presented earlier in this work, two different approaches are employed. First, nanoparticle erosion from a macroscopic PtNi precursor alloy was investigated. Secondly, it was tested whether the presence of Cu ions in the aqueous dispersion influences the top-down synthesis. Using microscopic, spectroscopic and crystallographic techniques, certain limitations of the top-down technique are revealed.

Parts of this chapter are in preparation for manuscript submission, including the following co-authors: Sarpey, T. K.; Fichtner, J.; Watzele, S.; Garlyyev, B.; Hou, S.; Michalička, J.; Macak, J. M.; Bandarenka, A. S.

6.1 Attempts Toward the Synthesis of Nanostructured Pt_xNi/C Alloy Electrocatalysts

Since bimetallic nanocomposites of Pt and 3d transition metal elements pose one of the most frequently investigated classes of the ORR electrocatalysts (see Chapter 1.4.2), several synthesis techniques to control their shape, size and composition are known.[283] However, synthesis of such structures is often based on complex wet-chemical bottom-up processes. Several studies have shown that especially supported Pt_xNi-type electrocatalysts exhibit promising activities toward the ORR, owed to strain and ligand effects.[126,154,284] For instance, investigation of de-alloyed PtNi/C catalysts led to “record activities” in single-cell PEMFC tests.[121] Moreover, the relatively high abundance and low costs of the 3d transition metal compound,[285] as well as the high activity enhancements compared to pure Pt/C contribute to their widespread usage.

According to the findings of Rodriguez *et al.*, [164] the top-down approach utilized in this work is applicable to different types of alloys, including 3d transition metal alloys of Pt such as Pt_xNi. Based on EDX and XRD analysis, the group claimed proper formation of a $Pt_{50}Ni_{50}$ nanoparticle alloy, synthesized using a macroscopic Pt_xNi host alloy. However, in this case a lack of support material and the resulting strong nanoparticle aggregation prevented the catalyst from being suitable for electrocatalytic applications. Nonetheless, the top-down synthesis of supported Pt_xNi/C electrocatalysts could potentially benefit the ORR catalysis in terms of both affordability and performance. In order to prepare Pt_xNi/C electrocatalyst, a preparation route similar to the one described in the previous chapters was employed. Here, a 1:1 atomic ratio PtNi precursor alloy served as the WE. Following the synthesis of the fresh Pt_xNi/C electrocatalyst (see Chapter 2.1.3), the powder was dispersed 1 M H_2SO_4 for 24 h. Such an acid treatment is frequently employed to dissolve surface Ni and generate a stable, strained Pt-rich shell.[121,286,287,288] It has to be noted that compared to the work of Rodriguez *et al.*,[164] KOH rather than NaOH was used as the electrolyte in order to ensure consistency with previous experiments.

Two characteristic STEM images and the corresponding EDX elemental mapping of freshly prepared Pt_xNi/C (before acid treatment) are shown in Figure 53A-D. Unexpectedly, the synthesized Pt_xNi nanostructures are significantly larger (in the order of several tens of nanometers) than previously produced pure Pt and Pt_xPr nanoparticles. Following the elemental traces, Pt and Ni are distributed homogeneously within these compounds, which implies an alloyed state of the nanomaterials prepared. For the depicted structures, global Pt:Ni ratios of 68:32 (B) and 62:38 (D) were found, being slightly lower than the initial atomic ratio of the precursor metal electrode.

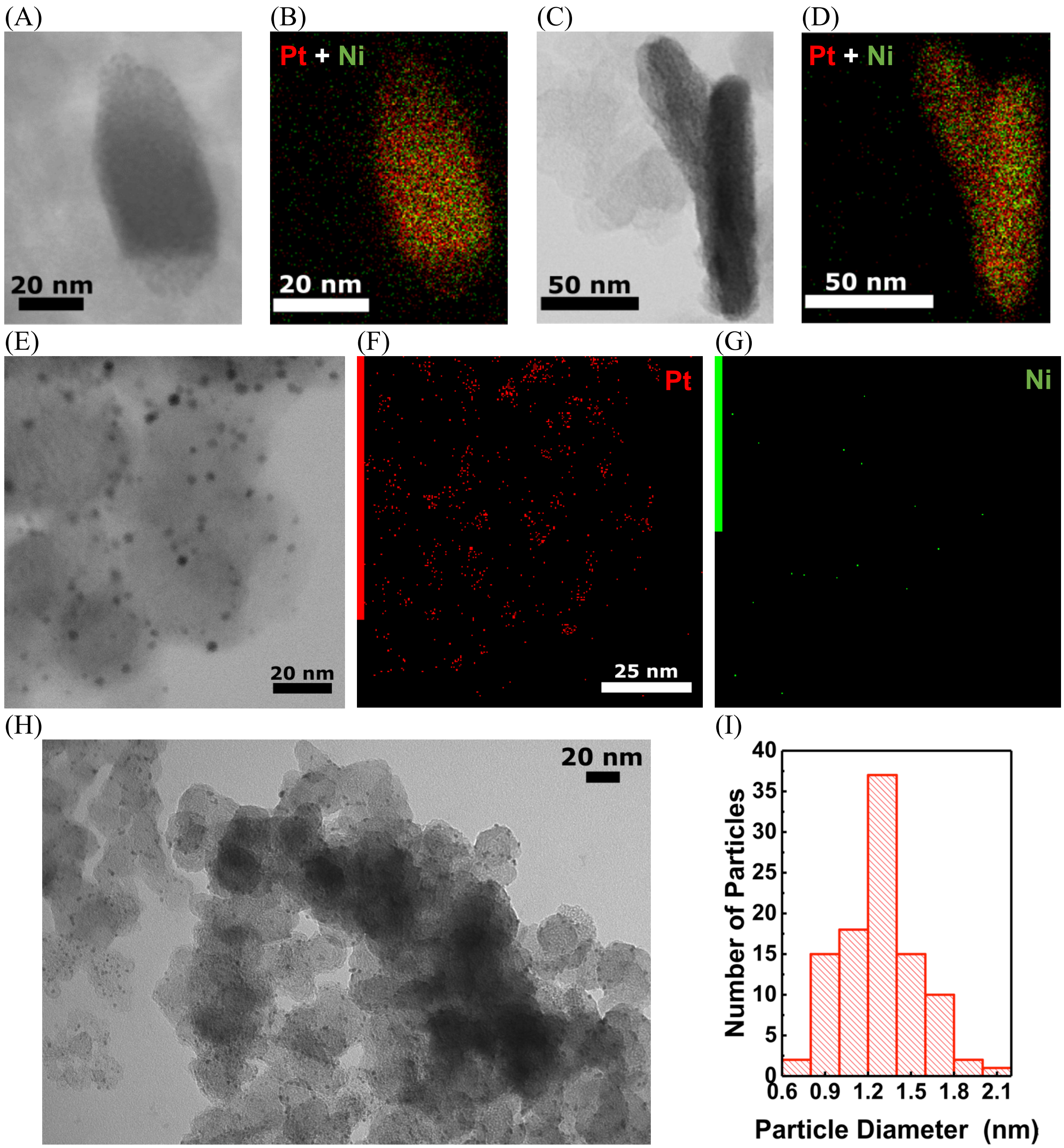

Figure 53. STEM-EDX analysis of the Pt_xNi/C electrocatalyst samples prepared by electrochemical decomposition of a macroscopic 1:1 ratio PtNi precursor electrode. (A, C) Representative STEM images and corresponding (B, D) Pt and Ni combined elemental mapping of as-prepared Pt_xNi/C, showing large nanostructures with homogeneous Pt and Ni distribution. (E) Representative STEM image and corresponding (F) Pt and (G) Ni elemental maps of the acid-treated (1 M H_2SO_4, 24 h) Pt_xNi/C sample, showing small, homogeneously distributed nanoparticles and dissolution of the whole Ni content. (H) TEM image of the acid-treated Pt_xNi/C electrocatalyst at a lower magnification and (I) corresponding PSD.

Surprisingly, the appearance of the catalyst changes significantly after the acid treatment, as shown in Figure 53E-G. After being subjected to 1 M H_2SO_4 for 24 h, uniform and well-distributed nanoparticles appear on the carbon support, which are several times smaller than the initial structures. The formed particles consistently show a nearly spherical shape and seem to be similar in size. Following the corresponding EDX elemental maps, no remaining Ni can be detected. Instead, the particles were found to consist of pure Pt. In Figure 53H, a corresponding TEM image of the Ni-leached Pt_xNi/C sample is shown. The image reveals similarly homogeneous Pt nanoparticle distribution in a larger scale. This observation has to be highlighted since dispersion of the Pt nanoparticles is significantly improved compared to previously prepared Pt/C_{TD} samples (Chapters 3 and 4). In accordance, aggregation of the nanoparticles is strongly reduced, which aids to prevent the loss of Pt active surface area. From the investigation of 100 individual nanoparticles, a number-averaged diameter of 1.28 ± 0.27 nm was determined using the imageJ software. Interestingly, this is the smallest size and narrowest size distribution reported in this work. For illustration, the lowest size prepared using the "direct" approach (Chapter 3) was 1.9 ± 0.7 nm. In the latter case, further reduction of the particle size was limited by the minimum concentration required to generate nanoparticles at all (0.2 M KOH at ±10 V, 200 Hz sinusoidal potential). With respect to the results presented in Chapter 3, opposite is expected, *i.e.* a significantly larger Pt nanoparticle size. Subsequently, the question arises, how the transition from single large nanostructures toward multiple small, well-distributed nanoparticles proceeds. Closer examination of the as-prepared Pt_xNi/C sample *via* STEM-EDX is presented in Figure 54. A nanostructure with the size in the order of ~100 nm is visible, as highlighted by the green frame. Within this structure, several small isolated dark spots are visible, as highlighted by the red frame. This observation, however, points toward the formation of a heterostructure rather than an alloy during the synthesis. Moreover, the previous observations (dissolution of whole Ni content) are not compatible with the formation of nanostructured bulk alloys since at least certain proportion of Ni should detectable in the core of the particle after acid treatment.[286,289] Besides, the EDX signal of Pt seems to follow the dark spots, while the Ni signal is locally enriched at the edges of the structure. This leads to the conclusion that Pt becomes encapsulated in a matrix framework of Ni or heavily aggregated core-shell particles are formed during the synthesis.

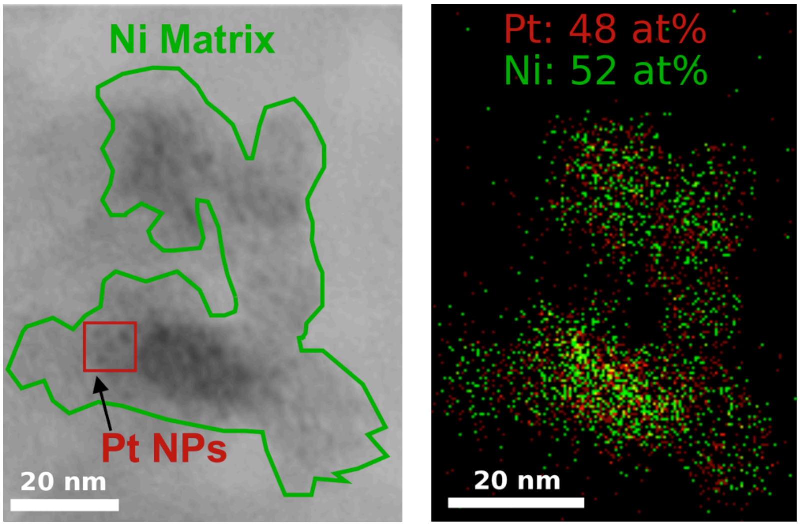

Figure 54. STEM-EDX analysis of as-synthesized Pt_xNi/C. On the left side STEM image, the whole nanostructure is marked by a green frame. The dark spots are assigned to small Pt nanoparticles encapsulated in a Ni-based matrix (as exemplarily highlighted by a red frame). On the right side, the corresponding EDX mapping is shown.

Since this observation contradicts the aforementioned findings of Rodriquez *et al.*,[164] it has to be further examined under varying synthesis conditions. Based on the presented observations, we propose that the formation of such a heterostructure is caused by the oxophilicity of Ni. In detail, surface oxidation takes place during the positive potential steps. Due to the oxophilicity of Ni, it segregates from Pt and constantly moves toward the electrode surface. Subsequently, Pt-core/Ni-shell (denoted as Pt@Ni) structures are formed and released into the electrolyte. The observations are supported by recent findings of Strasser and co-workers.[290] In their study addressing the influence of electrolyte pH on the activity of supported Pt_xNi alloy nanoparticles, they found certain segregation of Ni during alkaline fuel cell activity measurements, if the catalyst is pretreated in alkaline media. Moreover, they concluded that the presence of oxygen is decisive in initiating the separation rather than the sole presence of hydroxyl species. However, in order to deduce the exact mechanistic behavior of Pt_xM-type alloy segregation during the top-down synthesis, further experimental studies have to be conducted. For illustration, the hypothetical process is schematized in Figure 55.

Although Ni segregation is a disadvantage for the targeted ORR activity of the catalyst, some advantages can be noted. Especially the exceptional Pt nanoparticle distribution on the support material and the small particle size (distribution) of the prepared catalyst have to be highlighted. Recently, we showed that the precise tailoring of the Pt nanoparticle size, accompanied by a narrow

PSD, is one of the crucial factors contributing to enhanced ORR activities. For instance, we synthesized pure Pt nanoparticles with a number-averaged diameter of 1.1 ± 0.17 nm using a metal-organic framework (MOF)-based approach.[235] The prepared nanoparticles showed up to twofold enhanced MA and up to threefold enhanced SA compared to the commercial Pt/C_{TKK}. Moreover, Taylor *et al*. showed that a good Pt dispersion on the support material significantly benefits the ORR mass activity due to the high availability of the ECSA.[270] Contrary, the SA typically drops with increasing SSA due to the particles size effect. [107]

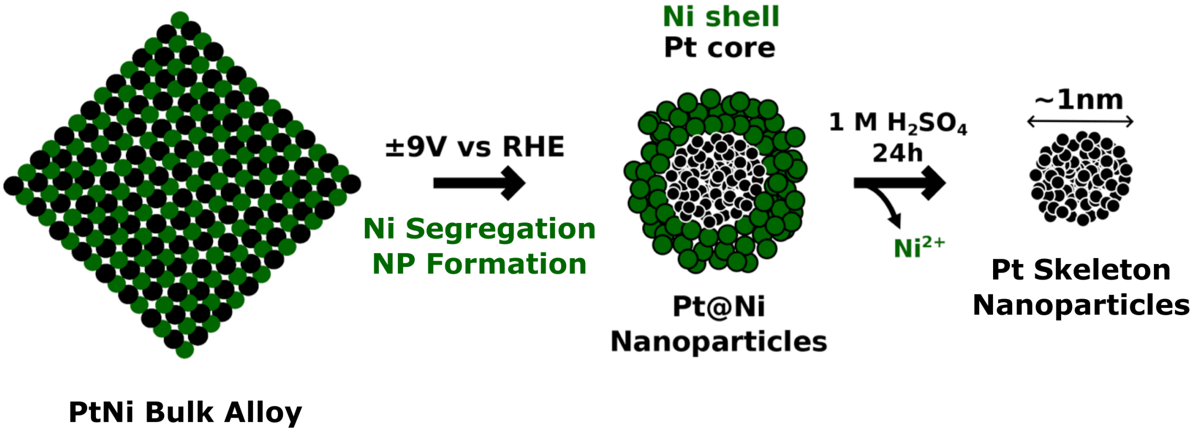

Figure 55. Schematic description of the Ni segregation-assisted Pt nanoparticle synthesis. Application of an alternating voltage to a macroscopic PtNi alloy in alkaline media leads to the segregation of the Ni during the nanoparticle (NP) formation. During the following acid treatment Ni leaches, which leads to a pure Pt skeleton structure of small diameter.

Thus, in order to probe the intrinsic activity of our catalyst, ORR activity measurements of acid-treated Pt@Ni/C were conducted in the RDE setup and compared to a commercial Pt/C reference electrocatalyst (5 wt% Pt/$C_{E\text{-}TEK}$). The reference was chosen due to its small average diameter (~1.8 nm) reported in the literature,[212] which is more reasonable for comparison than the one of Pt/C_{TKK}. Please note that the activity evaluation was conducted in a modified setup during a research stay abroad, using a commercial RHE reference electrode (for further details see experimental section). While the activity values determined for the reference catalyst are in accordance with previous results recorded in the same setup, they deviate from other results shown in this work. We assume that complications arise if the commercial RHE electrode is utilized in O_2-saturated electrolyte. Because of those complications, the enhancement factors are shown rather than absolute values, in order to obtain a fair comparison. The corresponding CVs of Pt/$C_{E\text{-}TEK}$ and Pt@Ni/C before and after the acid treatment are shown in Figure 56A. The corresponding polarization curves of Pt/C$_{\text{E-TEK}}$ and acid-treated Pt@Ni/C are shown in Figure 56B. The curves were recorded in Ar- or O_2-saturated 0.1 M $HClO_4$, respectively. Scan rates and rotation speeds are indicated in the inset of the graphs.

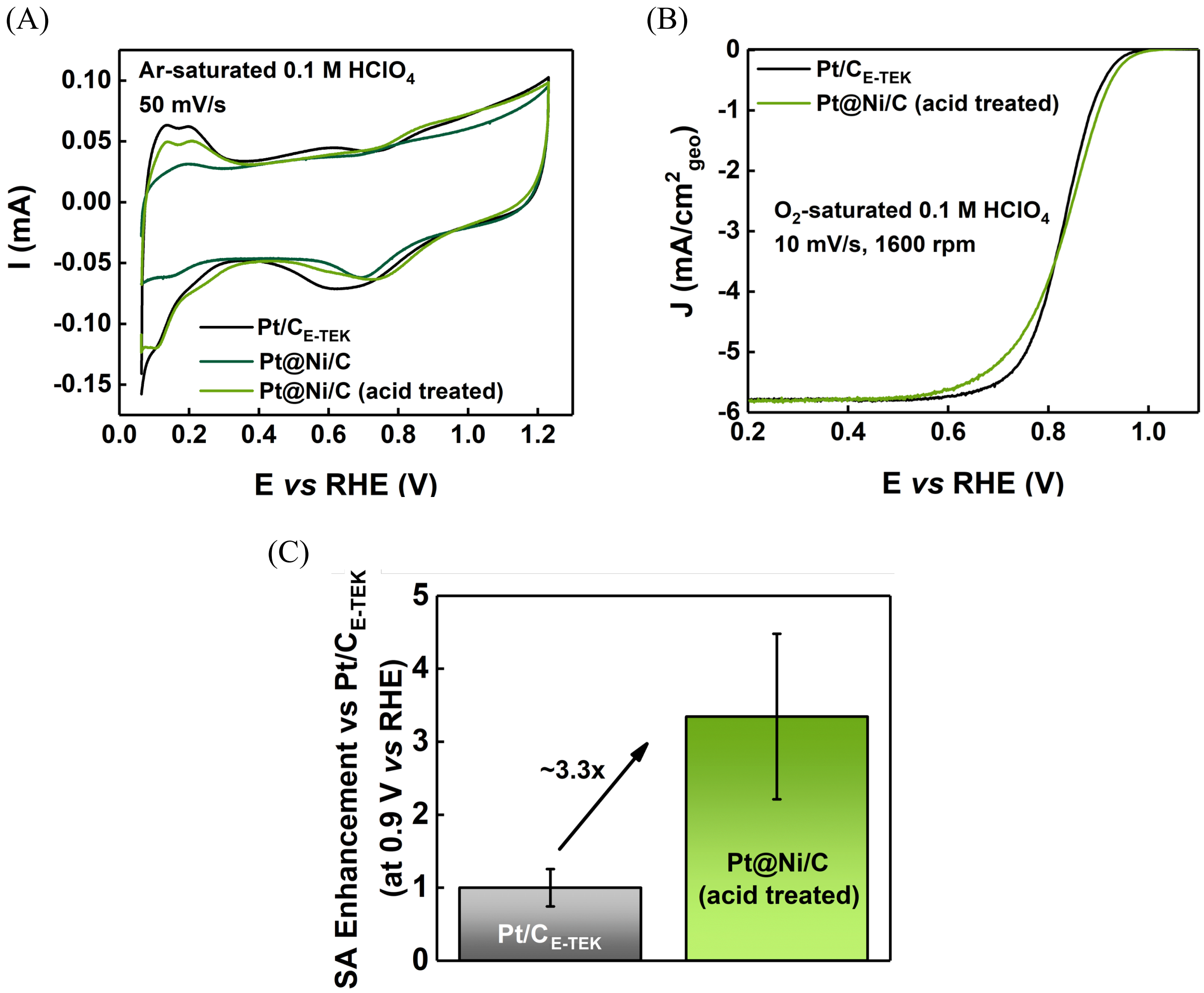

Figure 56. (A) Typical CVs for the 5 wt% Pt/C$_{\text{E-TEK}}$, Pt@Ni/C and acid-treated Pt@Ni/C catalysts, recorded in Ar-saturated 0.1 M $HClO_4$ (scan rate: 50 mV/s, room temperature).
(B) Typical *IR*-corrected anodic polarization curves of Pt/C$_{\text{E-TEK}}$ and acid-treated Pt@Ni/C. Pseudo(capacitive) background currents were subtracted from the recorded curves. Recorded in O_2-saturated 0.1 M $HClO_4$ at room temperature, 10 mV/s and 1600 rpm. (C) SA of acid-treated Pt@Ni/C relative to commercial Pt/C$_{\text{E-TEK}}$.

Comparison of the CVs shows that before the acid treatment of Pt@Ni/C, the $H_{ad/des}$ is largely suppressed. This observation can be traced back to Ni blocking the surface of Pt and further confirms the segregation and surface accumulation of Ni. After acid treatment of Pt@Ni/C, typical H_{UPD} features of Pt are visible, similar to the ones of the reference catalyst. Indeed, acid-treated

Pt@Ni/C shows a high ORR specific activity enhancement compared to the commercial catalyst (Figure 56C). According to Shoemaker *et al.*,[105] low specific activity is expected for such small Pt nanoparticles, while for the reference catalyst, higher SA is expected due to the increased average particle size. However, opposite can be observed, *i.e.* more than 3-times enhanced SA, which indicates a high intrinsic activity of the catalyst. The counterintuitive behavior could be owed to the narrow size distribution, in accordance with our previous publication noted earlier.[235] Indeed, the SA enhancement factor of 3.3 *vs* commercial Pt/$C_{E\text{-}TEK}$ is comparable to the one reported for MOF-derived Pt nanoparticles *vs* Pt/C_{TKK}.

6.2 Incorporation of Dissolved Cu Species into the Pt Nanoparticle Crystal Lattice

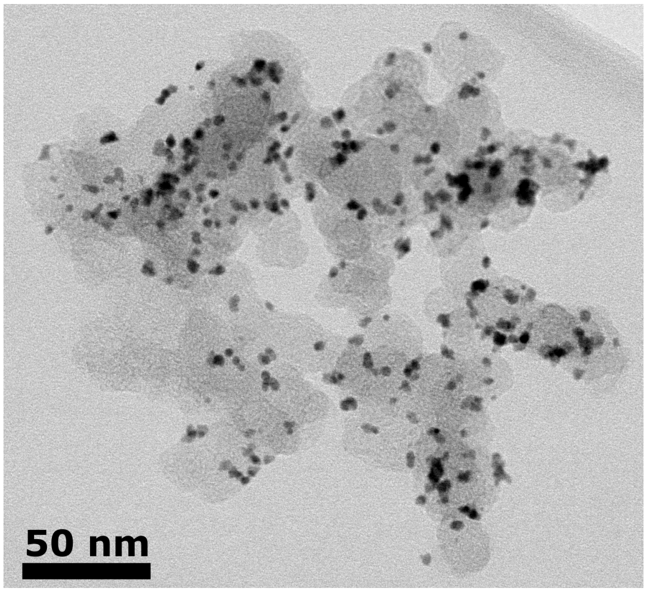

Figure 57. Typical STEM image of the Pt_xCu/C electrocatalyst, synthesized by subjecting Pt wires immersed in a dispersion of KOH, $CuSO_4$ and Vulcan carbon to a sinusoidal potential of ±15 V (200 Hz). The particles are homogeneously distributed on the carbon support and only show a small fraction of particle aggregates. From the investigation of 50 particles, a number-averaged diameter of ~3.9 nm was determined for the sample shown.

Pt_xCu/C electrocatalysts are another important group of catalysts for the ORR, showing promising activity values compared to pure Pt/C in both, RDE and MEA-based literature studies. For instance, the group of Strasser reported a ~3-4-times activity gain of ~4 nm-sized Pt_xCu nanoparticles in acidic media, accompanied by a good ORR performance even in alkaline environment.[119] Moreover, model studies indicate that the preparation of Cu/Pt(111) near-surface alloys, containing only sub-monolayer amounts of Cu, can lead to up to 8-fold improvement over Pt(111) electrode materials.[291]

As shown before, starting from the macroscopic alloy host material, the top-down synthesis of Pt_xM/C can be limited by the segregation of the 3d transition metal element. Surprisingly, one observes reverse phenomena when a corresponding salt is directly added to the alkaline electrolyte. For illustration, preliminary results indicate that by addition of $CuSO_4$ into KOH electrolyte (prior to the top-down synthesis with pure Pt wires), incorporation of Cu into the formed nanoparticle structure takes place. A TEM image of an accordingly prepared Pt_xCu/C catalyst is shown in Figure 57. The particles were synthesized by applying a sinusoidal potential of ±15 V (200 Hz) to pure Pt wires immersed in a dispersion of 0.5 mM $CuSO_4$ x 5 H_2O, 1 M KOH and Vulcan carbon. Analysis of the PSD discloses a d_N of 3.9 ± 1.1 nm, being slightly larger than the value expected in the case of pure Pt/C_{TD} from Figure 30C (under given conditions). The larger diameter could be owed to the incorporation of the Cu, however, it is still within a statistical error. STEM-EDX analysis of Pt_xCu/C is shown in Figure 58. The elemental maps of Pt and Cu indicate homogeneous distribution of both elements within the nanoparticles formed. It should be noted that Cu-containing STEM grids were used for the investigation, which most likely accounts for background Cu noise. However, this doesn't explain the Cu signal accumulation at the nanoparticle imaging spots. A first verification for the formation of an (partial) alloy phase is given by XRD measurements (Figure 59). In accordance with the literature studies on Pt_xCu bimetallic alloys and compared to the signals of pure Pt (reprinted from the corresponding PDF), a shift toward higher 2 theta angles is visible.[119,292,293] The observation indicates a successful implementation of Cu into the Pt lattice. However, more detailed analysis is required to validate the alloy state of the electrocatalyst synthesized. In accordance with the previous observations presented in Chapter 3, it might be possible to specifically tailor the particle size of these alloys. Moreover, adjustment of the Cu content by variation of the $CuSO_4$ concentration in the electrolyte has to be examined, which could be utilized to maximize the electrocatalysts' activity. However, regarding the ORR activity of the prepared Pt_xCu/C sample, preliminary RDE measurements indicate up to ~4-times increased MA compared to pure Pt/C, which is in accordance with typical activity enhancements reported in previous studies and has to be reproduced in future experimental studies.[119] Lastly, application of the method to different types of alloys has to be investigated.

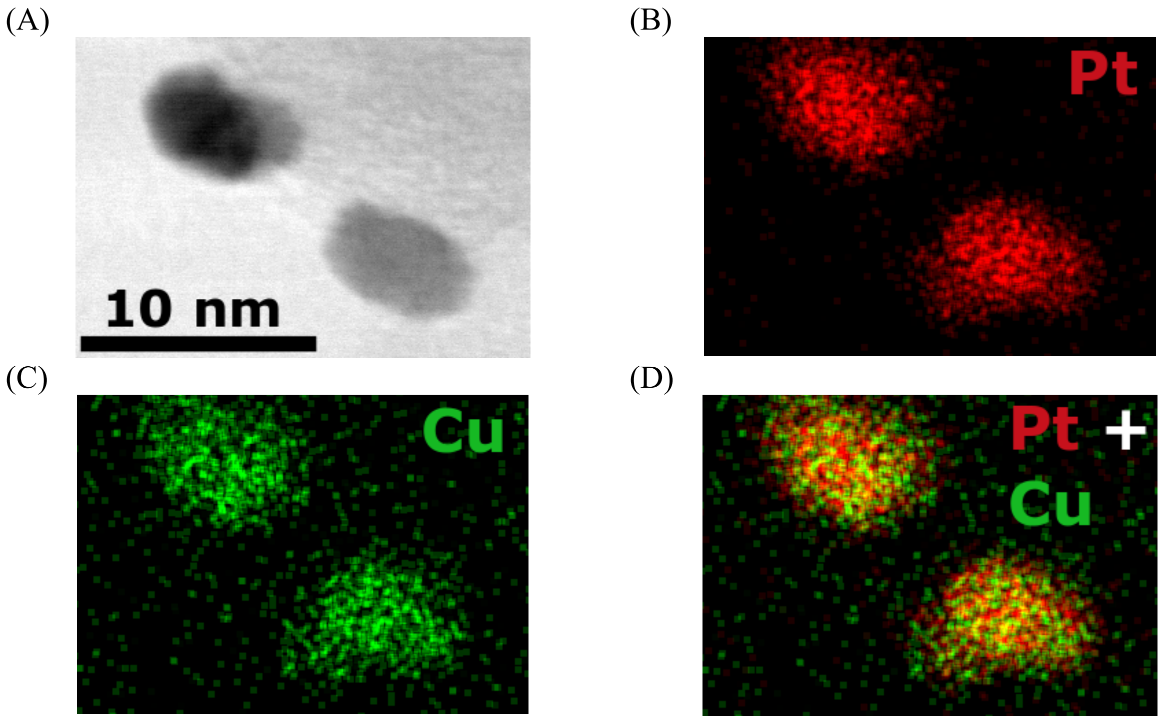

Figure 58. STEM-EDX analysis of the synthesized Pt_xCu nanoparticles. (A) STEM image with elemental maps of (B) Pt, (C) Cu and (D) Pt + Cu combined. The EDX traces indicate a homogeneous distribution of Pt and Cu within the nanoparticles shown.

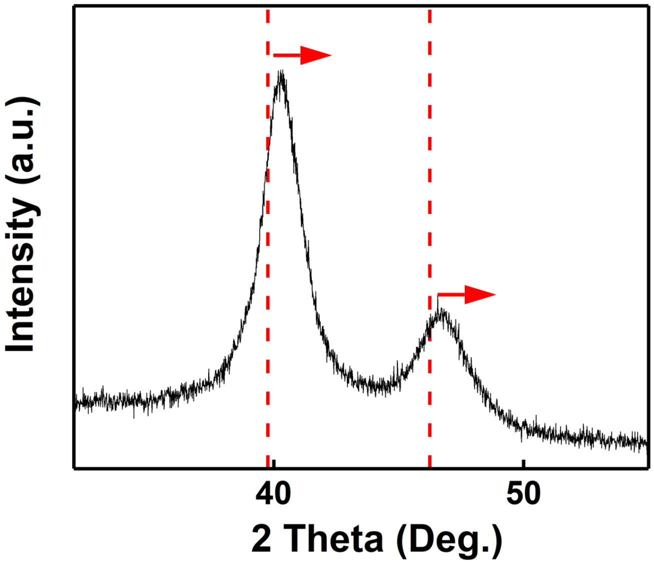

Figure 59. Typical XRD pattern of the synthesized Pt_xCu/C (black curve). Red dotted vertical lines correspond to the reference (111) and (200) signals of pure Pt (taken from PDF: 04-0802). As marked by red arrows, a peak shift toward higher angles compared to pure Pt can be observed.

Chapter 7. Summary and Outlook

In this work, the top-down preparation of electrocatalytically active Pt-based nanostructures for PEMFC applications was elaborated, based on previous findings by Bredig, Haber, Koper, Li, Smirnova and co-workers. The technique involves the electrochemical decomposition of macroscopic metal electrodes into nanoparticles by the application of high alternating voltages in alkaline electrolyte. While fundamental details were revealed by the aforementioned groups, optimization toward PEMFC catalyst layer applications was still pending. Hence, the following points were addressed in this work, as described below.

I. The synthesis of carbon-supported Pt nanoparticles *via* the top-down route was developed. The focus was set on the simple feasibility (one-step/one-pot synthesis without addition of surfactants and capping agents) and on the fine-tuning of the particle size and shape. Exploiting simple variations of the synthesis parameters (potential amplitude and shape, frequency, electrolyte species and concentration), it was possible to tailor a Pt particle size between less than 2 to more than 10 nm, including a narrow size distribution. Moreover, it was possible to modify the nanoparticle shape (spherical, cubic or disordered) using the developed approach. Except for the variation of the alkali metal cations present in the electrolyte (K, Na, Li, Cs), in all cases the particle size showed linear dependences on the varied parameters.

II. For electrocatalytic applications, the harsh synthesis conditions were exploited to generate concave surface defects, which were confirmed by theoretical and experimental studies to provide an exceptionally good catalytic activity toward the oxygen reduction in acidic media. Microscopic (*e.g.* STEM-HAADF tomography, HR-TEM), spectroscopic, crystallographic (WAXS) and electroanalytical (CV, CO oxidation voltammetry) characterization techniques were employed, which coherently confirmed a defect-rich surface structure.

III. Based on the experimental studies of polycrystalline extended Pt-lanthanide alloy electrodes and corresponding model nanostructures, which suggested an outstanding ORR activity increase compared to pure platinum, the top-down synthesis method was systematically extended to carbon-supported, alloyed Pt_xPr nanocatalysts. Since the synthesis of such Pt-lanthanide alloy nanostructures is a highly sophisticated endeavor, the successful one-pot and one-step top-down synthesis of Pt_xPr/C represents a promising alternative to complex state-of-the-art methods.

IV. The limits of this synthesis method were systematically investigated using Pt_xNi alloy nanoparticles as an example. It was shown that the strongly oxophilic properties of Ni in alkaline media lead to segregation of both elements during the top-down synthesis, resulting in the formation of undesired heterostructures instead of alloyed nanoparticles. However, upon dissolution of Ni, exceptionally well-dispersed pure Pt nanoparticles of small size and PSD were released on the carbon support, owed to the Ni matrix preventing their aggregation. Moreover, simple addition of $CuSO_4$ to the electrolyte prior to Pt nanoparticle synthesis leads to an incorporation of Cu and, in turn, formation of Pt_xCu/C bulk alloy nanoparticles.

V. The activity of these catalysts toward the oxygen reduction reaction was investigated using the rotating disk electrode configuration. Compared to the commercial Pt/C_{TKK}, electrochemical measurements revealed significant activity gains of up to 1.7-times in terms of the mass activity and up to 2.7- and 3.5-times in terms of the specific activity for Pt/C_{TD} and Pt_xPr/C, respectively. The relatively poor mass activity improvement of Pt_xPr/C over Pt/C_{TKK} is owed to the formation of mixed alloy phases, a large particle size and particle aggregation. Finally, the activity of Pt/C_{TD} was evaluated using a single-cell PEMFC configuration, confirming the improved activity of the synthesized catalyst over the commercial catalyst. However, the high current density performance was limited by the low specific surface area of the catalyst (due to particle aggregation).

In accordance, up-scaling of the catalyst batch sizes has to be technically improved in the future experimental studies in order to prevent aggregation of the particles. For instance, the application of strong ultrasonic sources or improved, industrial grade stirring can be considered as promising. Fundamentally, a precise control over the particle shape and size (distribution) has to be further elaborated and screened toward ORR applications. In the case of Pt-lanthanide nanoparticles, particle size reduction has to be attempted, which should strongly benefit their mass activity. Moreover, the universal applicability toward different types of Pt-lanthanide/-rare-earth alloys has to be examined. Importantly, preliminary studies in our group indicate that the method is suitable for the preparation of *e.g.* Pt_xGd nanoparticles. In order to enable the synthesis of different Pt-3d transition metal alloy nanoparticles, the mechanism of Pt_xCu/C electrocatalyst formation has to be unraveled. Moreover, adjustment of the Cu content could be targeted to optimize the mass activity.

References

---

1. Cairns, E. J.; Albertus, P. Batteries for Electric and Hybrid-Electric Vehicles. *Annu. Rev. Chem. Biomol. Eng.* **2010**, *1*, 299-320.

2. Long, Z.; Axsen, J.; Miller, I.; Kormos, C. What Does Tesla Mean to Car Buyers? Exploring the Role of Automotive Brand in Perceptions of Battery Electric Vehicles. *Transp. Res. A* **2019**, *129*, 185-204.

3. Electric Vehicles in Europe: Gearing Up for a New Phase? Amsterdam Round Table Foundation and McKinsey & Company Report, 2014, 14-18. https://www.mckinsey.com/featured-insights/europe/electric-vehicles-in-europe-gearing-up-for-a-new-phase (accessed April 02, 2020).

4. Pereirinha, P. G.; González, M.; Carrilero, I.; Anseán, D.; Alonso, J.; Viera, J. C. Main Trends and Challenges in Road Transportation Electrification. *Trans. Res. Proc.* **2018**, *33*, 235-242.

5. Electric Vehicle Sales: Facts & Figures. Edison Electric Institute Report, 2019, 1-4. https://www.eei.org/issuesandpolicy/electrictransportation/Documents/FINAL_EV_Sales_Update_April2019.pdf (accessed April 01, 2020).

6. Tsakalidis, A.; Thiel, C. Electric Vehicles in Europe from 2010 to 2017: Is Full-Scale Commercialisation Beginning. European Commision JRC Science for Policy Report, 2018, 8-13. https://publications.jrc.ec.europa.eu/repository/bitstream/JRC112745/jrc112745_kjna29401enn.pdf (accessed April 02, 2020).

7. Andwari, A. M.; Pesiridis, A.; Rajoo, S.; Martinez-Botas, R.; Esfahanian, V. A Review of Battery Electric Vehicle Technology and Readiness Levels. *Renew. Sust. Energ. Rev.* **2017**, *78*, 414-430.

8. Pollet, B. G.; Staffell, I.; Shang, J. L. Current Status of Hybrid, Battery and Fuel Cell Electric Vehicles: From Electrochemistry to Market Prospects. *Electrochim. Acta* **2012**, 84, 235-249.

9. Pollet, B. G.; Kocha, S. S.; Staffell, I. Current Status of Automotive Fuel Cells for Sustainable Transport. *Curr. Opin. Electrochem.* **2019**, *16*, 90-95.

10. Staffell, I.; Scamman, D.; Abad, A. V.; Balcombe, P.; Dodds, P. E.; Ekins, P.; Shah, N.; Ward, K. R. The Role of Hydrogen and Fuel Cells in the Global Energy System. *Energy Environ. Sci.* **2019**, *12* (2), 463-491.

11. O'Hayre, R.; Cha, S.-W.; Colella, W. G.; Prinz, F. B. Fuel Cell Fundamentals, 3rd ed.; John Wiley & Sons: Hoboken, 2016, pp 1-23, pp 135-145, pp 273-277, pp 303-317, pp 347-383.

12. von Helmolt, R.; Eberle, U. Fuel Cell Vehicles: Status 2007. *J. Power Sources* **2007**, *165* (2), 833-843.

13. Hyundai Nexo – Technical Specifications. https://www.hyundai.news/fileadmin/de/Pressemappen/Nexo/hyundai-nexo-sep2018-technische-daten.pdf (accessed May 05, 2019).

14. Tesla Model X – Product Page. https://www.tesla.com/de_de/modelx (accessed April 01, 2020).

15. Hong, B. K.; Kim, S. H.; Kim, C. M. Powering the Future through Hydrogen and Polymer Electrolyte Membrane Fuel Cells. *Johnson Matthey Technol. Rev.* **2020**, accepted, DOI: 10.1595/205651319X15744200036826.

16. ADAC Car Test of Tesla Model X 100D. https://www.adac.de/_ext/itr/tests/autotest/AT5619_Tesla_Model_X_100D/Tesla_Model_X_100D.pdf (accessed May 05, 2020).

17. Tesla - Supercharging. https://www.tesla.com/en_GB/support/supercharging?redirect=no (accessed April 02, 2020).

18. EV Charging Station Statistics Germany. https://www.goingelectric.de/stromtankstellen/statistik/Deutschland/ (accessed April 28, 2020).

19. Hydrogen Fueling Stations Directory Germany. https://h2.live/ (accessed April 28, 2020).

20. Kaiwen, L.; Bin, Y.; Tao, Z. Economic Analysis of Hydrogen Production from Steam Reforming Process: A Literature Review. *Energy Sources, Part B: Economics, Planning, and Policy* **2018**, *13* (2), 109-115.

21. Turner, J. A. Sustainable Hydrogen Production. *Science* **2004**, *305* (5686), 972-974.

22. Kumar, S. S.; Himabindu, V. Hydrogen Production by PEM Water Electrolysis – A Review. *Materials Science for Energy Technologies* **2019**, *2* (3), 442-454.

23. Barthelemy, H.; Weber, M.; Barbier, F. Hydrogen Storage: Recent Improvements and Industrial Perspectives. *Int. J. Hydrog. Energy* **2017**, *42* (11), 7254-7262.

24. Murray, P.; Omu, A.; Orehounig, K.; Carmeliet, J. Power-to-Gas for Decentralized Energy Systems: Development of an Energy Hub Model for Hydrogen Storage. Proceedings of the 15th IBPSA Conference, San Francisco, USA, Aug. 7-9, 2017, 1740-1749. http://www.ibpsa.org/proceedings/BS2017/BS2017_460.pdf (accessed April 28, 2020).

25. Teichmann, D.; Arlt, W.; Wasserscheid, P.; Freymann, R. A Future Energy Supply Based on Liquid Organic Hydrogen Carriers (LOHC). *Energy Environ. Sci.* **2011**, *4* (8), 2767-2773.

---

26. Brückner, N.; Obesser, K.; Bösmann, A.; Teichmann, D.; Arlt, W.; Dungs, J.; Wasserscheid, P. Evaluation of Industrially Applied Heat-Transfer Fluids as Liquid Organic Hydrogen Carrier Systems. *ChemSusChem* **2014**, *7* (1), 229-235.

27. Bilgili, M.; Ozbek, A.; Sahin, B.; Kahraman, A. An Overview of Renewable Electric Power Capacity and Progress in New Technologies in the World. *Renew. Sustain. Energy Rev.* **2015**, *49*, 323-334.

28. Yu, F.; Yu, L.; Mishra, I. K.; Yu, Y.; Ren, Z. F.; Zhou, H. Q. Recent Developments in Earth-Abundant and Non-Noble Electrocatalysts for Water Electrolysis. *Mater. Today Phys.* **2018**, *7*, 121-138.

29. Nikolaidis, P.; Poullikkas, A. A Comparative Overview of Hydrogen Production Processes. *Renew. Sust. Energ. Rev.* **2017**, *67*, 597-611.

30. Carmo, M.; Fritz, D. L.; Mergel, J.; Stolten, D. A Comprehensive Review on PEM Water Electrolysis. *Int. J. Hydrog. Energy* **2013**, *38* (12), 4901-4934.

31. Schmidt, O.; Gambhir, A.; Staffell, I.; Hawkes, A.; Nelson, J.; Few, S. Future Cost and Performance of Water Electrolysis: An Expert Elicitation Study. *Int. J. Hydrog. Energy* **2017**, *42* (52), 30470-30492.

32. Thompson, S. T.; James, B. D.; Huya-Kouadio, J. M.; Houchins, C.; DeSantis, D. A.; Ahluwalia, R.; Wilson, A. R.; Kleen, G.; Papageorgopoulos, D. Direct Hydrogen Fuel Cell Electric Vehicle Cost Analysis: System and High-Volume Manufacturing Description, Validation, and Outlook. *J. Power Sources* **2018**, *399*, 304-313.

33. Wilson, A.; Kleen, G.; Papageorgopoulos, D. Fuel Cell Systems Cost - 2017. DOE Hydrogen and Fuel Cells Program Record, 2017, 10. https://www.hydrogen.energy.gov/pdfs/17007_fuel_cell_system_cost_2017.pdf (accessed April 03, 2020).

34. Kongkanand, A.; Mathias, M. F. The Priority and Challenge of High-Power Performance of Low-Platinum Proton-Exchange Membrane Fuel Cells. *J. Phys. Chem. Lett.* **2016**, *7* (7), 1127-1137.

35. Wilberforce, T.; Alaswad, A.; Palumbo, A.; Dassisti, M.; Olabi, A. G. Advances in Stationary and Portable Fuel Cell Applications. *Int. J. Hydrog. Energy* **2016**, *41* (37), 16509-16522.

36. Siqens - Fuel Cell Products. https://www.siqens.de/produkte/ (accessed April 03, 2020).

37. Nikola Motor Company - Products. https://nikolamotor.com/motor (accessed April 03, 2020).

38. Flixbus Press Release: FlixBus plant ersten europäischen Fernbus mit Brennstoffzellenantrieb https://www.flixbus.de/unternehmen/presse/pressemitteilungen/flixbus-plant-fernbus-mit-brennstoffzellenantrieb (accessed April 03, 2020).

39. Mekhilef, S.; Saidur, R.; Safari, A. Comparative Study of Different Fuel Cell Technologies. *Renew. Sust. Energ. Rev.* **2012**, *16* (1), 981-989.

40. US Department of Energy – Comparison of Fuel Cell Technologies. https://www1.eere.energy.gov/hydrogenandfuelcells/fuelcells/pdfs/fc_comparison_chart.pdf (accessed April 03, 2020).

41. Wang, Y.; Chen, K. S.; Mishler, J.; Cho, S. C.; Adroher, X. C. A Review of Polymer Electrolyte Membrane Fuel Cells: Technology, Applications, and Needs on Fundamental Research. *Appl. Energy* **2011**, *88* (4), 981-1007.

42. ElringKlinger Press Release: Fuel Cell Stack Acknowledged as "Best Success Story" https://www.elringklinger.de/sites/default/files/dd_files_paragraph/elringklingerpressrelease2019-11-21.pdf (accessed January 30, 2020).

43. Bosch Products and Services - Fuel Cell Stack. https://www.bosch-mobility-solutions.com/en/products-and-services/passenger-cars-and-light-commercial-vehicles/powertrain-systems/fuel-cell-electric-vehicle/fuel-cell-stack/ (accessed Jan 30, 2020).

44. Zhang, J. (Ed.) PEM Fuel Cell Electrocatalysts and Catalyst Layers: Fundamentals and Applications. Springer: London, 2008, pp 1-17, pp 33-34, pp 149-159, pp 560-563, pp 1011-1015.

45. Li, X.; Sabir, I. Review of Bipolar Plates in PEM Fuel Cells: Flow-Field Designs. *Int. J. Hydrog. Energy* **2005**, *30* (4), 359-371.

46. Shimpalee, S.; Lilavivat, V.; McCrabb, H.; Khunatorn, Y.; Lee, H.-K.; Lee, W.-K.; Weidner, J. W. Investigation of Bipolar Plate Materials for Proton Exchange Membrane Fuel Cells. *Int. J. Hydrog. Energy* **2016,** *41* (31), 13688-13696.

47. Song, Y.; Zhang, C.; Ling, C.-Y.; Han, M.; Yong, R.-Y.; Sun, D.; Chen, J. Review on Current Research of Materials, Fabrication and Application for Bipolar Plate in Proton Exchange Membrane Fuel Cell. *Int. J. Hydrog. Energy* **2019**, accepted, DOI: 10.1016/j.ijhydene.2019.07.231.

48. Bahrebar, S.; Blaabjerg, F.; Wang, H.; Vafamand, N.; Khooban, M. H.; Rastayesh, S.; Zhou, D. A Novel Type-2 Fuzzy Logic for Improved Risk Analysis of Proton Exchange Membrane Fuel Cells in Marine Power Systems Application. *Energies* **2018**, *11* (4), 721.

---

49. Peighambardoust, S. J.; Rowshanzamir, S.; Amjadi, M. Review of the Proton Exchange Membranes for Fuel Cell Applications. *Int. J. Hydog. Energy* **2010**, *35* (17), 9349-9384.

50. Ji, M.; Wei, Z. A Review of Water Management in Polymer Electrolyte Membrane Fuel Cells. *Energies* **2009**, *2* (4), 1057-1106.

51. Francia, C.; Ijeri, V. S.; Specchia, S.; Spinelli, P. Estimation of Hydrogen Crossover through Nafion® Membranes in PEMFCs. *J. Power Sources* **2011**, *196* (4), 1833-1839.

52. Kim, K.-H.; Lee, K.-Y.; Kim, H.-J.; Cho, E.; Lee, S.-Y.; Lim, T.-H.; Yoon, S.-P.; Hwang, S. P.; Jang, J. H. The Effects of Nafion® Ionomer Content in PEMFC MEAs Prepared by a Catalyst-Coated Membrane (CCM) Spraying Method. *Int. J. Hydrog. Energy* **2010**, *35* (5), 2119-2126.

53. Mukundan, R.; Davey, J. R.; Fairweather, J. D.; Spernjak, D.; Spendelow, J.; Hussey, D. S.; Jacobson, D. L.; Wilde, P.; Schweiss, R.; Borup, R. L. Effect of Hydrophilic Treatment of Microporous Layer on Fuel Cell Performance. *ECS Trans.* **2010**, *33* (1), 1109-1114.

54. Cindrella, L.; Kannan, A. M.; Lin, J. F.; Saminathan, K.; Ho, Y.; Lin, C. W.; Wertz, J. Gas Diffusion Layer for Proton Exchange Membrane Fuel Cells - A Review. *J. Power Sources* **2009**, *194* (1), 146-160.

55. Yoshida, T.; Kojima, K. Toyota MIRAI Fuel Cell Vehicle and Progress Toward a Future Hydrogen Society. *Electrochem. Soc. Interface* **2015**, *24* (2), 45-49.

56. Lázaro, M. J.; Calvillo, L.; Celorrio, V.; Pardo, J. I.; Perathoner, S.; Moliner, R. Study and Application of Carbon Black Vulcan XC-72R in Polymeric Electrolyte Fuel Cells. In: Sanders, I. J.; Peeten, T. L. (Eds) Carbon Black: Production, Properties, and Uses. Nova Science Publishers: Hauppauge, 2011, pp 41-45.

57. Walter, C.; Kummer, K.; Vyalikh, D.; Brüser, V.; Quade, A.; Weltmann, K. D. Using a Dual Plasma Process to Produce Cobalt-Polypyrrole Catalysts for the Oxygen Reduction Reaction in Fuel Cells: I. Characterization of the Catalytic Activity and Surface Structure. *J. Electrochem. Soc.* **2012**, *159* (8), F494-F500.

58. Harzer, G. S.; Orfanidi, A.; El-Sayed, H.; Madkikar, P.; Gasteiger, H. A. Tailoring Catalyst Morphology Towards High Performance for Low Pt Loaded PEMFC Cathodes. *J. Electrochem. Soc.* **2018**, *165* (10), F770-F779.

59. Yarlagadda, V.; Carpenter, M. K.; Moylan, T. E.; Kukreja, R. S.; Koestner, R.; Gu, W.; Thompson, L.; Kongkanand, A. Boosting Fuel Cell Performance with Accessible Carbon Mesopores. *ACS Energy Lett.* **2018**, *3* (3), 618-621.

60. Orfanidi, A.; Madkikar, P.; El-Sayed, H. A.; Harzer, G. S.; Kratky, T.; Gasteiger, H. A. The Key to High Performance Low Pt Loaded Electrodes. *J. Electrochem. Soc.* **2017**, *164* (4), F418-F426.

61. Ott, S.; Orfanidi, A.; Schmies, H.; Anke, B.; Nong, H. N.; Hübner, J.; Gernert, U.; Gliech, M.; Lerch, M.; Strasser, P. Ionomer Distribution Control in Porous Carbon-Supported Catalyst Layers for High-Power and Low Pt-Loaded Proton Exchange Membrane Fuel Cells. *Nat. Mater.* **2020**, *19* (1), 77-85.

62. Klingele, M.; Breitwieser, M.; Zengerle, R.; Thiele, S. Direct Deposition of Proton Exchange Membranes Enabling High Performance Hydrogen Fuel Cells. *J. Mater. Chem. A* **2015**, *3* (21), 11239-11245.

63. Simon, C.; Hasché, F.; Gasteiger, H. A. Influence of the Gas Diffusion Layer Compression on the Oxygen Transport in PEM Fuel Cells at High Water Saturation Levels. *J. Electrochem. Soc.* **2017**, *164* (6), F591-F599.

64. Schulenburg, H.; Schwanitz, B.; Linse, N.; Scherer, G. G.; Wokaun, A.; Krbanjevic, J.; Grothausmann, R.; Manke, I. 3D Imaging of Catalyst Support Corrosion in Polymer Electrolyte Fuel Cells. *J. Phys. Chem. C* **2011**, *115* (29), 14236-14243.

65. Neyerlin, K. C.; Gu, W.; Jorne, J.; Clark, A.; Gasteiger, H. A. Cathode Catalyst Utilization for the ORR in a PEMFC Analytical Model and Experimental Validation. *J. Electrochem. Soc.* **2007**, *15*4 (2), B279-B287.

66. Liu, Y.; Murphy, M. W.; Baker, D. R.; Gu, W.; Ji, C.; Jorne, J.; Gasteiger, H. A. Proton Conduction and Oxygen Reduction Kinetics in PEM Fuel Cell Cathodes: Effects of Ionomer-to-Carbon Ratio and Relative Humidity. *J. Electrochem. Soc.* **2009**, *156* (8), B970-B980.

67. Amirinejad, M.; Rowshanzamir, S.; Eikani, M. H. Effects of Operating Parameters on Performance of a Proton Exchange Membrane Fuel Cell. *J. Power Sources* **2006**, *161* (2), 872-875.

68. Martens, S.; Asen, L.; Ercolano, G.; Dionigi, F.; Zalitis, C.; Hawkins, A.; Bonastre, A. M.; Seidl, L.; Knoll, A. C.; Sharman, J.; Strasser, P.; Jones, D.; Schneider, O. A Comparison of Rotating Disc Electrode, Floating Electrode Technique and Membrane Electrode Assembly Measurements for Catalyst Testing. *J. Power Sources* **2018**, *392*, 274-284.

69. Wan, Z.; Chang, H.; Shu, S.; Wang, Y.; Tang, H. A Review on Cold Start of Proton Exchange Membrane Fuel Cells. *Energies* **2014**, *7* (5), 3179-3203.

70. Weber, A. Z.; Borup, R. L.; Darling, R. M.; Das, P. K.; Dursch, T. J.; Gu, W.; Harvey, D.; Kusoglu, A.; Litster, S.; Mench, M. M.; Mukundan, R.; Owejan, J. P.; Pharoah, J. G.; Secanell, M.;

Zenyuk, I. V. A Critical Review of Modeling Transport Phenomena in Polymer-Electrolyte Fuel Cells. *J. Electrochem. Soc.* **2014**, *161* (12), F1254-F1299.

71. Wang, J. X.; Springer, T. E.; Adzic, R. R. Dual-Pathway Kinetic Equation for the Hydrogen Oxidation Reaction on Pt Electrodes. *J. Electrochem. Soc.* **2006**, *153* (9), A1732-A1740.

72. Neyerlin, K. C.; Gu, W.; Jorne, J.; Gasteiger, H. A. Study of the Exchange Current Density for the Hydrogen Oxidation and Evolution Reactions. *J. Electrochem. Soc.* **2007**, *154* (7), B631-B635.

73. Durst, J.; Siebel, A.; Simon, C.; Hasché, F.; Herranz, J.; Gasteiger, H. A. New Insights into the Electrochemical Hydrogen Oxidation and Evolution Reaction Mechanism. *Energy Environ. Sci.* **2014**, *7* (7), 2255-2260.

74. Zalitis, C. M.; Sharman, J.; Wright, E.; Kucernak, A. R. Properties of the Hydrogen Oxidation Reaction on Pt/C Catalysts at Optimised High Mass Transport Conditions and its Relevance to the Anode Reaction in PEFCs and Cathode Reactions in Electrolysers. *Electrochim. Acta* **2015**, *176*, 763-776.

75. Gasteiger, H. A.; Panels, J. E.; Yan, S. G. Dependence of PEM Fuel Cell Performance on Catalyst Loading. *J. Power Sources* **2004**, *127* (1-2), 162-171.

76. Sheng, W.; Gasteiger, H. A.; Shao-Horn, Y. Hydrogen Oxidation and Evolution Reaction Kinetics on Platinum: Acid vs Alkaline Electrolytes. *J. Electrochem. Soc.* **2010**, *157* (11), B1529-B1536.

77. James, B. D.; Huya-Kouadio, J. M.; Houchins, C.; DeSantis, D. A. Mass Production Cost Estimation of Direct H_2 PEM Fuel Cell Systems for Transportation Applications: 2018 Update. Strategic Analysis Inc.: Arlington, 2018, p 35. https://www.energy.gov/sites/prod/files/2019/12/f70/fcto-sa-2018-transportation-fuel-cell-cost-analysis.pdf (accessed April 28, 2020).

78. Cheng, X.; Shi, Z.; Glass, N.; Zhang, L.; Zhang, J.; Song, D.; Liu, Z.-S.; Wang, H.; Shen, J. A Review of PEM Hydrogen Fuel Cell Contamination: Impacts, Mechanisms, and Mitigation. *J. Power Sources* **2007**, *165* (2), 739-756.

79. Scura, F.; Barbieri, G.; Drioli, E. H_2 for PEM-FC: Effect of CO in the Purification by Means of Pd-Based Membranes. *Desalination* **2006**, *200* (1-3), 239-241.

80. Emerson, S.; Magdefrau, N.; She, Y.; Thibaud-Erkey, C. Advanced Palladium Membrane Scale-up for Hydrogen Separation. United Technologies Research Center: East Hartford, 2012, pp 1-53. https://www.osti.gov/servlets/purl/1063878.

81. Baschuk, J. J.; Li, X. Carbon Monoxide Poisoning of Proton Exchange Membrane Fuel Cells. *Int. J. Energy Res.* **2001**, *25* (8), 695-713.

82. Lee, S. J.; Mukerjee, S.; Ticianelli, E. A.; McBreen, J. Electrocatalysis of CO Tolerance in Hydrogen Oxidation Reaction in PEM Fuel Cells. *Electrochim. Acta* **1999**, *44* (19), 3283-3293.

83. Divisek, J.; Oetjen, H.-F.; Peinecke, V.; Schmidt, V. M.; Stimming, U. Components for PEM Fuel Cell Systems Using Hydrogen and CO Containing Fuels. *Electrochim. Acta* **1998**, *43* (24), 3811-3815.

84. Cao, L.; Liu, W.; Luo, Q.; Yin, R.; Wang, B.; Weissenrieder, J.; Soldemo, M.; Yan, H.; Lin, Y.; Sun, Z.; Ma, C.; Zhang, W.; Chen, S.; Wang, H.; Guan, Q.; Yao, T.; Wei, S.; Yang, J.; Lu, J. Atomically Dispersed Iron Hydroxide Anchored on Pt for Preferential Oxidation of CO in H_2. *Nature* **2019**, *565* (7741), 631-635.

85. Damjanovic, A.; Brusic, V. Electrode Kinetics of Oxygen Reduction on Oxide-Free Platinum Electrodes. *Electrochim. Acta* **1967**, *12* (6), 615-628.

86. Sepa, D. B.; Vojnovic, M. V.; Damjanovic, A. Reaction Intermediates as a Controlling Factor in the Kinetics and Mechanism of Oxygen Reduction at Platinum Electrodes. *Electrochim. Acta* **1981**, *26* (6), 781-793.

87. Anastasijević, N. A.; Vesović, V.; Adžić, R. R. Determination of the Kinetic Parameters of the Oxygen Reduction Reaction Using the Rotating Ring-Disk Electrode: Part I. Theory. *J. Electroanal. Chem. Interf. Electrochem.* **1987**, *229* (1-2), 305-316.

88. Anastasijević, N. A.; Vesović, V.; Adžić, R. R. Determination of the Kinetic Parameters of the Oxygen Reduction Reaction Using the Rotating Ring-Disk Electrode: Part II. Applications. *J. Electroanal. Chem. Interf. Electrochem.* **1987**, *229* (1-2), 317-325.

89. Antoine, O.; Bultel, Y.; Durand, R. Oxygen Reduction Reaction Kinetics and Mechanism on Platinum Nanoparticles Inside Nafion®. *J. Electroanal. Chem.* **2001**, *499* (1), 85-94.

90. Wroblowa, H. S.; Pan, Y.-C.; Razumney, G. Electroreduction of Oxygen: A New Mechanistic Criterion. *J. Electroanal. Chem. Interf. Electrochem.* **1976**, *69* (2), 195-201.

91. Nørskov, J. K.; Rossmeisl, J.; Logadottir, A.; Lindqvist, L.; Kitchin, J. R., Bligaard, T.; Jónsson, H. Origin of the Overpotential for Oxygen Reduction at a Fuel-Cell Cathode. *J. Phys. Chem. B* **2004**, *108* (46), 17886-17892.

92. Katsounaros, I.; Schneider, W. B.; Meier, J. C.; Benedikt, U.; Biedermann, P. U.; Auer, A. A.; Mayrhofer, K. J. J. Hydrogen Peroxide Electrochemistry on Platinum: Towards Understanding the Oxygen Reduction Reaction Mechanism. *Phys. Chem. Chem. Phys.* **2012**, *14* (20), 7384-7391.

93. Endoh, E.; Terazono, S.; Widjaja, H.; Takimoto, Y. Degradation Study of MEA for PEMFCs Under Low Humidity Conditions. *Electrochem. Solid-State Lett.* **2004**, *7* (7), A209-A211.

94. Maass, S.; Finsterwalder, F.; Frank, G.; Hartmann, R.; Merten, C. Carbon Support Oxidation in PEM Fuel Cell Cathodes. *J. Power Sources* **2008**, *176* (2), 444-451.

95. Markovic, N. M.; Gasteiger, H. A.; Ross, P. N. Jr. Oxygen Reduction on Platinum Low-Index Single-Crystal Surfaces in Sulfuric Acid Solution: Rotating Ring-Pt(hkl) Disk Studies. *J. Phys. Chem.* **1995**, *99* (11), 3411-3415.

96. Inaba, M.; Yamada, H.; Tokunaga, J.; Matsuzawa, K.; Hatanaka, A.; Tasaka, A. Hydrogen Peroxide Formation as a Degradation Factor of Polymer Electrolyte Fuel Cells. *ECS Trans.* **2006**, *1* (8), 315-322.

97. Viswanathan, V.; Hansen, H. A.; Rossmeisl, J.; Nørskov, J. K. Unifying the $2e^-$ and $4e^-$ Reduction of Oxygen on Metal Surfaces. *J. Phys. Chem. Lett.* **2012**, *3* (20), 2948-2951.

98. Greeley, J.; Stephens, I. E. L.; Bondarenko, A. S.; Johansson, T. P.; Hansen, H. A.; Jaramillo, T. F.; Rossmeisl, J.; Chorkendorff, I.; Nørskov, J. K. Alloys of Platinum and Early Transition Metals as Oxygen Reduction Electrocatalysts. *Nat. Chem.* **2009**, *1* (7), 552-556.

99. Stephens, I. E. L.; Bondarenko, A. S.; Grønbjerg, U.; Rossmeisl, J.; Chorkendorff, I. Understanding the Electrocatalysis of Oxygen Reduction on Platinum and its Alloys. *Energy Environ. Sci.* **2012**, *5* (5), 6744-6762.

100. Kulkarni, A.; Siahrostami, S.; Patel, A.; Nørskov, J. K. Understanding Catalytic Activity Trends in the Oxygen Reduction Reaction. *Chem. Rev.* **2018**, *118* (5), 2302-2312.

101. Bandarenka, A. S.; Hansen, H. A.; Rossmeisl, J.; Stephens, I. E. L. Elucidating the Activity of Stepped Pt Single Crystals for Oxygen Reduction. *Phys. Chem. Chem. Phys.* **2014**, *16* (27), 13625-13629.

102. Gasteiger, H. A.; Kocha, S. S.; Sompalli, B.; Wagner, F. T. Activity Benchmarks and Requirements for Pt, Pt-Alloy, and Non-Pt Oxygen Reduction Catalysts for PEMFCs. *Appl. Catal. B* **2005**, *56* (1-2), 9-35.

103. Markovic, N.; Gasteiger, H.; Ross, P. N. Kinetics of Oxygen Reduction on Pt(hkl) Electrodes: Implications for the Crystallite Size Effect with Supported Pt Electrocatalysts. *J. Electrochem. Soc.* **1997**, *144* (5), 1591-1597.

104. Perez-Alonso, F. J.; McCarthy, D. N.; Nierhoff, A.; Hernandez-Fernandez, P.; Strebel, C.; Stephens, I. E. L.; Nielsen, J. H.; Chorkendorff, I. The Effect of Size on the Oxygen

Electroreduction Activity of Mass-Selected Platinum Nanoparticles. *Angew. Chem. Int. Ed.* **2012**, *51* (19), 4641-4643.

105. Shao, M.; Peles, A.; Shoemaker, K. Electrocatalysis on Platinum Nanoparticles: Particle Size Effect on Oxygen Reduction Reaction Activity. *Nano Lett.* **2011**, *11* (9), 3714-3719.

106. Shinozaki, K.; Morimoto, Y.; Pivovar, B. S.; Kocha, S. S. Re-Examination of the Pt Particle Size Effect on the Oxygen Reduction Reaction for Ultrathin Uniform Pt/C Catalyst Layers Without Influence from Nafion. *Electrochim. Acta* **2016**, *213*, 783-790.

107. Nesselberger, M.; Ashton, S.; Meier, J. C.; Katsounaros, I.; Mayrhofer, K. J. J.; Arenz, M. The Particle Size Effect on the Oxygen Reduction Reaction Activity of Pt Catalysts: Influence of Electrolyte and Relation to Single Crystal Models. *J. Am. Chem. Soc.* **2011**, *133* (43), 17428-17433.

108. Perez, J.; Paganin, V. A.; Antolini, E. Particle Size Effect for Ethanol Electro-Oxidation on Pt/C Catalysts in Half-Cell and in a Single Direct Ethanol Fuel Cell. *J. Electroanal. Chem.* **2011**, *654* (1-2), 108-115.

109. Meier, J. C.; Galeano, C.; Katsounaros, I.; Witte, J.; Bongard, H. J.; Topalov, A. A.; Baldizzone, C.; Mezzavilla, S.; Schüth, F.; Mayrhofer, K. J. J. Design Criteria for Stable Pt/C Fuel Cell Catalysts. *Beilstein J. Nanotechnol.* **2014**, *5* (1), 44–67.

110. Bi, W.; Fuller, T. F. Temperature Effects on PEM Fuel Cells Pt/C Catalyst Degradation. *J. Electrochem. Soc.* **2008**, *155* (2), B215-B221.

111. Dubau, L.; Maillard, F. Unveiling the Crucial Role of Temperature on the Stability of Oxygen Reduction Reaction Electrocatalysts. *Electrochem. Commun.* **2016**, *63*, 65-69.

112. Durst, J.; Chatenet, M.; Maillard, F. Impact of Metal Cations on the Electrocatalytic Properties of Pt/C Nanoparticles at Multiple Phase Interfaces. Phys. Chem. Chem. Phys. **2012,** *14* (37), 13000-13009.

113. Asset, T.; Chattot, R.; Fontana, M.; Mercier-Guyon, B.; Job, N.; Dubau, L.; Maillard, F. A Review on Recent Developments and Prospects for the Oxygen Reduction Reaction on Hollow Pt-Alloy Nanoparticles. *ChemPhysChem* **2018**, *19* (13), 1552-1567.

114. Borup, R. L.; More, K. L.; Myers, D. J. FC-PAD: Fuel Cell Performance and Durability Consortium Update to USCAR Analysis of Toyota Mirai Components Provided by USCAR. USCAR Conference, Southfield, USA, May 11, 2018, 61-62. https://permalink.lanl.gov/object/tr?what=info:lanl-repo/lareport/LA-UR-18-24454 (accessed April 28, 2020).

---

115. Papadias, D. D.; Ahluwalia, R. K.; Kariuki, N.; Myers, D.; More, K. L.; Cullen, D. A.; Sneed, B. T.; Neyerlin, K. C.; Mukundan, R.; Borup, R. L. Durability of Pt-Co Alloy Polymer Electrolyte Fuel Cell Cathode Catalysts under Accelerated Stress Tests. *J. Electrochem. Soc.* **2018**, *165* (6), F3166-F3177.

116. Xiong, L.; Kannan, A. M.; Manthiram, A. Pt–M (M= Fe, Co, Ni and Cu) Electrocatalysts Synthesized by an Aqueous Route for Proton Exchange Membrane Fuel Cells. *Electrochem. Commun.* **2002**, *4* (11), 898-903.

117. Stamenkovic, V. R.; Fowler, B.; Mun, B. S.; Wang, G.; Ross, P. N.; Lucas, C. A.; Marković, N. M. Improved Oxygen Reduction Activity on Pt_3Ni (111) via Increased Surface Site Availability. *Science* **2007**, *315* (5811), 493-497.

118. Zhang, J.; Yang, H.; Fang, J.; Zou, S. Synthesis and Oxygen Reduction Activity of Shape-Controlled Pt_3Ni Nanopolyhedra. *Nano Lett.* **2010**, *10* (2), 638-644.

119 . Oezaslan, M.; Hasché, F.; Strasser, P. $PtCu_3$, PtCu and Pt_3Cu Alloy Nanoparticle Electrocatalysts for Oxygen Reduction Reaction in Alkaline and Acidic Media. *J. Electrochem. Soc.* **2012**, *159* (4), B444-B454.

120. Oezaslan, M.; Strasser, P. Activity of Dealloyed $PtCo_3$ and $PtCu_3$ Nanoparticle Electrocatalyst for Oxygen Reduction Reaction in Polymer Electrolyte Membrane Fuel Cell. *J. Power Sources* **2011**, *196* (12), 5240-5249.

121. Han, B.; Carlton, C. E.; Kongkanand, A.; Kukreja, R. S.; Theobald, B. R.; Gan, L.; O'Malley R.; Strasser, P.; Wagner, F. T.; Shao-Horn, Y. Record Activity and Stability of Dealloyed Bimetallic Catalysts for Proton Exchange Membrane Fuel Cells. *Energy Environ. Sci.* **2015**, *8* (1), 258-266.

122. Strasser, P.; Koh, S.; Anniyev, T.; Greeley, J.; More, K.; Yu, C.; Liu, Z.; Kaya, S.; Nordlund, D.; Ogasawara, H.; Toney, M. F.; Nilsson, A. Lattice-Strain Control of the Activity in Dealloyed Core–Shell Fuel Cell Catalysts. *Nat. Chem.* **2010**, *2* (6), 454-460.

123. Stamenković, V.; Schmidt, T. J.; Ross, P. N.; Marković, N. M. Surface Composition Effects in Electrocatalysis: Kinetics of Oxygen Reduction on Well-Defined Pt_3Ni and Pt_3Co Alloy Surfaces. *J. Phys. Chem. B* **2002**, *106* (46), 11970-11979.

124. Stamenkovic, V. R.; Mun, B. S.; Mayrhofer, K. J. J.; Ross, P. N.; Markovic, N. M. Effect of Surface Composition on Electronic Structure, Stability, and Electrocatalytic Properties of Pt-Transition Metal Alloys: Pt-Skin Versus Pt-Skeleton Surfaces. *J. Am. Chem. Soc.* **2006**, *128* (27), 8813-8819.

---

125. Mavrikakis, M.; Hammer, B.; Nørskov, J. K. Effect of Strain on the Reactivity of Metal Surfaces. *Phys. Rev. Lett.* **1998**, *81* (13), 2819-2822.

126. Kitchin, J. R.; Nørskov, J. K.; Barteau, M. A.; Chen, J. G. Role of Strain and Ligand Effects in the Modification of the Electronic and Chemical Properties of Bimetallic Surfaces. *Phys. Rev. Lett.* **2004**, *93* (15), 156801.

127. Deng, Y. J.; Tripkovic, V.; Rossmeisl, J.; Arenz, M. Oxygen Reduction Reaction on Pt Overlayers Deposited onto a Gold Film: Ligand, Strain, and Ensemble Effect. *ACS Catal.* **2016**, *6* (2), 671-676.

128. Bligaard, T.; Nørskov, J. K. Ligand Effects in Heterogeneous Catalysis and Electrochemistry. *Electrochim. Acta* **2007**, *52* (18), 5512-5516.

129. Stamenkovic, V.; Mun, B. S.; Mayrhofer, K. J. J.; Ross, P. N.; Markovic, N. M.; Rossmeisl, J.; Greeley, J.; Nørskov, J. K. Changing the Activity of Electrocatalysts for Oxygen Reduction by Tuning the Surface Electronic Structure. *Angew. Chem. Int. Ed.* **2006**, *45* (18), 2897-2901.

130. Kitchin, J. R.; Miller, S. D.; Sholl, D. S. Density Functional Theory Studies of Alloys in Heterogeneous Catalysis. In: Hinchliffe, A. (Ed.) Chemical Modelling: Applications and Theory (Vol. 5). RSC Publishing: Cambridge, 2008, pp 150-181.

131. Cao, L.; Mueller, T. Rational Design of Pt_3Ni Surface Structures for the Oxygen Reduction Reaction. *J. Phys. Chem. C* **2015**, *119* (31), 17735−17747.

132. Wang, Y.-J.; Zhao, N.; Fang, B.; Li, H.; Bi, X. T.; Wang, H. Carbon-Supported Pt-Based Alloy Electrocatalysts for the Oxygen Reduction Reaction in Polymer Electrolyte Membrane Fuel Cells: Particle Size, Shape, and Composition Manipulation and Their Impact to Activity. *Chem. Rev.* **2015**, *115* (9), 3433-3467.

133. Chattot, R.; Asset, T.; Bordet, P.; Drnec, J.; Dubau, L.; Maillard, F. Beyond Strain and Ligand Effects: Microstrain-Induced Enhancement of the Oxygen Reduction Reaction Kinetics on Various PtNi/C Nanostructures. *ACS Catal.* **2017**, *7* (1), 398–408.

134. Henning, S.; Kühn, L.; Herranz, J.; Durst, J.; Binninger, T.; Nachtegaal, M.; Werheid, M.; Liu, W.; Adam, M.; Kaskel, S.; Eychmüller, A.; Schmidt, T. J. Pt-Ni Aerogels as Unsupported Electrocatalysts for the Oxygen Reduction Reaction. *J. Electrochem. Soc.* **2016**, *163* (9), F998-F1003.

135. Chen, S.; Sheng, W.; Yabuuchi, N.; Ferreira, P. J.; Allard, L. F.; Shao-Horn, Y. Origin of Oxygen Reduction Reaction Activity on "Pt_3Co" Nanoparticles: Atomically Resolved Chemical Compositions and Structures. *J. Phys. Chem. C* **2009**, *113* (3), 1109-1125.

136. Hernandez-Fernandez, P.; Masini, F.; McCarthy, D. N.; Strebel, C. E.; Friebel, D.; Deiana, D.; Malacrida, P.; Nierhoff, A.; Bodin, A.; Wise, A. M.; Nielsen, J. H.; Hansen, T. W.; Nilsson, A.; Stephens, I. E. L.; Chorkendorff, I. Mass-Selected Nanoparticles of Pt_xY as Model Catalysts for Oxygen Electroreduction. *Nat. Chem.* **2014**, *6* (8), 732-738.

137. Velázquez-Palenzuela, A.; Masini, F.; Pedersen, A. F.; Escudero-Escribano, M.; Deiana, D.; Malacrida, P.; Hansen, T. W.; Friebel, D.; Nilsson, A.; Stephens, I. E. L.; Chorkendorff, I. The Enhanced Activity of Mass-Selected Pt_xGd Nanoparticles for Oxygen Electroreduction. *J. Catal.* **2015**, *328*, 297-307.

138. Cui, C.; Gan, L.; Li, H.-H.; Yu, S.-H.; Heggen, M.; Strasser, P. Octahedral PtNi Nanoparticle Catalysts: Exceptional Oxygen Reduction Activity by Tuning the Alloy Particle Surface Composition. *Nano Lett.* **2012**, *12* (11), 5885-5889.

139. Chen, C.; Kang, Y.; Huo, Z.; Zhu, Z.; Huang, W.; Xin, H. L.; Snyder, J. D.; Li, D.; Herron, J. A.; Mavrikakis, M.; Chi, M.; More, K. L.; Li, Y.; Markovic, N. M.; Somorjai, G. A.; Yang, P.; Stamenkovic, V. R. Highly Crystalline Multimetallic Nanoframes with Three-Dimensional Electrocatalytic Surfaces. *Science* **2014**, *343* (6117), 1339-1343.

140. Čolić, V.; Bandarenka, A. S. Pt Alloy Electrocatalysts for the Oxygen Reduction Reaction: From Model Surfaces to Nanostructured Systems. *ACS Catal.* **2016**, *6* (8), 5378-5385.

141. Escudero-Escribano, M.; Malacrida, P.; Hansen, M. H.; Vej-Hansen, U. G.; Velázquez-Palenzuela, A.; Tripkovic, V.; Schiøtz, J.; Rossmeisl, J.; Stephens, I. E. L.; Chorkendorff, I. Tuning the Activity of Pt Alloy Electrocatalysts by Means of the Lanthanide Contraction. *Science* **2016**, *352* (6281), 73−76.

142. Escudero-Escribano, M.; Verdaguer-Casadevall, A.; Malacrida, P.; Grønbjerg, U.; Knudsen, B. P.; Jepsen, A. K.; Rossmeisl, J.; Stephens, I. E. L.; Chorkendorff, I. Pt_5Gd as a Highly Active and Stable Catalyst for Oxygen Electroreduction. *J. Am. Chem. Soc.* **2012**, *134* (4), 16476-16479.

143. Garlyyev, B.; Pohl, M. D.; Čolić, V.; Liang, Y.; Butt, F. K.; Holleitner, A.; Bandarenka, A. S. High Oxygen Reduction Reaction Activity of Pt_5Pr Electrodes in Acidic Media. *Electrochem. Commun.* **2018**, *88*, 10-14.

144. Roy, C.; Knudsen, B. P.; Pedersen, C. M.; Velázquez-Palenzuela, A.; Christensen, L. H.; Damsgaard, C. D.; Stephens, I. E. L.; Chorkendorff, I. Scalable Synthesis of Carbon-Supported Platinum-Lanthanide and -Rare-Earth Alloys for Oxygen Reduction. *ACS Catal.* **2018**, *8* (3), 2071-2080.

---

145. Kepp, K. P. A Quantitative Scale of Oxophilicity and Thiophilicity. *Inorg. Chem.* **2016**, *55* (18), 9461-9470.

146. Calle-Vallejo, F.; Tymoczko, J.; Colic, V.; Vu, Q. H.; Pohl, M. D.; Morgenstern, K.; Loffreda, D.; Sautet, P.; Schuhmann, W.; Bandarenka, A. S. Finding Optimal Surface Sites on Heterogeneous Catalysts by Counting Nearest Neighbors. *Science* **2015**, *350* (6257), 185-189.

147. Calle-Vallejo, F.; Pohl, M. D.; Reinisch, D.; Loffreda, D.; Sautet, P.; Bandarenka, A. S. Why Conclusions from Platinum Model Surfaces Do Not Necessarily Lead to Enhanced Nanoparticle Catalysts for the Oxygen Reduction Reaction. *Chem. Sci.* **2017**, *8* (3), 2283-2289.

148. Rück, M.; Bandarenka, A.; Calle-Vallejo, F.; Gagliardi, A. Oxygen Reduction Reaction: Rapid Prediction of Mass Activity of Nanostructured Platinum Electrocatalysts. *J. Phys. Chem. Lett.* **2018**, *9* (15), 4463-4468.

149. Rück, M.; Bandarenka, A.; Calle-Vallejo, F.; Gagliardi, A. Fast Identification of Optimal Pure Platinum Nanoparticle Shapes and Sizes for Efficient Oxygen Electroreduction. *Nanoscale Adv.* **2019**, *1* (8), 2901-2909.

150. Rück, M.; Garlyyev, B.; Mayr, F.; Bandarenka, A. S.; Gagliardi, A. Oxygen Reduction Activities of Strained Platinum Core-Shell Electrocatalysts Predicted by Machine Learning. *J. Phys. Chem. Lett.* **2020**, *11* (5), 1773-1780.

151. Li, M.; Zhao, Z.; Cheng, T.; Fortunelli, A.; Chen, C.-Y.; Yu, R.; Zhang, Q.; Gu, L.; Merinov, B. V.; Lin, Z.; Zhu, E.; Yu, T.; Jia, Q.; Guo, J.; Zhang, L.; Goddard III, W. A.; Huang, Y., Duan, X. Ultrafine Jagged Platinum Nanowires Enable Ultrahigh Mass Activity for the Oxygen Reduction Reaction. *Science* **2016**, *354* (6318), 1414-1419.

152. Dubau, L.; Asset, T.; Chattot, R.; Bonnaud, C.; Vanpeene, V.; Nelayah, J.; Maillard, F. Tuning the Performance and the Stability of Porous Hollow PtNi/C Nanostructures for the Oxygen Reduction Reaction. *ACS Catal.* **2015**, *5* (9), 5333-5341.

153. Dubau, L.; Nelayah, J.; Moldovan, S.; Ersen, O.; Bordet, P.; Drnec, J.; Asset, T.; Chattot, R.; Maillard, F. Defects do Catalysis: CO Monolayer Oxidation and Oxygen Reduction Reaction on Hollow PtNi/C Nanoparticles. *ACS Catal.* **2016**, *6* (7), 4673-4684.

154. Chattot, R.; Le Bacq, O.; Beermann, V.; Kühl, S.; Herranz, J.; Henning, S.; Kühn, L.; Asset, T.; Guétaz, L.; Renou, G.; Drnec, J.; Bordet, P.; Pasturel, A.; Eychmüller, A.; Schmidt, T. J.; Strasser, P.; Dubau, L.; Maillard, F. Surface Distortion as a Unifying Concept and Descriptor in Oxygen Reduction Reaction Electrocatalysis. *Nat. Mater.* **2018**, *17* (9), 827–833.

155. Lebedeva, N. P.; Koper, M. T. M.; Feliu, J. M.; van Santen, R. A. Role of Crystalline Defects in Electrocatalysis: Mechanism and Kinetics of CO Adlayer Oxidation on Stepped Platinum Electrodes. *J. Phys. Chem. B* **2002**, *106* (50), 12938-12947.

156. Chen, A.; Holt-Hindle, P. Platinum-Based Nanostructured Materials: Synthesis, Properties, and Applications. *Chem. Rev.* **2010**, *110* (6), 3767–3804.

157. Bredig, G.; Haber, F. Ueber Zerstäubung von Metallkathoden bei der Elektrolyse mit Gleichstrom. *Ber. Dtsch. Chem. Ges.* **1898**, *31* (3), 2741– 2752.

158. Liu, J.; Huang, W.; Chen, S.; Hu, S.; Liu, F.; Li, Z. Facile Electrochemical Dispersion of Bulk Rh into Hydrosols. *Int. J. Electrochem. Sci.* **2009**, *4* (9), 1302-1308.

159. Huang, W.; Chen, S.; Zheng, J.; Li, Z. Facile Preparation of Pt Hydrosols by Dispersing Bulk Pt with Potential Perturbations. *Electrochem. Commun.* **2009**, *11* (2), 469– 472.

160. Chen, X.; Chen, S.; Huang, W.; Zheng, J.; Li, Z. Facile Preparation of Bi Nanoparticles by Novel Cathodic Dispersion of Bulk Bismuth Electrodes. *Electrochim. Acta* **2009**, *54* (28), 7370-7373.

161. Huang, W.; Fu, L.; Yang, Y.; Hu, S.; Li, C.; Li, Z. Simultaneous Fabrications of Nanoparticles and 3D Porous Films of Sn or Pb from Pure Electrodes. *Electrochem. Solid-State Lett.* **2010**, *13* (5), K46-K48.

162. Yanson, A. I.; Rodriguez, P.; Garcia-Araez, N.; Mom, R. V.; Tichelaar, F. D.; Koper, M. T. M. Cathodic Corrosion: A Quick, Clean, and Versatile Method for the Synthesis of Metallic Nanoparticles. *Angew. Chem. Int. Ed.* **2011**, *50* (28), 6346-6350.

163. Kromer, M. L.; Monzó, J.; Lawrence, M. J.; Kolodziej, A.; Gossage, Z. T.; Simpson, B. H.; Morandi, S.; Yanson, A.; Rodríguez-López, J.; Rodríguez, P. High Throughput Preparation of Metal Oxide Nanocrystals by Cathodic Corrosion and Their Use as Active Photocatalysts. *Langmuir* **2017**, *33* (46), 13295-13302.

164. Rodriguez, P.; Tichelaar, F. D.; Koper, M. T. M.; Yanson, A. I. Cathodic Corrosion as a Facile and Effective Method to Prepare Clean Metal Alloy Nanoparticles. *J. Am. Chem. Soc.* **2011**, *133* (44), 17626-17629.

165. Hersbach, T. J. P.; Kortlever, R.; Lehtimäki, M.; Krtil, P.; Koper, M. T. M. Local Structure and Composition of PtRh Nanoparticles Produced through Cathodic Corrosion. *Phys. Chem. Chem. Phys.* **2017**, *19* (16), 10301-10308.

166. Feng, J.; Chen, D.; Sediq, A. S.; Romeijn, S.; Tichelaar, F. D.; Jiskoot, W.; Yang, J.; Koper, M. T. M. Cathodic Corrosion of a Bulk Wire to Nonaggregated Functional Nanocrystals and Nanoalloys. *ACS Appl. Mater. Interfaces* **2018**, *10* (11), 9532-9540.

167. Bennett, E.; Monzó, J.; Humphrey, J.; Plana, D.; Walker, M.; McConville, C.; Fermin, D.; Yanson, A.; Rodriguez, P. A Synthetic Route for the Effective Preparation of Metal Alloy Nanoparticles and Their Use as Active Electrocatalysts. *ACS Catal.* **2016**, *6* (3), 1533-1539.

168. Reier, T.; Oezaslan, M.; Strasser, P. Electrocatalytic Oxygen Evolution Reaction (OER) on Ru, Ir, and Pt Catalysts: A Comparative Study of Nanoparticles and Bulk Materials. *ACS Catal.* **2012**, *2* (8), 1765-1772.

169. Lettenmeier, P.; Majchel, J.; Wang, L.; Saveleva, V. A.; Zafeiratos, S.; Savinova, E. R.; Gallet, J.-J.; Bournel, F.; Gago, A. S.; Friedrich, K. A. Highly Active Nano-Sized Iridium Catalysts: Synthesis and Operando Spectroscopy in a Proton Exchange Membrane Electrolyzer. *Chem. Sci.* **2018**, *9* (14), 3570-3579.

170. Bizzotto, F.; Quinson, J.; Zana, A.; Kirkensgaard, J. J. K.; Dworzak, A.; Oezaslan, M.; Arenz, M. Ir Nanoparticles with Ultrahigh Dispersion as Oxygen Evolution Reaction (OER) Catalysts: Synthesis and Activity Benchmarking. *Catal. Sci. Technol.* **2019**, *9* (22), 6345-6356.

171. Leontyev, I.; Kuriganova, A.; Kudryavtsev, Y.; Dkhil, B.; Smirnova, N. New Life of a Forgotten Method: Electrochemical Route Toward Highly Efficient Pt/C Catalysts for Low-Temperature Fuel Cells. *Appl. Catal. A* **2012**, *431-432*, 120-125.

172. Kuriganova, A. B.; Leontyev, I. N.; Avramenko, M. V.; Popov, Y.; Maslova, O. A.; Koval, O. Y.; Smirnova, N. V. One-Step Simultaneous Synthesis of Graphene and Pt Nanoparticles under the Action of Pulsed Alternating Current and Electrochemical Performance of Pt/Graphene Catalysts. *ChemistrySelect* **2017**, *2* (24), 6979-6983.

173. Hersbach, T. J. P.; McCrum, I. T.; Anastasiadou, D.; Wever, R.; Calle-Vallejo, F.; Koper, M. T. M. Alkali Metal Cation Effects in Structuring Pt, Rh, and Au Surfaces through Cathodic Corrosion. *ACS Appl. Mater. Interfaces* **2018**, *10* (45), 39363-39379.

174. Yanson, A. I.; Antonov, P. V.; Yanson, Y. I.; Koper, M. T. M. Controlling the Size of Platinum Nanoparticles Prepared by Cathodic Corrosion. *Electrochim. Acta* **2013,** *110*, 796-800.

175. Yanson, A. I.; Antonov, P. V.; Rodriguez, P.; Koper, M. T. M. Influence of the Electrolyte Concentration on the Size and Shape of Platinum Nanoparticles Synthesized by Cathodic Corrosion. *Electrochim. Acta* **2013**, *112*, 913-918.

176. Hersbach, T. J. P.; Yanson, A. I.; Koper, M. T. M. Anisotropic Etching of Platinum Electrodes at the Onset of Cathodic Corrosion. *Nat. Commun.* **2016**, *7*, 12653.

177. Carmo, M.; Linardi, M.; Poco, J. G. R. H_2O_2 Treated Carbon Black as Electrocatalyst Support for Polymer Electrolyte Membrane Fuel Cell Applications. *Int. J. Hydrog. Energy* **2008**, *33* (21), 6289-6297.

178. Fichtner, J.; Watzele, S.; Garlyyev, B.; Kluge, R. M.; Haimerl, F.; El-Sayed, H. A.; Li, W.-J.; Maillard, F. M.; Dubau, L.; Chattot, R.; Michalička, J.; Macak, J. M.; Wang, W.; Wang, D.; Gigl, T.; Hugenschmidt, C.; Bandarenka, A. S. Tailoring the Oxygen Reduction Activity of Pt Nanoparticles through Surface Defects: A Simple Top-Down Approach. *ACS Catal.* **2020**, *10* (5), 3131−3142.

179. Antolini, E. Formation of Carbon-Supported PtM Alloys for Low Temperature Fuel Cells: A Review. *Mater. Chem. Phys.* **2003**, *78* (3), 563-573.

180. Bard, A. J.; Faulkner, L. R. Electrochemical Methods: Fundamentals and Applications, 2nd ed.; Wiley: New York, 2001, pp 808-810.

181. Maciá, M. D.; Campiña, J. M.; Herrero, E.; Feliu, J. M. On the Kinetics of Oxygen Reduction on Platinum Stepped Surfaces in Acidic Media. *J. Electroanal. Chem.* **2004**, *564*, 141-150.

182. Wang, J. X.; Markovic, N. M.; Adzic, R. R. Kinetic Analysis of Oxygen Reduction on Pt(111) in Acid Solutions: Intrinsic Kinetic Parameters and Anion Adsorption Effects. *J. Phys. Chem. B* **2004**, *108* (13), 4127-4133.

183. Elgrishi, N.; Rountree, K. J.; McCarthy, B. D.; Rountree, E. S.; Eisenhart, T. T.; Dempsey, J. L. A Practical Beginner's Guide to Cyclic Voltammetry. *J. Chem. Educ.* **2018**, *95* (2), 197-206.

184. Scholz, F. Voltammetric Techniques of Analysis: The Essentials. *ChemTexts* **2015**, *1*, 17.

185. Schmidt, T. J.; Gasteiger, H. A.; Stäb, G. D.; Urban, P. M.; Kolb, D. M.; Behm, R. J. Characterization of High-Surface-Area Electrocatalysts Using a Rotating Disk Electrode Configuration. *J. Electrochem. Soc.* **1998**, *145* (7), 2354−2358.

186. Kocha, S. S.; Shinozaki, K.; Zack, J. W.; Myers, D. J.; Kariuki, N. N.; Nowicki, T.; Stamenkovic, V.; Kang, Y.; Li, D.; Papageorgopoulos, D. Best Practices and Testing Protocols for Benchmarking ORR Activities of Fuel Cell Electrocatalysts Using Rotating Disk Electrode. *Electrocatalysis* **2017**, *8* (4), 366-374.

187. Wei, C.; Rao, R. R.; Peng, J.; Huang, B.; Stephens, I. E. L.; Risch, M.; Xu, Z. J.; Shao-Horn, Y. Recommended Practices and Benchmark Activity for Hydrogen and Oxygen Electrocatalysis in Water Splitting and Fuel Cells. *Adv. Mater.* **2019**, *31* (31), 1806296.

188. Nikolic, J.; Expósito, E.; Iniesta, J.; González-Garcia, J.; Montiel, V. Theoretical Concepts and Applications of a Rotating Disk Electrode. *J. Chem. Educ.* **2000**, *77* (9), 1191-1194.

189. Zhou, R.; Zheng, Y.; Jaroniec, M.; Qiao, S.-Z. Determination of the Electron Transfer Number for the Oxygen Reduction Reaction: From Theory to Experiment. *ACS Catal.* **2016**, *6* (7), 4720-4728.

190. Sheng, W.; Chen, S.; Vescovo, E.; Shao-Horn, Y. Size Influence on the Oxygen Reduction Reaction Activity and Instability of Supported Pt Nanoparticles. *J. Electrochem. Soc.* **2012**, *159* (2), B96-B103.

191. Beyhan, S.; Şahin, N. E.; Pronier, S.; Léger, J.-M.; Kadırgan, F. Comparison of Oxygen Reduction Reaction on Pt/C, Pt-Sn/C, Pt-Ni/C, and Pt-Sn-Ni/C Catalysts Prepared by Bönnemann Method: A Rotating Ring Disk Electrode Study. *Electrochim. Acta.* **2015**, *151*, 565-573.

192. You, B.; Jiang, N.; Sheng, M.; Drisdell, W. S.; Yano, J.; Sun, Y. Bimetal-Organic Framework Self-Adjusted Synthesis of Support-Free Nonprecious Electrocatalysts for Efficient Oxygen Reduction. *ACS Catal.* ***2015*****,** *5* (12), 7068-7076.

193. Takahashi, I.; Kocha, S. S. Examination of the Activity and Durability of PEMFC Catalysts in Liquid Electrolytes. *J. Power Sources* **2010**, *195* (19), 6312-6322.

194. Garsany, Y.; Baturina, O. A.; Swider-Lyons, K. E.; Kocha, S. S. Experimental Methods for Quantifying the Activity of Platinum Electrocatalysts for the Oxygen Reduction Reaction, *Anal. Chem.* **2010**, *82* (15), 6321-6328.

195. Garsany, Y.; Singer, I. L.; Swider-Lyons, K. E. Impact of Film Drying Procedures on RDE Characterization of Pt/VC Electrocatalysts, *J. Electroanal. Chem.* **2011**, *662* (2), 396-406.

196. Shinozaki, K.; Zack, J. W.; Richards, R. M.; Pivovar, B. S.; Kocha, S. S. Oxygen Reduction Reaction Measurements on Platinum Electrocatalysts Utilizing Rotating Disk Electrode Technique I. Impact of Impurities, Measurement Protocols and Applied Corrections. *J. Electrochem. Soc.* **2015**, *162* (10), F1144-F1158.

197. Shinozaki, K.; Zack, J. W.; Pylypenko, S.; Pivovar, B. S.; Kocha, S. S. Oxygen Reduction Reaction Measurements on Platinum Electrocatalysts Utilizing Rotating Disk Electrode Technique II. Influence of Ink Formulation, Catalyst Layer Uniformity and Thickness. *J. Electrochem. Soc.* **2015**, *162* (12), F1384-F1396.

198. Watzele, S.; Hauenstein, P.; Liang, Y.; Xue, S.; Fichtner, J.; Garlyyev, B.; Scieszka, D.; Claudel, F.; Maillard, F.; Bandarenka, A. S. Determination of Electroactive Surface Area of Ni-, Co-, Fe-, and Ir-Based Oxide Electrocatalysts. *ACS Catal.* **2019**, *9* (10), 9222-9230.

---

199. Rodríguez, J. M. D.; Melián, J. A. H.; Peña, J. P. Determination of the Real Surface Area of Pt Electrodes by Hydrogen Adsorption Using Cyclic Voltammetry. *J. Chem. Educ.* **2000**, *77* (9), 1195-1197.

200. Pozio, A.; De Francesco, M.; Cemmi, A.; Cardellini, F.; Giorgi, L. Comparison of High Surface Pt/C Catalysts by Cyclic Voltammetry. *J. Power Sources* **2002**, *105* (1), 13-19.

201. Watt-Smith, M. J.; Friedrich, J. M.; Rigby, S. P.; Ralph, T. R.; Walsh, F. C. Determination of the Electrochemically Active Surface Area of Pt/C PEM Fuel Cell Electrodes Using Different Adsorbates. *J. Phys. D: Appl. Phys.* **2008**, *41* (17), 174004.

202. Chen, D.; Tao, Q.; Liao, L. W.; Liu, S. X.; Chen, Y. X.; Ye, S. Determining the Active Surface Area for Various Platinum Electrodes. *Electrocatalysis* **2011**, *2* (3), 207-219.

203. Binninger, T.; Fabbri, E.; Kotz, R.; Schmidt, T. J. Determination of the Electrochemically Active Surface Area of Metal-Oxide Supported Platinum Catalyst. *J. Electrochem. Soc.* **2014**, *161* (3), H121-H128.

204. Łukaszewski, M.; Soszko, M.; Czerwiński, A. Electrochemical Methods of Real Surface Area Determination of Noble Metal Electrodes - An Overview. *Int. J. Electrochem. Sci.* **2016**, *11* (6), 4442-4469.

205. Rudi, S.; Cui, C.; Gan, L.; Strasser, P. Comparative Study of the Electrocatalytically Active Surface Areas (ECSAs) of Pt Alloy Nanoparticles Evaluated by H_{upd} and CO-Stripping Voltammetry. *Electrocatalysis* **2014**, *5* (4), 408-418.

206. Myland, J. C.; Oldham, K. B. Uncompensated Resistance. 1. The Effect of Cell Geometry. *Anal. Chem.* **2000**, *72* (17), 3972-3980.

207. Oldham, K. B.; Stevens, N. P. Uncompensated Resistance. 2. The Effect of Reference Electrode Nonideality. *Anal. Chem.* **2000**, *72* (17), 3981-3988.

208. Čolić, V.; Tymoczko, J.; Maljusch, A.; Ganassin, A.; Schuhmann, W.; Bandarenka, A. S. Experimental Aspects in Benchmarking of the Electrocatalytic Activity. *ChemElectroChem* **2015**, *2* (1), 143-149.

209. Mayrhofer, K. J. J.; Strmcnik, D.; Blizanac, B. B.; Stamenkovic, V.; Arenz, M.; Markovic, N. M. Measurement of Oxygen Reduction Activities via the Rotating Disc Electrode Method: From Pt Model Surfaces to Carbon-Supported High Surface Area Catalysts. *Electrochim. Acta* **2008**, *53* (7), 3181-3188.

210. Harzer, G. S.; Schwämmlein, J. N.; Damjanović, A. M.; Ghosh, S.; Gasteiger, H. A. Cathode Loading Impact on Voltage Cycling Induced PEMFC Degradation: A Voltage Loss Analysis. *J. Electrochem. Soc.* **2018**, *165* (6), F3118-F3131.

211. Schwämmlein, J. N.; Harzer, G. S.; Pfändner, P.; Blankenship, A.; El-Sayed, H. A.; Gasteiger, H. A. Activity and Stability of Carbon Supported Pt_xY Alloys for the ORR Determined by RDE and Single-Cell PEMFC Measurements. *J. Electrochem. Soc.* **2018**, *165* (15), J3173-J3185.

212. Berliba-Vera, E. K.; Delariva, A. T.; Atanassov, P.; Datye, A. K.; Garzón, F. H. Nucleation of Platinum on Carbon Blacks. *ECS Trans.* **2010**, *33* (1), 73-82.

213. Delgass, W. N.; Hughes, T. R.; Fadley, C. S. X-ray Photoelectron Spectroscopy: A Tool for Research in Catalysis. *Catal. Rev.* **1971**, *4* (1), 179-220.

214. Shindo, D.; Oikawa, T. Analytical Electron Microscopy for Materials Science. Springer: Tokyo, 2002, pp 81-102.

215. Erni, R.; Rossell, M. D.; Kisielowski, C.; Dahmen, U. Atomic-Resolution Imaging with a Sub-50-pm Electron Probe. *Phys. Rev. Lett.* **2009**, *102* (9), 096101.

216. Smith, D. J. Ultimate Resolution in the Electron Microscope? *Mater. Today* **2008**, *11*, 30-38.

217. Su, D. Advanced Electron Microscopy Characterization of Nanomaterials for Catalysis. *Green Energy Environ.* **2017**, *2* (2), 70-83.

218. Zhang, L.; Shi, W.; Zhang, B. A Review of Electrocatalyst Characterization by Transmission Electron Microscopy. *J. Energy Chem.* **2017**, *26* (6), 1117-1135.

219. Seiler, H. Secondary Electron Emission in the Scanning Electron Microscope. *J. Appl. Phys.* **1983**, *54* (11), R1-R18.

220. Robinson, V. N. E. Imaging with Backscattered Electrons in a Scanning Electron Microscope. *Scanning* **1980**, *3* (1), 15-26.

221. Michler, G. H. Electron Microscopy of Polymers. Springer: Berlin, 2008, pp 7-49.

222. Klein, N. D.; Hurley, K. R.; Feng, Z. V.; Haynes, C. L. Dark Field Transmission Electron Microscopy as a Tool for Identifying Inorganic Nanoparticles in Biological Matrices. *Anal. Chem.* **2015**, *87* (8), 4356-4362.

223 . Bendersky, L. A.; Gayle, F. W. Electron Diffraction Using Transmission Electron Microscopy. *J. Res. Natl. Inst. Stand. Technol.* **2001**, *106* (6), 997-1012.

224. Otten, M. T. High-Angle Annular Dark-Field Imaging on a TEM/STEM System. *J. Electron Microsc. Tech.* **1991**, *17* (2), 221-230.

---

225. Ercius, P.; Alaidi, O.; Rames, M. J.; Ren, G. Electron Tomography: A Three-Dimensional Analytic Tool for Hard and Soft Materials Research. *Adv. Mater.* **2015**, *27* (38), 5638-5663.

226. Goodhew, P. J.; Humphreys, J.; Beanland, R. Electron Microscopy and Analysis, 3rd ed.; CRC Press: Boca Raton, 2000.

227. Schneider, C. A.; Rasband, W. S.; Eliceiri, K. W. NIH Image to ImageJ: 25 Years of Image Analysis. *Nat. Methods* **2012**, *9* (7), 671-675.

228. Garsany, Y.; Ge, J.; St-Pierre, J.; Rocheleau, R.; Swider-Lyons, K. E. Analytical Procedure for Accurate Comparison of Rotating Disk Electrode Results for the Oxygen Reduction Activity of Pt/C. *J. Electrochem. Soc.* **2014**, *161* (5), F628-F640.

229. Lee, M. X-ray Diffraction for Materials Research: From Fundamentals to Applications. Apple Academic Press: Waretown, 2017, pp 117-124.

230. Holder, C. F.; Schaak, R. E. Tutorial on Powder X-ray Diffraction for Characterizing Nanoscale Materials. *ACS Nano* **2019**, *13* (7), 7359-7365.

231. Bokhimi; Morales, A.; Lucatero, M. A.; Ramírez, R. Rietveld Refinement of Nanocrystalline Phases. *Nanostruct. Mater.* **1997**, *9* (1-8), 315-318.

232. Maniammal, K.; Madhu, G.; Biju, V. X-ray Diffraction Line Profile Analysis of Nanostructured Nickel Oxide: Shape Factor and Convolution of Crystallite Size and Microstrain Contributions. *Physica E Low Dimens. Syst. Nanostruct.* **2017**, *85*, 214-222.

233. Giannini, C.; Ladisa, M.; Altamura, D.; Siliqi, D.; Sibillano, T.; De Caro, L. X-ray Diffraction: A Powerful Technique for the Multiple-Length-Scale Structural Analysis of Nanomaterials. *Crystals* **2016**, *6* (8), 87.

234. Garlyyev, B.; Watzele, S.; Fichtner, J.; Michalička, J.; Schökel A.; Senyshyn, A.; Perego, A.; Pan, D.; El-Sayed, H. A.; Macak, J. M.; Atanassov, P.; Zenyuk, I. V.; Bandarenka, A. S. Electrochemical Top-Down Synthesis of C-Supported Pt Nanoparticles with Controllable Shape and Size: Mechanistic Insights and Application. *Nano Res.* **2020**, accepted, https://doi.org/10.1007/s12274-020-3281-z.

235. Garlyyev, B.; Kratzl, K.; Rück, M.; Michalička, J.; Fichtner, J.; Macak, J. M.; Kratky, T.; Günther, S.; Cokoja, M.; Bandarenka, A. S.; Gagliardi, A.; Fischer, R. A. Optimizing the Size of Platinum Nanoparticles for Enhanced Mass Activity in the Electrochemical Oxygen Reduction Reaction. *Angew. Chem. Int. Ed.* **2019**, *58* (28), 9596-9600.

---

236. Sharma, R.; Wang, Y.; Li, F.; Chamier, J.; Andersen, S. M. Particle Size-Controlled Growth of Carbon-Supported Platinum Nanoparticles (Pt/C) through Water-Assisted Polyol Synthesis. *ACS Omega* **2019**, *4* (13), 15711-15720.

237. Zhao, J.; Chen, W.; Zheng, Y.; Li, X.; Xu, Z. Microwave Polyol Synthesis of Pt/C Catalysts with Size-Controlled Pt Particles for Methanol Electrocatalytic Oxidation. *J. Mater. Sci.* **2006**, *41* (17), 5514-5518.

238. Yung, T.-Y.; Lee, J.-Y.; Liu, L.-K. Nanocomposite for Methanol Oxidation: Synthesis and Characterization of Cubic Pt Nanoparticles on Graphene Sheets. *Sci. Technol. Adv. Mat.* **2013**, *14* (3), 035001.

239. Kim, J. H.; Cheon, J. Y.; Shin, T. J.; Park, J. Y.; Joo, S. H. Effect of Surface Oxygen Functionalization of Carbon Support on the Activity and Durability of Pt/C Catalysts for the Oxygen Reduction Reaction. *Carbon* **2016**, *101*, 449-457.

240 . Wang, G.; Parrondo, J.; He, C.; Li, Y.; Ramani, V. Pt/C/Ni(OH)$_2$ Bi-Functional Electrocatalyst for Enhanced Hydrogen Evolution Reaction Activity under Alkaline Conditions. *J. Electrochem. Soc.* **2017**, *164* (13), F1307-F1315.

241. Li, Z.; Li, Y.; He, C.; Shen, P. K. Bimetallic PtAg Alloyed Nanoparticles and 3-D Mesoporous Graphene Nanosheet Hybrid Architectures for Advanced Oxygen Reduction Reaction Electrocatalysts. *J. Mater. Chem. A* **2017**, *5* (44), 23158-23169.

242. Lesiak, B.; Kövér, L.; Tóth, J.; Zemek, J.; Jiricek, P.; Kromka, A.; Rangam, N. C sp^2/sp^3 Hybridisations in Carbon Nanomaterials - XPS and (X) AES Study. *Appl. Surf. Sci.* **2018**, *452*, 223-231.

243. Han, H.; Lee, J.; Park, D. W.; Shim, S. E. Surface Modification of Carbon Black by Oleic Acid for Miniemulsion Polymerization of Styrene. *Macromol. Res.* **2010**, *18* (5), 435-441.

244. Walter, D. Primary Particles – Agglomerates – Aggregates. In: Nanomaterials. Wiley-VCH: Weinheim, 2013, pp 9-14. https://www.dfg.de/download/pdf/dfg_im_profil/gremien/senat/arbeitsstoffe/nanomaterials.pdf (accessed April 06, 2020).

245. Colmati, F.; Antolini, E.; Gonalez, E. R. Ethanol Oxidation on Carbon Supported Pt-Sn Electrocatalysts Prepared by Reduction with Formic Acid. *J. Electrochem. Soc.* **2007**, *154* (1), B39-B47.

246. Li, Y.; Zhang, X.; Wang, S.; Sun, G. Durable Platinum-Based Electrocatalyst Supported by Multiwall Carbon Nanotubes Modified with CeO$_2$. *ChemElectroChem* **2018**, *5* (17), 2442-2448.

247. Sneed, B. T.; Cullen, D. A.; Reeves, K. S.; Dyck, O. E.; Langlois, D. A.; Mukundan, R.; Borup, R. L.; More, K. L. 3D Analysis of Fuel Cell Electrocatalyst Degradation on Alternate Carbon Supports. *ACS Appl. Mater. Interfaces* **2017**, *9* (35), 29839– 29848.

248. Mayrhofer, K. J. J.; Meier, J. C.; Ashton, S. J.; Wiberg, G. K.; Kraus, F.; Hanzlik, M.; Arenz, M. Fuel Cell Catalyst Degradation on the Nanoscale. *Electrochem. Commun.* **2008**, *10* (8), 1144–1147.

249. Meier, J. C.; Galeano, C.; Katsounaros, I.; Topalov, A. A.; Kostka, A.; Schüth, F.; Mayrhofer, K. J. J. Degradation Mechanisms of Pt/C Fuel Cell Catalysts Under Simulated Start-Stop Conditions. *ACS Catal.* **2012**, *2* (5), 832– 843.

250. Maillard, F.; Schreier, S.; Hanzlik, M.; Savinova, E. R.; Weinkauf, S.; Stimming, U. Influence of Particle Agglomeration on the Catalytic Activity of Carbon-Supported Pt Nanoparticles in CO Monolayer Oxidation. *Phys. Chem. Chem. Phys.* **2005**, *7* (2), 385-393.

251. Zhang, Z.; Ódor, É.; Farkas, D.; Jóni, B.; Ribárik, G.; Tichy, G.; Nandam, S.-H.; Ivanisenko, J.; Preuss, M.; Ungár, T. Dislocations in Grain Boundary Regions: The Origin of Heterogeneous Microstrains in Nanocrystalline Materials. *Metall. Mater. Trans. A* **2020**, *51* (1), 513-530.

252. Kriston, Á.; Xie, T.; Gamliel, D.; Ganesan, P.; Popov, B. N. Effect of Ultra-Low Pt Loading on Mass Activity of Polymer Electrolyte Membrane Fuel Cells. *J. Power Sources* **2013**, *243*, 958-963.

253. Huang, X.; Zhao, Z.; Fan, J.; Tan, Y.; Zheng, N. Amine-Assisted Synthesis of Concave Polyhedral Platinum Nanocrystals Having {411} High-Index Facets. *J. Am. Chem. Soc.* **2011**, *133* (13), 4718-4721.

254. Wu, Y.; Wang, D.; Niu, Z.; Chen, P.; Zhou, G.; Li, Y. A Strategy for Designing a Concave Pt–Ni Alloy through Controllable Chemical Etching. *Angew. Chem. Int. Ed.* **2012**, *51* (50), 12524-12528.

255. Xia, B. Y.; Wu, H. B.; Wang, X.; Lou, X. W. Highly Concave Platinum Nanoframes with High-Index Facets and Enhanced Electrocatalytic Properties. *Angew. Chem. Int. Ed.* **2013**, *52* (47), 12337-12340.

256. Wang, C.; Ma, L.; Liao, L.; Bai, S.; Long, R.; Zuo, M.; Xiong, Y. A Unique Platinum-Graphene Hybrid Structure for High Activity and Durability in Oxygen Reduction Reaction. *Sci. Rep.* **2013**, *3*, 2580.

257. Li, Q.; Rellán-Piñeiro, M.; Almora-Barrios, N.; Garcia-Ratés, M.; Remediakis, I. N.; López, N. Shape Control in Concave Metal Nanoparticles by Etching. *Nanoscale* **2017**, *9* (35), 13089-13094.

258. Yu, T.; Kim, D. Y.; Zhang, H.; Xia, Y. Platinum Concave Nanocubes with High-Index Facets and Their Enhanced Activity for Oxygen Reduction Reaction. *Angew. Chem. Int. Ed.* **2011**, *50* (12), 2773-2777.

259. Wan, X. X.; Zhang, D.-F.; Guo, L. Concave Pt–Cu Nanocuboctahedrons with High-Index Facets and Improved Electrocatalytic Performance. *CrystEngComm* **2016**, *18* (18), 3216-3222.

260. Ma, Y.; Yin, L.; Yang, T.; Huang, Q.; He, M.; Zhao, H.; Zhang, D.; Wang, M.; Tong, Z. One-Pot Synthesis of Concave Platinum–Cobalt Nanocrystals and Their Superior Catalytic Performances for Methanol Electrochemical Oxidation and Oxygen Electrochemical Reduction. *ACS Appl. Mater. Interfaces* **2017**, *9* (41), 36164-36172.

261. Kühl, S.; Gocyla, M.; Heyen, H.; Selve, S.; Heggen, M.; Dunin-Borkowski, R. E.; Strasser, P. Concave Curvature Facets Benefit Oxygen Electroreduction Catalysis on Octahedral Shaped PtNi Nanocatalysts. *J. Mater. Chem. A* **2019**, *7* (3), 1149-1159.

262. Qin, W.; Szpunar, J. A. Origin of Lattice Strain in Nanocrystalline Materials. *Philos. Mag. Lett.* **2005**, *85* (12), 649– 656.

263. Montejano-Carrizales, J. M.; Morán-López, J. L. Geometrical Characteristics of Compact Nanoclusters. *Nanostruct. Mater.* **1992**, *1* (5), 397-409.

264. Montejano-Carrizales, J. M.; Aguilera-Granja, F.; Morán-López, J. L. Direct Enumeration of the Geometrical Characteristics of Clusters. *Nanostruct. Mater.* **1997**, *8* (3), 269-287.

265. Siegel, R. W. Positron Annihilation Spectroscopy. *Annu. Rev. Mater. Sci.* **1980**, *10*, 393-425.

266. Chen, Z.-Y.; Chen, Z. Q.; Wang, D. D.; Wang, S. J. Correlation Between Interfacial Defects and Ferromagnetism of $BaTiO_3$ Nanocrystals Studied by Positron Annihilation. *Appl. Surf. Sci.* **2011**, *258* (1), 19-23.

267. Sharma, S. K.; Pujari, P. K.; Sudarshan, K.; Dutta, D.; Mahapatra, M.; Godbole, S. V.; Jayakumar, O. D.; Tyagi, A. K. Positron Annihilation Studies in ZnO Nanoparticles. *Solid State Commun.* **2009**, *149* (13-14), 550-554.

268 . Vidal-Iglesias, F. J.; Arán-Ais, R. M.; Solla-Gullón, J.; Herrero, E.; Feliu, J. M. Electrochemical Characterization of Shape-Controlled Pt Nanoparticles in Different Supporting Electrolytes. *ACS Catal.* **2012**, *2* (5), 901– 910.

269. Sheng, W.; Zhuang, Z.; Gao, M.; Zheng, J.; Chen, J. G.; Yan, Y. Correlating Hydrogen Oxidation and Evolution Activity on Platinum at Different pH with Measured Hydrogen Binding Energy. *Nat. Commun.* **2015**, *6*, 5848.

270. Taylor, S.; Fabbri, E.; Levecque, P.; Schmidt, T. J.; Conrad, O. The Effect of Platinum Loading and Surface Morphology on Oxygen Reduction Activity. *Electrocatalysis* **2016**, *7* (4), 287-296.

271. Maillard, F.; Eikerling, M.; Cherstiouk, O. V.; Schreier, S.; Savinova, E.; Stimming, U. Size Effects on Reactivity of Pt Nanoparticles in CO Monolayer Oxidation: The Role of Surface Mobility. *Faraday Discuss.* **2004**, *125*, 357-377.

272. Chattot, R.; Martens, I.; Scohy, M.; Herranz, J.; Drnec, J.; Maillard, F.; Dubau, L. Disclosing Pt-Bimetallic Alloy Nanoparticle Surface Lattice Distortion with Electrochemical Probes. *ACS Energy Lett.* **2020**, *5* (1), 162-169.

273. Kuttiyiel, K. A.; Sasaki, K.; Choi, Y.; Su, D.; Liu, P.; Adzic, R. R. Bimetallic IrNi Core Platinum Monolayer Shell Electrocatalysts for the Oxygen Reduction Reaction. *Energy Environ. Sci.* **2012**, *5* (1), 5297-5304.

274. Godínez-Salomón, F.; Rhodes, C. P.; Alcantara, K. S.; Zhu, Q.; Canton, S. E.; Calderon, H. A.; Reyes-Rodríguez, J. L.; Leyva, M. A.; Solorza-Feria, O. Tuning the Oxygen Reduction Activity and Stability of $Ni(OH)_2$@Pt/C Catalysts through Controlling Pt Surface Composition, Strain, and Electronic Structure. *Electrochim. Acta* **2017**, *247*, 958-969.

275. Pizzutilo, E.; Knossalla, J.; Geiger, S.; Grote, J.-P.; Polymeros, G.; Baldizzone, C.; Mezzavilla, S.; Ledendecker, M.; Mingers, A.; Cherevko, S.; Schüth, F.; Mayrhofer. K. J. J. The Space Confinement Approach Using Hollow Graphitic Spheres to Unveil Activity and Stability of Pt-Co Nanocatalysts for PEMFC. *Adv. Energy Mater.* **2017**, *7* (20), 1700835.

276. Borup, R. L.; Davey, J. R.; Garzon, F. H.; Wood, D. L.; Inbody, M. A. PEM Fuel Cell Electrocatalyst Durability Measurements. *J. Power Sources* **2006**, *163* (1), 76-81.

277. Greszler, T. A.; Caulk, D.; Sinha, P. The Impact of Platinum Loading on Oxygen Transport Resistance. *J. Electrochem. Soc.* **2012**, *159* (12), F831-F840.

278. Fichtner, J.; Garlyyev, B.; Watzele, S.; El-Sayed, H. A.; Schwämmlein, J. N.; Li, W.-J.; Maillard, F. M.; Dubau, L.; Michalička, J.; Macak, J. M.; Holleitner, A.; Bandarenka, A. S. Top-Down Synthesis of Nanostructured Platinum-Lanthanide Alloy Oxygen Reduction Reaction Catalysts: Pt_xPr/C as an Example. *ACS Appl. Mater. Interfaces* **2019**, *11* (5), 5129–5135.

---

279. Greenwood, N. N.; Earnshaw, A. Chemistry of the Elements, 2nd ed.; Elsevier: Oxford, 2012, pp 1232-1235.

280. Corradini, P. G.; Antolini, E.; Perez, J. Structural and Electrochemical Characterization of Carbon Supported Pt–Pr Catalysts for Direct Ethanol Fuel Cells Prepared Using a Modified Formic Acid Method in a CO Atmosphere. *Phys. Chem. Chem. Phys.* **2013**, *15* (28), 11730-11739.

281. Um, N.; Hirato, T. Dissolution Behavior of La_2O_3, Pr_2O_3, Nd_2O_3, CaO and Al_2O_3 in Sulfuric Acid Solutions and Study of Cerium Recovery from Rare Earth Polishing Powder Waste via Two-Stage Sulfuric Acid Leaching. *Mater. Trans.* **2013**, *54* (5), 713-719.

282. Savin, V. D.; Elyutin, A. V.; Mikhajlova, N. P.; Eremenko, Z. V.; Opolchenova, N. L. Regularities of Praseodymium Oxide Dissolution in Acids. *Tsvetnye Metally* **1989**, *8*, 75-79.

283. You, H.; Yang, S.; Ding, B.; Yang, H. Synthesis of Colloidal Metal and Metal Alloy Nanoparticles for Electrochemical Energy Applications. *Chem. Soc. Rev.* **2013**, *42* (7), 2880-2904.

284. Yang, H.; Vogel, W.; Lamy, C.; Alonso-Vante, N. Structure and Electrocatalytic Activity of Carbon-Supported Pt-Ni Alloy Nanoparticles toward the Oxygen Reduction Reaction. *J. Phys. Chem. B* **2004**, *108* (30), 11024-11034.

285. Rhodes, C. J. Endangered Elements, Critical Raw Materials and Conflict Minerals. *Sci. Progress* **2019**, *102* (4), 304-350.

286. Durst, J.; Lopez-Haro, M.; Dubau, L.; Chatenet, M.; Soldo-Olivier, Y.; Guétaz, L.; Bayle-Guillemaud, P.; Maillard, F. Reversibility of Pt-Skin and Pt-Skeleton Nanostructures in Acidic Media. *J. Phys. Chem. Lett.* **2014**, *5* (3), 434-439.

287. Jeon, T. Y.; Kim, S. K.; Pinna, N.; Sharma, A.; Park, J.; Lee, S. Y.; Lee, H. C.; Kang, S.-E.; Lee, H.-K.; Lee, H. H. Selective Dissolution of Surface Nickel Close to Platinum in PtNi Nanocatalyst toward Oxygen Reduction Reaction. *Chem. Mat.* **2016**, *28* (6), 1879-1887.

288. Strasser, P.; Kühl, S. Dealloyed Pt-Based Core-Shell Oxygen Reduction Electrocatalysts. *Nano Energy* **2016**, *29*, 166-177.

289. Wang, C.; Chi, M.; Li, D.; Strmcnik, D.; van der Vliet, D.; Wang, G.; Komanicky, V.; Chang, K.-C.; Paulikas, A. P.; Tripkovic, D.; Pearson, J.; More, K. L.; Markovic, N. M.; Stamenkovic, V. R. Design and Synthesis of Bimetallic Electrocatalyst with Multilayered Pt-Skin Surfaces. *J. Am. Chem. Soc.* **2011**, *133* (36), 14396-14403.

290. Rudi, S.; Teschner, D.; Beermann, V.; Hetaba, W.; Gan, L.; Cui, C.; Gliech, M.; Schlögl, R.; Strasser, P. pH-Induced Versus Oxygen-Induced Surface Enrichment and Segregation Effects in Pt-Ni Alloy Nanoparticle Fuel Cell Catalysts. *ACS Catal.* **2017**, *7* (9), 6376-6384.

291. Stephens, I. E. L.; Bondarenko, A. S.; Perez-Alonso, F. J.; Calle-Vallejo, F.; Bech, L.; Johansson, T. P.; Jepsen, A. K.; Frydendal, R.; Knudsen, B. P.; Rossmeisl, J.; Chorkendorff, I. Tuning the Activity of Pt(111) for Oxygen Electroreduction by Subsurface Alloying. *J. Am. Chem. Soc.* **2011**, *133* (14), 5485-5491.

292. Kang, W.; Li, R.; Wei, D.; Xu, S.; Wei, S.; Li, H. CTAB-Reduced Synthesis of Urchin-Like Pt–Cu Alloy Nanostructures and Catalysis Study Towards the Methanol Oxidation Reaction. *RSC Adv.* **2015**, *5* (114), 94210-94215.

293. Ammam, M.; Easton, E. B. PtCu/C and Pt(Cu)/C Catalysts: Synthesis, Characterization and Catalytic Activity Towards Ethanol Electrooxidation. *J. Power Sources* **2013**, *222*, 79-87.